Study of long-term sustained operation of gaseous detectors for the high rate environment in CMS

Jérémie Merlin

UNIVERSITÉ DE STRASBOURG

ÉCOLE DOCTORALE Physique et Chimie physique

[ED 182]

THÈSE présentée par :

Jérémie MERLIN

soutenue le : **25 Avril 2016**

pour obtenir le grade de : **Docteur de l'université de Strasbourg**

Discipline/ Spécialité : Physique des particules élémentaires

Etude du fonctionnement à long terme de détecteur gazeux pour l'environnement à haut flux de CMS

THÈSE dirigée par :

[M. J-M. BROM]	Directeur de recherches, université de Strasbourg
[Mme A. SHARMA]	Senior Scientist Physics Departement, CERN

RAPPORTEURS :

[M. J. COLLOT]	Professeur, Université Grenoble Alpes
[M. G. WORMSER]	Directeur de recherches, Centre Scientifique d'Orsay

---

AUTRES MEMBRES DU JURY :

[M. J. BAUDOT]	Professeur, Université de Strasbourg

University of Strasbourg

Doctoral Thesis

Study of long-term sustained operation of gaseous detectors for the high rate environment in CMS

Author:
Jeremie A. Merlin

Supervisors:
Dr. Archana Sharma
Dr. Jean-Marie Brom

A thesis submitted in fulfilment of the requirements for the degree of Doctor of Science : Particle Physics

in the

Institut Pluridisciplinaire Hubert Curien (IPHC)
Conseil Européen pour la Recherche Nucléaire (CERN)

May 2016

UNIVERSITY OF STRASBOURG

Abstract

Institut Pluridisciplinaire Hubert Curien (IPHC)
Conseil Européen pour la Recherche Nucléaire (CERN)

Doctor of Science : Particle Physics

Study of long-term sustained operation of gaseous detectors for the high rate environment in CMS

by Jeremie A. Merlin

The muon system of CMS aims to provide an efficient and fast identification of the muons produced in the proton-proton collisions. However, the forward region of the end-caps is only instrumented with Cathode Strip Chambers (CSC). This lack of redundancy will be problematic after the high-luminosity upgrade of the LHC (HL-LHC), for which the increase of the background rate would degrade the Level-1 trigger performance and thus the selection of interesting physics channels. Moreover, the possible degradation of the CSC performance due to the sustained operation in a high-rate environment could drastically affect the entire muon system. The goal of the CMS muon upgrade is to maintain the L1 trigger rate with maximum selection efficiency in order to fully exploit the HL-LHC. The CMS GEM Collaboration has proposed to instrument the vacant high-eta region of the muon end-caps with Gas Electron Multiplier (GEM) detectors, called GE1/1 chambers. The GEM technology, already used in various high-energy physics experiments, is capable of operating in high-rate environments with detection performance compatible with the CMS requirements.

The Ph.D. subject proposed by the CMS GEM Collaboration aims to demonstrate that the GE1/1 technology is the most suitable choice for the upgrade of the muon end-caps. Three main research projects were conducted in this context.

The first project included the precise measurement of the fundamental characteristics of the triple-GEM detectors produced with the single-mask technique. The geometry of such GEM foils differs from the standard double-mask technique, inducing differences in the effective gain, the short-term stability and the rate capability. Those characteristics are essential to ensure that the detectors can operate in the forward region of CMS. In addition, the detection performance of the GE1/1 detectors were measured with intense beams of high energy muons and hadrons. The detectors under test were associated

to a reference detector system in order to extract the detection efficiency, the spatial resolution and the time resolution. As a result, several working configurations were proposed for the CMS application.

The second project was focused on the long-term operation of GE1/1 detectors, in particular the study of the aging phenomenon. The aging is one of the most critical limitations of the use of gaseous detectors in high-rate environments. It includes all the processes that lead to a significant and permanent degradation of the performance of the detectors (e.g. gain drop, non-uniformity, dark current, self-sustained discharges and resolution loss). Several aging tests were performed at the CERN irradiation facilities to prove that the GE1/1 chambers can operate during at least 10 years at HL-LHC without suffering from performance losses. To complement the aging tests, an extensive outgassing study was conducted with the GE1/1 materials to make sure that none of them will release pollution in the gas mixture and trigger premature aging.

The excellent properties measured during the *R&D* phase led to the approval of the GE1/1 project by the CMS Collaboration. The third project, conducted in the framework of the mass production, consisted of developing of the main steps of the Quality Control of the GE1/1 chambers. A particular attention was paid to the uniformity of the effective gain, which relates to the uniformity of the detection performance over the entire surface of the GE1/1 chambers. A new technique was proposed to measure simultaneously the gain in all the 3072 readout channels of one chamber. This technique allows reducing the duration of the test down to two days while maintaining the maximum granularity.

A majority of the results obtained during the three years of Ph.D. contributed to the success of the project and its approval by CMS and the LHCC. Moreover, numerous tools and procedures were established both for *R&D* activities and the mass production.

UNIVERSITY OF STRASBOURG

Résumé

Institut Pluridisciplinaire Hubert Curien (IPHC)
Conseil Européen pour la Recherche Nucléaire (CERN)

Grade de docteur : physique des particules

Study of long-term sustained operation of gaseous detectors for the high rate environment in CMS

par Jeremie A. Merlin

Le spectromètre à muons de CMS doit permettre l'identification rapide et efficace des muons produits lors des collisions proton-proton au LHC. Cependant, à cause d'un environnement de détection extrême, seules les chambres à piste cathodique (CSC) équipent actuellement les bouchons de CMS. Cette faiblesse dans le système de détection pourrait devenir problématique après l'amélioration du LHC. L'augmentation du taux de particules dans les bouchons va dégrader les performances du système de déclenchement L1 ainsi que l'efficacité de sélection des phénomènes physiques intéressants. De plus, la possible dégradation des chambres CSC provoquée par l'utilisation prolongée dans un environnement à fort taux de particules affecterait directement le spectromètre à muons. Le but du programme d'amélioration de CMS est de maintenir le taux de déclenchement L1 tout en gardant une efficacité de sélection maximale. La collaboration CMS GEM propose d'équiper les régions vacantes des bouchons avec des détecteurs basés sur la technologie d'amplification des électrons dans un gaz (GEM), appelés GE1/1. La technologie GEM, déjà utilisée dans différentes expériences de physique des particules, est capable de fonctionner dans des environnements extrêmes avec des performances adaptées aux besoins de CMS.

Dans ce contexte, le sujet de thèse proposé par la collaboration CMS GEM a pour but de démontrer les qualités des détecteurs GE1/1 et de justifier le choix de la technologie GEM pour l'amélioration de CMS. Ainsi, trois projets ont été suivis pendant la thèse.

L'une des particularités des feuilles de GEM utilisées dans les nouveaux détecteurs GE1/1 est la méthode de fabrication. En effet, la technique initiale, dite "double-masque", consiste à transférer la géométrie des trous microscopiques à l'aide de deux masques identiques apposés sur chaque face de la feuille. La gravure électrochimique se faisant simultanément à travers les deux masques, la géométrie des trous ainsi obtenue

est parfaitement symétrique. Toutefois, bien que cette méthode soit validée et déjà utilisée dans des expériences de physique à hautes énergies, elle n'est pas adaptée à la production de grandes feuilles de GEM à cause d'un problème d'alignement des masques. Une autre technique, dite "simple-masque", est alors nécessaire pour produire les GEM des grands détecteurs GE1/1. Cette méthode consiste à graver les trous microscopiques à partir d'un masque unique. Cependant la forme finale des trous n'est pas parfaitement symétrique, ce qui pourrait affecter le fonctionnement des détecteurs en induisant des différences de comportement selon l'orientation des feuilles de GEM. Ainsi, la première partie du projet de thèse consistait à mesurer précisément les caractéristiques fondamentales des détecteurs triple-GEM produit par la technique simple-masque. Cette étude comprend la mesure du gain effectif, de la stabilité à court terme, du taux maximum de détection et de la probabilité de décharge. Ces éléments sont essentiels pour s'assurer que les détecteurs pourront fonctionner en toute sécurité dans l'environnement des bouchons de CMS. Dans un second temps, les performances de détection ont également été mesurées, à l'aide de faisceaux intenses de muons, afin de prouver que les détecteurs GE1/1 pourront améliorer la détection des muons après leur installation dans CMS. Les détecteurs en test ont été associés à un dispositif de référence pour extraire des informations telles que l'efficacité de détection, la résolution spatiale, qui définit la précision avec laquelle les muons seront localisés dans CMS, et la résolution temporelle qui décrit la qualité des signaux de déclenchement générés par les chambres GE1/1. Les résultats ainsi obtenus ont permis d'établir plusieurs configurations de fonctionnement adaptées à CMS.

Le deuxième projet consistait à prouver que les excellentes performances des détecteurs GE1/1 ne vont pas se dégrader pendant leur utilisation dans CMS. Cette étape comprend l'étude du fonctionnement à long terme des détecteurs GE1/1, en particulier le phénomène de vieillissement. Le vieillissement inclue tous les processus physiques et chimiques qui provoquent la dégradation graduelle et permanente des performances de détection (perte de gain, non-uniformité, courant de fuite, décharges et pertes de résolution). C'est l'une des principales limites pour l'utilisation des détecteurs dans des environnements à très fort taux de particules. Dans le cas de la technologie triple-GEM, l'amplification des signaux est partagée sur plusieurs couches de GEM, et pour chaque GEM sur plusieurs trous. Cette multitude de canaux d'amplification va permettre de réduire la possibilité de déclencher les processus physiques et chimiques responsables du vieillissement. Toutefois, de part leur dimension microscopique, les trous de GEM peuvent être affectés très rapidement par certains effets de vieillissement, même réduit. Plusieurs tests de vieillissement ont été menés dans des zones d'irradiations spécifiques au CERN pour reproduire un minimum de 10 ans de fonctionnement réel dans l'environnement de CMS après la montée en puissance du LHC. En complément de

ces tests, une série d'études de dégazage a été menée avec les matériaux des chambres GE1/1 pour exclure toute source de contamination qui pourrait déclencher ou aggraver le processus de vieillissement.

Enfin, les excellentes propriétés mesurées lors de la phase de *R&D* ont permis de valider la technologie triple-GEM, qui fut ensuite approuvée par la collaboration CMS et le comité du LHC. La production de 144 grands détecteurs GE1/1 sera partagée entre différents sites de production à travers le monde. Pour assurer une production uniforme et une même qualité pour tous les détecteurs, une procédure de contrôle qualité a dû être établie sur la base des résultats obtenus pendant la phase de recherche et d'optimisation des prototypes GE1/1. Le troisième projet de thèse fut donc le développement des principales étapes du contrôle qualité des chambres GE1/1, depuis la réception des composants jusqu'à l'installation finale. Une étape particulièrement importante consiste à mesurer l'uniformité du gain effectif, qui décrit les propriétés géométriques et électriques des détecteurs et qui reflète aussi l'uniformité des performances de détection. Alors que la technique initiale de mesure "secteur-par-secteur" nécessitait plusieurs jours de tests avec un fort risque de perturber les résultats, une nouvelle technique a été mise au point pour mesurer simultanément le gain effectif sur chacun des 3072 canaux de lectures d'un détecteur. Cette technique permet de réduire le temps de mesure à deux jours tout en conservant une granularité maximale et des mesures complètement indépendantes de l'environnement de test.

La majorité des résultats obtenus pendant ces trois années de thèse ont participé au succès du projet et à son approbation pour l'amélioration de CMS. De plus, plusieurs outils de recherche et procédures ont été développés pour la phase de *R&D* et la production en série.

Acknowledgements

All the work achieved during these three years of Ph.D. would not have been possible without the great help from many colleagues and friends. I will do my best to give here a clear list of these people and their contributions to what was, without doubts, the most intense years of my life, so far ...

First of all I would like to thank my supervisors Archana Sharma and Jean-Marie Brom for their great support. You gave me the opportunity to work in the most amazing place for particle physics and thus to make my child dream come true. It has been a real honor to work under your supervision.

I also would like to express my sincere gratitude to Duccio Abbaneo for welcoming me in the CERN PH-CMX group as well as Christelle Roy, Daniel Bloch and Ulrich Goerlach from the French institute IPHC for supporting my work.

I am very grateful to professors Johann Collot, Guy Wormser and Jérôme Baudot who accepted to be part of my jury during the defense of my thesis.

I am also very grateful to professors Luigi Rolandi, Peter Jenni, Albert De Roeck and Alexei Safonov who have taken the time to review the physics introduction of my thesis.

I would like to give a very special thank to Leszek Ropelewski, Marcus Hohlmann and Luigi Benussi, who spent a lot of time and effort to review my work with a great care and give me invaluable advices for my projects.

I would like to give a really big thank to all the RD51 team, the CERN GDD and DT groups, in particular, Eraldo Oliveri, Filippo Resnati, Maxim Titov, Patrik Thuiner, Silvia Franchino, Dorothea Pfeiffer, Hans Müller, Chilo Garabatos Cuadrado, Miranda Van Stenis, Vladimir Peskov, Givi Sekhniaidze, George Glanti, Niel Dixon, Ourania Sidiropoulou and Mar Capeans Garrido. I am not able to describe in few lines all the interactions we had together, both from professional and personal points of view. Your advices were essential to unblock the situation when I had suspicious results or seemingly unsolvable problems. I'll always remember our barbecue parties, dinners, and of course our very fruitful coffee breaks.

There are many people in the CMS GEM Collaboration I would like thank: Gilles De Lentdecker, Paolo Vitulo, Marcello Maggi, Paul Aspell, Anna Colaleo, Paul Karchin, Stefano Bianco, Michael Tytgat, Antonio Ranieri, Kerstin Hoepfner and Antonio Conde Garcia, who spent some of their time to push my work in the right direction. I also would like to warmly thank my colleagues Christopher, Mohsin, Brian, Andrey, Stefano, Ilaria, Sinem, Alejandro, Marek, Michele, Vallary, Aiwu, Jared, Aashaq, Waqar, Florian,

Thierry, Ram, Minkyoo and many more. In addition to your precious help and support, you also made these years truly memorable. Additionally most of my ideas would not have been feasible without the expertise of Hans Postema, Jean-François Pernot, Eric Albert and Herve Sauce. I also want to thank the summer students who came from all over the world to participate to our project: Stephen, Valerio, Rémi, Marco, Manu, Hugo, Tristan, Thomas, Quentin, Jean, Samuel, Dikshant and all the Indian students.

There are many people outside the CMS GEM Collaboration who participated to the success of my experiments: Roberto Guida, Beatrice Mandelli, Richard Fortin and Nicolas Bourgois for the installation of my aging test setup at GIF; Barbora Bartova, Ana Teresa Fontenla and Marina Garcia for the SEM analysis; Andre Zibell, Filippo Costa and Kondo Gnanvo for the DATE and AMORE analysis frameworks; Rui de Oliveira and all his team for the production of the detectors. Thank you very much for your time and your expertise.

Finally, nothing could have been possible without the great support of my parents, my family and my friends who pushed me to pursue my studies and make my dream come true. A special thank goes to my fiancée Alicia who, despite of the stress and sometimes my bad mood, has accepted to become my wife.

Thank you very much to all of you.

Contents

List of Figures

List of Tables

Abbreviations

ADC	**A**nalog to **D**igital **C**onverter
ALICE	**A** **L**arge **I**on **C**ollider **E**xperiment
APV25	**A**nalog **P**ipeline **V**oltage mode - 0.**25** μm CMOS technology
ASIC	**A**pplication-**S**pecific **I**ntegrated **C**ircuit
ATLAS	**A** **T**oroidal **L**HC **A**pparatu**S**
BR	**B**ranching **R**atio
BX	**B**unch **cross**ing
CERN	**C**onseil **E**uropéen pour la **R**echerche **N**ucléaire
CMS	**C**ompact **M**uon **S**olenoid
CSC	**C**athode **S**trip **C**hamber
DAQ	**D**ata **A**c**Q**uisition
DATE	**D**ata **A**cquisition and **T**est **E**nvironment
DT	**D**rift **T**ube
DTC	**D**ata, **T**rigger and **C**ontrol
ECAL	**E**lectromagnetic **CAL**orimeter
EM	**E**lectro**M**agnetic
FEC	**F**ront-**E**nd **C**ard
FPGA	**F**ield **P**rogrammable **G**ate **A**rray
GBT	**G**iga**B**it **T**ransceiver
GC	**G**as **C**hromatography
GEB	**G**EM **E**lectronic **B**oard
GEM	**G**as **E**lectron **M**ultiplier
GE1/1	**G**EM **E**ndcap station **1** ring **1**
GIF	**G**amma **I**rradiation **F**acility
GPIB	**G**eneral **P**urpose **I**nterface and **B**us

HCAL	**H**adronic **CAL**orimeter
HEP	**H**igh **E**nergy **P**hysics
HV	**H**igh **V**oltage
LEP	**L**arge **E**lectron **P**ositron collider
LHC	**L**arge **H**adron **C**ollider
LHCb	**L**arge **H**adron **C**ollider **b**eauty
LINAC	**LI**near **AC**celerator
LS1	**L**ong **S**hutdown **1**
LSP	**L**ightest **S**USY **P**article
ME1/1	**M**uon **E**ndcap station **1** ring **1**
MFC	**M**ass-**F**low **C**ontroller
MPGD	**M**icro-**P**attern **G**aseous **D**etector
MSGC	**M**icro-**S**trip **G**aseous **C**hamber
MSSM	**M**inimal **S**upersymmetric **S**tandard **M**odel
MWPC	**M**ulti-**W**ire **P**roportional **C**hamber
Micromegas	**Micro-me**sh **ga**seous **s**tructure
MIP	**M**inimum **I**onizing **P**article
NIM	**N**uclear **I**nstrument **M**odule
NMSSM	**N**ext-to-**M**inimal **S**upersymmetric **S**tandard **M**odel
OB	**O**utgassing **B**ox
OH	**O**pto-**H**ybrid
PCB	**P**rinted **C**ircuit **B**oard
PLC	**P**rogammable **L**ogic **C**ontroller
PS	**P**roton **S**ynchrotron
PU	**P**oly**U**rethane
QC	**Q**uality **C**ontrol
QDC	**Charge** to **D**igital **C**onverter
QCD	**Q**uantum **C**hromo**D**ynamics
QED	**Q**uantum **E**lectro**D**ynamics
R & D	**R**esearch **&** **D**evelopment
RPC	**R**esistive **P**late **C**hamber
SEM	**S**canning **E**lectron **M**icroscope
SM	**S**tandard **M**odel

SPS	**S**uper **P**roton **S**ynchrotron
SRS	**S**calable **R**eadout **S**ystem
SRU	**S**calable **R**eadout **U**nit
SUSY	**SU**per **SY**mmetry
SWPC	**S**ingle **W**ire **P**roportionnal **C**hamber
TDC	**T**ime to **D**igital **C**onverter
TMB	**T**rigger **M**other **B**oard
TTC	**T**rigger, **T**iming and **C**ontrol
μ **TCA**	**MICRO T**elecommunication and **C**omputing **A**rchitecture
VBF	**V**ector **B**oson **F**usion
VFAT	**V**ery **F**orward **A**TLAS and **T**OTEM
VME	**V**ersa **M**odule **E**uropa bus
ZS	**Z**ero-**S**uppression

To my fiancée Alicia

Chapter 1

General Introduction

The specificity of the scientific research is to demonstrate the veracity of an hypothesis by the experiment and the observation of the processes predicted by this hypothesis. It is particularly true for particle physics, where most of the hypotheses involve infinitesimal objects and invisible phenomena. During the past century, a large community of physicists developed the knowledge and numerous tools to go beyond our limitations and made the invisible world accessible to us. Particle detectors are certainly the most prominent example of this common effort.

This thesis was conducted in the framework of the detector development for the upgrade of the Compact Muon Solenoid (CMS) muon system. The work was mainly focused on the characterization and the long-term operation study of large gaseous detectors based on the Gas Electron Multiplier (GEM) technology. The goal was to ensure that such new detectors can sustain the difficult environment of the CMS muon end-caps with detection performance that significantly improve the overall detection system.

In the next chapter we will give a general introduction on the research in particle physics. After a brief description of the Standard Model (SM) and its limitations, we will highlight the need of exploring physics phenomena beyond the SM in order to validate theories that give a full description of our universe. In this framework we will discuss several important mechanisms of the Higgs physics and non-standard phenomena, devoting a particular attention to the importance of the muon detection for physics discovery.

In the third chapter, we will describe the Large Hadron Collider (LHC) at CERN, in which the proton-proton collisions at high energy and high rate give access to the fundamental components and mechanisms of the universe. We will then discuss the upgrade plan of the LHC that is necessary to explore the physics beyond the SM. In the second part of the chapter we will give a general presentation of the CMS experiment

and its subsystems, with a particular attention to the muon spectrometer. After a general presentation of the CMS upgrades, we will focus on the forward region of the CMS muon end-caps and show how it can be improved by introducing a new technology of detection.

The fourth chapter will introduce the concept of gaseous detector, which is the preferred option for the CMS muon system. A first part will be dedicated to the interaction between particles and matter, especially gaseous media. We will essentially discuss the processes that can be encountered in the CMS environment or during the thesis work. Then we will give a general overview on the operation of gaseous detectors, their development since the beginning of the 20^{th} century and their current applications. We will finish with the GEM-based detectors, the technology chosen for the upgrade of the CMS muon end-caps.

The next chapter will present the GEM proposal for the upgrade of the first station of the CMS muon end-caps, namely the GE1/1 project. We will discuss the technical details of the large GEM-based detectors especially designed for CMS, their particularities and what needs to be done to ensure that they will sustain the operation in the end-cap environment and fulfil the CMS requirements.

In the sixth chapter, we will present the results of the characterization of the GE1/1 detectors: first the study of the fundamental characteristics of the GEM technology for the CMS application, which differs from the ones used in other experiments; then, the measurements of the detection performance when irradiated with high energy muons and hadrons. Finally, we will compare the properties of the GE1/1 detectors with the CMS requirements.

The next chapter will be dedicated to the study of the long-term operation of the GE1/1 chambers. After presenting the different processes that can affect the longevity of the detectors, we will discuss the various aging tests that were performed at CERN in different operating conditions. We will also highlight the effects of the pollution of the gas mixture on the longevity of the chambers and how to extend their lifetime by using non-outgassing materials.

The last chapter will deal with the mass production and the Quality Control (QC) of the GE1/1 detectors. After a general presentation of the QC plan, we will focus on several crucial steps: the electrical test of the GEM foils, the gas leak test and the measurement of the uniformity of the gain, which relates to the uniformity of the detection performance. The discussion will be accompanied with the results obtained with the first prototypes of GE1/1 chambers, and the outlook on the future developments to improve the QC and the commissioning of the detectors.

My Ph.D. work aims to demonstrate the capability of the GEM-based technology and to develop detectors that suit the CMS requirements. The results I obtained during the last three years participated to the success of the project and its approval by CMS and the LHC Committee.

Chapter 2

Physics at the LHC

2.1 Introduction

The purpose of the research in particle physics is to determine the fundamental components of the matter, their properties and the way they interact with each other. In this second chapter, we will briefly introduce the Standard Model of particle physics that describes the elementary particles and their interactions. We will then highlight some of its main limitations and thus the motivations to explore new physics beyond this model. With several examples of the Higgs physics and non-standard phenomena, we will demonstrate the importance of the muon detection for physics discovery and justify the need of improving the muon systems in the High-Energy Physics (HEP) experiments.

2.2 The Standard Model of particle physics

The theoretical elements of the modern particle physics are grouped into the "Standard Model" (SM), a theory based on the gauge invariance principle in the framework of the quantum field theory. This thesis being focused on experimental works, the detailed development of the SM will not be discussed here. However, a complete description can be found at [17].

All predictions given by the SM were verified with a great precision by various experiments, in particular at the LEP (CERN), the Tevatron (Fermilab), HERA (Desy) and more recently at the LHC (CERN). Nevertheless, several experimental observations, discussed in Sec. 2.2.4, are not explained by the SM.

2.2.1 Elementary particles of matter

In the SM, the matter is composed by 12 elementary particles called fermions, identified by their spin equal to 1/2. The fermions are themselves divided into two categories, the charged leptons (electrons e^-, muons μ^- and taus τ^-) with their associated neutrinos (ν_e, ν_μ and ν_τ), and the quarks of the first (u,d), second (c,s) and third (t,b) generation that form the hadronic matter. Additionally, all particles are associated to anti-particles. Elementary particles of the SM and some of their intrinsic properties are listed in Tab. 2.1.

Lepton	**Charge**	**Mass** $[1/c^2]$	**Quark**	**Charge**	**Mass**$[1/c^2]$
Electron e^-	-1	0.511 MeV	u	$+2/3$	2.3 MeV
Electron neutrino ν_e	0	≤ 3 eV	d	$-1/3$	4.8 MeV
Muon μ^-	-1	105.66 MeV	c	$+2/3$	1.275 GeV
Muon neutrino ν_μ	0	≤ 0.19 MeV	s	$-1/3$	95 MeV
Tau τ^-	-1	1777 MeV	t	$+2/3$	173.21 GeV
Tau neutrino ν_τ	0	≤ 18.2 MeV	b	$-1/3$	4.18 GeV

TABLE 2.1: The 12 fermions of the Standard Model with their charge and mass (adapted from [17]). A more detailed description on the mass of the quarks is given at [18] and [11].

2.2.2 Elementary interactions

The SM also defines the quanta of interaction fields, called gauge bosons with a spin-1, which carry the electromagnetic force (neutral boson γ), the strong interaction (eight gluons g_i) and the weak interaction (charged bosons $W^\pm$ and neutral Z). The elementary forces are associated to coupling constants that refer to their strength.

- The Electromagnetic force (EM) applies on all charged particles. It was the first elementary interaction observed by scientists. Initially described by the Maxwell equations in classical physics, it was later expressed by Feynman in the Quantum ElectroDynamics (QED) theory [20]. The EM interaction is the process that allows detecting particles with gaseous detectors.

- The strong interaction influences only the quarks and its own gauge bosons. The force is carried by eight gluons, which can interact with each other. The strong interaction processes are fully described by the Quantum ChromoDynamic (QCD). Because of the confinement principle, only color neutral objects (hadrons) exists free in the nature i.e. the quarks are always grouped together to form baryons (e.g. protons and neutrons) and in bound states of quark and anti-quark pairs (mesons) or three anti-quarks (anti-baryons) [17].

- All elementary particles interact via the weak force that allows heavier fermions decay into lighter fermions. The EM and the weak interactions are unified in the electroweak theory, formulated by Glashow, Salam and Weinberg, which predicts the existence of the gauge bosons $W^{\pm}$ and Z that were discovered at CERN in 1983.

The elementary interactions and their associated bosons are listed in Tab. 2.2.

Interaction	**Influenced particles**	**Strength**	**Gauge bosons**	**Mass**$[1/c^2]$
Strong	quarks, gluons	1	gluons g_i	0
Electromagnetic	charged particles	1/137	photon γ	0
Weak	quarks, leptons	$10^{-5} - 10^{-7}$	$W\pm$ Z	80.42 GeV 91.19 GeV

TABLE 2.2: The three interactions described by the Standard Model and the associated gauge bosons (adapted from [17] and [11]). The strength is relative to the strong interaction.

The fourth elementary interaction, the gravitation, is not included in the SM and already constitutes one of its main limitations.

2.2.3 The Brout-Englert-Higgs mechanism

The Brout-Englert-Higgs (BEH) mechanism was introduced to the SM in order to generate the mass of the heavy bosons and can be extended to generate the mass of the fermions. This hypothesis predicts the existence of a scalar boson with a spin-0, the Higgs boson. The observation of this boson would therefore confirm the BEH mechanism and complete the picture given by the SM. The new particle recently discovered at CERN, discussed in Sec. 2.4.2.3, is most probably the SM Higgs boson.

2.2.4 Limitations

The SM was successfully measured in the last decades with a great precision and over a very large energy range. However, several elements show that the SM cannot be considered as the ultimate theory, but a specific case or an approximation of a wider unified theory. Among others, these elements are:

- Despite of the good matching between predictions and data, there is no theoretical justification for the choice of the SM gauge groups and, by construction, the three generations of fermions. Moreover, the SM is not fully defined by theoretical arguments, but depends on 19 free parameters, such as the mass of the fermions and the interaction coupling constants, which can only be determined by the experiment.

- The SM predicts the existence of anti-matter that is not present in our visible universe.
- Cosmological studies reveal that only 4.9 % of the universe consists of baryons (ordinary matter), the rest being shared between the dark matter and the dark energy. Therefore, the SM only describes a reduced portion of the actual universe.
- The SM does not explain the large differences between the coupling constant of the elementary forces and why they do not converge at high energies.
- The SM does not include the fourth elementary interaction: the gravitation.

2.3 Beyond the Standard Model

Regarding the limitations listed previously, it is believed that another theory, including the SM and covering its missing elements, must be developed and validated by the experiment. One of the most promising candidates is the Super Symmetry, briefly described in the next section.

2.3.1 The Minimal Supersymmetric Standard Model

The Super Symmetry (SUSY) introduces a new gauge invariance relating bosons and fermions in order to overcome the limitations of the SM, unify the coupling constants and include dark matter candidates. As a result, each particle of the SM has a SUSY partner with the same quantum numbers except for the spin which differs by 1/2, i.e. we can associate SUSY bosons (called "sfermions") to the SM fermions. For example the superpartner of the top quark is the "stop" ($\tilde{t}$). Similarly, SUSY fermions (called "bosinos") are the superpartners of the SM bosons. The new particles introduced by the SUSY model are listed in Tab. 2.3.

SM Particle	**SUSY Particle**	**Physical state**
lepton	slepton	$\tilde{e}$, $\tilde{\mu}$, $\tilde{\tau}$
quarks	squarks	$\tilde{u}$, $\tilde{d}$, $\tilde{c}$, $\tilde{s}$, $\tilde{t}$, $\tilde{b}$
gluons	gluinos	$\tilde{g}$
bosons $W^{\pm}$ boson h	winos charged Higgsinos	Mix into charginos $\tilde{\chi}^{\pm}_{1,2}$
boson Z boson γ boson h	zino photino neutral Higgsinos	Mix into neutralinos $\tilde{\chi}^{0}_{1,2,3,4}$

TABLE 2.3: SM particles and the corresponding SUSY partners (adapted from [19]).

The simplest SUSY extension of the SM is the Minimal Supersymmetric Standard Model (MSSM), with the minimum number of five free parameters. In addition to the SUSY partners, this model predicts the existence of an extended Higgs sectors with five bosons: the lightest Higgs h_0 (which is similar to the SM Higgs), two neutral heavy Higgs H, A, and two charged bosons $H^{\pm}$. Two of the most important parameters introduced by the MSSM are the mass of the pseudo-scalar A noted m_A and the parameter $tan\beta$ defined by the ratio of the vacuum expectation values of the Higgs fields. Therefore, the validation of the MSSM must involve the discovery of the predicted particles: sfermions, bosinos and the heavy Higgs and the precise measurement of the free parameters.

SUSY particles could be produced in collider experiments and decay into a cascade of SM particles and Lightest Supersymmetric Particles (LSP) in the final state. However, the LSP are weakly interacting with the matter and would escape the detector system without producing signals. Therefore, the identification of SUSY particles must take into account the missing energy.

Even though no evidence of SUSY particles was found yet, recent studies on the gluinos pair production and the search for dark matter candidates at the LHC already bring limits and constraints on the mass of the SUSY particles [21].

2.4 Search for the Higgs boson at the LHC

2.4.1 Introduction

The Higgs physics plays a major role in particle physics. The discovery of the Higgs boson and the measurements of its properties, both in the SM or in the extended Higgs sector, helped to complete the SM and unlock the physics beyond it. In this section we will present the search for the SM and the MSSM Higgs at the LHC with several examples of the most interesting decay modes. In particular, we will highlight the importance of the muons in the final state to obtain a clear signature of the Higgs particles. We will also discuss the discovery of a new particle in the framework of the search for the SM Higgs boson.

2.4.2 Search for the SM Higgs boson

The production of the SM Higgs boson is a very rare process at the LHC, largely dominated by the production of quarks and gluons. Fig. 2.1 shows the production cross-sections of different particles of the SM in the proton-proton collisions. The production

of pairs $b\bar{b}$ is clearly the dominant process while the production of gauge or Higgs bosons are several orders of magnitude smaller.

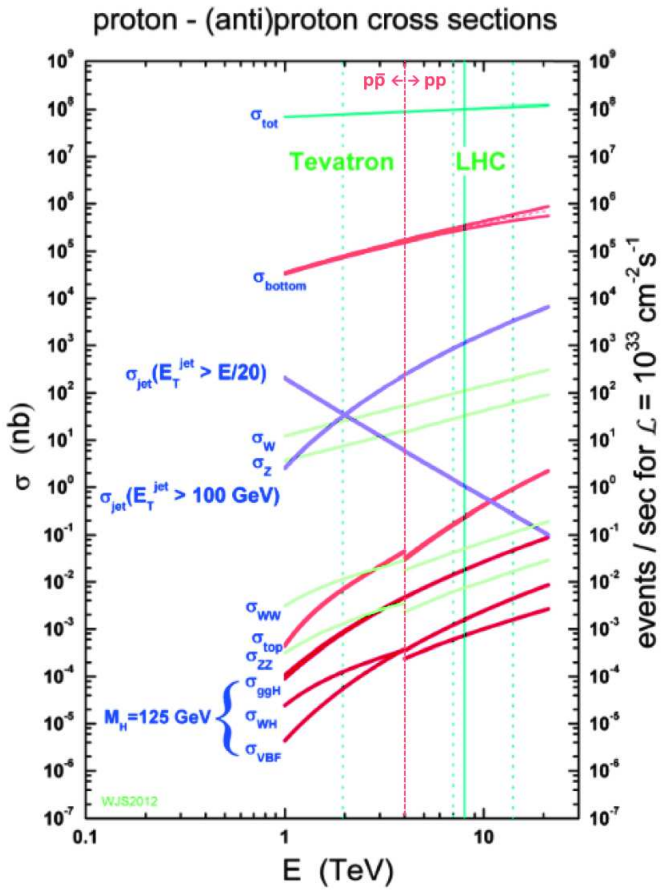

FIGURE 2.1: SM production cross-sections as functions of the center-of-mass energy [1].

2.4.2.1 Production of the SM Higgs at the LHC

At the LHC, the Higgs boson is mostly produced through four modes, of which the Feynman diagrams are represented on Fig. 2.2:

- The gluon fusion (ggH) $gg \to h$: The Higgs boson production is mediated by a loop of heavy quarks, mostly the top quark. The gluon fusion is the main Higgs mechanism at the LHC and represents about 87 % of the total Higgs production at the center-of-mass energy $\sqrt{s} = 8$ TeV and for the Higgs mass $m_h = 125$ GeV.
- The Vector Boson Fusion (VBH) $qq \to qqh$: in this mode the Higgs particle is originated from the fusion of two bosons $W^{\pm}$ or Z, themselves radiated from high energy quarks. The VBF represents about 7 % of the total Higgs production at the LHC.

- Associated production with vector bosons (VH) $q\bar{q} \to Vh$: also called Higgsstrahlung, a virtual boson decays into a real boson $W^{\pm}$ or Z and a Higgs boson. It represents about 5 % of the overall Higgs production.

- Associated production with heavy quarks (qqH) $gg.qq \to qqh$: the Higgs boson is generated from the annihilation of $q\bar{q}$ of through gluon fusion processes that also generate quarks. The most probable qqH production gives top quarks in the final state and is noted ttH. This mode represents nearly 1 % of the Higgs production at $\sqrt{s} = 8$ TeV.

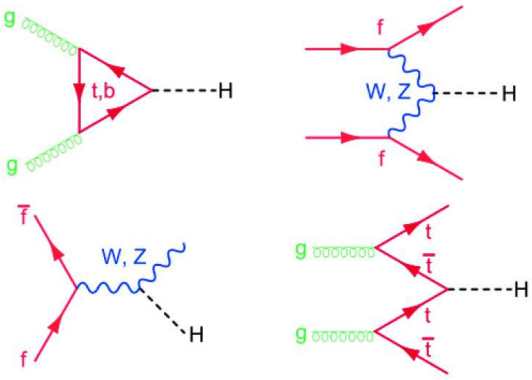

FIGURE 2.2: Feynman diagrams of the main production processes of the Higgs boson at the LHC. Top: production via gluon fusion and Vector Boson Fusion (VBF). Bottom: production in association with a vector boson or a pair of quarks.

The expected production cross-sections for the SM Higgs are shown on Fig. 2.3 as functions of the Higgs mass (left) and the center-of-mass energy (right).

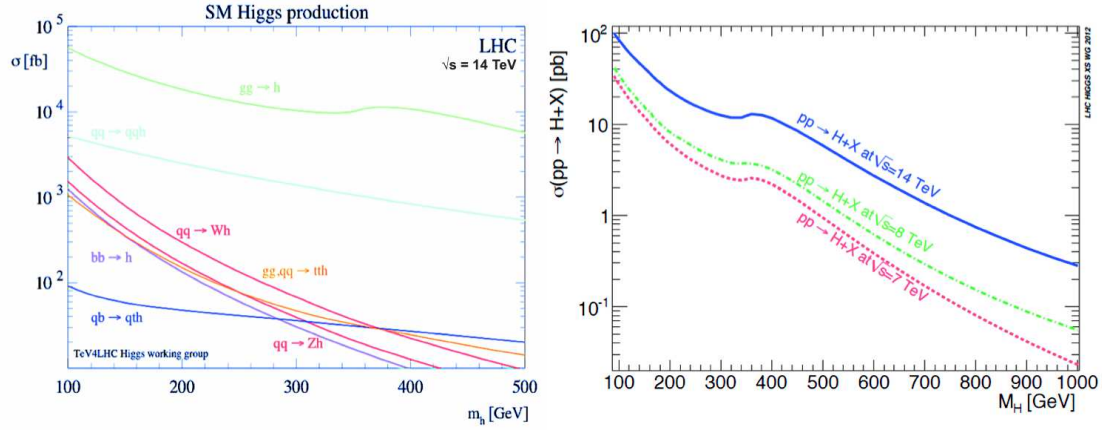

FIGURE 2.3: Left: production cross-section of the SM Higgs boson showing the gluon fusion $gg \to h$, the VBF $qq \to qqh$, the association VH $q\bar{q} \to Vh$ and the association with quarks $gg.qq \to tth$. Right: total cross-section for the center-of-mass energies $\sqrt{s} = 7, 8$ and 14 TeV [2].

2.4.2.2 Decay modes of the SM Higgs

Since the Higgs boson is an unstable particle with a short lifetime, it is not directly measured but observed through its various decay modes. The relative importance of the decay modes depends on the Branching Ratio (BR) and also on the sensitivity to the final state particles, the resolution and the background contamination. Some of the most interesting decay modes of the SM Higgs are listed below [22] [19]:

- $h \to \gamma\gamma$: it is the most sensitive channel for masses up to 150 GeV, giving a very clean signature with two energetic photons in the final state. The Higgs signal consists of a narrow peak in the invariant mass distribution of the reconstructed photons. The background is a continuous distribution mainly caused by the QCD di-photon production. The $h \to \gamma\gamma$ is a loop-induced decay mode, as represented on Fig. 2.4. It involves a loop of heavy quarks (mostly top quarks), heavy charged fermions or gauge bosons $W^{\pm}$. Therefore, this channel gives the indirect access to the Higgs coupling to the top quark and the weak charged boson.

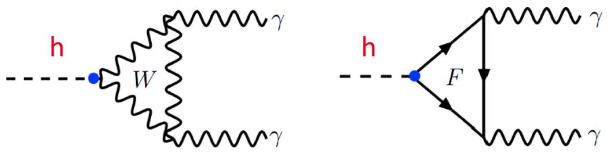

FIGURE 2.4: Feynman diagram of the loop-induced decay of the Higgs boson with photons in the final state. "F" indicates a heavy charged fermion.

- $h \to ZZ^* \to 4l$ ($l = e, \mu$): with the branching ratio of the order 0.1 % at 125 GeV, the so-called "golden channel" has a very high signal-to-background ratio (~ 1). The background mainly consists of QCD events and electroweak di-boson processes (e.g. $pp \to ZZ^* \to 4l$). The lepton reconstruction, in particular the muons, is essential to obtain a narrow mass resonance corresponding to the Higgs signal and to keep the reducible background ($Z \to b\bar{b}, t\bar{t}$ and $Z + jets$) to the minimum level. By measuring the angular distribution of the decay particles, it is possible to determine the quantum numbers associated to the Higgs boson.

- $h \to WW \to l\nu l\nu$: this decay mode has a very interesting branching ratio, almost 20 % at 125 GeV. The leptonic decay of the boson W is preferred because of the lowest background contamination, mainly due to di-boson, top quarks and $Z+jets$ productions. However, the mass resolution is strongly degraded by the presence of undetectable neutrinos in the final state. With this decay mode it is possible to obtain directly the coupling to the bosons $W^{\pm}$ and, as for the ZZ decay, to determine the spin of the Higgs particle.

- $h \to \mu\mu$: the Higgs decay into the di-muon final state has a low branching ratio (about 3×10^{-4} at 125 GeV) but the reconstruction of the muons with opposite signs shows a narrow mass resonance at the Higgs mass. The background is composed of Drell-Yan events ($q\bar{q} \to \gamma, Z \to l^+l^-$) and top quark production. The resolution of the analysis strongly relates on the quality of the muon reconstruction.

- $h \to \tau\tau$: the branching ratio of the Higgs decay to di-τ is close to 6 % at 125 GeV. Then, the τ leptons decay into various channels: $\mu\tau_h$, $e\tau_h$, $\tau_h\tau_h$ and $e\mu$. However, the most interesting final states involve the hadronic decay of one τ, noted τ_h, and one lepton (e or μ). It combines the high branching ratio of the τ hadronic decay and the high efficiency in the reconstruction and the selection of the lepton. The background is constituted by QCD events, Drell-Yan events with τ in the final state, $W + jets$ and $Z \to ll$ with misreconstruction of one lepton as τ_h. The $h \to \tau\tau$ channel allows the direct observation of the Higgs coupling to leptons.

- $h \to b\bar{b}$: this is the dominant process for the mass region below 135 GeV but also very challenging due to the large QCD contamination ($pp \to b\bar{b}$). However, if the Higgs is produced in association with vector bosons, it is possible to increase the sensitivity of the $b\bar{b}$ analysis by looking for missing energy and leptons in the final state (e.g. $Z \to \nu\nu$, $W \to l\nu$ or $Z \to ll$). The quality of the identification of the leptons (electrons or muons) impacts the sensitivity of the measurement. The decay into a pair of b-quarks gives the direct access to the coupling to a down-type quark.

  Additionally, in the case the Higgs boson is produced with a pair of top quarks, the decay $pp \to t\bar{t}h \to t\bar{t}b\bar{b}$ allows the direct measurement of the Higgs coupling to top quarks. Then , the most interesting signature of the top decay are $l\nu + jets$ and $l\nu l\nu$. Nevertheless, this channel is highly contaminated with background processes such as $pp \to t\bar{t}b\bar{b} + X$, where X stands for another decay product.

The branching ratio and the cross-section at $\sqrt{s} = 8$ TeV of the various decay modes of the SM Higgs boson are shown on Fig. 2.5

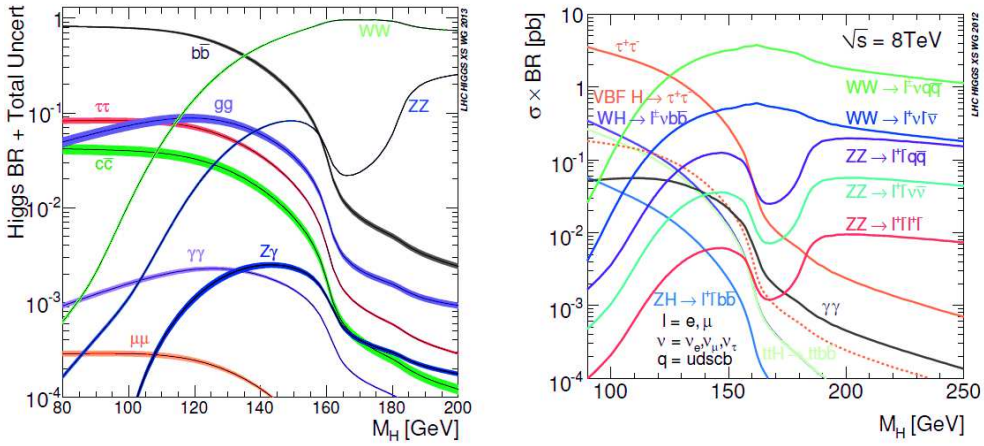

FIGURE 2.5: Left: branching ratios of the various decay modes of the Higgs boson as a function of the Higgs mass. Right: branching ratio of the Higgs decay multiplied by the cross-section at the center-of-mass energy $\sqrt{s} = 8$ TeV [3].

2.4.2.3 Discovery of a new Boson at the LHC

A new boson was discovered by the ATLAS [23] and the CMS [24] collaborations at CERN into the di-bosons decays $h \to \gamma\gamma$ [25], $h \to ZZ$ [26] and $h \to WW$ [27]. Fig. 2.6 (CMS) shows the corresponding invariant mass distributions with the excess signal near 125 GeV. The data were taken during the first operation of the LHC at integrated luminosities up to 5.1 fb^{-1} at $\sqrt{s} = 7$ TeV and 19.7 fb^{-1} at $\sqrt{s} = 8$ TeV. The combined data from both experiments reveal that the mass of this boson is 125.09 ± 0.24 GeV [28]. Additional studies on the properties of this boson were conducted via its decay into $\tau\tau$ [29], bb [30] and $\mu\mu$ [31] pairs for the same data set.

The combination of these analysis helps to identify the new boson and verify its compatibility with the SM. In particular, the mass dependence of the couplings is an essential feature, very well defined by the SM.

In order to easily compare the deviation of the coupling constants of the new boson with respect to SM, one introduces the common scaling factors κ_f and κ_V. These factors refer to the ratio between the best fit of the measurements and the expected values for the SM Higgs. Therefore, if the boson discovered at the LHC is the Higgs boson, the corresponding scaling factors must be close to 1. Moreover, the coupling between the Higgs boson and the fermions is proportional to the mass of the fermions while the coupling with the vector bosons is proportional to the square of their mass. In order to compare the coupling constants of both fermions and bosons on the same plot, one also introduces the reduced coupling constant, noted λ_f. The complete description of the parameters κ_f, κ_V and λ_f can be found at [4].

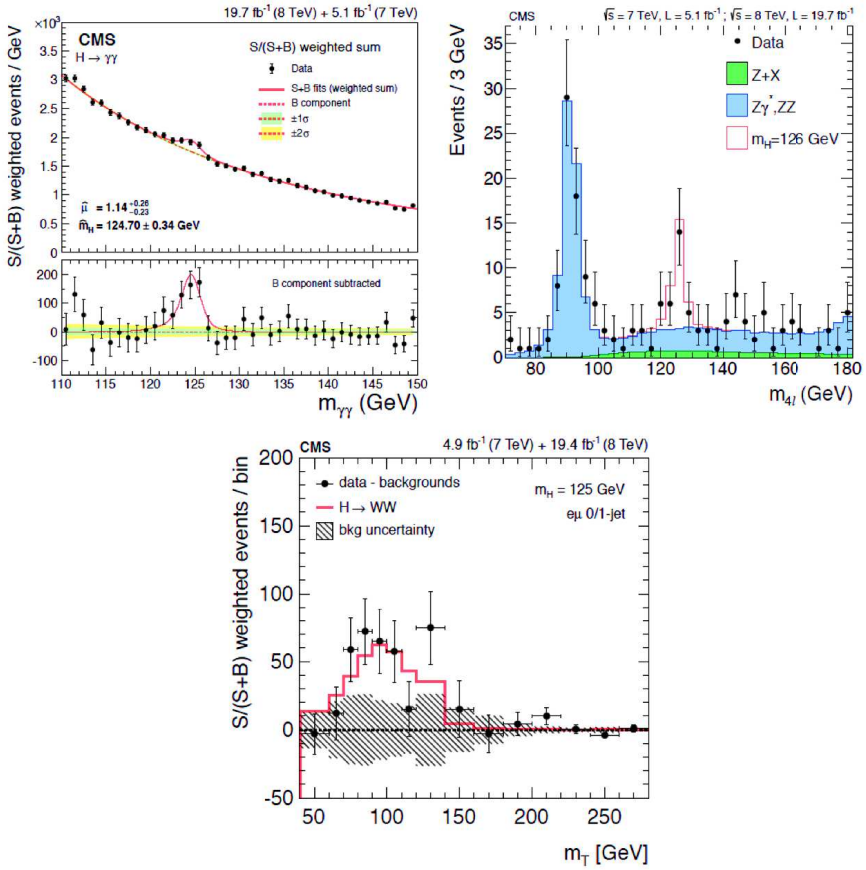

FIGURE 2.6: CMS observations of the Higgs boson via the di-boson decay modes $h \to \gamma\gamma$ (top left), $h \to ZZ^* \to 4l$ (top right), $h \to WW$ (bottom) .

Fig. 2.7 shows the 68 % confidence regions of the Higgs decays discussed previously for the scaling factors κ_f and κ_V. The combined data, indicated by the grey region, includes the SM expectations. The figure also shows the reduced coupling constants as a function of the mass of the particles and compared to the SM.

Additionally to the coupling to fermions and bosons, the measurement of the quantum numbers like the spin J and the parity P can indicate if the new particle is a pure scalar boson as predicted by the SM. Recent studies conducted by ATLAS and CMS [5] tend to confirm this hypothesis with the favored number $J^P = 0^+$ (Fig. 2.8).

In the present situation, it seems that the new boson observed by the ATLAS and CMS experiments is compatible with the SM. However, the situation is not clear enough to ensure that this new particle is the unique Higgs boson of the SM and thus reject the possibility of having discovered a boson from an extended Higgs sector that looks like the SM one. It is therefore essential to refine the current results by measuring the properties of this boson, to continue the investigations on other Higgs candidates with higher masses and to explore non-standard decays, reflecting a new physics beyond the SM.

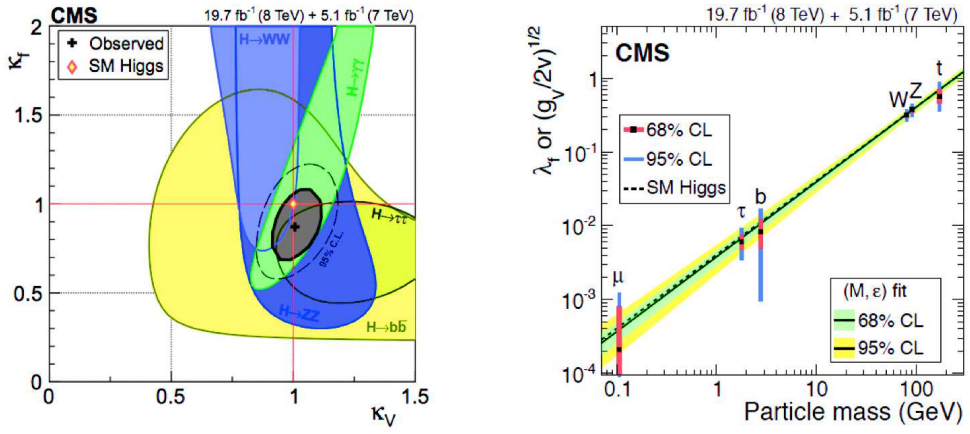

FIGURE 2.7: Left: the 68 % confidence regions of the various decay channels for the scaling factors κ_f and κ_V. The cross indicates the best fit of the combined results. Right: reduced coupling constants of the boson discovered at the LHC as a function of the particle mass. The measurements are compared to the SM expectations (dashed line) [4].

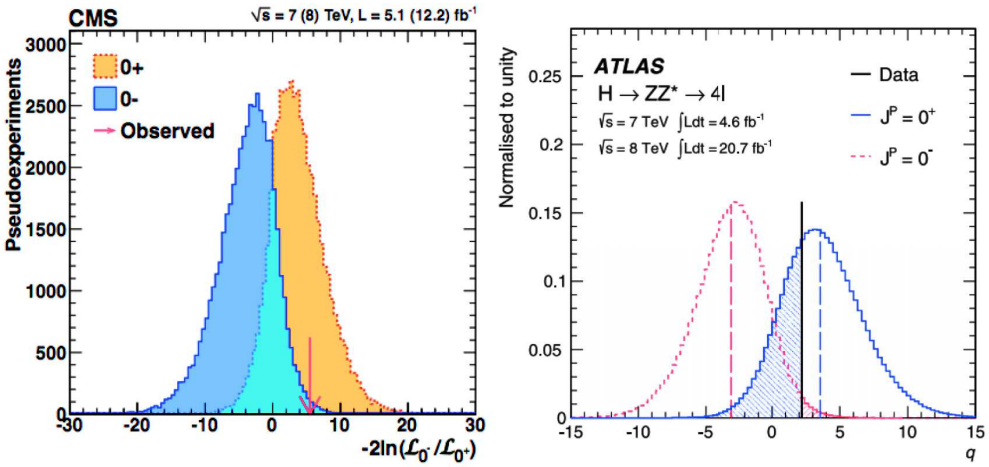

FIGURE 2.8: Expected distribution of the log-likehood ratio $\mathcal{L}_{J^P=0^+}/\mathcal{L}_{J^P=0^-}$ (and $q = log(\mathcal{L}_{J^P=0^+}/\mathcal{L}_{J^P=0^-})$) and comparison with the ATLAS and CMS data in the $h \to ZZ^* \to 4l$ decay channel [5].

2.4.3 Search for the MSSM Higgs bosons

As discussed in Sec. 2.3.1, the MSSM predicts the existence of five Higgs bosons. In this section we will focus on the search for the neutral bosons h_0, H and A in the *mhmax* benchmark scenarios defined by the parameter m_A and $tan\beta$, the other free parameters being fixed [32]. The three neutral bosons will be represented by the variable ϕ.

2.4.3.1 Production of the MSSM Higgs at the LHC

At the LHC we can distinguish two main production processes, of which the Feynman diagrams are represented on Fig. 2.9:

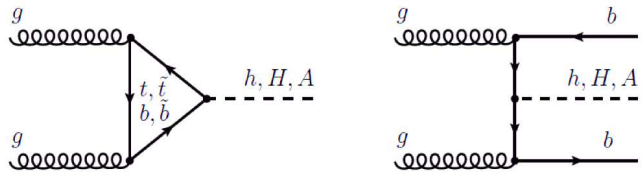

FIGURE 2.9: Feynman diagrams of the main production processes of the MSSM Higgs bosons at CERN. Left: production via gluon fusion. Right: production in association with a pair of bottom quarks.

- The gluon fusion $gg \to \phi$: it is the dominant mechanism for low values of $tan\beta$. The gluon fusion includes a loop of heavy quarks and the corresponding SUSY partners.
- Associated production with heavy quarks $gg, qq \to bb\phi$: the boson is radiated from heavy quarks, most probably bottom quarks for large values of $tan\beta$.

The expected production cross-sections for the MSSM Higgs bosons are shown on Fig. 2.10 for different scenarios of $tan\beta$ at $\sqrt{s} = 8$ TeV [6].

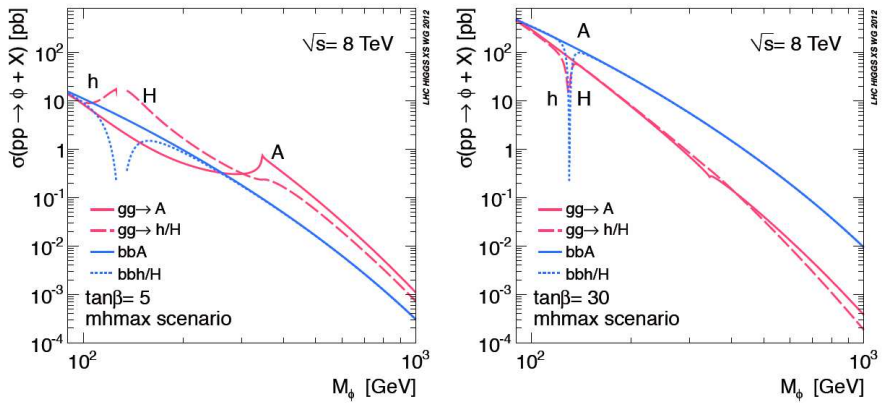

FIGURE 2.10: Expected cross-sections for the MSSM Higgs production as a function of the mass for $tan\beta = 5$ (left) and $tan\beta = 30$ (right) [6].

2.4.3.2 Decay modes of the MSSM Higgs

- $\phi \to b\bar{b}$: the Higgs decay into a pair of b-quarks is the dominant process at high values of $tan\beta$ because of the strong coupling with bottom quarks. However, this

channel is contaminated by a huge QCD background, mostly $pp \to b\bar{b}$. The identification of the Higgs signal thus requires an efficient identification and selection of the jets initiated by the b-quarks, called b-tagging.

- $\phi \to \tau\tau$: the decay mode with the di-τ final state has a lower branching ratio than the $b\bar{b}$ decay but the presence of leptons in the final state gives a clean signature of the Higgs particle. The τ leptons can decay into various modes: $\mu\tau_h$, $e\tau_h$, $\tau_h\tau_h$ and $e\mu$. Therefore, the analysis requires the efficient reconstruction of the τ objects, electrons and muons. Additionally, the tagging of b-jets can be used to disentangle the gluon fusion production of the Higgs and the association with b-quarks.

No evidence of MSSM Higgs particles was observed during the first operation of the LHC in the $b\bar{b}$ decay [33] nor the $\tau\tau$ final state [34]. However, the upgrade of the accelerator will give access to higher mass ranges and luminosity and possibly highlight interesting MSSM mechanisms.

2.5 Other examples of the search for new physics

The validation of physics theories that address the missing elements of the SM does not only include the Higgs physics but also the identification of non-standard decay modes and the observation of new particles.

2.5.1 Search for SUSY

The SUSY-based theories postulate the existence of supersymmetric partners to the SM particles that could have a mass of the order of the TeV, i.e. accessible at the LHC. There are many different models based on the supersymmetry and even more possible scenarios for each model. However, interesting examples of non-standard phenomena are the production of gluinos, squarks of the third generation and chargino-neutralinos in the framework of the next-to-leading order of the SUSY QCD model [35]. Fig. 2.11 shows the production cross-section of SUSY particles as a function of their mass [7].

Then one can identify several decay processes that are being investigated at the LHC [7]:

- $\tilde{g} \to t\bar{t}\tilde{\chi}_1^0$: the decay of a gluino pair into four top quarks. Then the top quarks decay into bosons W that have a clean lepton signature with a large branching ratio.

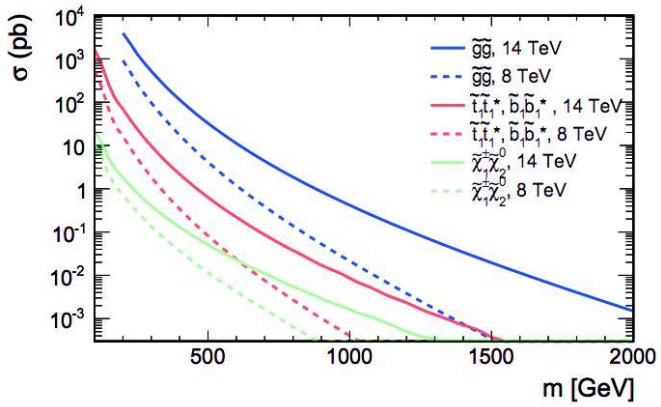

FIGURE 2.11: Next-to-leading order production cross-section as a function of the mass of the SUSY pair particles [7].

The lightest SUSY particle χ_1^0 escapes the detection system and is therefore identified through the measurement of the missing energy. The Feynman representation of this process is shown on Fig. 2.12 [7].

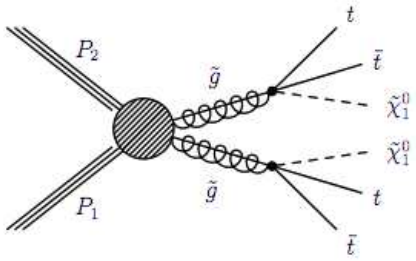

FIGURE 2.12: Feynman diagrams of the gluino pair production and decay into top quarks and neutralinos [7].

- $\tilde{t} \to t\tilde{\chi}_1^0$ and $\tilde{t} \to b\tilde{\chi}^+$: the decay of the stop squarks into top quarks and neutralinos or into bottom quarks and charginos. The chargino $\tilde{\chi}^+$ is an unstable particle that decays into neutralinos and bosons W. Because of the presence of bosons W, the search for leptons in the final state can enhance the sensitivity to these SUSY topologies. The Feynman representations of the stop production and its decays into heavy quarks are shown on Fig. 2.13 [8].

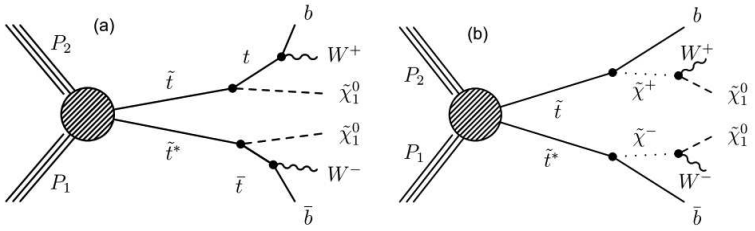

FIGURE 2.13: Feynman diagrams of the stop squark pair production and decay into neutralinos, heavy quarks and bosons W [8].

- $\tilde{b} \rightarrow tW\tilde{\chi}_1^0$: the decay of sbottom squarks into top quarks and charginos. Then the charginos decay into bosons W and neutralinos and the top quark into W and bottom quarks. The corresponding Feynman diagram is shown on Fig. 2.14 [7].

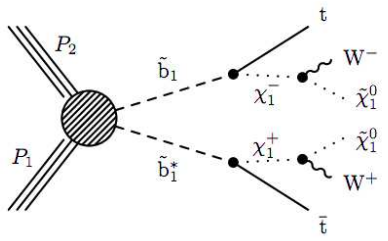

FIGURE 2.14: Feynman diagram of the sbottom squark pair production and decay into top quarks and charginos.

- $\tilde{\chi}_2^0 \rightarrow Z\tilde{\chi}_1^0$ and $\tilde{\chi}_1^\pm \rightarrow W\tilde{\chi}_1^0$: the decay of chargino-neutralino into bosons Z and W and lightest neutralinos. The presence of several leptons in the final state gives a clear signature of the process with large branching fractions. The Feynman representation is shown on Fig. 2.15 [7].

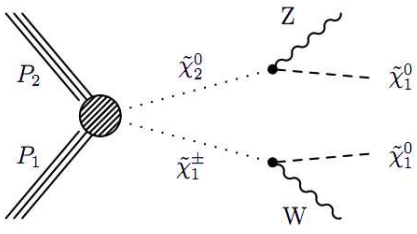

FIGURE 2.15: Feynman diagram of the chargino-neutralino pair production and decay into gauge bosons and lightest neutralinos.

- $\tilde{\chi}_2^0 \rightarrow H\tilde{\chi}_1^0$ and $\tilde{\chi}_1^\pm \rightarrow W\tilde{\chi}_1^0$: the decay of chargino-neutralino into a W boson, lightest neutralinos and a Higgs boson, with a clean multi-lepton final state. The corresponding Feynman process is represented on Fig. 2.16 [7].

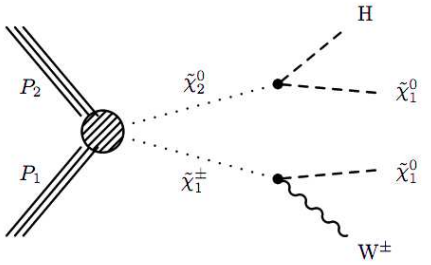

FIGURE 2.16: Feynman diagram of the chargino-neutralino pair production and decay into a Higgs boson, W boson and lightest neutralinos.

As a general example, Fig. 2.17 shows a simplified SUSY spectrum with the SUSY partners possibly accessible at the LHC. In this model, the heavy squarks and the gluinos typically decay into charginos and neutralinos. The charginos then decay into gauge bosons that can be identified through the leptonic decays. The most interesting final states involve muons that can be disentangled from the background contributions with a precise measurement of their momentum.

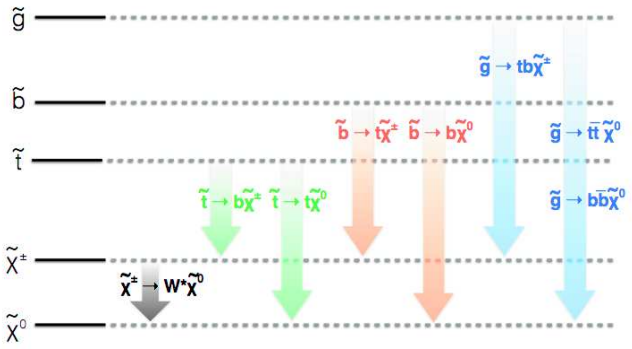

FIGURE 2.17: Example of a simplified SUSY "natural" spectrum showing the SUSY partners accessible at the LHC and the typical decay modes. The neutralino $\tilde{\chi}^0$ is considered as the lightest SUSY particle [9].

2.5.2 Search for exotic new particles

Several new physics scenarios also predict the existence of heavy "exotic" particles that can be explored at the LHC:

- The Z' bosons is a heavier version of the SM Z bosons that can decay into a pair of charged leptons $Z' \rightarrow ll$ in the form of a narrow resonance. The discovery of this new particle would lead to the better understanding of mass mechanism, quantum gravitation, extra-dimensions and dark matter [36].
- Similarly, several models predicts the existence of heavy charged gauge bosons W' that can decay into an isolated lepton with a high transverse momentum p_t and a neutrino (i.e. missing transverse energy) [37].

Additional searches for exotic particles include dark matter candidates and heavy stable charged particles. In most of the cases, the final topologies with leptons are the most interesting, combining high sensitivity, branching fraction and signal-to-noise ratio [7].

2.5.3 Other processes

Many other processes beyond the SM will be investigated at the LHC, especially after the increase of the maximum energy available in the proton-proton collisions. Among others, these processes are the multi-boson production, the top quark physics or the search for vector-like quarks [7]. Additionally, specific heavy ions runs at the LHC are dedicated to the study of the nuclear matter, in particular the quark-gluon plasma state [7].

As a general comment, the identification of new physics requires powerful detection systems with a very efficient reconstruction of heavy quarks, missing energy and leptons (electrons and muons).

2.6 Conclusions

The success of the SM to describe the elementary particles and their interactions has been clearly demonstrated in the last decades. The recent discovery of a new boson that seems to be compatible with the SM Higgs boson would complete the test of the SM.

However, several theoretical mechanisms of the Standard Model are not fully justified and, more problematic, several experimental observations are not addressed by the SM. Therefore, it is believed that the SM is just an approximation of a deeper theory that can unify the four elementary forces and describe all the physics phenomena. One of the most promising candidates is the Super Symmetry, which predicts the existence of SUSY partners to the SM particles and five Higgs bosons.

The search for the ultimate unified theory must be waged on several fronts:

- the refinement of the measurements of the SM, especially in the Higgs sector (coupling to the SM particles and precise measurement of the Higgs quantum numbers).
- the investigation, in higher mass regions, on the existence of heavy Higgs bosons related to a non-standard Higgs sector.
- the exploration of physics models beyond the SM with the identification of non-standard decays and the discovery of new exotic particles.

These items justify by themselves the irreducible need of powerful accelerators to provoke collisions at high rate and high energy in order to reveal the elementary properties of the

particles. Similarly, it is necessary to design precise and sophisticated detector systems in order to observe all the products of the collisions.

We also discussed in this chapter some of the most interesting decay modes of the Higgs boson(s) and SUSY particles. In general, the fully hadronic decays have very high branching ratios but they are also very challenging because of the background contamination. However, it was shown that the presence of leptons in the final state gives a clear signature of interesting decay modes, especially when bosons $W^{\pm}$, Z or Higgs bosons are involved. The usually low branching fraction of the lepton-decay is compensated by a good signal-to-noise ratio and an excellent resolution. The muons have the advantage to be less affected than electrons by radiation losses that can degrade the detection resolution. Therefore, physics discoveries require the development of effective muon detection systems that combine efficient muon reconstruction and good resolution of the muon momentum.

Chapter 3

The upgrade of the LHC and the CMS experiment

3.1 Introduction

In this chapter we will introduce the Large Hadron Collider, where the high-energy proton-proton collisions can reveal interesting physics phenomena of the SM and of the extended models discussed in the previous chapter. We will also present the CMS experiment, paying a particular attention to the muon system. After a brief introduction on the general upgrade of the LHC and CMS, we will focus on the upgrade of the CMS muon system and on the detection environment that will be encountered at the high-luminosity LHC. We will finally highlight the need of introducing a new technology of detection in the forward region of the muon spectrometer.

3.2 CERN and the LHC

3.2.1 Motivations and principle

CERN, the European laboratory for nuclear research, was created in 1954 by 12 European countries with the idea of bringing together technical, financial and human resources in order to build the most sophisticated particle accelerator complex, essential for the research in particle physics. The scientific goals are, among others, the precise measurement of the SM, the understanding of the mass of the elementary particles and the look for physics beyond the SM.

Today, CERN is ruled by 21 member states and involves more than 10 000 scientists, engineers, technicians and administrative staff native of more than 100 different countries. Apart from the numerous discoveries and the various SM hypothesis already confirmed, the fundamental research at CERN has many applications in industry, medical sciences and also in everyday life. One of the most famous example is the creation of the World Wide Web (www) by Tim Berners-Lee in 1989. Initially developed to facilitate the sharing of scientific content between research institutes, the "web" became the most popular tool in nowadays communication. Many other applications are developed at CERN, like the use of particle detectors for medical imaging, hadron therapy and numerous other computer and electronics tools. CERN is also in charge of the knowledge transfer and the training of hundreds of students every year, both in fundamental research and engineering.

The success of this unique international collaboration was highlighted with the recent discovery of the Higgs boson.

3.2.2 Overview of the particle accelerators

The main asset of CERN is the accelerator complex (Fig. 3.1), which allows to gradually accelerate protons until they reach the nominal energy of 7 TeV. The acceleration consists of four main steps: the initial acceleration in the Linear Accelerator (LINAC 2) with energies up to 50 MeV; the injection into the booster then the Proton Synchrotron, up to 26 GeV; the intermediate acceleration in the Super Proton Synchrotron (SPS) up to 450 GeV; the final acceleration in the Large Hadron Collider (LHC), with energies up to 7 TeV.

The circumference of the LHC ring is about 27 km. The beam pipes, placed at 100 m underground, are made of super-conducting magnets that bend the protons and quadrupoles and octupoles for the focusing of the beam. The full system is kept at 1.9 K to ensure the super-conductivity properties.

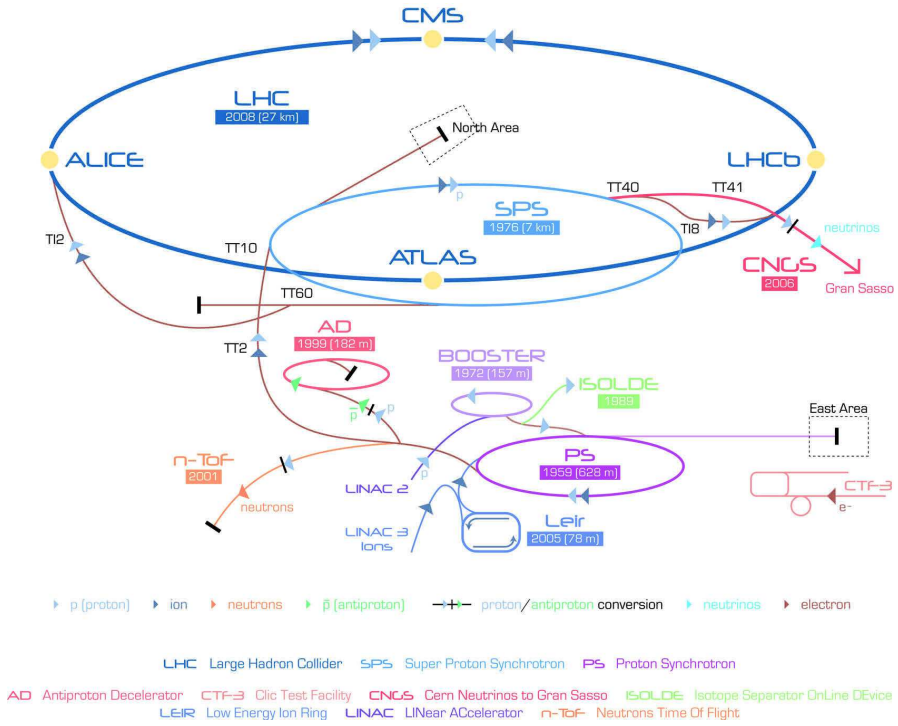

FIGURE 3.1: Overview of the accelerator system and the main CERN experiments.

3.2.3 Important characteristics of the LHC

In the LHC, the protons are grouped in bunches of 10^{11} particles with a length of 9 cm. Two beams are accelerated simultaneously with opposite directions before being merged in four different places to provoke the proton-proton collisions, which happen every 25 ns. The performance of the LHC is described by two parameters: the center-of-mass energy and the luminosity:

- The luminosity $\mathcal{L}$ is a function of the number of particles per bunch, noted n_1 and n_2 for the two beams, the transverse beam profiles σ_y and σ_x, and the frequency of the particle crossings f [11]:

$$\mathcal{L} = f \frac{n_1 n_2}{4\pi\sigma_x\sigma_y} \tag{3.1}$$

  The luminosity integrated over a time period refers to the number of bunch crossings during this period (and thus the amount of collected data). It is often expressed in inverse femtobarn fb^{-1}. The integrated luminosity multiplied by the interaction cross-section gives the total number of events produced during a time period.

- The center-of-mass energy $\sqrt{s}$ defines the total energy available in the collisions. It depends on the energies E_1 and E_2 of the particles of the two beams and of their momenta $\vec{p}_1$ and $\vec{p}_2$. Since the LHC is a collider, $\vec{p}_1 = -\vec{p}_2$. The center-of-mass energy is then given by:

$$\sqrt{s} = \sqrt{(E_1 + E_2)^2 - (\vec{p}_1 + \vec{p}_2)^2} = \sqrt{(E_1 + E_2)^2} \tag{3.2}$$

  Therefore, the center-of-mass energy at the LHC and is equal to the sum of the energies of the two opposite beams.

The LHC first operated for one year at the center-of-mass energy of 7 TeV for a total integrated luminosity of 5.1 fb^{-1}. Then the energy was increased to 8 TeV until the integrated luminosity reached 19.7 fb^{-1}.

The collisions at a high center-of-mass energy allows the production of massive particles that are interesting for physics discoveries (e.g. heavy MSSM Higgs, top-squarks , bottom-squarks or gluinos). A high luminosity, and thus a high rate of events, gives access to rare phenomena (e.g. SM Higgs production).

3.2.4 Overview of the LHC experiments

Four large detector systems, called experiments, are placed at the collision points: ATLAS (A Toroidal Lhc ApparatuS) in point 1, CMS (Compact Muon Solenoid) in point 5, LHCb (LHC beauty) in point 8 and ALICE (A Large Ion Collider Experiment) in point 2.

ATLAS and CMS are multi-purpose experiments that are able to measure new physics through the precise detection of the elementary particles, the reconstruction of hadron jets and the identification of the missing energy corresponding to weakly interacting particles (e.g. neutrinos and the possible neutralinos). They have a similar layout, which consists of: an inner tracker that measures the charge and the momentum of charged particles; an electromagnetic calorimeter that measures the energy of electrons and photons: a hadron calorimeter used to measure the energy of hadrons and jets; a muon spectrometer that reconstructs muon tracks. The detectors are embedded inside of a super-conducting magnet that helps to bend the charged particles in order to measure their momentum. Both experiments are made with different technologies of detectors and a different assembling.

LHCb is a specific-purpose experiment that aims to study the asymmetry between the matter and the anti-matter in the universe. LHCb focuses on the detection of rare processes involving b-quarks and its anti-particle.

ALICE was designed to study the confinement of the quarks through the quark-gluon plasma produced in heavy ion collisions. The detection of muons is particularly important to identify the particles made of heavy quarks. ALICE essentially collects data when the LHC operates with heavy ions beams.

3.3 The CMS experiment

The CMS experiment is a worldwide collaboration that includes more than 3500 scientists and engineers from 186 institutes and 42 countries. The scientific goals are the precise measurement of the SM, the discovery of the origin of the mass of the particles, the search for new particles and more generally the search for physics processes beyond the SM.

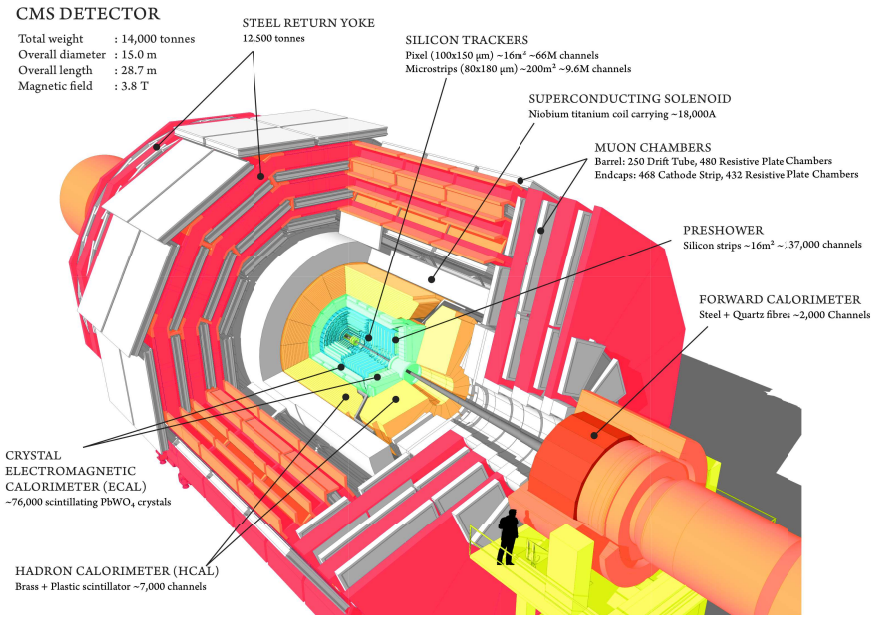

FIGURE 3.2: Overview of the CMS experiment showing the detectors subsystems.

The detector system, located at point 5, is a cylinder of 14000 tons, 21 m long and 15 m in diameter (Fig. 3.1). The position of the objects inside of CMS is usually described in the polar coordinate system ($R = \sqrt{x^2 + y^2}$, θ, ϕ), the origin being the theoretical point of interaction between the two proton beams. The angle θ defines the polar angle with respect to the beam line. However, one prefers the pseudo-rapidity η, which describes the geometrical properties of a particle:

$$\eta = -ln(tan\frac{\theta}{2}) = \frac{1}{2}ln\left(\frac{|\vec{p}| + p_L}{|\vec{p}| - p_L}\right) \tag{3.3}$$

where $\vec{p}$ is the momentum of the particle and p_L its projection on the axis defined by the beam line. The coordinate system is shown on Fig. 3.3.

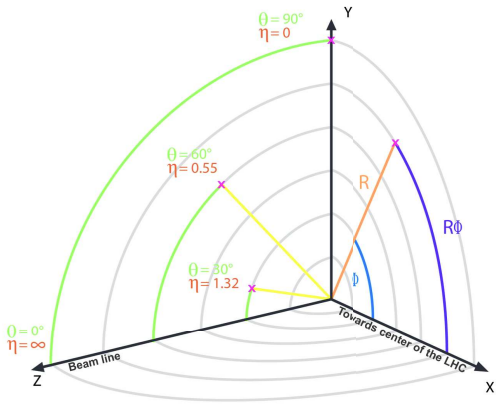

FIGURE 3.3: The CMS coordinate system.

3.3.1 Overview of the CMS subsystems

CMS includes five subsystems, organized in layers around the interaction point where the collisions occur (Fig. 3.4). We distinguish the barrel region, where the detectors form tube sections around the beam line, and the end-cap stations. Each layer has a specific task and characteristics:

- The tracker is the central part of CMS. It is constituted by three layers of silicon pixel detectors in the barrel near the beam line and ten layers of silicon strip sensors in the outer region and the end-caps. The overall system covers the detection region $\eta < 2.5$, including about 66 millions of pixels and 10 millions of strips. The tracker allows the measurement the bending angle of charged particles in magnetic field and the reconstruction of the primary vertices [38].

- The electromagnetic calorimeter (ECAL) is a hermetic calorimeter that consists of more than 61 000 $PbWO_4$ scintillating crystals in the barrel and 15 000 in the end-caps. When electrons and photons enter the calorimeter, they initiate EM showers during which their energy is converted into light. Then, the light is collected by photo-diodes (barrel) and photo-triodes (end-caps). The ECAL covers the pseudorapidity region up to $\eta = 3$ [39].

- The hadronic calorimeter (HCAL) alternate brass converters and scintillators to measure the energy dissipated by objects made of quarks and gluons. Additionally, it allows the indirect detection of weakly interacting particles by measuring the missing energy. Therefore, the HCAL must be completely hermetic to capture all the products of collisions. The HCAL contains about 70 000 scintillator tiles and photo-detectors that cover the region $\eta < 3$ [19].

- The magnet is a superconducting solenoid that generates an uniform magnetic field of 3.8 T in the tracker system and the calorimeters. The magnetic field is essential to bend the charged particles and allows the precise measurement of their momentum.

- The muon system plays a major role in CMS since the muons are clean signatures of interesting physics processes. The CMS system covers the detection region $\eta < 2.4$ and consists of three different technologies of gaseous detectors for the muon identification, the measurement of their momentum and the general triggering. A more detailed description of the muon system is given in Sec. 3.3.2.

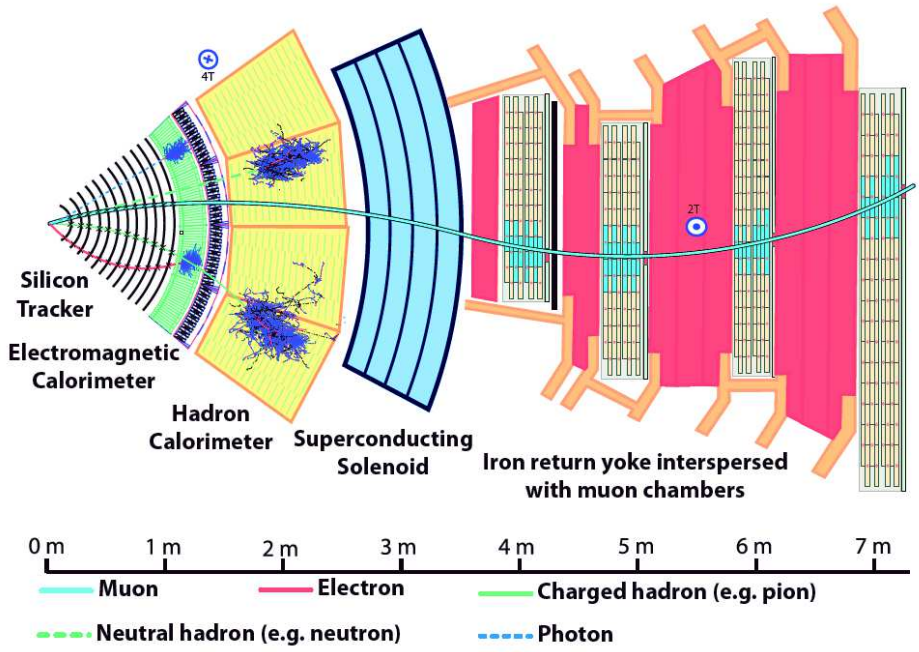

FIGURE 3.4: Overview of the CMS experiment showing the interaction of particles in the different layers of detection.

Tab. 3.1 gives a summary of the CMS subsystems, including the composition and the main characteristics (adapted from [39], [38],[40], [41]).

Subsystem	**Composition**	**Characteristics**
Tracker	silicon strip and pixel detectors	isolated track efficiency $\varepsilon > 95$ % within jets $\varepsilon \backsim 90$ % primary vertex resolution: $10 - 20$ μm p_T resolution: $\Delta p_T/p_T = 1$ % (0.1 TeV) , 10 % (TeV) coverage $\eta < 2.5$
ECAL	$PbWO_4$ crystals	energy resolution: $\left(\frac{\sigma}{E}\right)^2 = \left(\frac{2.7\%}{\sqrt{E}}\right)^2 + \left(\frac{210}{E}\right)^2 + 0.55$ % (barrel) $\left(\frac{\sigma}{E}\right)^2 = \left(\frac{5.7\%}{\sqrt{E}}\right)^2 + \left(\frac{245}{E}\right)^2 + 0.55$ % (end-caps) coverage $\eta < 3$
HCAL	Cu-Zn scintillators	energy resolution $\left(\frac{\sigma}{E}\right)^2 = \left(\frac{68\%}{\sqrt{E}}\right)^2 + 4.5$ % coverage $\eta < 3$
Muon system	gaseous detectors	efficiency $\varepsilon \backsim 98$ % $\Delta p_T/p_T = 8 - 15$ % (0.01 TeV) / $20 - 40$ % (TeV) coverage $\eta < 2.4$

TABLE 3.1: Main characteristics of the CMS subsystems.

3.3.2 The CMS muon system

Since the reconstruction of muons is a powerful tool to identify interesting decay modes, the muon spectrometer is one of the major assets of the CMS experiment. It is placed outside of the calorimeters and the magnet, embedded in the iron yokes. The overall system covers the pseudo-rapidity range $\eta < 2.4$. In order to reach the maximum efficiency and momentum resolution, the CMS design includes three different technologies of gaseous detectors: the Drift Tubes (DT), the Cathode Strip Chambers (CSC) and the Resistive Plate Chambers (RPC) for a redundant and complementary trigger ([40]). Fig. 3.5 shows the longitudinal cross-section of the CMS experiment with the details of the muon system. The chambers "MB" represent the Drift tubes, "RB" and "RE" the RPC in the barrel and in the end-caps and "ME" represents the CSC detectors.

In this section we will give an overview of the different technologies used for the muon detection in CMS (the detailed discussion about the operation of gaseous detector will be found in Chapter 4). Then we will discuss the different steps of the muon reconstruction and how it participates to the CMS trigger system.

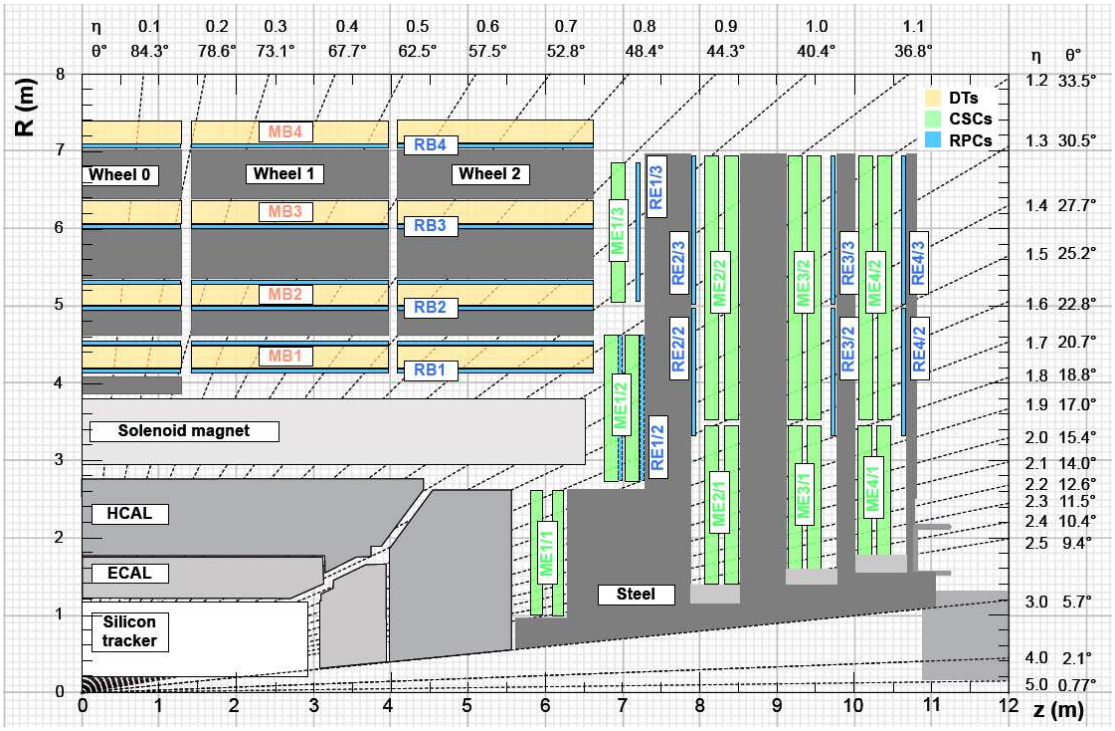

FIGURE 3.5: A quadrant of the CMS longitudinal cross-section showing the current muon spectrometer. The Z axis corresponds to the beam line and the origin is the interaction point.

3.3.2.1 Drift Tube

The Drift Tube (DT) is the main detection technology of the CMS barrel. It consists of a set of rectangular wire chambers with a specific inner geometry that ensures the uniformity of the electric field and thus the homogeneity of the drift velocity inside of the gas volume (see Fig. 3.6). The position of the muon with respect to the wire is calculated based on the drift time of the charge induced in the gas by the muon. By combining several layers of DTs, it is possible to reconstruct the track of a muon with a space resolution of the order of 100 μm. The resulting muon reconstruction efficiency is higher than 95 % for a time resolution of few nanoseconds, which allows the proper identification of the proton bunch crossing (BX) related to a particular muon.

The CMS DT system consists of 250 chambers (about 200 000 channels) covering the pseudo-rapidity $\eta < 1.3$. The barrel is organized in five wheels, each one including four concentric layers. Each layer is composed of twelve 30° chambers that cover the full ϕ coordinate. The detectors are filled with a gas mixture of Ar/CO_2 (85 : 15) and operate at a gas gain of 10^5.

Despite of its good performance, the DT technology cannot operate at particle rates higher than several 10 Hz because the long drift time of the charges inside of the chamber

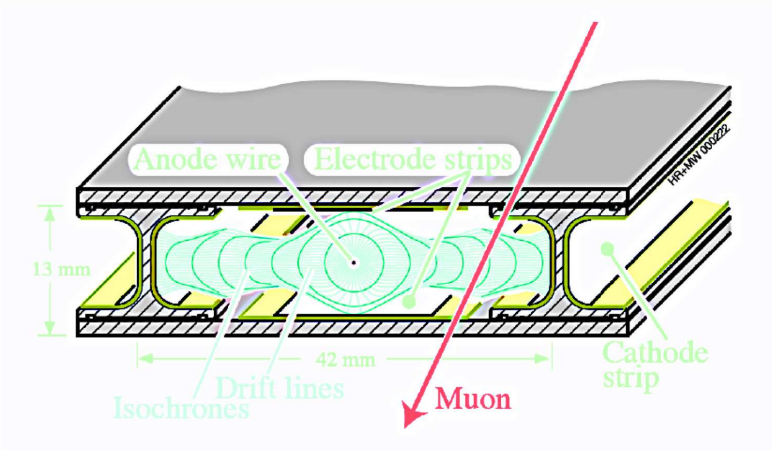

FIGURE 3.6: Schematic view of a CMS Drift Tube detection cell showing the geometry of the chamber and the electric field lines.

($\sim$ 400 ns [40]). Moreover, they have to operate in a uniform and low magnetic field in order to maintain the linearity of the space-time relationship (i.e. the homogeneous drift velocity). Therefore, the DTs cannot be used in the CMS end-caps, where the particle flux is between $10^2 - 10^3$ Hz/cm^2 (mostly background radiations) and the magnetic field can reach up to 3.1 T.

3.3.2.2 Cathode Strip Chamber

The Cathode Strip Chamber (CSC) serves the same function as the DT in the end-caps of the muon system. It consists of a multi-wire proportional chamber, in which the cathode plane is segmented into strips perpendicular to the wire direction (see Fig. 3.7). A muon crossing the detector will induce signals both on the wires and the cathode strips. The combination of the two signals gives the position of the muon hit with a typical space resolution of 75 μm. With a time resolution of 6 ns, each CSC layer provides the proper BX identification with 92 % probability.

The CSC system includes 540 10° and 20° detectors (i.e. 273 000 strips and 211 000 wire groups) organized into four stations in each end-cap. The chambers cover the pseudo-rapidity range $0.9 < \eta < 2.4$. The CSCs operate in $Ar/CO_2/CF_4$ (40 : 50 : 10) at a gas gain of 7×10^4. The CF_4 component is used to prevent aging of the wires and thus extend the lifetime of the detectors.

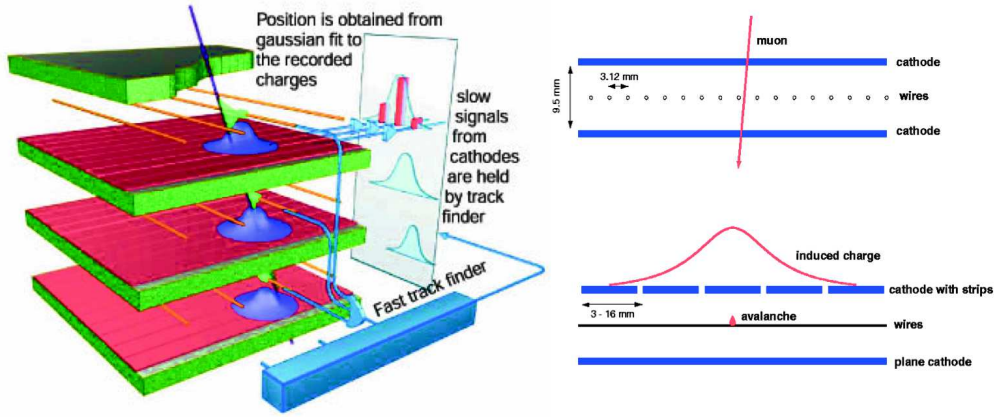

FIGURE 3.7: Schematic view of a CMS Cathode Strip Chamber showing the wire plane and the segmented cathode. The signals from both electrodes are combined to recover the exact position of the muon hit.

3.3.2.3 Resistive Plate Chamber

In order to ensure the redundancy of the muon spectrometer, another technology, the Resistive Plate Chamber (RPC) complements the DT and CSC systems. It consists of two parallel conductive plates separated by a gas volume of few millimeters and covered with a thin layer of resistive resin (see Fig. 3.8). The RPCs are very fast detectors with a time resolution of the order of 1 ns, which makes this technology particularly suitable for the BX identification and the first level triggering. Moreover, despite of the coarse spatial resolution (of the order the centimeter), the additional RPC hits can be combined with the data from the DTs and the CSCs to resolve tracking ambiguities.

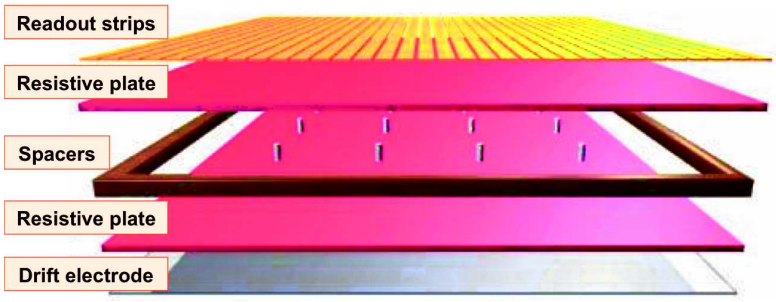

FIGURE 3.8: Schematic view of a Resistive Plate Chamber showing the parallel plate structure and the spacers. The readout strips are separated from the amplification region thanks to thin resistive layers.

CMS contains 360 RPC chambers for the six stations of the barrel and 252 chambers for the four stations of each end-cap, for a total of about 162 000 readout channels. The CMS RPCs operate in avalanche mode in $C_2H_2F_4/i - C_4H_{10}$ (95 : 5).

The resistive coating is used to decouple the amplification region and the readout plane in order to protect the detector in case of a discharge. However, the high resistivity

of the resin also induces charging up effects and excessive current that bring the rate capability of the RPC down below 1 kHz/cm^2. For this reason, the RPC system cannot operate in the high rate environment of the end-caps and only covers the pseudo-rapidity $\eta < 1.6$. The forward end-cap region $1.6 < \eta < 2.4$ is therefore only equipped with CSC detectors.

3.3.2.4 The muon reconstruction

The reconstruction of the muons is based on the hits recorded in the muon chambers, the tracker and also in some cases with events from the calorimeters. We can define four main types of reconstruction [42]:

- Local muon reconstruction: the hits collected by each muon chamber are combined to build muon segments (or track stubs).
- Standalone muon reconstruction: the various segments are used to reconstruct tracks in the muon system with the first estimation of the muon transverse momentum p_t.
- Global muon reconstruction ("outside in"): the standalone muon tracks are matched with the tracks of the inner tracker (or "tracker tracks") that gives a better p_t resolution. This method is the most accurate for muons that penetrate through several muon stations.
- Tracker muon reconstruction ("inside out"): the tracker tracks of the possible muon candidates are extrapolated to the muon station to match with at least one muon segment. The inside out method is more efficient for low momentum muons since it only requires one segment in the muon system.

Several reconstruction algorithms with different selection criteria (number of stubs, position, isolated objects etc ...) can be used depending on the target physics to give different levels of reconstruction efficiency and purity [43].

3.3.2.5 Importance of the muon system in the CMS trigger

The role of the CMS trigger system consists of reducing the trigger rate by selecting only the interesting events. It is organized in two main levels:

- Level 1 (L1): at the level of the detectors, the L1 trigger combines the preliminary reconstruction from the muon system and from the calorimeters. The best candidates are compared to p_t and E_t thresholds before being rejected or accepted and transferred to the next trigger level Fig. 3.9. The tracker is not included in the L1 trigger since it contains too many channels that would slow down the triggering process. The L1 trigger system has not more than 3.2 μs to make a decision. After the L1 selection, the event rate is reduced from 400 MHz to maximum 100 kHz.

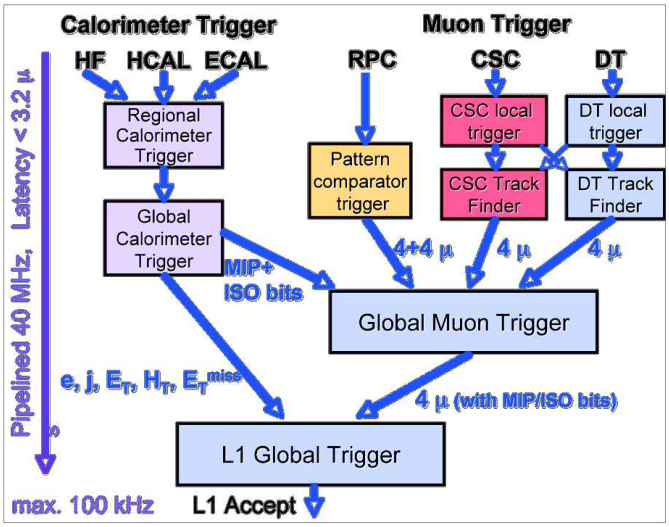

FIGURE 3.9: Representation of the CMS L1 trigger system. The preliminary reconstruction of muons is associated to the calorimeter signals to apply selection cuts and reduce the initial rate down to 100 kHz.

- High Level Trigger (HLT): the HLT is a sophisticated software algorithm processed by a computer farm. The algorithm includes all the CMS subsystems in order to select interesting candidates of a particular event topology defined by the physics of interest. The entire process takes few milliseconds and brings the event rate down to about 100 Hz. At the end, the selected events are stored on magnetic tape.

As a very last step, all the information is shared with the physics community that will perform fine analysis of the data sets and extract the relevant signatures of a particular decay channel or physics phenomenon.

Therefore, the muon system plays a major role in the selection of the interesting events and the reduction of the L1 trigger rate . The time performance and the possibility of doing a fast muon reconstruction are thus essential for the good operation of CMS.

3.4 The Upgrades of the LHC

In order to increase its discovery potential, the LHC needs to be upgraded gradually, both the accelerator systems and the experiments. We can distinguish two major aspects of the upgrade: the increase of the center-of-mass energy in order to provide more energy during the collisions and reveal massive particles; the increase of the instantaneous luminosity to access very rare physics phenomena.

The first upgrade was successfully performed during Long Shutdown 1 (LS1) between 2013 and 2014. The improvement of the magnet interconnections allowed to increase the center-of-mass energy from $7 - 8$ TeV to 13 and soon 14 TeV. The instantaneous luminosity, previously about 7.5×10^{33} cm^{-2}s^{-1}, can now approach the nominal value $\mathcal{L} = 10^{34}$ cm^{-2}s^{-1}. After LS1, the LHC Run 2 started and the operation will continue until it reaches the integrated luminosity of 150 fb^{-1}. Then, the accelerators will stop again the operation during LS2, foreseen in 2019, during which the injector chain upgrade will allow increasing the luminosity up to 2×10^{34} cm^{-2}s^{-1}. The LHC is expected to start the Run 3 in 2021 and operate continuously until it reaches 300 fb^{-1}. Finally, during the LS3, planned for 2024, a major upgrade will bring the luminosity up to $5 - 7 \times 10^{34}$ cm^{-2}s^{-1}. The LHC phase 2, also renamed High-Luminosity LHC (HL-LHC), will restart the continuous operation before the end of 2026 with the aim of integrating a total luminosity of 3000 fb^{-1}. Fig. 3.10 shows the present schedule of the upgrade of the LHC with the various shutdowns and the expected beam performance.

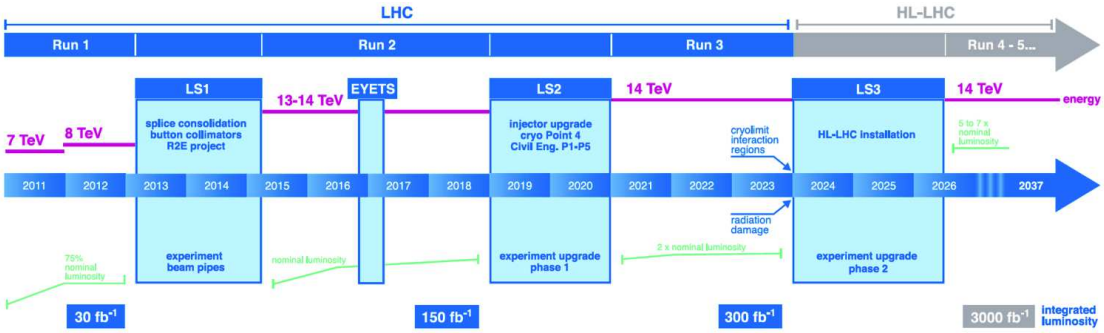

FIGURE 3.10: The LHC upgrade schedule.

3.5 Upgrade of the CMS experiment

As the LHC operation is being improved, the CMS experiment must follow the LHC evolution and also perform detector upgrades to fully exploit the collisions at higher energy and high luminosity.

3.5.1 Overview of the CMS upgrades

The goal of the CMS upgrade is to maintain the physics performance of the detector subsystems and optimize the reconstruction of the particles for LHC luminosities up to $5-7\times10^{34}$ cm^{-2}s^{-1}. The major concerns induced by the upgrade of the LHC are: the high multiplicity of proton-proton collisions per bunch crossing, or pileup (PU), which will be close to 140 at HL-LHC; the increase of the background rate; the radiation damages of the detectors and their electronics.

The upgrade is organized in two steps: the phase I upgrade that covers LS1, LS2 and the various technical stops until 2023; the phase II upgrade that aims to prepare the detectors for the HL-LHC operation after LS3 in 2024 (see Sec. 3.4).

Most of the phase I upgrade is already completed or will be finalized during LS2 (2019-2020):

- Tracker: the replacement of the pixel detectors in the tracker system and the improvement of the front-end electronics in order keep the maximum tracking efficiency at high luminosity.
- Calorimeters: the HCAL photo-detectors must be replaced by silicon photo-multipliers that provide a better efficiency, signal-to-noise ratio and a better immunity to magnetic fields.
- Muon system: four layers of CSC chambers need to be inserted in the ME4/2 station in order to reduce the fake trigger rate and maintain the transverse momentum p_t threshold for the L1 trigger. The RPC system will also be extended to $\eta < 1.6$. One of the major phase I upgrade is the introduction of the GEM-based technology in the first station of the forward end-caps of the muon system at $1.55 < \eta < 2.18$ (GE1/1). The justification for this project will be discussed in the next sections of this chapter and a detailed description of the detectors will be presented in Chapter 5 . The rest of the thesis will be dedicated to the characterization, the longevity test and the quality control of these new chambers for the CMS upgrade.

In addition to the detectors and their readout electronics, the upgrade also includes the data acquisition system (to increase the bandwidth for the data collection and transfer) and the beam monitoring system (to improve the measurement of the beam background and of the luminosity). The technical details of the CMS upgrade for phase I can be found at [44].

Similarly, several major upgrades are foreseen for the phase II operation of the LHC:

- Tracker: it is foreseen to completely replace the current tracking system to overcome the radiation damages and increase the granularity by a factor ~ 4. Additional layers of detection will be installed in the end-caps and the overall system will be extended to $\eta = 4$. During phase II, the tracking data will participate to the L1 trigger to maximize the rate reduction and the selection efficiency.

- Calorimeters: the so-called High Granularity Calorimeter (HGCal) upgrade will replace the current end-cap system and include an EM and a hadronic components. The system will alternate metallic absorbers (tungsten/copper in the EM part and brass/copper in the hadronic one) and silicon sensors. The overall detector will ensure the $3D$ reconstruction of the showers.

- Muon system: the second station of the forward muon system will be equipped with GEM-based (GE2/1) detectors while the third station will be made of low-resistivity RPC. Those upgrades aim to preserve the redundancy of the muon end-caps. Another project under development consists of introducing several layers of GEM-based detectors in the last stage of the end-cap calorimeters, which would be free after the HGCal upgrade. This project, called ME0, would extend the muon coverage to $\eta = 3$.

As for the phase I upgrade, a significant effort will be dedicated to the improvement or the replacement of the readout electronics, data acquisition systems and the beam monitoring system. The technical details of the CMS upgrade for phase II can be found at [45].

3.5.2 Needs for the upgrade of the CMS forward muon system

The upgrade of the CMS muon spectrometer is necessary to ensure an acceptable L1 trigger rate while maintaining a high selection efficiency. The first station of the forward muon system is particularly important for the quality of the muon reconstruction. Since the magnetic field is higher compared to the other stations, the muon bending angle is the largest so the p_t resolution and the sensitivity to low p_t are best. The presence of reconstructed stubs in the first station also helps to disentangle interesting tracks and background events.

However, the first station is also subject to the highest background level. One can distinguish several types of background:

- The muon background that is due to the prompt muons from heavy flavor (mostly b and c decays), non-prompt muons from the decay of π and K and cosmic muons.

In this case, the hits induced in the detectors are correlated, defining muon tracks and segments with low p_t.

- The uncorrelated background, which dominates the overall background environment, is mostly due to neutrons and the products of their interaction with matter. A more detail study on the neutron background at HL-LHC will be discussed in the next section.
- Other background contributions are due to the hadron punch-through, beam halo particles or high-energy particles produced by the de-excitation of the materials surrounding the detectors.

With the upgrade of the LHC, the increase of the background hit rate will confuse the segment reconstruction, give birth to fake segments and degrade the momentum resolution. As a result, the misidentification of interesting muons will increase in the high-eta region and induce a rise of the L1 muon trigger rate. Fig. 3.11 shows the simulated L1 trigger rate as a function of the pseudo-rapidity with a p_t threshold > 15 GeV. This effect is even more pronounced in the region $\eta > 1.6$ that is only instrumented by CSC chambers.

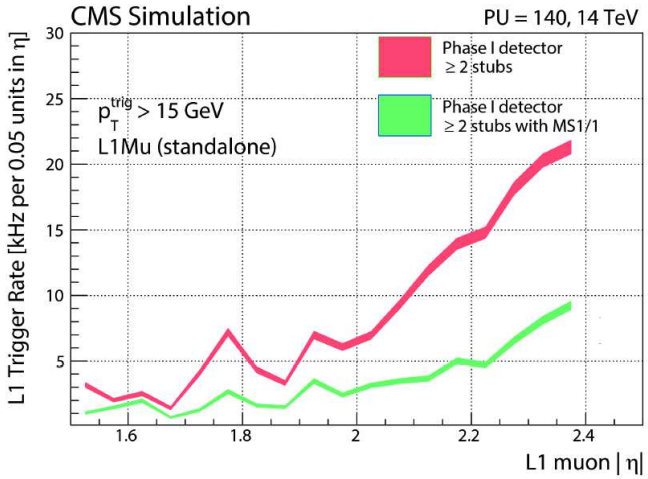

FIGURE 3.11: L1 trigger rate as a function of the muon η with more than two reconstructed stubs (red) and the presence of hits in the first station $MS1/1$ (green). The the rate at high-η is dominated by the mismeasurement of the muon momentum due to the high background contribution.

The introduction of a new detection technology in the first station of the forward end-cap would therefore bring additional hits that can be used to resolve tracking ambiguities, improve the momentum resolution and reduce the L1 trigger rate while maintaining the maximum selection efficiency.

The upgrade proposal of the current muon system was conducted in the framework of the GE1/1 project, which will be presented in Chapter 5. However, for the comprehension

of the next sections, it is important to notice that the "GE1/1" label refers to the GEM-based detectors that will be installed in the first station of the CMS end-cap during LS2 (see Fig. 5.1).

3.5.2.1 Evaluation of the background rate

The high-eta region is subject to intense background radiations, which will become even worst after the high-luminosity upgrade of the LHC. The understanding of the background radiations is particularly important since it can induce misreconstruction of tracks and mismeasurements of the muon momentum. Moreover, the intense radiations may accelerate the aging of the muon detectors and provoke the degradation of the performance with time. Finally, the background rate also defines the detection environment and, as a consequence, the choice of the detection technology that can operate in the end-caps.

The background in the CMS end-caps is dominated by the neutrons produced from the interaction of hadrons with the materials near the beam line. The neutrons, from thermal energies to few GeV, also interact with the materials surrounding the detectors to produce secondary particles, mostly high-energy photons and electrons. The expected background rate and the different contributions were calculated with the CMS adaptation of the FLUKA simulation tool at the instantaneous luminosity $\mathcal{L} = 5 \times 10^{34}$ $\mathrm{cm}^{-2}\mathrm{s}^{-1}$. The details of the study are discussed in [10]. The results for the first station of the CMS end-caps are shown in Tab. 3.2 and Fig. 3.12 top).

Particle type	**R** [**cm**]	**Z** [**cm**]	**Flux** [**Hz/cm**^{2}] ($\mathcal{L} = 10^{34}$ **cm**$^{-2}$**s**$^{-1}$)	**Flux** [**Hz/cm**^{2}] ($\mathcal{L} = 5 \times 10^{34}$ **cm**$^{-2}$**s**$^{-1}$)
Neutrons	150	560	2.9×10^4	1.5×10^5
	210	560	0.9×10^4	0.4×10^5
Photon	150	560	1.5×10^4	7.6×10^5
	210	560	0.6×10^4	3.0×10^5
e^+/e^-	150	560	2.8×10^2	1.4×10^3
	210	560	1.0×10^4	5.2×10^2

TABLE 3.2: Results of the background simulation in the CMS end-cap first station.

Most of the background particles will not interact with the muon detectors. In addition to the background study, the sensitivity of muon detectors to background particles with different energies was computed in the GEANT4 framework (See Fig. 3.13 [10]). Then, the background spectrum is convoluted with the sensitivity to provide the expected hit rate in the detectors. Fig. 3.13 shows the hit rate in GE1/1 detectors placed in the first station of the muon system. Since the GE1/1 sensitivity to neutrons, photons and electrons is comparable to other muon detectors, one can simply extend these results

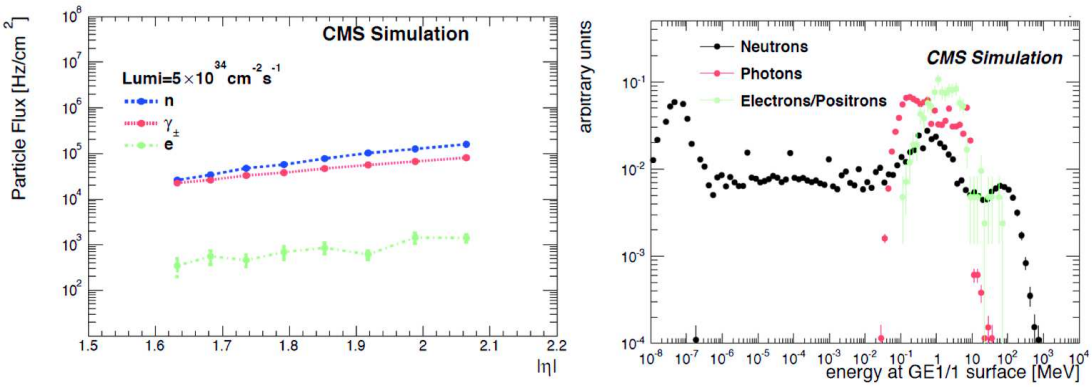

FIGURE 3.12: Background flux as a function of the pseudo-rapidity (left) and expected energy distribution of the different contributions (right).

to CSC and RPC chambers in order to estimate the environment that will be faced by other technologies.

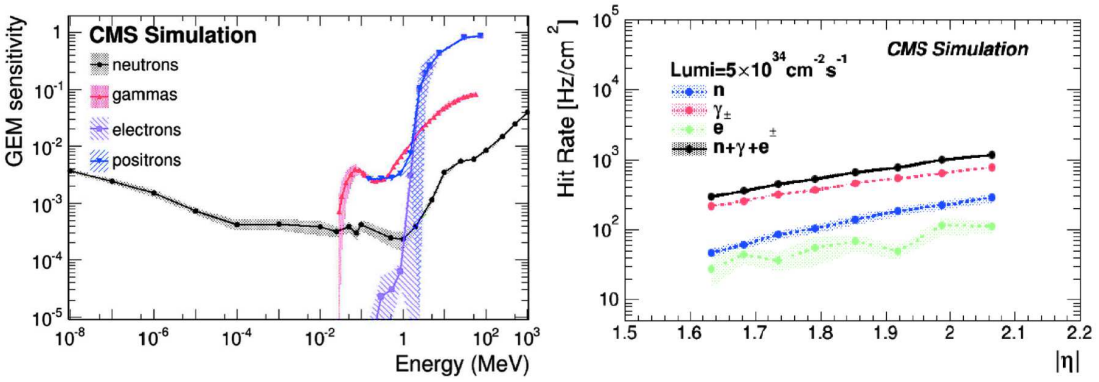

FIGURE 3.13: Left: computed sensitivity of a GE1/1 detector to the CMS endcap background particles. Right: Expected hit rate in a GE1/1 detector placed in front of the CMS ME1/1 station at HL-LHC.

Therefore, the maximum hit rate in the first muon station is expected to be as high as 1 kHz/cm^2 at HL-LHC (Fig. 3.13). This implies that the forward muon system for the upgrade must be resistant to radiations (up to $\sim$ 500 Gy), have a high rate capability and be capable to disentangle muon tracks and fake events.

3.5.2.2 Impact on the phase I trigger

The six layers of CSC chambers in the first muon station covers a muon path length of 11.7 cm. Because of this, the bending angle cannot be utilized in the p_t measurement and the momentum resolution is not good enough to disentangle interesting muons and mismeasured tracks from the background. As an example, for L1 p_t-cuts below 20 GeV, the rate of mismeasured muons is more than one order of magnitude higher than the rate of muons originated from bosons $W^{\pm}$ and Z. With the increase of the LHC luminosity,

the contribution of the mismeasurements to the L1 trigger rate will increase, unless the p_t threshold is raised, to the detriment of the efficiency.

The introduction of a second technology of detection would extend the path length and provide additional hits that will help to refine the stub reconstruction and improve the momentum resolution. Therefore, the rate of misidentified muons is reduced as well as the L1 trigger rate. Fig. 3.14 (left) illustrates the segment reconstruction efficiency at different simulated muons η for the current CSC system and the integrated CSC+GE1/1 upgrade. The right plot shows the L1 rate reduction at the LHC luminosity $\mathcal{L} = 2 \times 10^{34}$ $\mathrm{cm}^{-2}\mathrm{s}^{-1}$ and for a constant efficiency of 94 %.

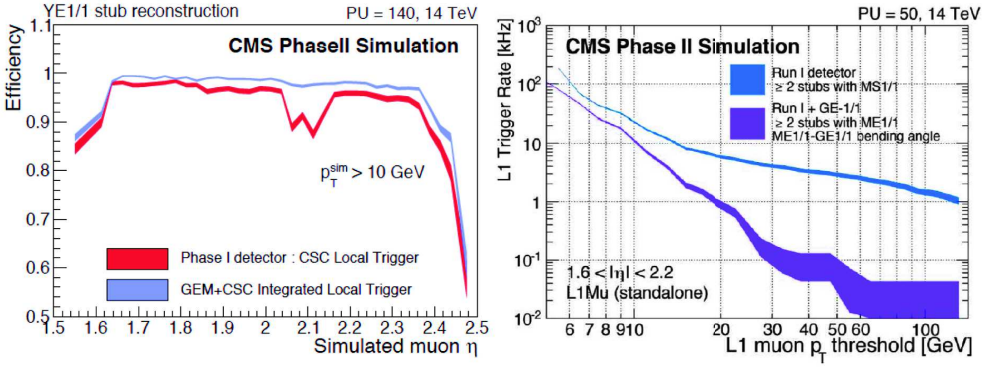

FIGURE 3.14: L1 trigger rate as a function of the applied p_t threshold with and without the additional detection layer based on the GEM technology (GE1/1). The data have been simulated with the instantaneous luminosity $\mathcal{L} = 2 \times 10^{34}$ $\mathrm{cm}^{-2}\mathrm{s}^{-1}$, for a constant efficiency of 94 %.

As a result, the reduction of the trigger rate allows maintaining a low p_t threshold, which means increasing the acceptance and the efficiency of reconstruction of soft muons, particularly interesting for physics discoveries in the SM, extended Higgs sectors, and also for SUSY candidates. As an example, Fig. 3.15 (left) shows the muon p_t distribution for three interesting physics channels: the SM Higgs decay to τ-leptons, a heavy Higgs decay into τ-leptons and quarks and the SUSY "stop" squarks production. The right plot illustrates the increase of the selection efficiency when lowering the p_t threshold.

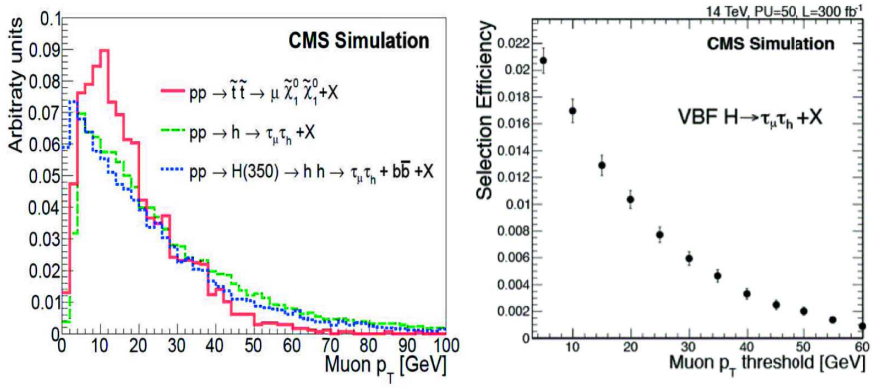

FIGURE 3.15: Left: muon p_t distribution for several interesting physics processes: the SM Higgs coupling to τ leptons $h \to \tau\tau + X$; the heavy Higgs decay into τ leptons $H \to hh \to \tau\tau bb$; the production of SUSY "stop" particles $p \to \tilde{t}\tilde{t} \to \mu\tilde{\chi}_1^0\tilde{\chi}_1^0 + X$. Right: selection efficiency of the Higgs decay into τ leptons for the $\mu\tau_h$ final state as a function of the p_t threshold.

3.5.2.3 Impact on the phase II trigger

The new CMS L1 trigger system after LS3 will allow the significant improvement of the efficiency and the quality of the muon reconstruction by matching the standalone muons "L1Mu" and the tracker data ("track-trigger tracks"). The resulting combined object "L1TkMu" will ensure a high-purity and low-rate trigger at low p_t thresholds.

However, the maintaining of the high quality of the standalone muon trigger will still be essential for the HL-LHC. Several physics scenarios predict the existence of heavy long-lived exotic particles that can decay far away from the interaction point into a pair of muons. Because of this, only few muon hits will be left in the tracker, resulting in a drastic inefficiency of the tracking trigger. Therefore, the muon standalone trigger is the only viable solution to identify these events. Such scenarios arise from the extension of SUSY like the NMSSM [46], the "hidden valleys" (Dark SUSY) [47] or heavy resonance models [48]. As an example, Dark SUSY scenarios predict the production of new bosons during the decay of a SM-like Higgs boson of 125 GeV H(125) into neutralinos n_1. In this model the neutralinos decay into dark neutralinos n_D and low-mass dark photons γ_D or dark neutralinos and heavy dark bosons Z_D. Then the dark bosons can decay into a pair of muons. Fig. 3.16 shows the trigger reconstruction efficiency of the two dark SUSY decays as a function of the transverse distance between the decay vertex and the beam line. The combined L1TkMu efficiency drops immediately when this distance is increasing while the standalone L1Mu efficiency is maintained.

Therefore, the upgrade of the first muon station will also help to preserve the L1 standalone muon trigger at the HL-LHC and improve the identification of displaced muons.

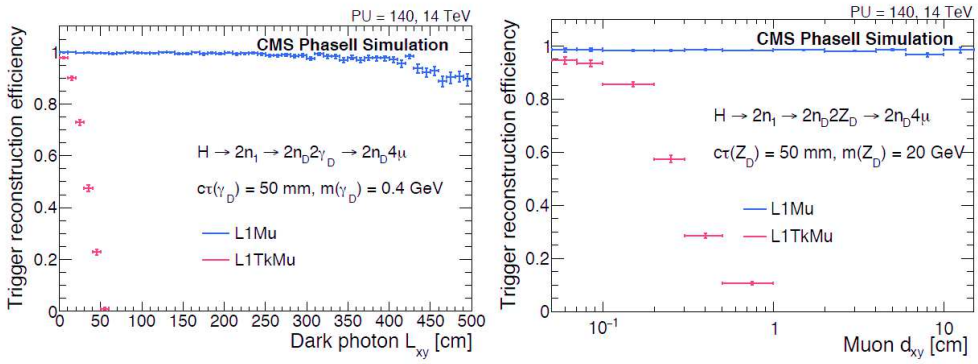

FIGURE 3.16: Left: comparison between the combined L1TkMu trigger and the standalone L1Mu trigger efficiencies for the dark SUSY decays $H(125) \to 2n_1 \to 2n_D 2\gamma_D \to 2n_D 4\mu$ (left) and $H(125) \to 2n_1 \to 2n_D 2Z_D \to 2n_D 4\mu$ (right) as a function of the distance between the decay vertex and the beam line. A more detailed description of the simulation parameters can be found at [10].

3.5.2.4 Aging of the CSC system

As for all detectors operating in high-radiation environment, the CSC chambers can be subject to aging, i.e. the degradation of their detection performance with time. Since it is the only system currently installed in the forward end-caps, a loss of performance or a loss of detection areas would drastically affect the entire muon spectrometer, both for the L1 trigger (phase I and phase II) and the off-line muon reconstruction. The aging concern will be particularly critical at the HL-LHC since the background rate will reach ~ 1 kHz/cm^2 in the first station.

We can distinguish four types of aging: the normal electronics degradation, which causes about 1 % losses every year; problematic low voltage and signal connections, evaluated at $10-15$ % losses; problems with the data transmission and data loss; the classical aging of gaseous detectors, particularly problematic with wire chambers. This last item however is very difficult to estimate since it depends on the operation environment. Several scenarios were investigated by the CMS muon group, for all of them, the expected fraction of non-working CSC is about 15 % at HL-LHC [49].

The introduction of a second layer of detection will help to compensate the possible losses in the CSC system and maintain the best reconstruction and selection efficiency. Fig. 3.17 shows the trigger efficiency at the p_t plateau as the function of the fraction of non-triggering CSCs for the CSC system only and associated with GE1/1 detectors.

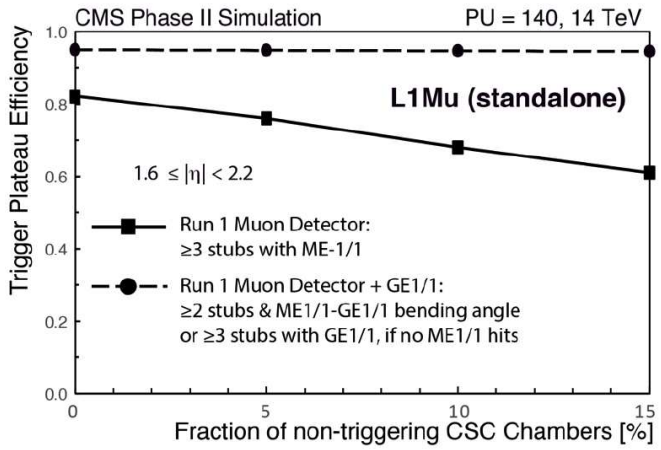

FIGURE 3.17: Single muon trigger efficiency as a function of the fraction of non-triggering CSC chambers, both with and without GEM-based detectors in addition to the CSC system.

3.6 Conclusions

The upgrade of the LHC will allow for the increasing of the center-of-mass energy to 14 TeV and the gradual increasing of the luminosity up to $5 - 7 \times 10^{34}$ cm^{-2}s^{-1}. As a result, the HL-LHC will give access to higher energy ranges and to rare decays that could validate or invalidate theories beyond the SM.

However, the increase of the collision rate will also affect the detection environment in CMS. In particular, the increase of the background rate in the forward region of the CMS muon end-caps will provoke a rise of the L1 muon trigger rate and a degradation of the selection efficiency at given bandwidth limitations. Additionally, the high-radiation background may accelerate the aging of the current CSC system and possibly cause performance losses and dead regions.

The solution proposed by the CMS GEM Collaboration consists of introducing additional gaseous detectors in the forward end-caps to complement the current CSC system. These new chambers will be based on the GEM technology, which can operate at very high rates with good performance while offering excellent trigger information to improve the CMS operation.

Chapter 4

Introduction to gaseous detectors

4.1 Introduction

In this chapter, we will introduce the theoretical concepts of the particle detection, in particular with gaseous detectors. Since this thesis is devoted to the upgrade of the CMS muon system, we will focus on the physics processes that can be encountered in the CMS end-caps or during the $R\&D$ activities in laboratory. Similarly, we will give practical examples of the detection properties with gas molecules commonly used in CMS muon system: Ar, CO_2 and CF_4. In the second part of this chapter, we will describe the basic operation gaseous detectors and give a brief historical overview of their development. Then we will conclude with the specific case of the triple-GEM detector and its applications.

4.2 Particles and matter interactions

This first section aims to remind the main processes that allow the detection of particles through their interaction with matter, especially in gaseous media. All the elements described below, the theoretical concepts, the hypothesis and the pictures are adapted from [20], [50], [17], [51], [52], [53] and [11]. Other specific references will be indicated in the text.

4.2.1 Interaction between charged particles and matter

A fast charged particle traversing a medium will interact with it via EM, weak or strong forces. However, the weak interaction is by definition negligible for most of the particles

(except neutrinos) and the typical range of the strong interaction is at the order of the nuclear section, i.e. 10^8 to 10^{10} orders of magnitude lower than the atomic section. The EM interaction is thus the predominant process for the detection of charged particles. The highest probable process within the EM interactions is the Coulomb interaction between the EM fields of the particle and of the medium. It leads to the excitation and/or the ionization of the medium itself, resulting in the release of free charges that can be used to generate electronics signals.

4.2.1.1 Energy loss due to Coulomb interactions

A heavy charged particle (i.e. with a mass much greater than the electron mass) crossing a layer of matter will interact with the atomic electrons and transfer part of its energy, resulting in the ionization and/or the excitation of the medium. In the case of ionization, the atomic electrons acquire a sufficient amount of energy to be ejected from the atom, forming electron-positive ion pairs in the medium. Sometimes, the atoms are not ionized but excited by the incoming particle and release electrons through de-exciting processes. The average energy lost by a particle passing through a material is given by the Bethe-Bloch formula:

$$-\left\langle \frac{dE}{dx} \right\rangle = \frac{2\pi e^4 z^2}{m_e c^2 \beta^2} NZ \left[ln\left(\frac{2m_e c^2 \beta^2 \gamma^2 T_m}{I^2} \right) - 2\beta^2 - \delta(\beta\gamma) \right] \tag{4.1}$$

where ze is the charge of the incoming particle, m_e the mass of the electron at rest, N and Z the atomic density and atomic number of the medium. The parameter I represents the average ionization and excitation potential of the medium. The maximum energy transfer for a single interaction is represented by the parameter T_m given by:

$$T_m = \frac{2m_e c^2 \beta^2}{1 - \beta^2} \tag{4.2}$$

The validity of the Bethe-Bloch formula in this form is limited to $0.1 \lessapprox \beta\gamma \lessapprox 1000$. For $\beta\gamma \gtrapprox 4$ we observe a relativistic rise of the stopping power due to the increase of the transverse electric field of the particle and therefore the increase of distant interaction contributions. However, the polarization of the medium limits the field extension and acts as a shielding of the electrical field far from the particle path, cutting the long-range contributions. The Fermi density effect correction $\delta(\beta\gamma)$ is introduced in Equ. (4.1) to cover this phenomenon. At very low energies ($\beta\gamma \lessapprox 0.1$), the assumption that the electron is at rest is no longer valid. The particle velocity is comparable to the orbital velocity of the atomic electrons, which allows electron capture processes. Additional

corrections such as shell corrections, Bloch correction and Barkas correction are required to fully describe the low energy range. At higher energies ($\beta\gamma \gtrapprox 10^4$ for muons), radiative processes become more important than ionization. The average energy loss $\left\langle \frac{dE}{dx} \right\rangle$ is no longer a continuous function of the parameter $\beta\gamma$, based on Coulombs interactions, but a complex combination of various effects such as e^+e^- pair production, Bremsstrahlung and photo-nuclear interactions.

In the case of the HEP experiments, and particularly the CMS muon system, most of the relativistic particles have a mean energy loss close to the minimum, they are identified as "Minimum Ionizing Particles" (MIP). An example of the average energy loss of a positive muon in copper is shown on Fig. 4.1.

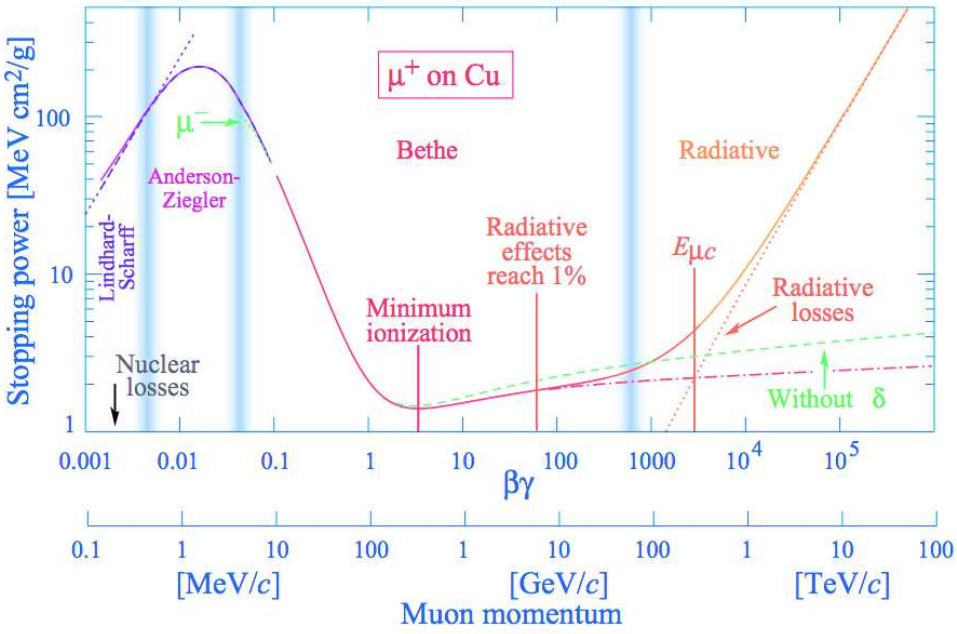

FIGURE 4.1: Stopping power for positive muons in copper as a function of $\beta\gamma$. Solid curves represents the total stopping power [11].

The CMS muon detectors essentially operate in argon-based mixtures. As indicated on Fig. 4.2, the average energy loss of MIPs in argon is close to 1.53 MeV g^{-1} cm^2. Considering the density of argon $\rho = 1.78 \times 10^{-3}$ g cm^{-3}, the total energy loss per unit length in pure argon becomes:

$$\Delta E_{argon} = -\left\langle \frac{dE}{dx} \right\rangle \times \rho \times d = 1.53 \times 1.78 \times 10^{-3} \times 1 = 2.72\ keV/cm \tag{4.3}$$

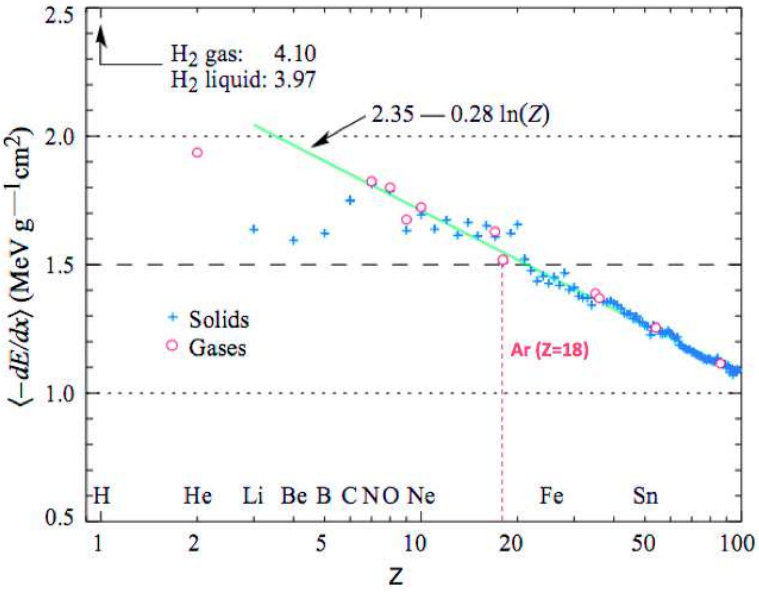

FIGURE 4.2: Energy loss of a MIP as a function of the atomic number of the medium [11]. The red line refers to the Argon (Z=18).

4.2.1.2 Energy loss fluctuations

The energy loss described in the previous section is an average value. Since it involves collisions with atoms, which are subject to statistical fluctuations, the energy loss and the electron-ion pair production for a given path length are also subject to fluctuations. Similarly, for a given energy loss value, the path length before the particle is stopped, or range of the particle, fluctuates. This phenomenon is called straggling and leads to the widening of the energy loss distribution of a particle passing through a medium, especially on the side of the high energy losses. In the case of a thin layer of absorber, the energy loss distribution is described by the Landau-Vavilov expression:

$$f_{L,V}(\Delta, \beta\gamma, x) = \phi(\lambda) = \frac{1}{\sqrt{2\pi}} e^{-\frac{1}{2}(\lambda + e^{-\lambda})} \tag{4.4}$$

where x is the thickness of the medium. The energy variable λ represents the deviation between the specific case energy loss Δ/x and the most probable energy loss Δ_p/x:

$$\lambda = \frac{\Delta/x - \Delta_p/x}{\xi} \tag{4.5}$$

The most probable energy loss is defined as:

$$\Delta_p/x = \xi \left[ln\frac{2m_e c^2 \beta^2 \gamma^2}{I} + ln\frac{\xi}{I} + 0.2 - \beta^2 - \delta(\beta\gamma) \right] \tag{4.6}$$

And ξ is given by :

$$\xi = \frac{2\pi e^4 z^2}{m_e c^2 \beta^2} NZx \tag{4.7}$$

Apart from the MIPs crossing the muon chambers in the CMS end-caps, the landau parameterization is also useful during the *R&D* phase to fit the energy spectra from muon beams, cosmic rays or high energy electrons. Fig. 4.3 shows an example of a landau distribution obtained from the interaction of high energy electrons with a gaseous detector. The electrons are secondary particles produced from the Compton scattering of ^{137}Cs photons in copper (see Sec. 7.3.2.1).

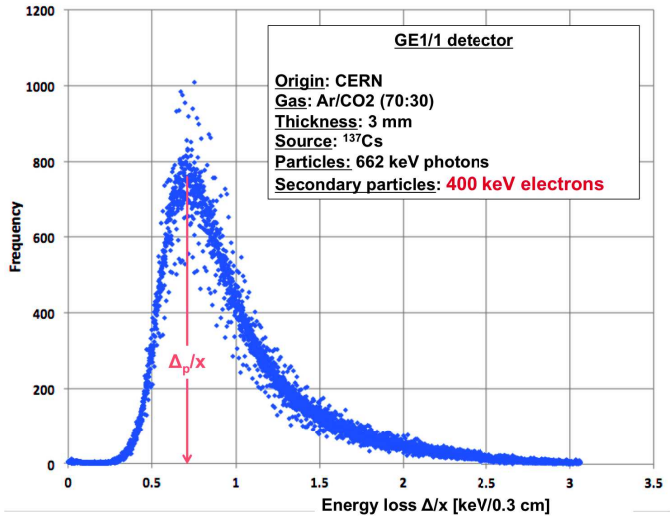

FIGURE 4.3: Energy distribution of $\sim$ 400 keV electrons in a gaseous detector operating in Ar/CO_2 $(70:30)$. The electrons are produced from the Compton interaction of 662 keV photons with copper in front of the gas volume.

4.2.1.3 Ionization processes

In the case the energy is lost by ionization, the incoming particle liberates a discrete number of electron-positive ion pairs in the medium. This process is called primary ionization. The freed electron may possess sufficient kinetic energy to cause secondary ionization events in the medium. Such electrons are sometimes called δ-rays and their number n per unit length dx for a kinetic energy between T and dT can be estimated by:

$$\frac{d^2 n}{dT dx} = \frac{2\pi z^2 e^4}{m_e c^2 \beta^2} NZ \frac{1}{T^2} \left[1 - \beta^2 \frac{T}{T_m}\right] \tag{4.8}$$

where ze is the charge of the incoming particle, m_e the mass of the electron at rest and N and Z the atomic density and atomic number of the medium. The maximum energy that can be transferred to the electron by a massive particle is given by [54]:

$$T_m = 2m_e c^2 \beta^2 \gamma^2 \tag{4.9}$$

The total number of electron-positive ion pairs in a given volume produced by both primary and secondary ionization can be expressed by:

$$n_T = \frac{\Delta E}{W_i} \tag{4.10}$$

where ΔE is the total energy loss transferred to the given volume and W_i is the effective average energy to produce one electron-positive ion pair. The parameter W_i is usually bigger than the average ionization and excitation potential I (Equ. (4.1)) since a fraction of the deposited energy is absorbed by excitation processes and doesn't necessarily release electrons in the medium.

If the target medium contains several components, the average energy W_i of the medium is calculated following a simple composition law. For example, we can calculate the total number of primary electrons produced by MIPs in a muon detector operating in Ar/CO_2 (70 : 30). Following the same procedure as for Equ. (4.3), the total energy loss transferred to the medium over a distance of 3 mm (typical conversion length for a GE1/1 detector) is $\Delta E = 861$ eV. Therefore:

$$n_T = \Delta E \left[\frac{0.7}{W_i(Ar)} + \frac{0.3}{W_i(CO_2)} \right] = 861 \left[\frac{0.7}{26} + \frac{0.3}{33} \right] \approx 31 \; pairs \tag{4.11}$$

4.2.2 Interaction between photons and matter

In addition to the muons and the high energy electrons, the CMS muon detectors will be subject to high energy photons in the end-caps. As indicated in Sec. 3.2, the photon energies are spread from few hundred keV to several tens of MeV. Moreover, most of the calibration tests and characterization of gaseous detectors are performed with X-ray sources of several keV. It is therefore interesting to remind the main processes of interaction of photons with matter.

The photons also interact via electromagnetic effects. But while a charged particle shows a continuous energy loss in the medium, the absorption of a photon is a single localized

event. Considering a beam of photons with the energy E and an intensity I crossing a medium with a thickness x, the intensity loss is given by:

$$dI = -N\sigma(E, Z)Idx \tag{4.12}$$

where σ is the total cross-section of the interaction for a given material with an atomic number Z and an atomic density N. If the initial intensity of the beam is I_0, the total attenuation is:

$$\frac{I}{I_0} = e^{-N\sigma(E,Z)x} = e^{-(\mu/\rho)X} \tag{4.13}$$

where $(\mu/\rho) = N(\sigma/\rho)$ is, by definition, the mass attenuation coefficient, $X = \rho x$ is the reduced thickness of the medium and ρ the density of the medium.

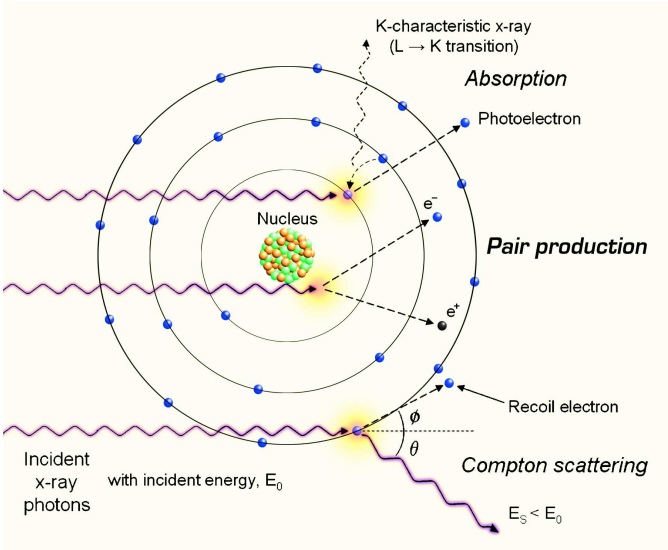

FIGURE 4.4: The main absorption processes of the photon interaction.

There are several mechanisms of absorption with different relative importances depending on the energy of the photons, as shown in Fig. 4.4. At energies lower than several 10 keV, the dominant process is the photoelectric absorption; then the Compton scattering (or incoherent scattering) up to several tens of MeV; at higher energies, the dominant process is the electron-positron pair production. The total attenuation coefficient is simply defined as the sum of all the partial coefficients:

$$\left(\frac{\mu}{\rho}\right)_{total} = \left(\frac{\mu}{\rho}\right)_{photoelectric} + \left(\frac{\mu}{\rho}\right)_{Compton} + \left(\frac{\mu}{\rho}\right)_{pair} \tag{4.14}$$

Fig. 4.5 shows a practical example of the photon attenuation in the gas mixture Ar/CO_2 (70 : 30) as a function of the photon energy.

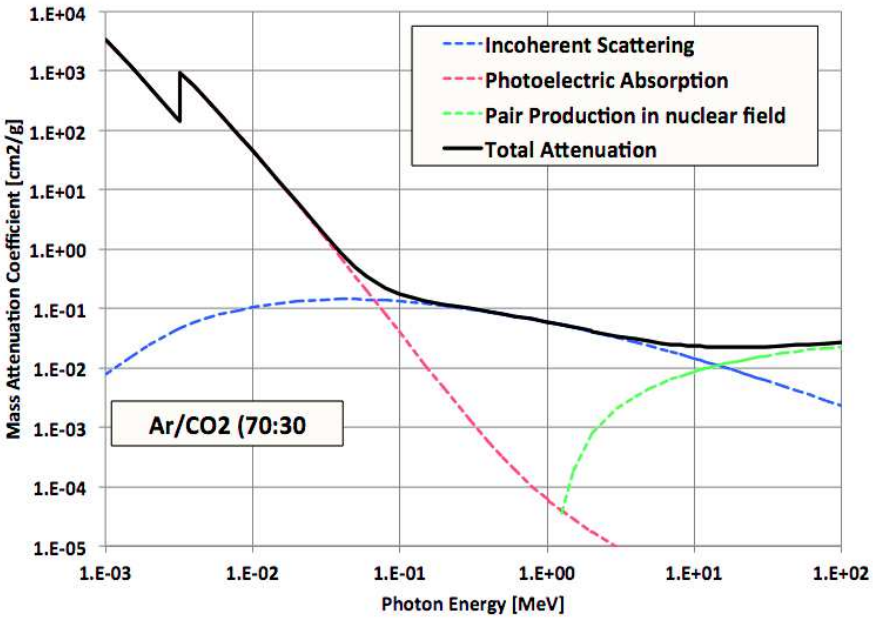

FIGURE 4.5: Total and partial mass attenuation coefficients in Ar/CO_2 (70 : 30) [12].

Each of these processes is complex and accompanied with secondary effects such as fluorescent radiations, emission of Auger electrons, recoil electrons or annihilation of positrons.

4.2.2.1 The photoelectric effect

In the case of photoelectric absorption, the total energy of the incoming photon is spent to remove one electron from an inner shell of the atom. This process is possible only if the energy E_γ of the photon is higher than the binding energy E_j of the electron to be removed. All the levels having $E_j \leq E_\gamma$ contributes to the photoelectric absorption. The effect is maximum at the edge and then decreases with the energy, giving a series of characteristic jumps in the absorption coefficient as seen in Fig. 4.5. The electron ejected from the atom has an energy $E_e = E_\gamma - E_j$ and leaves the medium in an excited state. The medium then returns to its ground state through two competing mechanisms:

- The first possibility, called Auger process, corresponds to an internal electronic rearrangement and the emission of an electron. For example, a vacancy in the K-shell may be filled by an electron from the L-shell which gives its energy to a M-shell electron that is ejected from the atom. This electron is called Auger electron and its kinetic energy is given by:

$$E_{Auger} = E_K - E_L - E_M \tag{4.15}$$

- In the second process called fluorescence, the vacancy on a j-shell is filled by an electron from a outer i-shell by emitting an X-ray photon with an energy $E_{Xray} = E_j - E_i$ where E_j and E_i are respectively the binding energies of the j-shell and the i-shell. The fraction of de-excitation by fluorescence, called fluorescence yield, is shown for the shells K and L on Fig. 4.6.

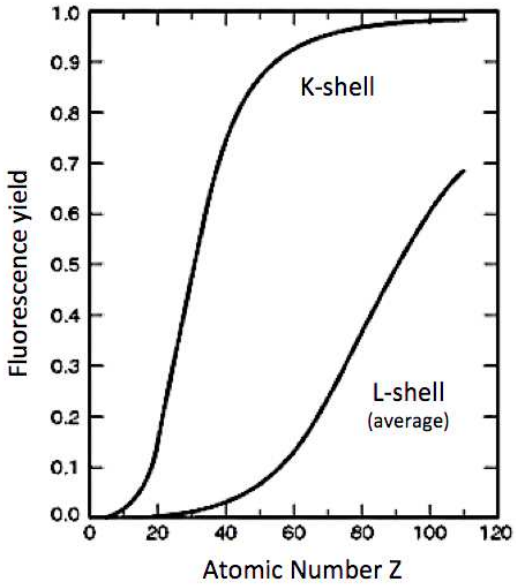

FIGURE 4.6: Fluorescence yields for K and L shells as a function of the atomic number Z. The curve for the L-shell is an average of L_1,L_2 and L_3 effective yields.

4.2.2.2 The Compton scattering

The photoelectric absorption cross-section falls very quickly after the K-edge, as shown in Fig. 4.5. At energies above the highest atomic level, the intensity loss of a photon beam is dominated by the elastic incoherent scattering on nearly free electrons of the medium, also called the Compton scattering. When an incident photon is scattered an angle θ, the electron recoils with an angle ϕ as shown on Fig. 4.4. The energy $E_{\gamma'}$ of the scattered photon and the energy E_e of the recoil electron are given by:

$$E_{\gamma'} = \frac{E_\gamma}{1 + \varepsilon(1 - cos\ \theta)} \tag{4.16}$$

$$E_e = \frac{E_\gamma \varepsilon(1 - cos\ \theta)}{1 + \varepsilon(1 - cos\ \theta)} \tag{4.17}$$

with $\varepsilon = E_\gamma/m_e$. In the case of back scattering (i.e $\theta = \pi$), the electron obtains the maximum energy:

$$E_e^{max} = \frac{E_\gamma}{1 + \frac{1}{2\varepsilon}} \tag{4.18}$$

Fig. 4.7 shows the energy distribution of the recoil electrons for different incident photon energies. The maximum energy, corresponding to the back scattering event is known as the Compton edge.

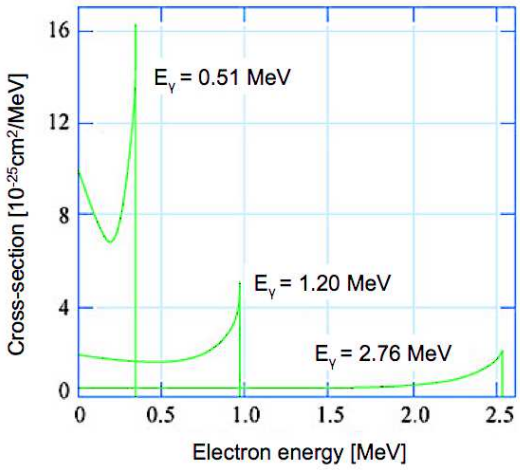

FIGURE 4.7: Energy distribution of Compton electrons for several incident photon energies.

The emission angle of the recoil electron is given by:

$$cot(\phi) = (1 + \varepsilon)\ tan\ \theta/2 \tag{4.19}$$

At low energies (i.e $\varepsilon << 1$), the scattering cross-section for a single electron can be reduced to:

$$\sigma_c^e = \sigma_{Th}^e(1 - \varepsilon) \quad with \quad \sigma_{Th}^e = \frac{8}{3}\pi r_e^2 \tag{4.20}$$

Where σ_{Th}^e is the Thomson cross-section and r_e the electron radius. At high energies (i.e $\varepsilon >> 1$), the cross-section is:

$$\sigma_c^e = \frac{\pi r_e^2}{\varepsilon}(\frac{1}{2} - ln(2\varepsilon)) \tag{4.21}$$

The total differential cross-section for a solid angle Ω is given by the Klein-Nishina angular distribution:

$$\frac{d\sigma_c^e}{d\Omega}(\theta) = r_e^2 \left(\frac{1}{1+\varepsilon(1-cos\ \theta)}\right)^2 \left(\frac{1+cos^2\ \theta}{2}\right) \left(1+\frac{\varepsilon^2(1-cos\ \theta)^2}{(1+cos^2\ \theta)(1+\varepsilon(1-cos\ \theta))}\right) \tag{4.22}$$

The atomic cross-section is:

$$\sigma_c^{atom} = Z\sigma_c^e \tag{4.23}$$

where Z is the atomic number of the medium. The angular distribution as a function of the incident energy and the polar diagram of the total cross-section are shown in Fig. 4.8 and Fig. 4.9.

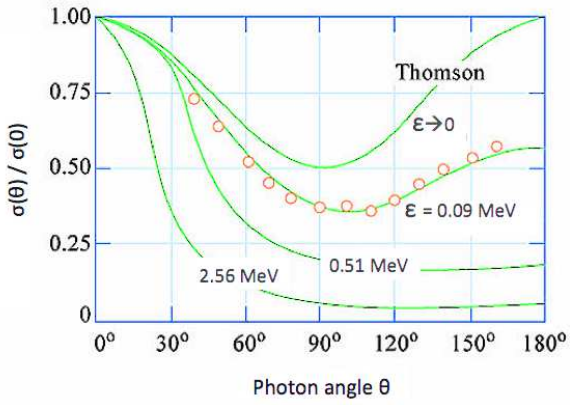

FIGURE 4.8: Angular distribution of scattered photons for several incident energies ε.

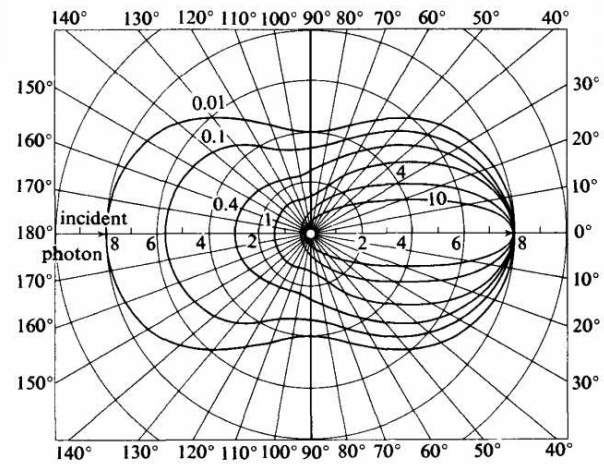

FIGURE 4.9: Polar diagram of the differential Compton cross-section per electron. Curves labeling corresponds to the incident photon energy ε. $d\sigma/d\Omega$ is expressed in $\text{cm}^2\ \text{sr}^{-1}$

4.2.2.3 The electron-positron pair production

During the pair production, or materialization, the photon is absorbed by producing an electron-positron pair in the medium. This is the dominant process of interaction at high energies and requires the presence of a nucleus or an electron to balance the momentum conservation during the transformation.

A particle at rest has a minimum energy $E^2 = m_0^2c^4$ with negative and positive solutions. The region between these solutions corresponds to the forbidden energies, as shown in Fig. 4.10. The materialization energy is used to bring a particle from a negative energy state, also called the Dirac sea, to the positive domain. A "hole" is then left in the Dirac sea corresponding to an anti-matter particle. In the case of an electron-positron pair produced by a photon crossing the electric field of a nucleus, the threshold energy is $2m_ec^2 = 1.022$ MeV. The positron has a high probability to be annihilated in the medium, producing one or several energetic photons. If the secondary photons have an energy higher than the threshold energy, they will trigger more materialization and annihilation processes and create an electromagnetic shower in the medium.

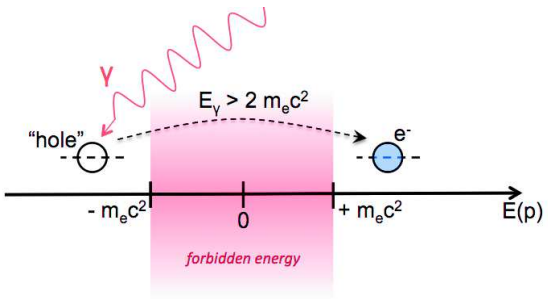

FIGURE 4.10: Schematic view of the Dirac sea in the case of an electron-positron pair production.

4.2.3 Interaction between neutrons and matter

Finally, the dominant background in the CMS end-caps will be neutrons with energies from 10^{-8} to 10^3 MeV (see Sec. 3.2). Since neutrons are uncharged particles, they are not sensitive to Coulomb interactions with the medium but they can provoke collisions with the atoms or interact directly with the nuclei via nuclear reactions. Therefore it is very difficult to detect free neutrons, especially with gaseous detectors. However, a neutron passing through a detector can interact with the material surrounding the gas volume and produce secondary emission of charged particles or photons that may ionize or excite the gas. We can identify five main interactions with different probabilities depending on the neutron incident energy, as shown on Fig. 4.11.

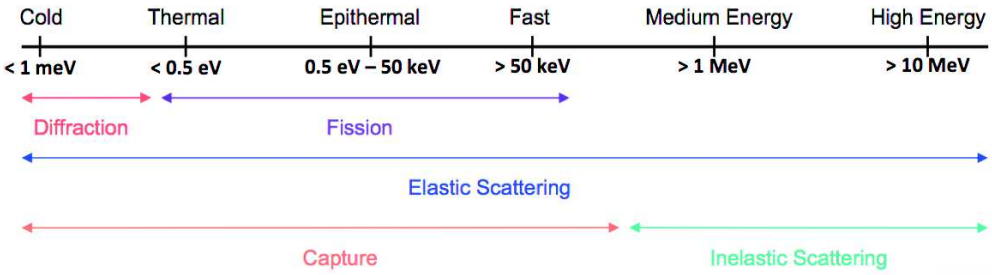

FIGURE 4.11: Classification of free neutrons with the most probable type of interaction with matter.

The neutron-induced fission occurs at relatively low energies. The target nucleus is split into two or more smaller nuclei and releases a large amount of energy in the form of a secondary emission of neutrons, photons or other types of radiations. This leads to the concept of neutron multiplication and chain reactions used in the nuclear reactors.

The elastic neutron-nucleus scattering $A(n,n)A$ is mainly responsible of the slowing down of the incident neutron, also called the neutron moderation. In this case, the energy and the direction of the neutron are altered and the target nucleus recoils and stays in its ground state. The neutron moderation is the dominant energy loss process from intermediate to high energies.

The neutron capture consists of the absorption of the neutron by the medium, followed by the emission of gamma rays in case of a radiative capture (n,γ) or the emission of charged particles such as protons (n,p) or alpha particles (n,α).

At energies higher than several MeV, the neutrons interact via inelastic scattering $A(n,n')A^*$ with the medium. The neutrons lose a large fraction of their energy and leave the target nuclei in an excited state. Secondary radiations are then emitted from the nuclei when returning to the ground state.

4.2.4 Drift and diffusion in gases

As seen in the previous sections, most of the particles interacting with a gaseous medium produces free charges by ionization, called the primary charge. This clear signature of the crossing of a particle can be extracted from the gas to produce electrical signals that will be transferred to a data acquisition system. However, the charges moving in the gas will also interact with the atoms before being collected. The understanding of these interactions is necessary for the choice of the gas mixture in particle detectors.

The primary electrons and ions gradually lose their energy in collisions with the gas molecules and diffuse by multiple scattering following a Maxwell distribution for their energy ϵ [13]:

$$\frac{dN}{d\epsilon} = F(\epsilon) = C\sqrt{\epsilon}\ e^{-\epsilon/kT} \tag{4.24}$$

with N the number of charges, T the temperature and k the Boltzmann constant. These charges assume the thermal energy of the gas with an average value $\epsilon_T = \frac{3}{2}kT$. A Gaussian distribution gives the dislocation of the charges at the distance x from the origin and after a time t:

$$\frac{dN}{N} = \frac{1}{\sqrt{4\pi Dt}} e^{\frac{-x^2}{4Dt}} dx \tag{4.25}$$

where D represents the constant of diffusion which depends on the nature of the charges and the medium. We can define the mean free path λ as the average distance between two collisions:

$$\lambda = \frac{1}{N\sigma_{collision}} \tag{4.26}$$

with σ the cross-section of the interaction and N the number of atoms per volume.

In the presence of a uniform electric field E across the medium, the free charges move along the field direction and accelerate until they reach their drift velocity v_d. Then, the electrical mobility of the charges can be defined as:

$$\mu = \frac{v_d}{E} \tag{4.27}$$

The Einstein's relation shows that the mobility is related to the coefficient of diffusion :

$$\mu = \frac{e}{kT} D \tag{4.28}$$

In the case of electrons moving in a gaseous medium under the influence of an electric field, the drift velocity and thus the mobility are not constant since the electrons can acquire energy between two collisions due to their small mass. Townsend gives a simple expression of the electron velocity:

$$v_d^e = \frac{e}{2m_e} E\tau \tag{4.29}$$

where τ is the mean time between collisions. With the ideal gas approximation, the drift velocity becomes proportional to the reduced electric field E/P and the temperature T of the medium, P being the pressure of the gas:

$$v_d^e \propto \frac{ET}{P} \tag{4.30}$$

Since the wavelength of such electrons is comparable to the size of the gas molecules, the interaction cross-section σ, and therefore the time τ, strongly varies with the energy ϵ of the electrons. These variations, described by the Ramsauer-Townsend effect, reach maxima and minima as shown in Fig. 4.12.

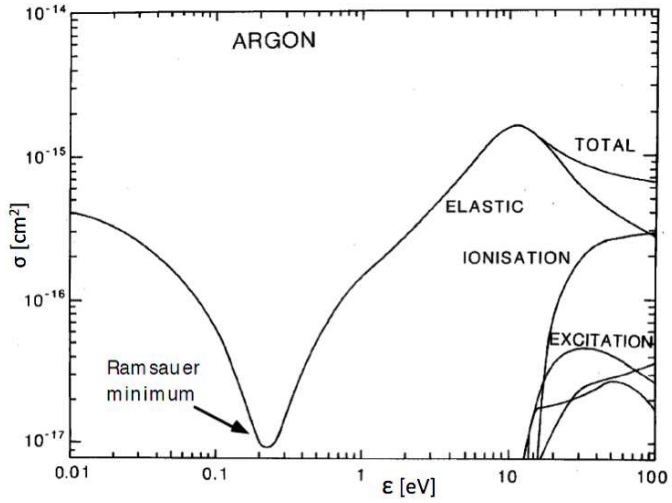

FIGURE 4.12: Interaction cross-section of electrons in Ar.

This relation is particularly important for the operation of gaseous detectors, where the charges freed by an incoming particle move inside of the gas volume to reach a readout electrode. It is interesting to minimize the interaction of the electrons with the medium in order to minimize the diffusion of the charges, which could degrade the performance of detection.

4.3 Development of gaseous detectors

The highlighting of interesting physics phenomenon requires the use of powerful detectors to identify infinitesimal objects and their properties. Many types of particle detectors were invented and developed in the 20^{th} century. Gaseous detectors are by definition

very light devices and they give a very high level of flexibility in term of geometry, composition and thus performance. For this reason, gaseous detectors are used in many HEP experiments with custom made designs and specific operating conditions. On the other hand, because of the very low density of the detection medium, the total amount of primary charges produced by a particle in the detector is relatively small compared to other technologies. Therefore, gaseous detectors often require an additional amplification stage before the particle signals are collected. This section aims to describe the basic operation of gaseous detectors and their evolution from the wire chambers to the modern micro-pattern detectors. The basic amplification processes and the various modes of operation discussed below are adapted from [13], [55], [56] and [20].

4.3.1 Amplification process in a gaseous medium

In electric fields higher than few kV/cm, the electrons acquire sufficient energy between two collisions to provoke the excitation and/or the ionization of the gas and produce free charges that can ionize further atoms. This chain reaction, also called avalanche, is responsible for the amplification of the primary charge in gaseous detectors. The ionization mean free path is the average distance that an electron can travel before being involved in an ionization process. The inverse of the mean free path is called first Townsend coefficient α and is given by the Korff's approximation:

$$\frac{\alpha}{P} = Ae^{-BP/E} \tag{4.31}$$

where P is the pressure of the gas and A and B are parameters depending on the gas type and on the electric field range. If n is the number of electrons at a given position, after a path dx along the drift direction, the number of electrons after amplification is:

$$dn = n\alpha dx \tag{4.32}$$

One can therefore obtain the amplification factor M by integrating Equ. (4.32):

$$M = \frac{n}{n_0} = e^{\alpha x} \tag{4.33}$$

In the case of a non-uniform electric field, the Townsend coefficient is a function of the distance x. The amplification factor between x_1 and x_2 can be expressed as:

$$M = exp\left[\int_{x_1}^{x_2} \alpha(x)dx\right] \tag{4.34}$$

The amplification factor thus increases exponentially with the electric field strength but shows a limit around $M = 10^8$ due to the influence of the space charge on the electric field and because of the spread of the avalanches by photon emission. This condition is known as the Raether limit and corresponds to $\alpha x \sim 20$.

4.3.2 Operation regimes of gaseous detectors

The basic principle of operation of gaseous detectors can be simplified with the example of the parallel plate detector. The signal generated by such detectors is produced when the free charges released by a particle drift inside of the detection medium under the influence of the electric field created by the two electrodes. We distinguish four main operation regimes depending on the magnitude of the electric field in the amplification region. Fig. 4.13 shows the relation between collected charge and the amplification field in the different regions of operation.

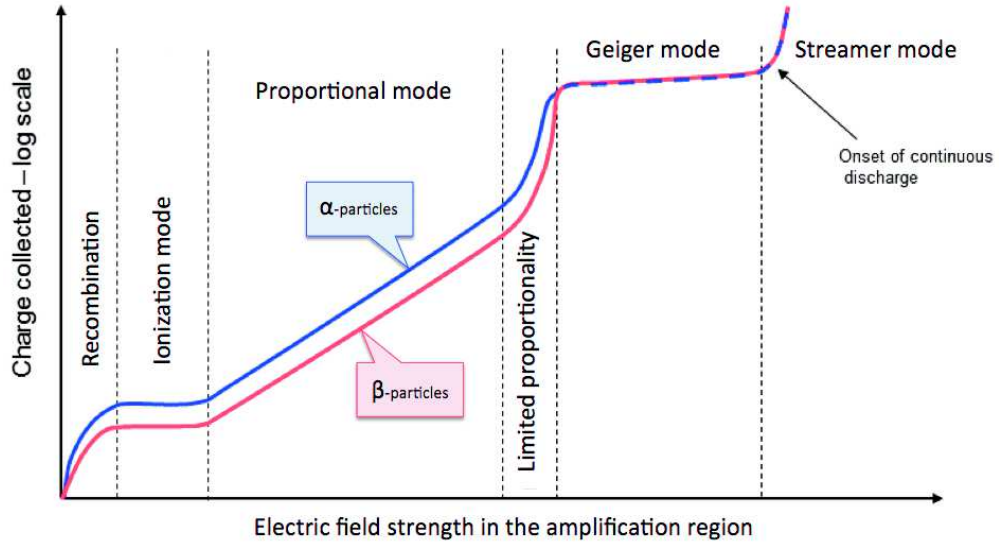

FIGURE 4.13: Gain-voltage characteristics for gaseous detectors showing the different operating modes. The y-axis is refers to the collected charge in logarithmic scale.

4.3.2.1 Ionization mode

As described Sec 4.2, the number of primary charges left in a detector by a particle depends on the type, the energy of the particle and also on the properties of the detection medium. In the case of highly ionizing events, a large amount of charge is released in

the gas and moves along the electric field lines, inducing a large signal on the electrodes (Fig. 4.14). In this mode, called ionization regime, it is not necessary to amplify the primary charge before the collection. Therefore, a relatively low electric field is enough to generate signals above the electronic noise (typically lower than 10 kV/cm). However, for very low electric fields, a significant portion of the primary charge is lost by electron-ion recombination or electron attachment to neutral molecules of the medium.

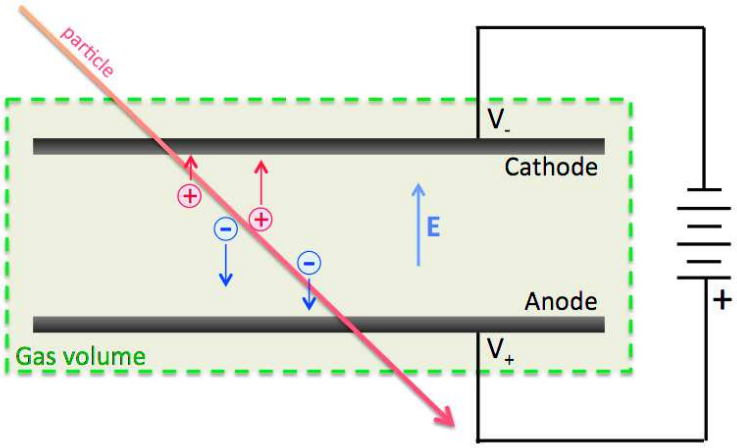

FIGURE 4.14: Schematic representation of ionization chambers.

The ionization chamber is the ancestor of most of the modern gaseous detectors but such chambers are still used today, in particular in some industrial smoke detectors where the smoke can enter the amplification region and attenuate the current induced by a constant source of α-particles, usually ^{241}Am.

4.3.2.2 Proportional mode

A large part of gaseous chambers is used to detect charged particles and/or high energy photons. In this condition, the primary charge deposited in the chamber is not large enough to produce signals above the average noise of the readout systems. It is then necessary to amplify this charge before collecting of the signal.

At a certain threshold voltage V_T (depending on the geometry of the detector), a critical electric field E_C is established between the electrodes and is intense enough so that the free electrons trigger further ionization of the gas and produce avalanches. As seen in Sec 4.3.1, the avalanche process depends on the magnitude the electric field and on the properties of the gas mixture. The number of electrons after amplification is proportional to the primary charge (see Equ. (4.32)). The signal produced by proportional detectors is therefore representative to the energy deposited by the crossing particles. Fig. 4.15 shows a schematic view of the amplification process in a proportional chamber. It is

however important to notice that when increasing the field strength, the amplification factor increases and more secondary charges are freed, forming large avalanches. At a certain point, the space charge provokes the distortion of the electric field in the vicinity of the avalanche and lead to a gradual loss of proportionality.

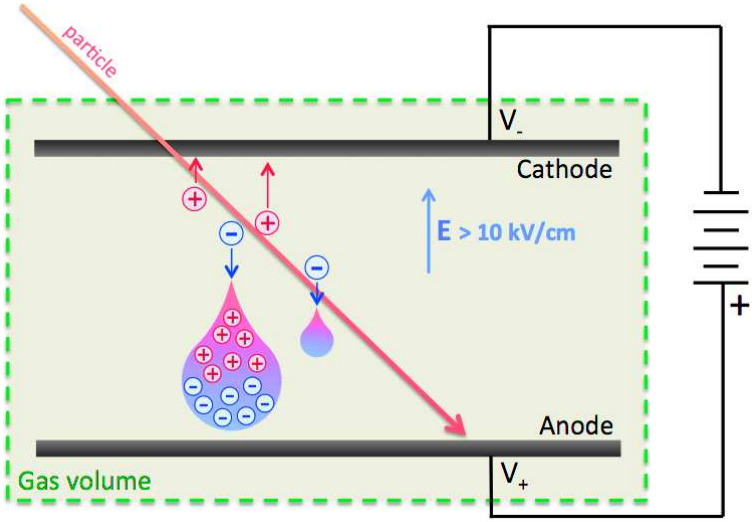

FIGURE 4.15: Schematic representation of proportional chambers.

This mode of operation is widely used in gaseous detectors, such as proportional counters, multi-wire chambers and more recently the micro-pattern gaseous detectors. At CMS, the DTs, CSCs and RPCs operate in proportional mode. Sec 4.3.4 describes how to establish a proportional amplification with several examples of famous detectors.

4.3.2.3 Geiger mode

At higher amplification fields, the primary avalanche triggers multiple secondary avalanches, mostly by the emission of UV photons or by recombination of avalanche ions on the surface of the cathode . A chain reaction occurs and spreads through the entire detection volume until the process is stopped by a voltage drop on the electrodes or by the space charge of ions in the case of "self-quenching" detectors. The total charge produced after the amplification is thus independent from the initial deposition. This operation regime, called saturation or Geiger mode, is described in Fig. 4.16.

Geiger detectors are essentially used to counts number of particles since the primary charge information is lost during the amplification process. A particular choice of materials and gas composition can increase the interaction probability with certain particles such as gamma rays, α-particles or neutrons in order to make Geiger detectors useful for radio-protection applications. The CMS muon detectors do not operate in Geiger mode

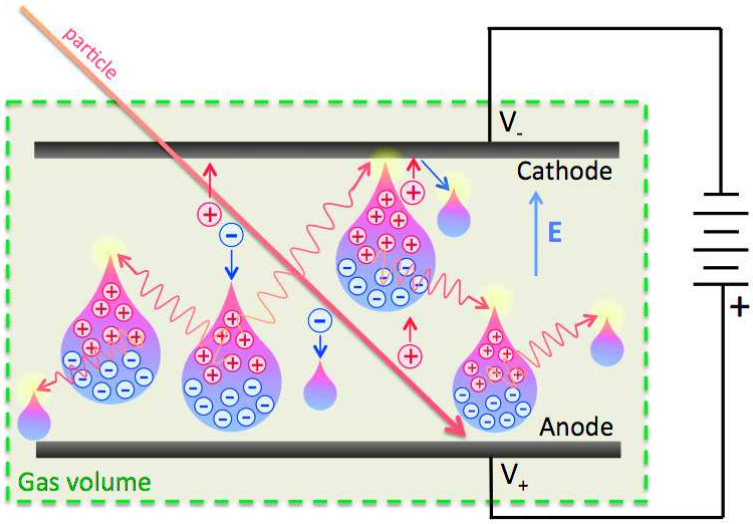

FIGURE 4.16: Schematic representation of Geiger-Muller chambers.

since it would be impossible to reconstruct the exact position of the muon hits. Moreover, the detectors would need more time to evacuate all the charges produced during the amplification, which is not compatible with the minimum rate capability required in the CMS end-caps.

4.3.2.4 Streamer mode

At even higher fields, the space charge density in the avalanche becomes comparable to the surface charge density of the electrodes causing the focusing of the field lines toward the avalanche region. Then, the secondary photoelectrons seen in the Geiger mode can drift along the distorted field toward the avalanche region and induce additional avalanches that sum up with the original one, producing a thin plasma filament in the detection medium. This filament, also called streamer, can propagate toward the electrodes and trigger a discharge in the chamber as seen in Fig. 4.17. For most of the detectors, this phenomenon appears when the Raether limit is overcome (see Sec 4.3.1).

The advantage of the streamer mode is that a simple and cheap structure can produce very large signals. However, the streamers can provoke a powerful breakdown which releases most of the electrostatic charge accumulated in the electrodes. It is customary to cover the electrodes with highly resistive layers to limit the energy and the propagation of the discharges and protect the elements forming the detector as well as the readout electronics. RPCs were initially designed for such operation mode and are today widely used in HEP experiments.

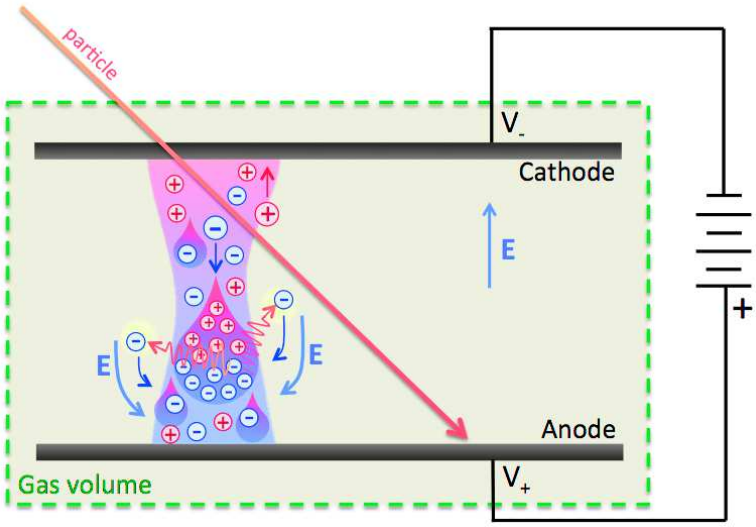

FIGURE 4.17: Schematic representation of a Streamer in parallel plate detectors.

4.3.3 Choice of the gas mixture

The choice of the gas is essential to ensure the good operation of particle detectors. As seen in the previous sections, the number of primary charges, the amplification factor and its proportionality strongly depend on the properties of the gas. In addition, specific applications impose experimental requirements that also rely on the choice of gas, such as a high rate capability, a maximum longevity, good time and space resolutions or a low discharge probability. We will focus here on the properties of the mixtures proposed for the upgrade of the CMS end-caps, namely Ar/CO_2 (70 : 30) and $Ar/CO_2/CF_4$ (45 : 15 : 40).

Since most of the polyatomic molecules can de-excite through non-ionizing processes, noble gases are prefered to detect MIPs at relatively low electric field. Among the noble gases, argon gives an acceptable number of electron-ion pairs per unit length for MIP and is relatively cheap compared to xenon or krypton. However, excited argon atoms return to ground state only by the emission of photons with energies higher than 11.6 eV that can induce secondary avalanches (see Sec. 4.16). The addition of "quenching" gas is thus necessary to absorb these photons and dissipate the energy through non-ionizing processes. In particular, weakly-bound polyatomic molecules, such as CO_2, have a very efficient absorption in the energy range corresponding to the argon emission and they de-excite through vibrational or rotational transitions.

The addition of so-called "cold" gases also helps to improve the space and time performance of the detectors. For example, molecules such as CF_4 have a large inelastic cross

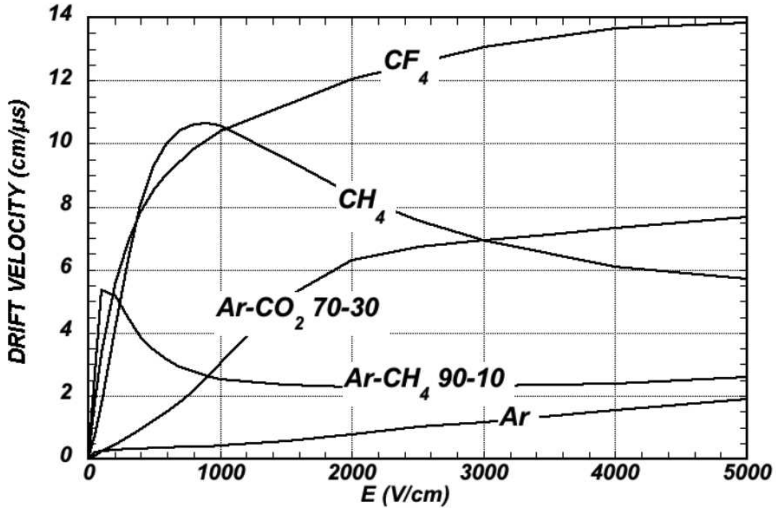

FIGURE 4.18: Comparison of electron drift velocity for different gas species [13].

section and can "cool down" the electrons into energy ranges close to the Ramsauer-Townsend minimum (see Fig. 4.12). The total scattering cross section in Ar then decreases while the electrons drift velocity increases, as seen in Fig. 4.18, resulting in a lower volume diffusion of the electrons (Fig. 4.19).

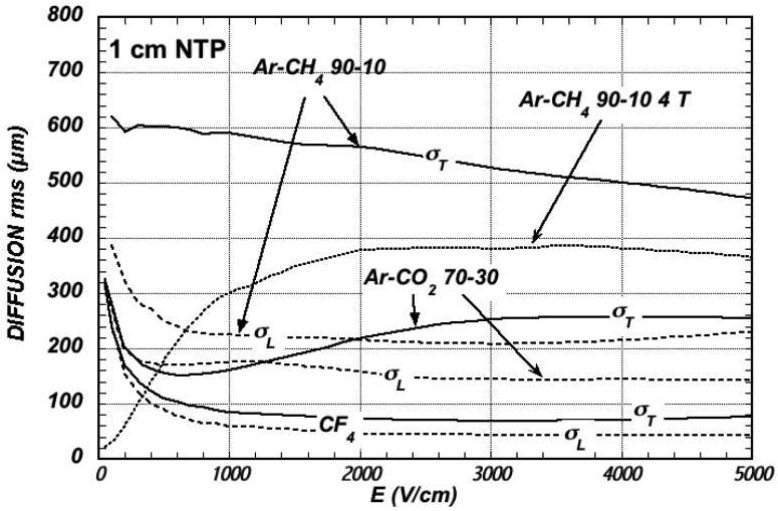

FIGURE 4.19: Comparison of electron longitudinal (σ_L) and transverse (σ_T) diffusions for different gas species.

Moreover, for thin gap detectors, the average distance between the primary ionization clusters strongly affects the localization accuracy and the time resolution. The addition of a molecule giving a high number of total ionization per unit length, such as the CF_4, enhances the uniformity of the primary cluster distribution of the mixture and thus improves the performance of the detectors.

However, some molecules can also affect the amplitude the signal induced by particles. For example in CF_4, the electron capture cross section becomes very large in electric

fields higher than 8 kV/cm, causing a signal reduction along the drift path.

Tab. 4.1 shows the detection properties of commonly used gases.

Gas	Z	Density [mg cm^{-3}]	E_X [eV]	E_I [eV]	W_I [eV]	$(dE/dx)_{MIP}$ [keV cm^{-1}]	N_P [cm^{-1}]	N_T [cm^{-1}]
He	2	0.179	19.8	24.6	41.3	0.32	3.5	8
Ne	10	0.839	16.7	21.6	37	1.45	13	40
Ar	18	1.66	11.6	15.7	26	2.53	25	97
Xe	54	5.495	8.4	12.1	22	6.87	41	312
CH_4	10	0.667	8.8	12.6	30	1.61	28	54
iC_4H_{10}	34	2.49	6.5	10.6	26	5.67	90	220
C_2H_6	18	1.26	8.2	11.5	26	2.91	48	112
CO_2	22	1.84	7.0	13.8	34	3.35	35	100
CF_4	42	3.78	10.0	16.0	54	6.38	63	120

TABLE 4.1: Some properties of noble gases and polyatomic molecules at normal conditions (T : 20 ° C, P : 1 atm). Z is the atomic number, E_X and E_I the first excitation and the ionization energy, W_I and $(dE/dx)_{MIP}$ the average electron-ion pair energy and the differential energy loss, N_P and N_T the primary and total number of pairs per unit length in MIP events.

4.3.4 Historical aspects of gaseous detector

The first gaseous detector was introduced in 1906, by H. Geiger and E. Rutherford under the form of a cylindrical single wire chamber. The principle has been developed and improved in the next period, in particular by W. Muller with the Geiger-Muller detector in 1928. However, one of the biggest improvement was achieved by G. Charpak and his collaborators in 1968 [57], with the effective operation of the first modern electronically-readout detector, the Multi-Wire Proportional Chamber (MWPC). With this technology was also introduced the concept of pattern, that allows large detection volumes and precise localization of the particle hits. This crucial achievement was awarded the 1992 Nobel Prize and triggered extensive work and studies that had resulted in the modern world of gaseous detectors. This section aims to briefly describe the evolution of particle detectors from the MWPCs to the Micro-Pattern Gaseous Detectors (MPGD) by showing their typical performance and limitations.

4.3.4.1 MWPCs, principle and limitations

The MWPC consists of a plane of parallel anode wires running through two parallel cathode plates as shown in Fig. 4.20. The typical wire spacing is 2 mm while the distance between the wire plane and the cathode plates is three or four times larger. By applying a positive voltage to the wires, an electric field E develops from the external plates and focuses on the wires [13].

When filled with the appropriate gas mixture (see Sec. 4.3.3), a particle crossing the detector releases primary electrons that drift along the field lines toward the closest anode wire. In the vicinity of the wire, the electric field becomes intense enough to accelerate the electrons and trigger the avalanche multiplication.

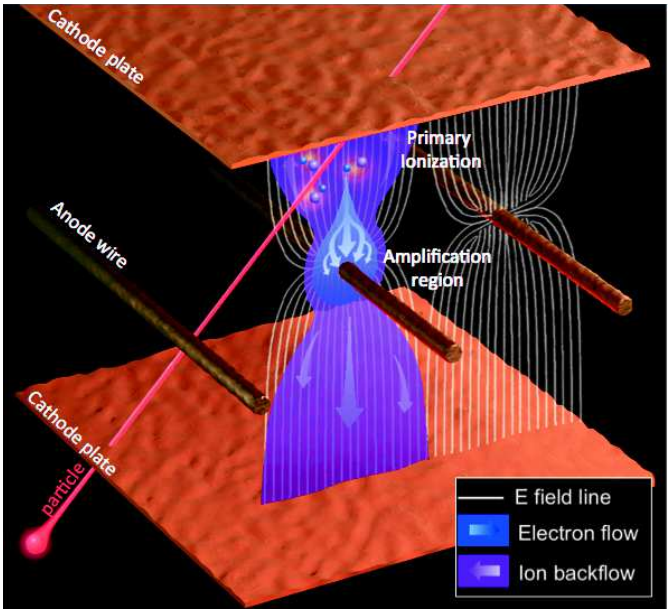

FIGURE 4.20: Schematic representation of a MWPC in operation.

Because of the pattern structure of the wire plane, the spatial resolution can be evaluated by $\sigma = pitch/\sqrt{12}$, where the pitch is defined by the distance between the wires. For a typical MWPC with a pitch of 2 mm, the spatial resolution is at the level of $\sim 0.5 - 1$ mm. However, this resolution can be improved by combining several layers of MWPCs with different orientations and segmented cathode plates with a fine pitch. The typical time resolution is of the order of 10 ns in Ar/CO_2 (70 : 30). Today, the MWPCs are essentially used as beam profile analyzers, slow triggering systems or in some applications as spectrometers for low energy particles. In CMS a variant of the MWPC, the CSCs, are used for the L1 trigger and the muon reconstruction in the forward end-caps.

Large sizes MWPCs can be produced at a reasonable cost but require a very precise geometry and a sufficient structural strength to ensure the same tension for all the wires. Moreover, the electrostatic forces inside of the chamber can induce displacement of the wires that affect the quality of the electric field and thus the uniformity of the gain. Additionally, the wire technology is very sensitive to the classical aging of gaseous detectors (described in Sec. 7.2.2) and requires particular operation conditions and longevity studies to ensure an acceptable lifetime of the detectors. However, the most critical limitation of MWPCs is the gain reduction when subject to high fluxes of particles. The large distance between the anode wires and the cathode plates induces a long transit time necessary for the positive ions to reach the cathode (~ 100 μs). This

effect generates a build-up of positive space charge that results in the modification of the electric field and thus the perturbation of the charge amplification. The effective gain of MWPCs, shown in Fig. 4.21, drops quickly at particle fluxes above 10^4 Hz/mm^2 [13].

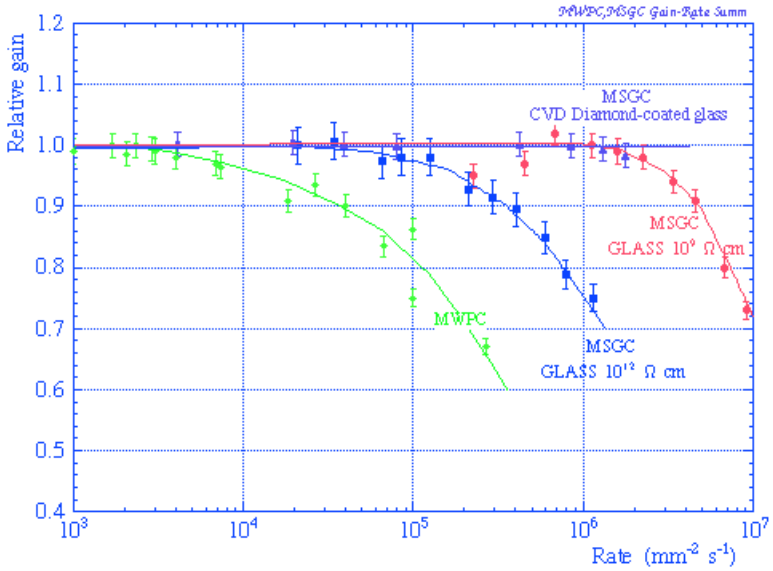

FIGURE 4.21: Rate capability of the MWPC and MSGC (see next section) technologies.

For these reasons, a novel concept of gaseous detector based on microscopic structures was introduced in the late 80's in order to instrument high rate and long duration experiments.

4.3.4.2 MSGCs, principle and limitations

The various progress in semiconductor industry, in particular the photolithography techniques, allowed producing microscopic electrodes of the order of 100 μm with a very good position accuracy. Such a short distance between anodes and cathodes brings the positive ions transit time down to the sub-microsecond scale and thus increases the rate capability by several orders of magnitude compared to MWPCs (seen in Fig. 4.21). The Micro-Strip Gas Chamber (MSGC) was the first Micro-Pattern Gaseous Detector (MPGD), proposed in 1988 by A. Oed as an alternative solution of the expensive solid-state detectors for high rate applications that require fine spatial resolution for particle tracking [58]. It is made by a plane of small parallel metal strips, alternately connected as anodes and cathodes, engraved on a thin resistive layer. By applying a sufficient voltage between the anodes and the cathodes, an electric field develops between the strips and becomes intense enough in the vicinity of the anode strips to trigger the avalanche multiplication (Fig. 4.22).

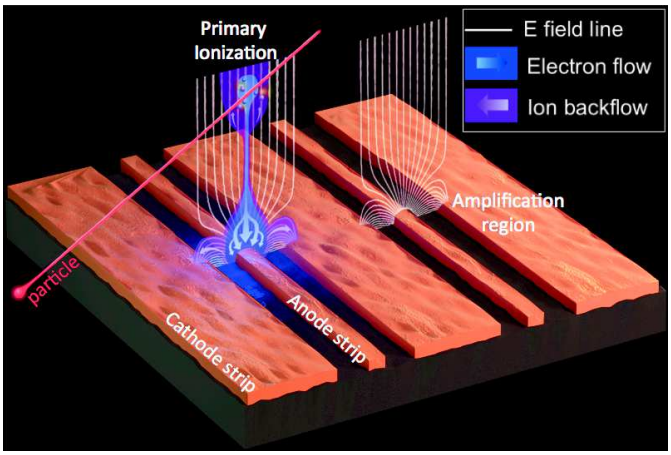

FIGURE 4.22: Schematic representation of a MSGC in operation.

Systematic studies performed in the 90's showed very promising performance : gas gain over 10^4 [59]; space resolution down to 30 μm rms [60]; rate capability above 10^6 Hz/mm^2 [61].

However, the use of high resistivity substrates induced problem of gain stability at high rates. On a short time scale, the charging up of the substrate and the ion migration within the material induces gain fluctuations of the order of several tens of percents of the initial value, depending on the particle rate and energy, causing non uniformity and detection instability [61]. On a long time scale, the operation of the detectors at high rate is affected by the polymerization of the gas and the pollutants present in the gas volume, also called classical aging (see Sec. 7.2.2). Due the small size of the electrodes and the type of materials used in the assembly of the detectors, the first MSGCs were prone to classical aging [62]. To overcome the stability problems, the high resistivity substrate was replaced by a reduced resistivity and electronic conductive materials such as diamond-like coated glass and Pestov-glass coating [63]. Moreover, an extensive study on clean gas mixtures, non-outgassing materials, and electric field configurations helped to increase the long-term stability of MSGCs at high rates. [64].

Nevertheless, despite of the good performance and stability, the operation of MSGCs in high rate environments is limited by the discharge probability. In the case a large amount of energy is released in the drift gap, the total number of electrons in the avalanche may reach the Raether limit and trigger the development of a streamer between the electrodes. Additionally, the presence of dust on the readout board can create an electrical bridge between the cathodes and the anodes strips and trigger a streamer. Because of the small size of the amplification structure, such discharges can seriously and permanently damage the detector (see Fig. 4.23). Although extensive studies on gas mixture and operating conditions allowed to reduce the discharge probability [65], the uncertainty on the long-term integrity of MSGCs in harsh environments triggered the development

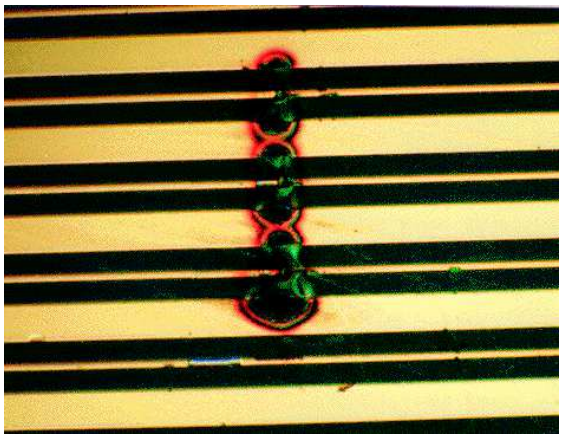

FIGURE 4.23: Microscopic view of a damage MSGC after a destructive discharge.

of alternative solutions. One of these solutions was elaborated by F. Sauli and consists of pre-amplifying the signal by a factor $\sim$ 100 with a Gas Electron Multiplier (GEM) before it reaches the micro-strip plane in order to reduce the voltage required on the strips.

The CSC+GEM technology was initially foreseen for the forward tracker CMS [66], but finally abandoned in favor of the silicon detectors. Nevertheless, MSGCs are still in use in many HEP experiments, in particular in the inner detector of HERA-B (DESY) [67].

4.3.4.3 Micro-Pattern Gaseous technologies and applications

The Micro-Pattern Gaseous Detectors (MPGD) were developed in the continuity of the MSGCs. They represent the latest generation of gaseous detectors, already used in several HEP experiments. The most common MPGDs are the Gas Electron Multiplier (GEM) and the MICRO MEsh GAseous Structure (Micromegas)

The GEM technology was introduced by F. Sauli in 1996 to pre-amplify signals in MSGCs. It consists of a thin layer of insulating polymer, usually a 50 μm thick polyimide, coated on both sides with 5 μm of copper and chemically perforated with a high density of microscopic holes. The typical diameter of the holes is 70 μm, with a pitch of 140 μm. When applying a difference of potential between the two copper layers, an electric field with an intensity as high as several 10 kV/cm is established inside of the holes. When primary electrons created by the crossing of a particle reach the GEM holes, they are accelerated in the intense electric field and acquire sufficient energy to produce an avalanche, as shown in Fig. 4.24. Then, the charge after the amplification can drift toward a readout board where it induces an electrical signal.

The GEM can be the unique amplification technology in a detector, or in association with another detection structure in order to share the amplification and reach high

gas gains. The main benefits and the general performance of this technology are fully described in Sec. 6.5 and Chapter. 7.

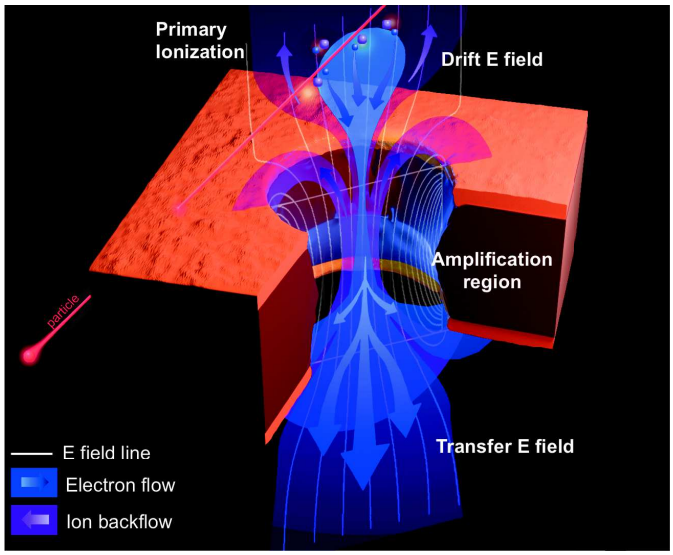

FIGURE 4.24: Schematic representation of a GEM hole in operation.

The Micromegas structure was proposed by G. Charpak and I. Giomataris in 1992. The principle is the same than for a parallel plate detector, but the amplification gap is reduced to the sub-millimeter scale, typically 100 μm. To keep a high conversion efficiency as well as a large number of primary charges, a conversion gap of several millimeters is placed on top of the parallel plate structure. By replacing the top plate by a microscopic mesh, the primary electrons can drift toward the anode and enter the amplification field to trigger avalanches (see Fig. 4.25). Later versions include a resistive layer on top of the anode strips in order to reduce the energy released during a spark formation and protect the readout electronics. Because of an excellent rate capability, a space resolution better than 100 μm and a time resolution of the order of the nanosecond, the Micromegas technology was identified as a suitable choice for the ATLAS small wheel upgrade in 2018.

GEM-based and Micromegas-based detectors are used in many HEP experiments: COMPASS (CERN), TOTEM (CERN), STAR and PHENIX (RHIC), ALICE TPC (CERN), LHCb (CERN), SuperFRS, PANDA and CBM (FAIR) and many others ...

Despite of the complexity of their microscopic structures, cylindrical versions of GEM-based and Micromegas-based detectors were developed, in particular for KLOE-2 (DAFNE), BESIII (Beijing), CLAS12 (JLAB), ASACUSA (CERN) and CMD-3 (BINP).

Numerous variations of the GEM and the Micromegas technologies were also developed in the last decade, with many applications in hadron physics, particle tracking and heavy ions physics. Among others, the THick GEMs (THGEM), the resistive GEMs,

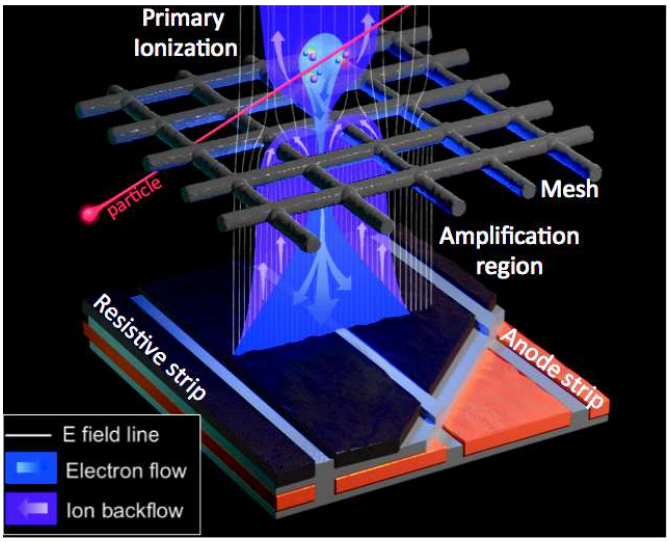

FIGURE 4.25: Schematic representation of a Micromegas in operation.

the Micro-PIxel Chambers (μ-PIC) and the InGrid structures will be used in the next ATLAS and CMS upgrades and for the new linear colliders.

All details about the recent MPGD applications and future developments can be found at the 4^{th} international conference on MPGDs (MPGD2015) in October 2015 in Trieste (Italy), in particular at [68].

Illustrative pictures of the most common MPGD structures are shown on Fig. 4.26.

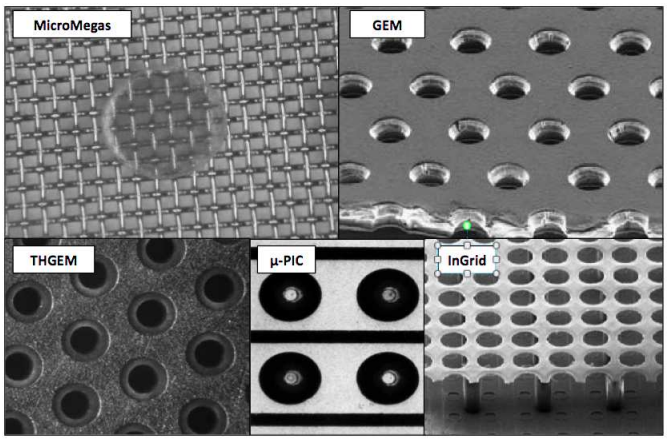

FIGURE 4.26: Microscopic pictures of the common MPGD structures.

4.3.4.4 Triple-GEM technology and applications

The maximum amplification of single GEM layer is of the order of 5×10^3. In this conditions the foil is very close to its electrical breakdown and the discharge probability is about several percents [69]. However, the specificity of the GEM technology is that,

after the amplification, a signal induced by a particle is not immediately re-absorbed by the GEM electrodes and thus it can be transfered to another structure for further amplification. It is therefore possible to obtain large amplification factors (up to 10^5) by combining several layers of GEM, without approaching the electrical breakdown of each layer. The production of large signals with a low probability of discharges significantly reduces the complexity and the cost of the readout electronics and ensures the maximum protection against destructive events.

The most used GEM-based detector consists of a triple-GEM structure embedded between a drift plane (cathode) and a readout board (anode). One can therefore distinguish different regions in the detector: the drift region between the drift electrode and the first GEM foil, where the primary charge is deposited; the transfer gaps between GEM1 and GEM2 then GEM2 and GEM3; the induction gap between the last GEM and the readout board, where the amplified charge induces the final readout signal. The general layout of the triple-GEM detectors is shown on Fig. 4.27.

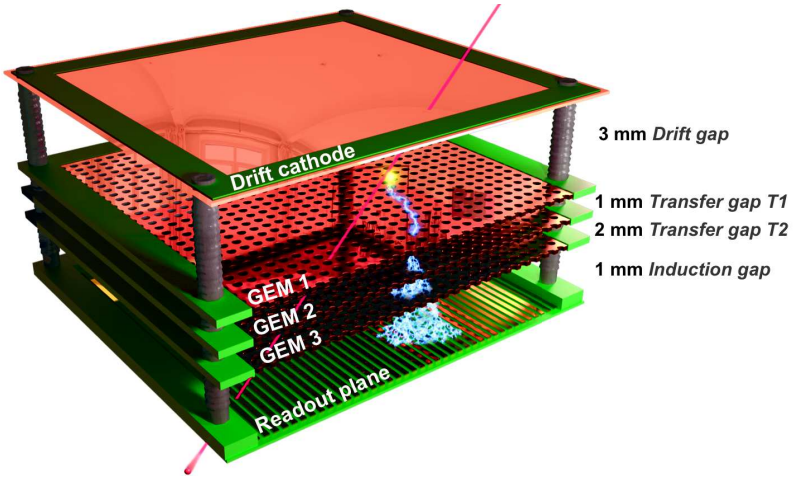

FIGURE 4.27: Schematic view of a triple-GEM detector.

The gaps between the GEMs varies with the application but they are usually of the order of the millimeter, a good compromise between the mechanical constraints and the magnitude of the electric fields necessary to transfer the charges from an electrode to another. However, the drift gap, where the conversion takes place, is usually bigger in order to maximize the sensitivity to incoming particles and make sure that the number of primary electrons is large enough to compensate possible losses before the amplification. As an example, the gap configuration called "3/2/2/2" and the corresponding electric fields are shown on Tab. 4.2.

Region	**Gap [mm]**	**Electric field [kV/cm]**
Drift	3	2.4
Transfer 1	2	3.6
Transfer 2	2	3.6
Induction	2	3.6
Region	**Voltage [V]**	**Average Electric field [kV/cm]**
Δ_{GEM1}	400	80
Δ_{GEM2}	360	72
Δ_{GEM3}	325	65

TABLE 4.2: The electric field configuration of the triple-GEM detector in the 3/2/2/2 gap configuration at the nominal voltage 4400 V. The parameters Δ_{GEM1}, Δ_{GEM2}, Δ_{GEM3} correspond to the difference of potential between the copper electrodes of GEM1, GEM2 and GEM3.

The triple-GEM detectors are used in several HEP experiments, in particular:

- COMPASS (CERN): the first high-luminosity experiment to use the GEM technology [70]. twenty two 30×30 cm^2 (medium-size) triple-GEM detectors are installed in the inner tracking stations. With the gap configuration 3/2/2/2, the chambers operate in the $Ar/C0_2$ (70 : 30) at a typical gain of 8×10^3. The background fluxes can reach up to 2.5 MHz/cm^2.

- TOTEM (CERN): twenty semi-circular shape detectors compose the $T2$ telescope [71]. The triple-GEM chambers, in the configuration 3/2/2/2, operate in $Ar/C0_2$ (70 : 30) at a gain of 8×10^3.

- LHCb (CERN): twenty four medium-size chambers are installed in the $M1$ muon station [72]. The LHCb configuration includes the gap configuration 3/1/2/1 and the gas mixture $Ar/CO_2/CF_4$ (45 : 15 : 40). The chambers operate at a gas gain of $4 - 6 \times 10^3$ in a radiations environment close to 500 kHz/cm^2.

- PHENIX (RHIC): twenty medium-size detectors form the Hadron Blind Detector [73]. The GEM foils are covered with a CsI coating to make the chambers sensitive to Cerenkov radiations from electrons. The gap configuration is 1.5/1.5/1.5/2 and the GEMs operate in pure CF_4 at a gas gain of few 10^3.

In this thesis, we will often refer to "GEM-based detector" with simply "GEM detector", even though it requires a drift plane and a readout electrode to be used as a particle detector.

4.4 Conclusions

The gaseous detector technology offer a high level flexibility in term of size, geometry, configuration, mode of operation and sensitivity to energetic particles. For these reasons they play a major role in many applications in high energy physics. The recent development of the MPGDs made possible the use of gaseous detectors with excellent detection performance in high rate environments.

One of the most interesting MPGDs is the GEM structure, which was deeply studied during the last decade and used in several major HEP experiments. Based on the past experience with the GEM technology, the CMS GEM Collaboration developed a specific version of large triple-GEM detectors for the upgrade of the forward CMS muon endcaps.

Chapter 5

The GE1/1 project for CMS

5.1 Introduction

In this chapter we will present the CMS GEM Collaboration and the GE1/1 project for the upgrade of the CMS muon end-caps. After a general discussion on the different phases of the project, we will describe the particularities of the large GEM-based detectors for CMS and the various prototypes that were produced since 2009. Finally, we will explain what needs to be done in order to validate this technology.

5.2 Overview of the CMS GEM project

5.2.1 The CMS GEM Collaboration

The CMS GEM collaboration is a wide international collaboration that started in 2009, with almost 192 scientists from 37 institutions in 18 countries. The central $R\&D$ laboratory and the production facility is based at CERN, near the GEM foil production workshop. Other main production sites are: Florida Institute of Technology (FIT) - USA; INFN Laboratori Nazionali di Frascati (INFN-LNF) - Italy; INFN Sezione di Bari - Italy; Ghent University (UGent) - Belgium; Bhabha Atomic Research Center (BARC) - India. Many other research institutes and countries are participating to the CMS GEM project, namely Belgium, Bulgaria, China, Colombia, Egypt, Finland, France, Germany, Hungary, India, Italy, Korea, Pakistan, Qatar and USA. The full list of institutions and the corresponding collaborators can be found at [10].

5.2.2 Description of the GE1/1 project

The aim of the CMS GEM Collaboration is the development and the installation of triple-GEM detectors in the forward region of the CMS muon end-caps during the LS2 upgrade foreseen in 2018. The project is named GE1/1, where "G" stands for GEM, "E" for End-cap, the first "1" corresponds to the first muon station and the second "1" the first ring of the station. 144 large trapezoidal chambers will be organized by pair to form super-chambers that will cover the full ϕ coordinate and the pseudo-rapidity region $1.55 < \eta < 2.18$. The detectors will be inserted in front of the ME1/1 station in the slots originally foreseen for RPC detectors (see Fig. 5.1).

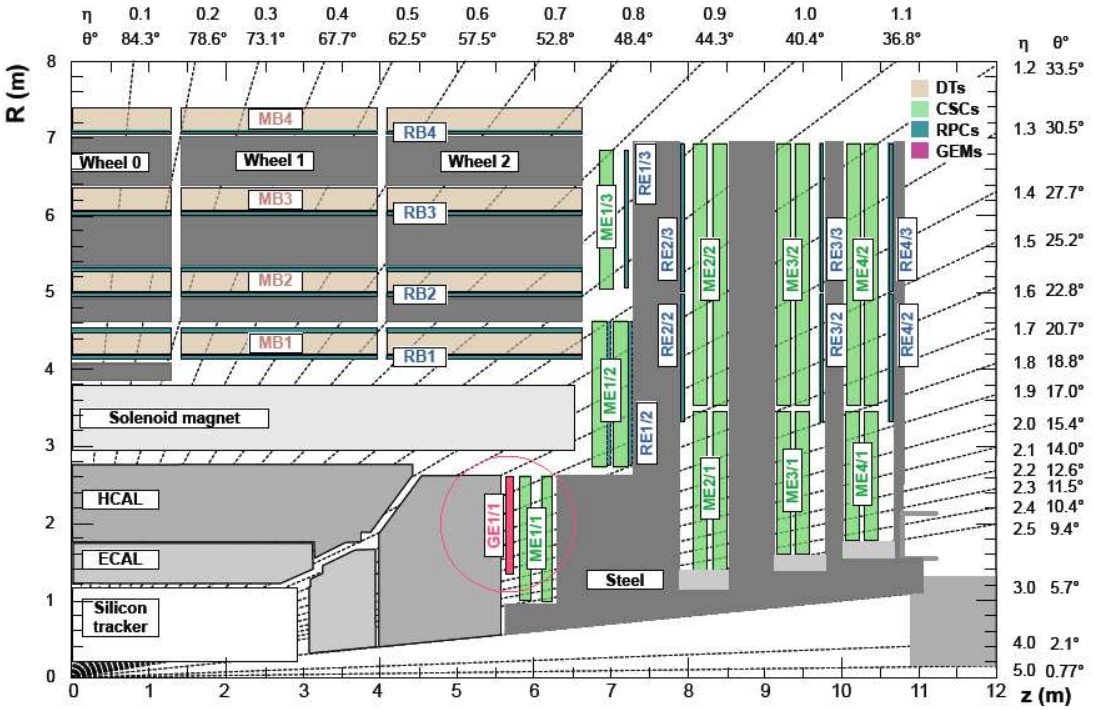

FIGURE 5.1: A quadrant of the CMS longitudinal cross-section showing the current muon spectrometer and the GE1/1 project.

The goal is to complement the CSC system to ensure the best reconstruction and selection efficiency after the high-luminosity upgrade of the LHC, while keeping the L1 trigger to an acceptable rate. The CMS minimum requirements, based on the desired trigger and physics performance [10], are shown on Tab. 5.1.

The CMS GEM project is organized in two steps: the *R&D* phase that consists of studying the fundamental characteristics of the triple-GEM technology and developing the GE1/1 detectors that fulfil the CMS requirements; the production of the 144 final detectors and their quality control before the CMS installation.

Properties	**CMS requirements**
Rate capability	$> 10\ kHz/cm^2$
Single chamber efficiency (MIP)	$> 97\ \%$
Angular resolution	$< 300\ \mu rad$
Single chamber time resolution	$< 10\ ns$
Gain uniformity	$< 15\ \%$
Longevity	$> 60\ mC/cm^2$

TABLE 5.1: The minimum requirements for the upgrade of the CMS muon endcaps.

5.2.2.1 R&D phase

After the GE1/1 concept was validated by simulation and the results from the past experiences, several GE1/1 prototypes of various sizes were tested in laboratory (characterization) and in irradiation facilities (performance test). The goals of the *R&D* phase is to ensure that the GEM technology in the GE1/1 configuration can operate in the harsh environment of the CMS end-caps. Moreover, the *R&D* phase is essential to define the set of working configurations that best suit the CMS requirements.

Three main parts of the GE1/1 *R&D* program were conducted in the framework of the Ph.D. thesis:

- The study of the fundamental characteristics of the triple-GEM technology, such as the stability and the uniformity of the effective gas gain, the rate capability and the discharge probability. All these elements were tested in laboratory with X-ray sources and small prototypes of triple-GEM detectors. It helped to establish the best configuration for large chambers with different options of gas mixture and internal geometry.

- The measurement of the performance of the large detectors with minimum ionizing particles, such as the detection efficiency, the spatial resolution and the time resolution. Most of these tests were performed in irradiation facilities with intense muon or hadron beams. In these conditions, it was possible to determine the typical response to MIPs in different configurations of high voltage, gas mixture and with different readout electronics.

- The study of the longevity of the detectors when operating continuously in an intense radiation environment. A set of aging tests was performed at the CERN Gamma Irradiation Facility (GIF) with several GE1/1 prototypes of different generations. Additionally, outgassing studies helped to define the best choice of materials and extend the lifetime of the detectors.

Moreover, simulations of the GE1/1 operation, studies of the CMS background and simulations of the impact of the GE1/1 station on the CMS trigger and muon reconstruction were performed in parallel to the detector development by dedicated institutes, with the aim of defining the minimum requirements on the chambers and to confirm the choice of the GEM-based technology for the upgrade of the muon end-cap.

5.2.2.2 Large scale production of the GE1/1 chambers

The results obtained during the *R&D* phase have demonstrated the excellent performance of the GE1/1 detectors. As a result, the CMS collaboration approved the GE1/1 project for the next upgrade during LS2. Additionally, a preliminary installation of 8 detectors, called the slice test, will be conducted at the end of 2016 during a technical stop of the accelerators.

The project enters now in a large-scale production phase, during which the 144 detector will be assembled and tested in the various production sites before being collected at CERN for the final verification. The quality control, based on the 6 years of experience with the GE1/1 technology, was first established at CERN and shared with other institutes. It consists of several crucial steps, detailed in the Chapter 8: the electrical test of the GEM foils; the gas leak test and the HV characterization; the gain uniformity test; the efficiency and resolution tests in cosmic stand.

In parallel to the production of the chamber, dedicated groups are investigating the optimum techniques and tools to facilitate the integration of the GE1/1 station to the current CMS end-cap, both from hardware and software point of view.

5.2.3 Schedule

The challenge of the CMS GEM Collaboration is to produce 144 large triple-GEM detectors and complete their quality control before the end of 2018.

After the validation of the final design in the beginning of 2016, the different parts of the detectors will be purchased and shipped to all the production sites. Then, the assembly and quality control will be conducted together until the end of 2017 before being sent to CERN for last verifications and controls. All the chambers are expected to be operational in the first quarter of 2018. The detailed schedule of the GE1/1 production can be found at [10].

In parallel to the LS2 installation, the CMS GEM Collaboration is going to install eight large detectors at the end of 2016 in order to demonstrate the capability of the GE1/1

detectors, to validate the production process and the quality control, and to anticipate the integration of the GE1/1 station to the current CMS end-caps. The production of these chambers will be completed in the first quarter of 2016.

5.3 GE1/1 chambers for the CMS GEM project

5.3.1 General description

144 large GE1/1 chambers will equip both positive and negative end-caps of the CMS muon system, covering the detection region $1.55 < \eta < 2.18$. Each GE1/1 chamber consists of a trapezoidal gas volume containing a large triple-GEM structure embedded between a drift electrode and a readout board. The gap configuration, shown on Tab. 5.2, was optimized for the CMS application to ensure the best time resolution. The first transfer gap was reduced to 1 mm in order to minimize the charge released after the first GEM and make sure it will not disturb the final signal. Similarly, the induction gap was set to 1 mm so that the induction field can reach 5 kV/cm without increase too much the potential on the entire structure.

Region	**Gap** $[mm]$	**Electric field** $[kV/cm]$
Drift	3	3
Transfer 1	1	3.5
Transfer 2	2	3.5
Induction	1	5
Region	**Voltage** $[V]$	**Average Electric field** $[kV/cm]$
Δ_{GEM1}	450	89
Δ_{GEM2}	440	88
Δ_{GEM3}	420	84

TABLE 5.2: Electric field configuration of the CMS GEM detector in the 3/1/2/1 gap configuration at the nominal voltage 4250 V. The parameters Δ_{GEM1}, Δ_{GEM2}, Δ_{GEM3} correspond to the difference of potential between the copper electrodes of GEM1, GEM2 and GEM3.

The layer structure is shown in Tab. 5.3.

By applying the appropriate voltages on the various elements of the chamber, we can establish the amplification fields and the transfer fields necessary to bring the primary electrons from the conversion gap to the readout board, passing by the amplification stages (see Fig. 5.3). The GEM foils are produced by "single-mask" photolithography that allows producing large surfaces with a good uniformity and the proper alignment of the top and bottom holes (see Sec. 5.3.2). The top electrode of each foil, oriented toward the drift, is segmented into 40 HV sectors in order to restrict the energy released

Layer	**Material**	**Thickness [mm]**
Protective cover	Al	1.0
Cooling pipe	Cu/H_2O	2.0/6.0
Cooling pads	Cu	1.0
GEB board	Cu/FR4	0.140/0.856
Readout board	Cu/FR4/Cu	0.035/3.2/0.035
Induction gap	$Ar/CO_2/CF_4$	1.0
GEM 3	Cu/polyimide/Cu	0.005/0.050/0.005
Transfer gap 2	$Ar/CO_2/CF_4$	2.0
GEM 2	Cu/polyimide/Cu	0.005/0.050/0.005
Transfer gap 1	$Ar/CO_2/CF_4$	1.0
GEM 1	Cu/polyimide/Cu	0.005/0.050/0.005
Drift gap	$Ar/CO_2/CF_4$	3.0
Drift board	Cu/FR4/Cu	0.035/3.2/0.035
	Total	20.585

TABLE 5.3: Layer structure and materials of a single GE1/1 detector.

during a discharge and thus protect the foils from irreversible damages. As shown in Fig. 5.2, the readout board is divided into 8 partitions, or η-sectors, consisting of 384 copper strips with a trapezoidal shape. Each sector has three 128 signal-pins connectors outside of the gas volume. The connection between the strips and the connectors is ensured by metallic vias running through the board.

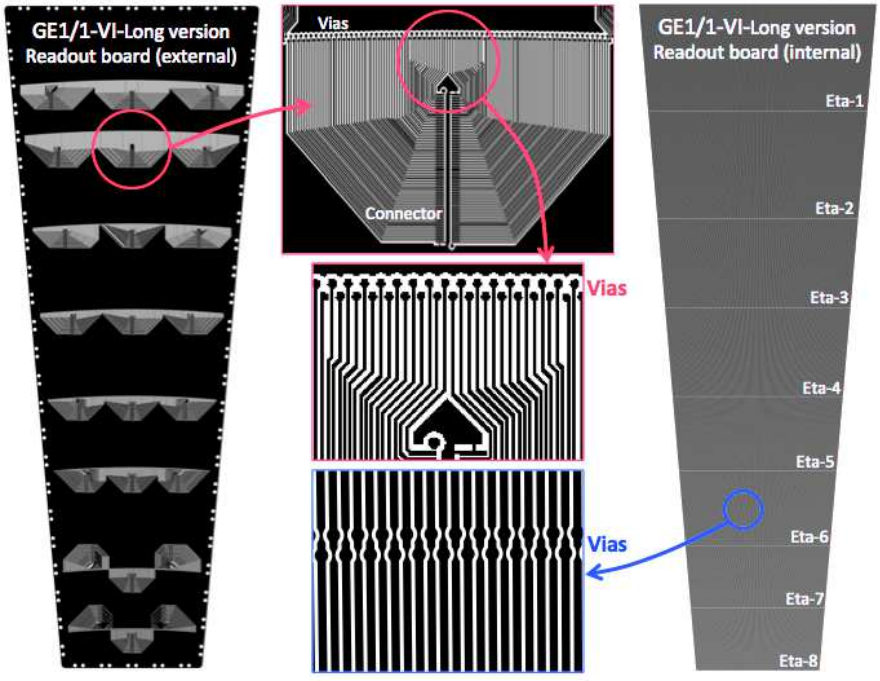

FIGURE 5.2: Left: External face of the readout board of the GE1/1 detectors. Right: Internal face of the readout board with the readout strips.

Because of mechanical constraints in the GE1/1 station, two versions of detectors are proposed in order to keep the maximum detection coverage: the long chambers with a

length of 120.9 *cm* and the short chambers with a length of 106.1 *cm*. Tab. 5.4 shows the technical specifications of the GE1/1 detectors for both short and long versions. Two identical GE1/1 detectors are combined to form a "super chamber" in order to obtain two detection planes and thus maximize the efficiency and the redundancy of the GE1/1 layer. In CMS, the super chambers alternate in the azimuthal direction between the long and the short versions to ensure the full coverage of the muon end-caps (see Fig. 5.3).

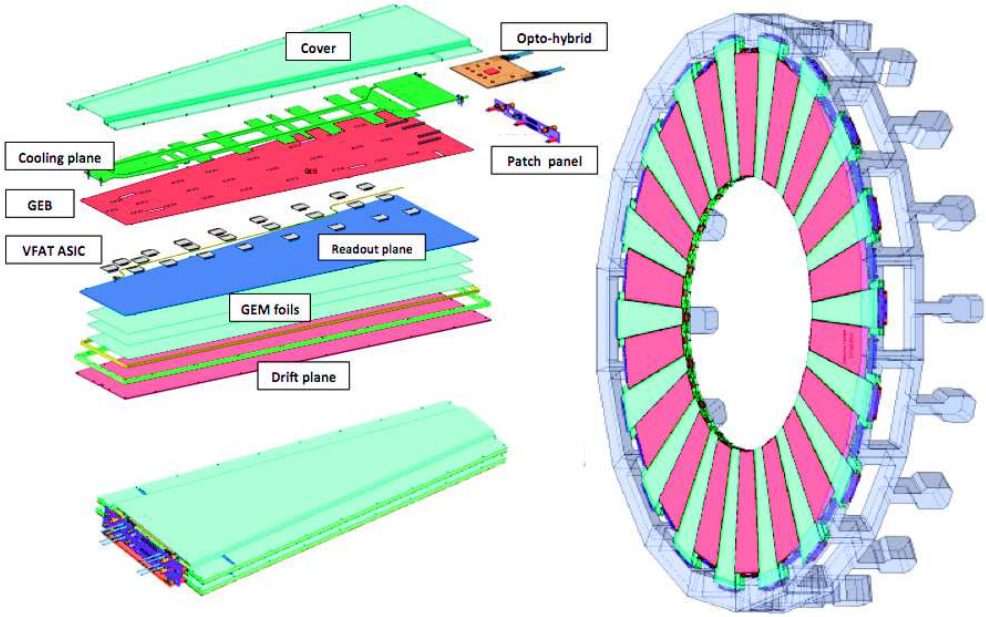

FIGURE 5.3: Top left: exploded view of a GE1/1 chamber showing the electrodes layout, the electronics and the cooling plane and the protection cover. Bottom left: Assembled super chamber. Right: Mechanical drawings of the GE1/1 station with both long and short chambers.

Specification/parameter	**GE1/1 detector**
Detector technology	Gaseous detector / MPGD
Charge Amplification element	triple-GEM structure (tensioned at $\backsim$ $5N/m$)
Number of chambers in overall system	144 (72 in each end-cap)
Chamber shape (active readout area)	Trapezoidal / opening angle 10.15°
Active area overlap between chambers	2.6 $mrad$
Short chamber dimensions	L: 106.1 cm, W: (23.1 – 42.0) cm, D: 0.7 cm
Long chamber dimensions	L: 120.9 cm, W: (23.1 – 44.6) cm, D: 0.7 cm
Total chamber thickness	D: 3.5 cm
Active readout area	0.345 m^2 (short ch.) / 0.409 m^2 (long ch.)
Active chamber volume	2.6 $liters$ (short ch.) / 3 $liters$ (long ch.)
Radial distance from beam line	130.2 cm (at inner edge of active area)
Geometric acceptance in η	1.61 – 2.18 (short ch.) / 1.55 – 2.18 (long ch.)
Signal readout structure	Truly radial copper strips
Readout strip angular dimensions	230 μrad width / 436 μrad pitch
Number of η-segments in readout	8
Number of readout strips per η-segment	384
Number of readout strips per chamber	3,072
Counting gas mixture	Ar/CO_2 70 : 30 or $Ar/CO_2/CF_4$ 45 : 15 : 40
Nominal operational gas flow	1 chamber volume per hour
Number of gas inlets / outlets	1 / 1
Nominal HV applied to drift electrode	3200 V (Ar/CO_2) / 4000 V $(Ar/CO_2/CF_4)$
Nominal operational gas gain	$1 - 2 \times 10^4$
Demonstrated rate capability	100 MHz/cm^2

TABLE 5.4: Main technical specifications and parameters of the GE1/1 detectors.

5.3.2 Overview of the GEM production techniques

The GEM foils are produced by photolithographic techniques very similar to the ones established for the production of printed circuit boards. The initial technique, called double-mask, consists of transferring the hole pattern to the copper-clad polyimide substrate thanks to microscopic masks placed on the top and on the bottom of the substrate. However, because the masks and the base material are flexible, the proper alignment of the two masks is impossible for foil dimensions exceeding 40 cm. The production of large size GEM foils for the GE1/1 detectors is achieved by using a single mask to transfer the hole pattern to only one side of the substrate and thus remove the alignment step.

The production steps of the double-mask and the single-mask techniques, both developed by the CERN PCB workshop [74], are shown in Fig. 5.4. The first step consists of applying a 15 μm-thick photo-resistive layer on both sides of the substrate. Then the mask is placed on top of the base material and engraved on the photo-resist by UV-light exposure. The copper layer is then etched with several solvent and acid baths to form the copper holes. Afterwards, the polyimide is dissolved by chemical etching using the

copper layer as a mask. The dissolvent is a complex mixture of anisotropic and isotropic etching solutions that allows to precisely define the speed, the direction of the etching and thus the shape of the holes. For the single-mask technique, the polyimide layer is used as a mask to etch the bottom copper layer, including an over-etching to adjust the diameter of the bottom holes. A second polyimide etching is performed from the bottom to transform the hole geometry and give the typical bi-conical shape. Finally, the full structure is masked to remove the unnecessary copper and to define the electrodes. After several cleaning and drying steps, the GEM foil is ready to be mounted on its frame and inserted into a detector.

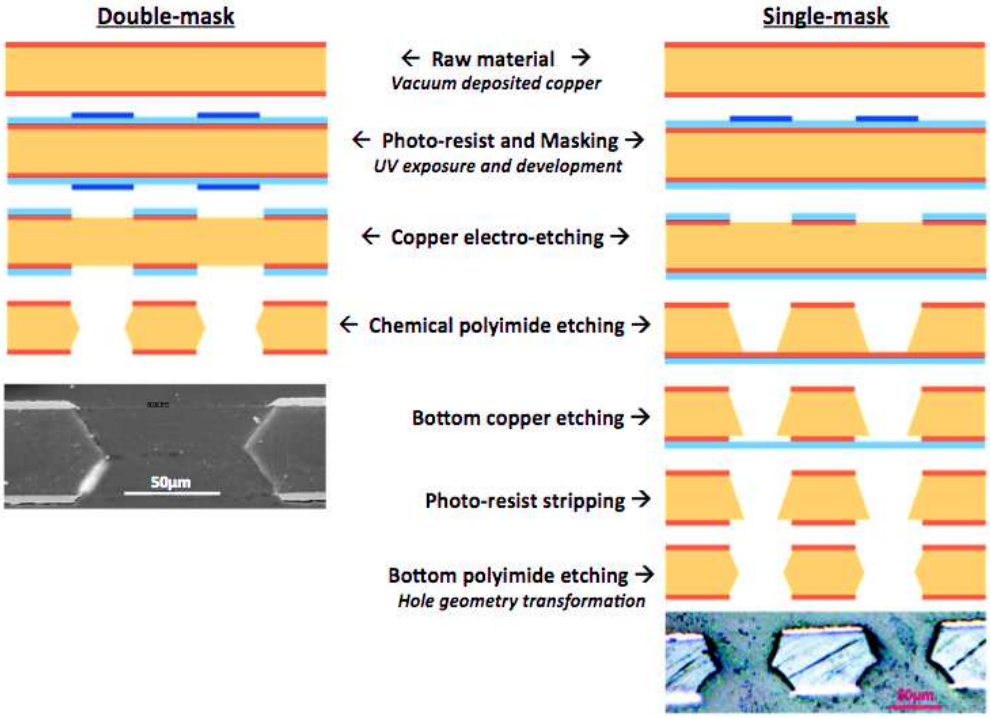

FIGURE 5.4: Overview of the double-mask (left) and the single-mask (right) production processes.

The single-mask photolithography has been optimized in order to approach the perfect bi-conical shape and obtain the same performance as the double-mask technology. However, the final result seen on Fig. 5.5 indicates that there is still a significant difference between the top and the bottom hole geometries. The average diameter of the bottom holes is 20 % larger than on the top layer. In addition, the bottom holes show an over-etch of the polyimide of several micrometers. These variations will affect the configuration of the electric field inside of the holes and induce different behaviors between the two production techniques. Moreover, the loss of the geometrical symmetry with respect to the middle of the foil may induce different amplification characteristics depending on the orientation of the foils in the detectors. These differences must be

measured and understood in order to validate the single-mask technology for the GE1/1 project.

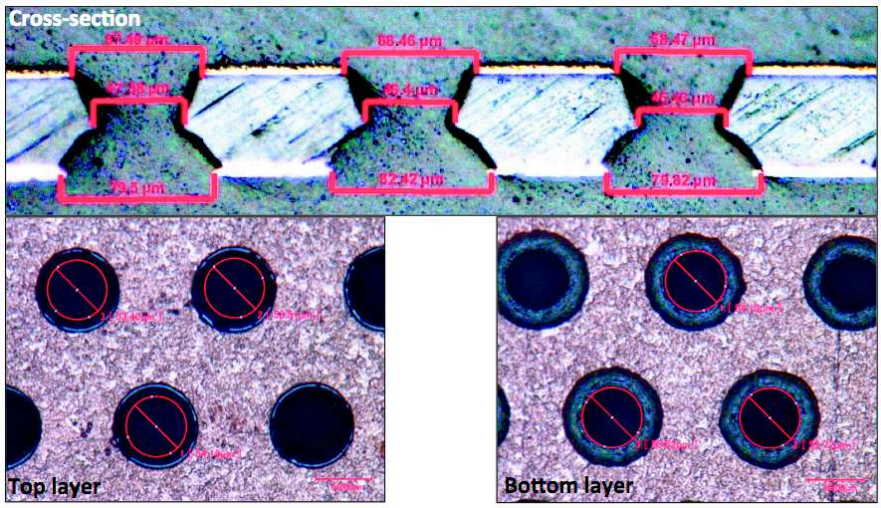

FIGURE 5.5: Microscopic view of a single-mask GEM cross-section (top), the top layer (left) and the bottom layer (right).

5.3.3 A new stretching technique

Initially, for all the large GEM-based detectors, the tension of the GEM foils was based on a thermo-stretching technique : the foils are attached to a Plexiglas frame which expands when heated to 39 $°C$. The foils are then glued to the detector frame with a spacer grid to ensure the uniformity of the various gaps in the chamber. The entire process take several days and requires a special equipment for a proper stretching and gluing of the foils. The thermo-stretching technique was validated with the successful operation of two large chambers, however, the various gluing steps increase the risk of contamination or damage of the foils during the assembly and prevent the re-opening of the chambers after drying. With this technique, the use of spacer grids between the GEMs is also necessary to maintain the uniformity of the detector performance but it also creates dead regions (several %) where the particles cannot be detected. Moreover, the glue in contact with the gas volume can possibly outgas contaminants and provokes premature aging (see Sec. 7.4).

For all these reasons, a new stretching technique was developed in 2013 by the CERN PCB workshop, in collaboration with the CMS GEM hardware group. The technique is based on a fully mechanical self-stretching : the GEM foils are attached with screws to an internal frame that can move inside of the chamber. This frame is then pulled outward thanks to lateral screws going through brass pull-outs, which are fixed to the drift and the readout boards (see Fig. 5.6 and Fig. 5.7). The lateral screws are tightened

to about 0.1 Nm to ensure the stable tensioning of the large foils and the uniformity of the gaps (without spacers). With this glue-free technique, it is therefore possible to open the chambers at anytime to replace internal parts or to extract the GEM foils for additional cleaning. This self-stretching technique was adopted after the second generation of GE1/1 prototypes and was fully validated with more than ten working detectors.

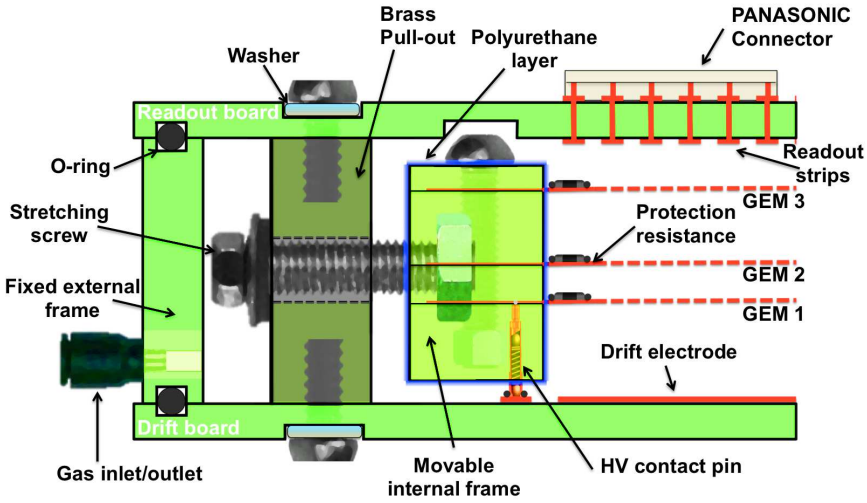

FIGURE 5.6: Cross-section of a single GE1/1 detector showing the main components and the self-stretching structure.

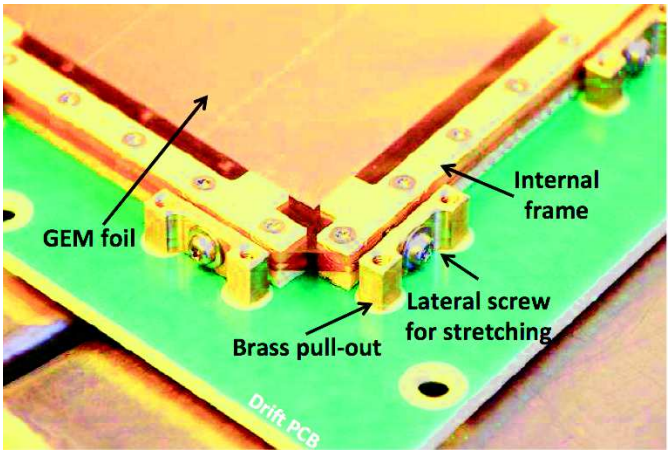

FIGURE 5.7: Bottom left corner of a GE1/1 detector during the assembly showing the self-stretching structure.

Six generations of GE1/1 prototypes were designed and produced by the CMS GEM collaboration between 2009 and 2015 (Fig. 5.8), each new generation being a significant improvement of the previous one. The final readout scheme with 24 readout sectors was introduced at the 2^{nd} generation and the mechanical stretching technique was implemented from the 3^{rd} generation. The next generations included the improvement of the stretching structure, mechanics and the final positioning of the readout connectors. A detailed description of the development of the GE1/1 prototypes can be found at [75].

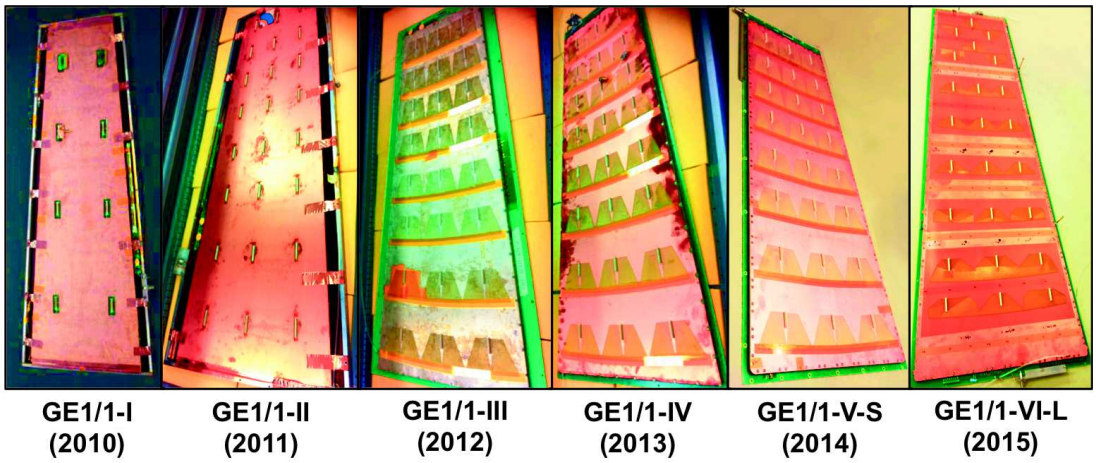

FIGURE 5.8: Six generations of GE1/1 prototypes assembled and tested by the CMS GEM collaboration.

5.3.4 The readout electronics

Each GE1/1 detector contains 3072 readout strips. The strips are organized in groups of 128 channels connected to 128-pins connectors distributed over the eight η-partitions.

In CMS, the readout strips will be connected to the VFAT3 front-end ASIC. The VFAT3 architecture is an upgrade of the VFAT2 already in use within the TOTEM experiment. It consists of 128 channels, each one being made of a charge sensitive pre-amplifier, a shaper and a constant fraction discriminator. The data, synchronized with the 40 MHz LHC clock, is then splits into a first path with a fixed latency for trigger signals and a second path, with a variable latency, for tracking data. The power, control and readout of the VFAT3 is made via E-links through a multi-layer PCB placed on the readout board and called GEM Electronic Board (GEB). All the links from the 24 readout sectors concentrate to an Opto-Hybrid board (OH) that ensures the interface between the front-end and the OFF-detector systems. The OH provides two optical paths, the first is unidirectional and transfers the fixed latency trigger from the VFAT3 to the CSC system. The second path, bidirectional, connects the OH and the back-end electronics and is responsible for carrying the tracking and triggering data from the ASIC as well as the configuration and the control commands (power supply, threshold and readout settings).

The back-end electronics is based on the μTCA standard, recently developed for the Telecom industry and adopted by CMS to replace the VME electronics. This technology is compact and combines very high data throughput (2 $Tbits/s$) and high availability. For the GEM application, the μTCA crate is equipped with eight Advanced Mezzanine Cards (AMC) based on the Virtex 7 FPGA (MP7). The first Carrier Hub (MCH) slot is occupied by a commercial MCH that provides a Gigabit Ethernet (GbE) communication

for the Slow controls and the configuration signals. The second slot is reserved for a CMS standard MCH module called AMC13 to interface the crate to the CMS DAQ system and take care of the Trigger, Timing and Control (TTC) signals. Fig. 5.9 gives an overview the GE1/1 electronics system and the main connections between the various DAQ elements.

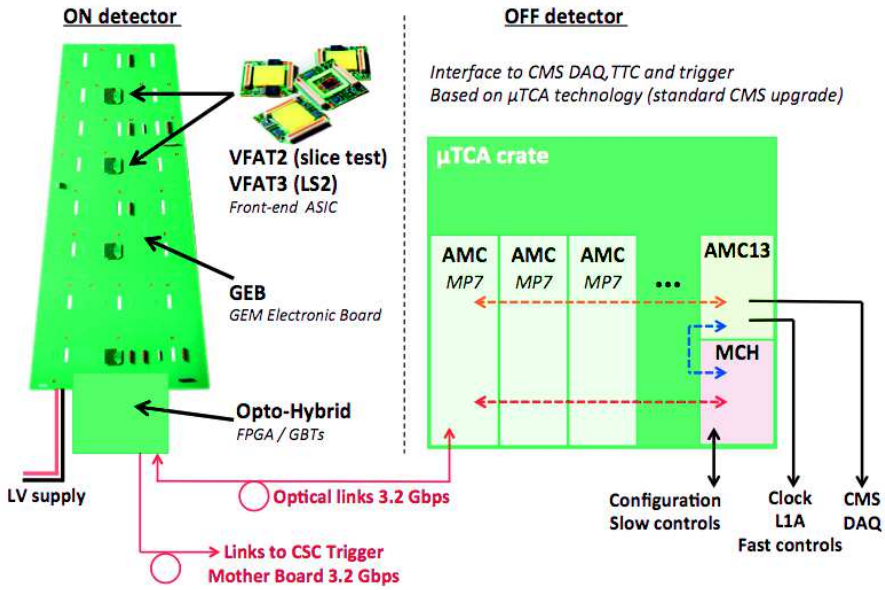

FIGURE 5.9: Overview of ths CMS GEM electronics system.

5.4 Conclusions

The CMS GEM Collaboration proposed a new design of triple-GEM detectors for the CMS application. The so-called GE1/1 chambers were the first large detectors assembled with single-mask GEM foils and a new stretching technique especially developed for this application. Despite of the past experience with GEM-based detectors, the new concepts introduced for the GE1/1 chambers must be fully validated and approved by the CMS collaboration.

The first step consists of measuring the fundamental characteristics of the single-mask GEM technology, evaluating the differences with the standard double-mask design and measuring the detection performance of the large detectors. These studies have to be performed for different configurations of gas mixture and electric fields in order to propose several suitable options for the CMS application.

The second step is the study of the longevity of the GE1/1 detectors when operating under high radiations. Aging tests have to be conducted in the CMS conditions and for the different options of configuration. Additionally, the materials forming the detectors

must be tested and validated to make sure they will not contaminate the gas mixture and trigger premature aging.

Finally, it is necessary to establish a complete quality control of all the GE1/1 chambers that will be installed in the CMS end-caps.

Chapter 6

Characterization of the GEM technology for the GE1/1 application

6.1 Overview of the R&D phase

Even though the GEM technology was extensively studied in the past decade, the base materials, the fabrication techniques and more generally the operating configuration have evolved in the past few years to fulfil the requirements of the new HEP experiments. One of the main goal of the Ph.D. work was to measure the fundamental characteristics of the recent GEM detectors to demonstrate that the GE1/1 chambers can operate in the CMS end-cap and offer the best performance.

The first part of the CMS GEM *R&D* program, presented in Sec. 6.2, shows the basic properties of the single-mask GEM technology compared to the standard double-mask foils. The second part of the *R&D* program , discussed in Sec. 6.4; aims to summarize the various irradiation campaigns where several large chambers were irradiated by narrow beams of high energy muons and mixed hadrons with the idea of extracting the detection efficiency, time and space resolutions with MIPs.

6.2 Comparison between the single-mask and the double-mask technologies

We discussed in Sec. 5.3.2 the standard double-mask production technique, its limitations and the recent development of the single-mask technique that is necessary to produce

large GEM foils. We've seen that the single-mask technique induces differences in the geometry of the holes. In particular, it creates an asymmetry in the diameter of the holes between the two GEM copper layers.

The goals of the characterization is to determine the differences between the two different production techniques and measure the absolute characteristics of the single-mask foils, which are used in the large GE1/1 detectors. We will discuss the study of the effective gas gain, the energy response to an X-ray source, the short-term stability and the typical behavior when irradiated by an intense flux of particles. Since most of these parameters are governed by local phenomena, the measurements were performed with small prototypes of triple-GEM detectors (10×10 cm^2) for a better convenience but without affecting the final results.

6.2.1 Description of the detectors under test

Two types of 10×10 cm^2 triple-GEM detectors were produced in order to compare the characteristics of the single-mask and the standard double-mask GEMs. The detectors were tested in the same conditions and following the same procedures.

6.2.1.1 Prototype with standard double-mask GEM foils

The chamber described in Fig. 6.1 contains three double-mask GEM foils with an active area of 100 cm^2. The gaps between the foils and the induction gap are 2 mm thick while the drift gap is larger by 1 mm in order to increase the conversion efficiency with X-ray photons. Even though this configuration slightly differs from the CMS configuration, it facilitates the measurements without affecting significantly the results of the comparative study. The drift electrode is a single piece of copper while the readout board consists of 256 copper strips with a pitch of 0.4 mm. However, for this application, all the strips are physically connected together and terminate as one single output for the whole detector. The drift and the three GEM foils are attached to the readout PCB with nylon screws. The gas volume is closed thanks to the lateral epoxy frame and the cap PCB. Two VITON O-rings are placed between the lateral frame and the PCBs to ensure the gas tightness. The cap PCB has a large opening window covered with a thin Kapton layer to make sure that the low energy photons can penetrate the drift volume.

The various electrodes of the detector are powered with a HV divider that provides the appropriate voltages for a safe operation. The electric field configuration, at the nominal voltage 4400 V applied on the divider, is shown in Tab. 4.2. A detailed study on the electric field configuration for general purpose detectors can be found at [76].

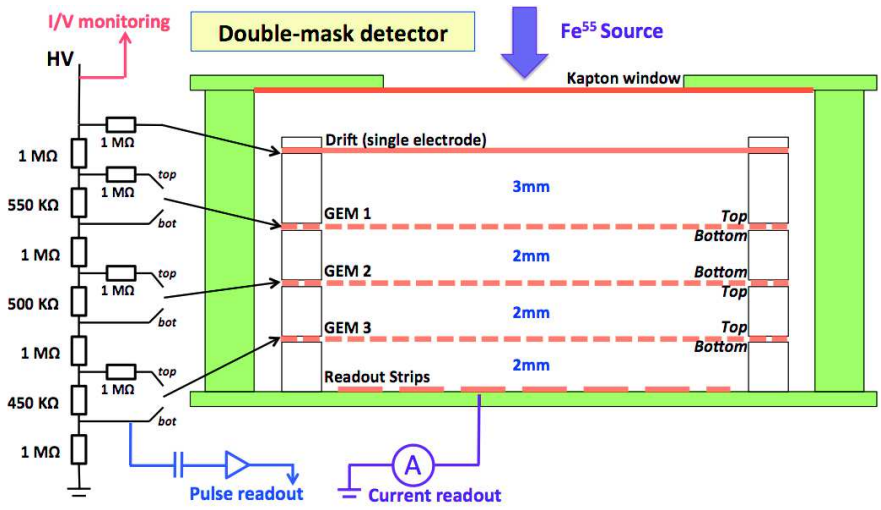

FIGURE 6.1: Schematic view of the double-mask chamber showing the GEM configuration and the HV divider.

Additionally, several 1 MΩ protection resistances are placed between the divider and the top of each GEM foil in order to restrict the current flowing through the foils in case of a discharge and to stop its propagation.

6.2.1.2 Prototype with single-mask GEM foils

Because of the asymmetry of the single-mask foils, it is necessary to test the characteristics of the triple-GEM detector for the two orientations of the foils.

A special detector with three single-mask GEM foils was designed with the idea of testing the two orientations without opening the chamber, the three foils being always oriented in the same way. In the orientation "A", the copper layer with the larger holes is facing the drift board (i.e. the radioactive source) while in orientation "B", the large holes are facing the readout board (Fig. 6.2).

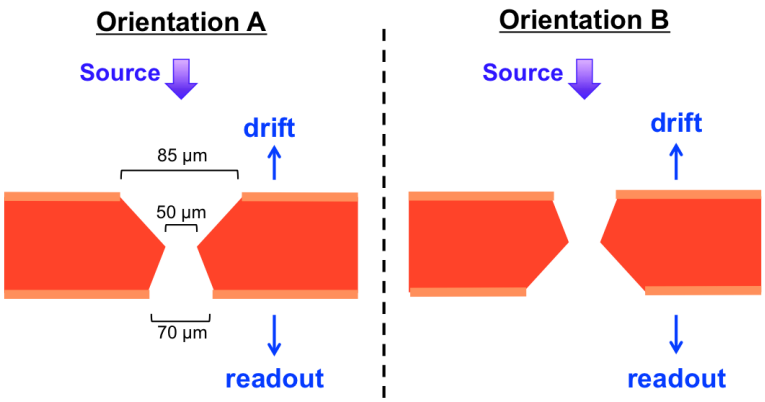

FIGURE 6.2: Schematic representation of the GEM foils orientation in the configuration A and B.

As shown in Fig. 6.3, for the orientation A, GEM 1 is facing the single drift electrode whereas GEM 3 is facing the readout electrode, which consists a single piece of copper. The drift gap was reduced to 2 mm to ensure the gap configuration remains the same when changing the orientation of the chamber. The divider was also modified so that the drift field in the 2 mm gap is identical to the standard field in a 3 mm gap.

In the orientation B, the HV circuit is simply inverted to power the previous readout electrode as the new drift. The voltages applied to the GEM stack are also inverted and the previous drift in orientation A is used as the readout electrode in B. The previous readout PCB was replaced by a cap PCB with a thin Kapton window to make possible the irradiation from the bottom.

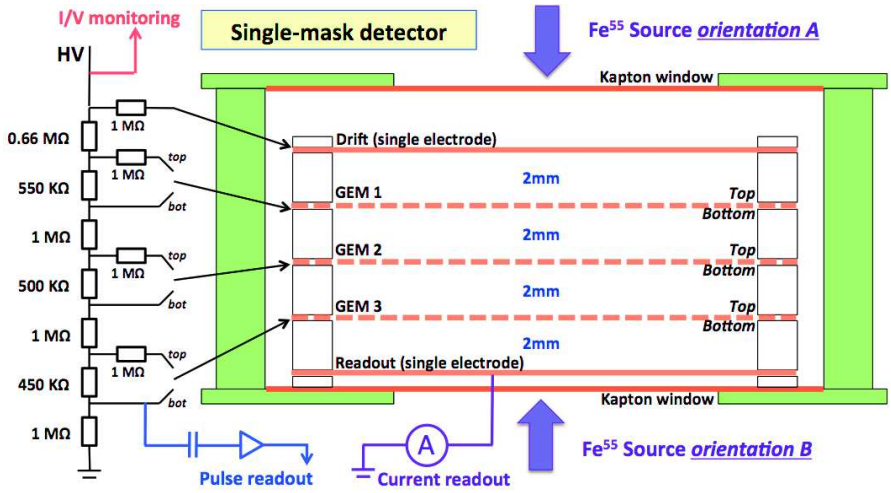

FIGURE 6.3: Schematic view of the symmetric prototype showing the GEM configuration and the HV divider.

6.2.2 Study of the effective gas gain

The effective gas gain is the central parameter of a triple-GEM detector. It describes the geometrical and the electrical characteristics together with the gas composition. It is driven by several parameters:

- The amplification factors of the three GEM layers, which depends on the geometry of the foils and the electric field inside of the holes. The combination of the three amplification factors defines the absolute gain of the detector.
- The fraction of electrons lost by recombination with ions or by attachment to neutral molecules, which depend on the gas composition and the electric fields between the GEMs.

- The loss of electrons on the GEM electrodes. This last item is the main reason why the effective gain is lower than the absolute gain. It strongly depends on the electric fields outside of the GEM holes. When the above electric field is greater that ~ 3 kV/cm, some of the electrons cannot reach the GEM holes and terminate on the top copper layer. This fraction increases when increasing the strength of the field. The ratio between the number of electrons that enter the holes and the number of electrons lost on the copper is known as the collection efficiency. Similarly, when the electric field below the GEM hole is low, some of the electrons cannot be extracted from the holes and are lost on the bottom copper layer. The ratio between the electrons exiting the holes and the ones lost on the copper is the extraction efficiency. The combination of the collection and the extraction efficiencies defines the electron transparency of the GEM foil. The transparency is a function of the electric fields above and below the GEM, but also depends on the internal electric field and the diameters of the holes. A detailed study of these effects can be found at [76].

Thereby, the effective gain is a unique parameter used to relate the general properties of a detector and to compare the operation of different chambers.

The effective gain was measured in Ar/CO_2 (70 : 30) by comparing the primary current, deposited in the drift region by a mono-energetic X-ray source, and the amplified current induced on the readout board. The detectors were irradiated by a ^{55}Fe isotope producing photons with an average energy of 5.9 keV that fully convert into the drift gap via photo-electric effect.

Even at interaction rates of the order of the kHz, the primary current doesn't exceed several tens of fA. It is therefore very challenging to measure it directly, especially since it should be collected from the drift plane or from the first GEM, which are set to HV and thus subject to noise. To overcome this issue, we measure the interaction rate R by counting the number of pulses induced by particles. To do so, the bottom of the last GEM foil is connected to an ORTEC pre-amplifier through a 500 pF capacitance in order to de-couple the line from the HV. The analog pulses are sent to a discriminator to generate digital signals that are counted by a scaler unit. Then, knowing the average ionization energy of the gaseous medium, we calculate the number of primary electrons n_T per incoming particles:

$$n_T = \Delta E \times \left[\frac{0.7}{W_i(Ar)} + \frac{0.3}{W_i(CO_2)} \right] = 5900 \times \left[\frac{0.7}{26} + \frac{0.3}{33} \right] \approx 212 \tag{6.1}$$

where $W_i(Ar)$ and $W_i(CO_2)$ are the effective average energies to produce one electron-ion pair in Ar and CO_2. Finally, we determine the primary current by multiplying the particle rate, the number of electrons per photon and the elementary charge.

The measurement of the amplified current is easier since it varies from 10^{-10} to 10^{-8} A depending on the voltage applied on the divider. In this condition, the amplified current I_a is simply readout with a KEITHLEY 6487 pico-ammeter connected to the anode.

Finally, the effective gain G is given by:

$$G = \frac{I_a}{R \times n_T \times e} \tag{6.2}$$

Fig. 6.4 shows a picture of the typical setup for gain measurement. The detector and the readout elements are shielded with copper plates to minimize the electronic noise and its contribution to the measurements.

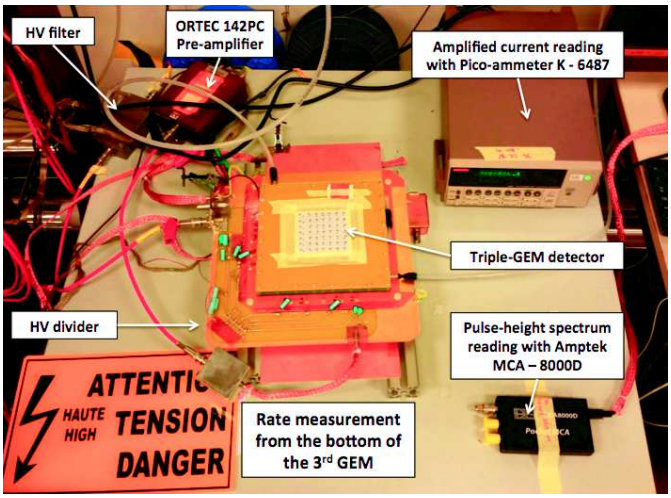

FIGURE 6.4: Picture of the gain calibration setup with the detector and the various readout elements.

The curves shown on Fig. 6.6 are obtained by measuring the effective gain at different operating points represented by the value of the current flowing through the HV divider. The plot shows the gain curves in Ar/CO_2 $(70:30)$ of the double-mask GEM detector and the single-mask prototype for both orientations. The right axis corresponds to the ratio between the gains of the two single-mask orientations. Additionally, the pulse height distribution was measured for every operating points in order to double check the gain variations and to confirm the good operation of the detector. Fig. 6.5 shows the typical distribution of ^{55}Fe in Ar/CO_2 $(70:30)$ and $Ar/CO_2/CF_4$ $(45:15:40)$, calibrated in energy.

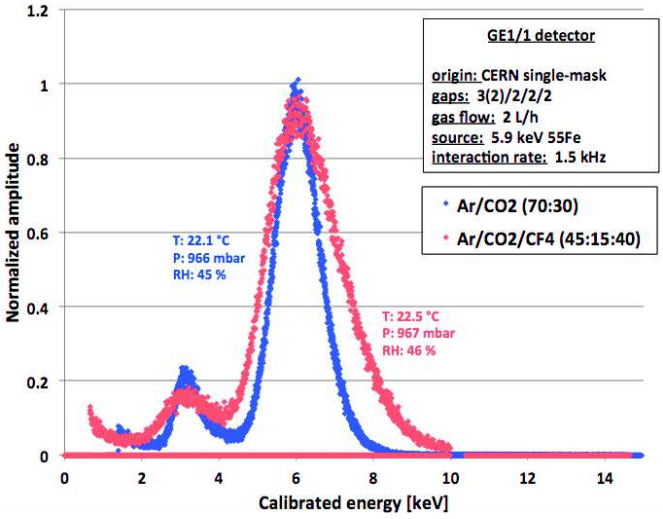

FIGURE 6.5: Energy distribution of the ^{55}Fe source in Ar/CO_2 (70 : 30) (blue) and $Ar/CO_2/CF_4$ (45 : 15 : 40) (red) showing the main photo-peak and the argon escape peak.

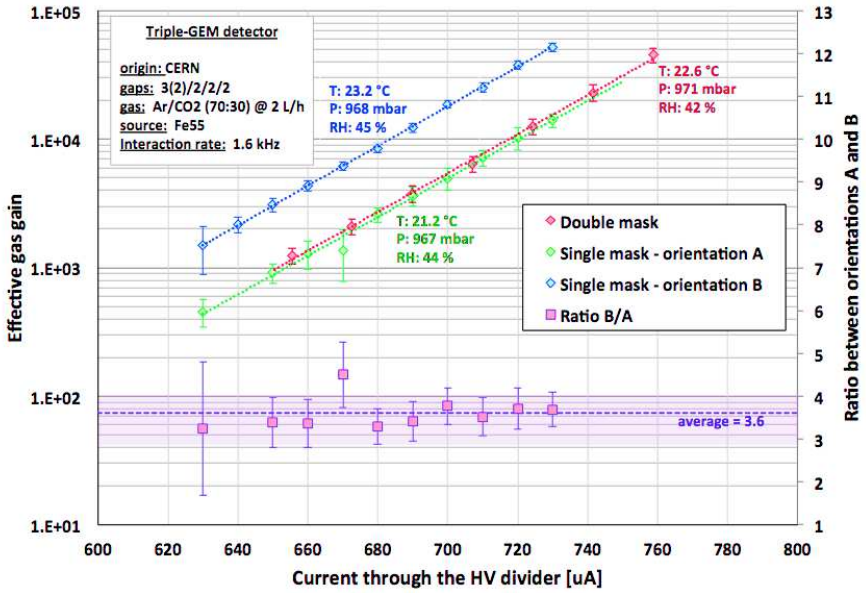

FIGURE 6.6: Gain calibration of the double-mask detector and the two orientations of the single-mask chamber in Ar/CO_2 (70 : 30). The detectors were irradiated by a ^{55}Fe source with an interaction rate of 1.6 kHz. The ratio between the gains of the two single-mask orientations is shown on the right axis.

The results clearly indicate that the effective gain of the double-mask GEM detector is identical to the single-mask orientation A while the single-mask configuration in the orientation B has an effective gain higher by a factor ~ 3.6. In the three cases, the potential applied on the electrodes of the detectors are identical, which means that the drift, the transfer and the induction fields are identical. However, the amplification and the transparency of the GEM foils can be different and thus induce the difference of effective gains. Two main hypothesis can be formulated:

- The absolute gain is lower in the single-mask configurations because of the larger holes on one side of the GEM foils. In this region, the electric field lines are defocused, resulting in a lower electric field and thus a lower amplification. However, in the orientation A, the loss of amplification is compensated by the increase of the collection efficiency due to the larger entrance holes. In this orientation, the extraction efficiency is identical to the double-mask detector since the exit holes are identical. As a result, the effective gain is similar to the double-mask configuration. In the orientation B, the collection efficiency is similar to the double-mask detector because the entrance holes are identical. But the extraction efficiency is higher because of the larger exit holes. Looking at the results, it seems that this effect not only compensates the loss of amplification, but dominates it, resulting in an increasing of the effective gain.

- Since the potentials applied on the GEMs are identical in all the configurations, the absolute gains are also identical. In the orientation A, the increase of the holes diameter on the entrance of the GEM does not affect the collection efficiency that is already close to the maximum value. The extraction efficiency is not affected either since the exit holes are identical to the double-mask detector. At the end, the effective gain is identical to the double-mask configuration. In the orientation B, the extraction efficiency if higher due to the larger exit holes. As a result, the effective gain is larger than with the double-mask configuration.

Other hypothesis could explain this behavior, including the variations of the electric field distribution inside of the single-mask holes and their effects on the amplification and the transparency of the foils. In any cases, the measurements show that the extraction efficiency plays a major role in the effective gain and dominates the other effects.

The difference of gain between the two single-mask orientations is particularly interesting for the GE1/1 application: for a given voltage applied to the chambers, the orientation B gives the highest gain, i.e. better detection performance. The orientation A would require higher voltage to reach the same performance, which means an operating point slightly closer to the electrical breakdown of the detector.

6.2.3 Short-term stability : charging up effect

The gain stability of a triple-GEM detector can be affected by two phenomena: the polarization and the radiation effects: the polarization, which describes the movement of the charges inside of the polyimide layer, is independent from the charge deposited by particles and becomes stable several hours after the detector was powered ON [77]. The

radiation effects occur during the amplification. They are mostly due to the attachment free charges to the surface of the polyimide in the holes. Because of the high resistivity of the polyimide, the charges accumulate on the walls until the equilibrium condition is reached. This effect strongly depends on the amount of charge crossing the holes per unit time and the geometry of the GEM. The amplitude and the stabilization time are thus related to the interaction rate, the primary charge and the gain of the detector [76]. Moreover, the time needed to evacuate the attached charges is directly driven by the surface conductivity of the polyimide that is affected by the relative humidity of the gas mixture.

Because of all these dependencies, the measurement of the charging-up effect requires a very well controlled environment and a clearly defined procedure. As seen on Fig. 6.7, the detectors are thermally insulated from the laboratory environment in order to reduce the temperature fluctuations that can affect the gas gain. The chambers are also covered with copper foils to reduce the electronic noise and minimize the water transfer through the Kapton windows. The entire gas system is made of stainless steel for the same reason. Ambient pressure, temperature and relative humidity are continuously monitored during the test thanks to a Meteo-station. The chambers are flushed with the standard gas mixture Ar/CO_2 (70 : 30) and irradiated by a constant source of ^{55}Fe with an interaction rate of 1.1 kHz.

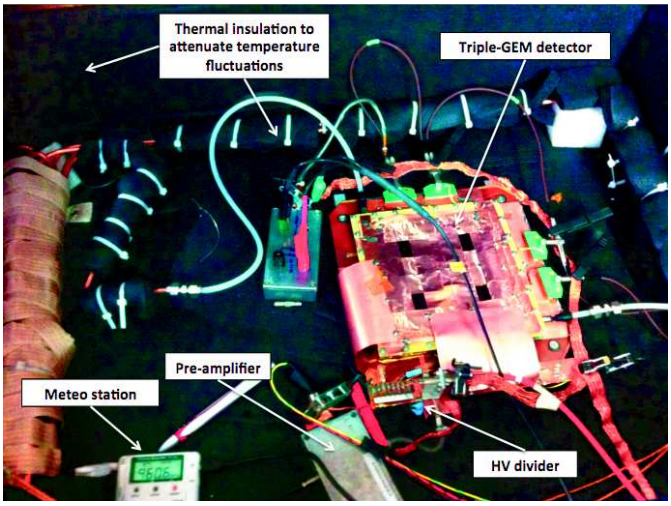

FIGURE 6.7: Picture of the charging-up setup showing the thermal insulation of the detector and the readout electronics.

The chambers, as well as the readout electronics, are switched ON several days before the beginning of the test to avoid polarization fluctuations and a possible instability of the electronics modules. The gas gain is initially set to 2×10^4, close to the CMS operating conditions. After placing the radioactive source on top the detector window, the readout current and the pulse-height distribution are recorded every minute for a

total testing duration of several hours until the detector is stable. Moreover, since the charging-up is a local phenomenon, a gain scan is performed before and after the test to disentangle the global and the local gain fluctuations. An example of the comparison between the initial and final gain scans on the double-mask detector is shown on Fig. 6.9. The source was placed in position 2 for 2.5 hours. After removing the environmental fluctuations, the gain in the positions that were not irradiated is identical to the initial value while the gain in the irradiated region has increase by several tens of percent.

Fig. 6.8 shows the results of the charging-up measurement for the double-mask technology and the two single-mask orientations.

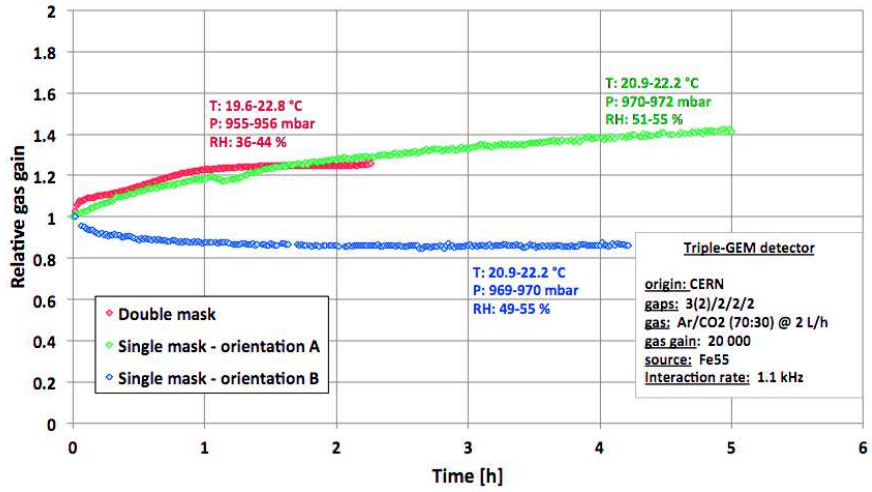

FIGURE 6.8: Charging-up curves of the double-mask triple-GEM detector and both orientations of the single-mask chamber. The detectors are irradiated by an ^{55}Fe source with an interaction rate of 1.1 kHz.

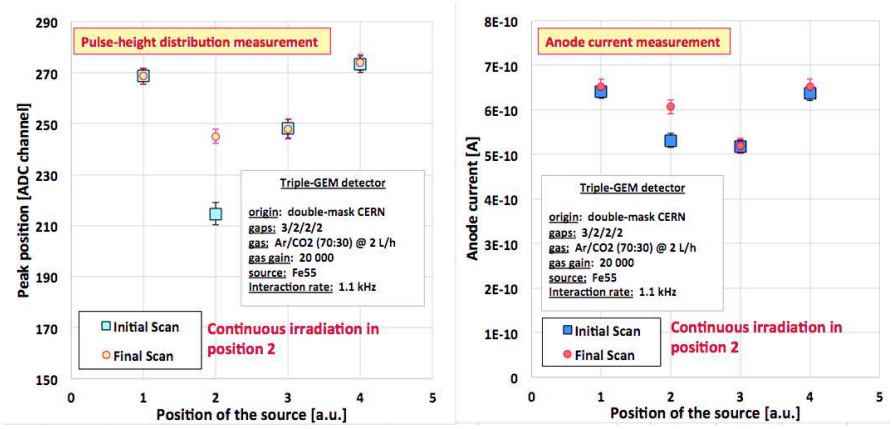

FIGURE 6.9: Comparison between the initial and final gain scans for the charging-up measurement of the double-mask foils. The detector was irradiated in position 2 by an ^{55}Fe source with an interaction rate of 1.1 kHz.

The single-mask orientation A and the double-mask geometries have again similar behaviors while the result obtained with the orientation B is highly different, with gain

variations of the opposite polarity and with a lower amplitude. This observation confirms that the charging up strongly depends on the geometry of the holes, as discussed in [76], in particular on the lower region near the exit holes.

In the same operating conditions, the single-mask orientation B seems to be more appropriate for the GE1/1 application since the amplitude of the charging and the stabilization time are significantly lower compared to the other configurations.

6.2.4 Rate capability

The MPGD technologies were mainly introduced and developed in response to the limited rate capability of the MWPC: at interaction fluxes higher than several kHz/mm^2, the space-charge density provokes a local perturbation of the electric field that lead to a drop of gain (see Fig. 4.21). By reducing the size of the amplifying structure to the microscopic scale, the time necessary to evacuate the avalanche ions is reduced to the sub-microsecond scale, reducing therefore the space-charge effects. In the particular case of the triple-GEM technology, we can distinguish three different regions depending on the incoming flux of particles [78]:

- At fluxes up to 10^4 Hz/mm^2, the space-charge does not affect the electric field in the holes or in the transfer regions and the effective gain remains constant.
- At particle fluxes between 10^4 and 10^5 Hz/mm^2, the ion space-charge in the transfer regions tends to decrease the electric field near the top of the GEM foils and increase it near the bottom holes. As a result, the electron collection and extraction efficiencies increase, as well as the effective gain.
- At even higher fluxes ($10^5 - 10^6$ Hz/mm^2), the ion extraction decreases, inducing the accumulation of ions in front of the holes. Therefore, the amplification field decreases while the probability of electron-ion recombination increases, resulting in a drop of the effective gain.

These phenomena are mostly driven by the transparency of the GEM foils. Therefore, the rate capability may be affected by the variations of hole geometry induced by the single-mask production technique.

In order to measure the rate capability of both double-mask and single-mask GEMs, the detectors were irradiated with a very intense X-ray source, providing 23 keV photons with adjustable fluxes up to 10^6 Hz/mm^2 (Fig. 6.10). In order to measure the effective gain as a function of the particle flux, the amplified current was measured at different

operating point of the X-ray source thanks to a pico-ammeter connected to the anode of the detector. However, it was impossible to measure the interaction rate and the primary current since the signal pulses passing through the pre-amplification stage overlap in time at rates higher than 30 kHz. A solution consisted of measuring the interaction rate with copper attenuators. Then, knowing the attenuation factor, we can extrapolate the real interaction rate without attenuation. Fig. 6.11 shows the extrapolated and the measured interaction rates for different configurations of the X-ray source. Finally, the interaction rate is divided by the irradiated surface to obtain the interaction flux.

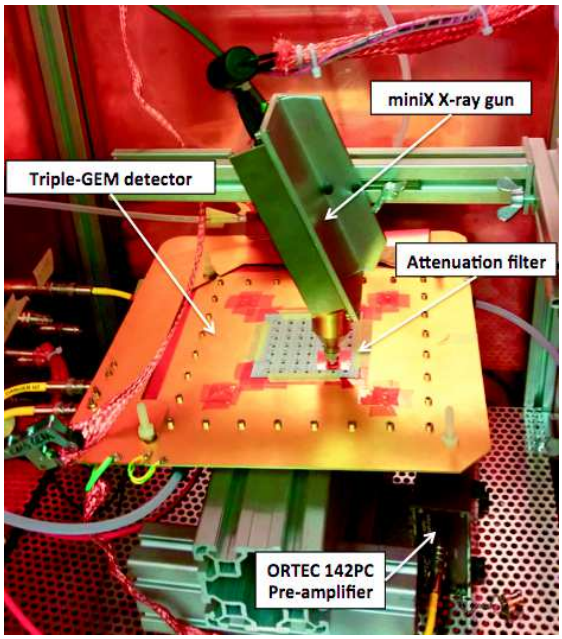

FIGURE 6.10: Picture of the rate capability setup showing the X-ray source and the readout electronics.

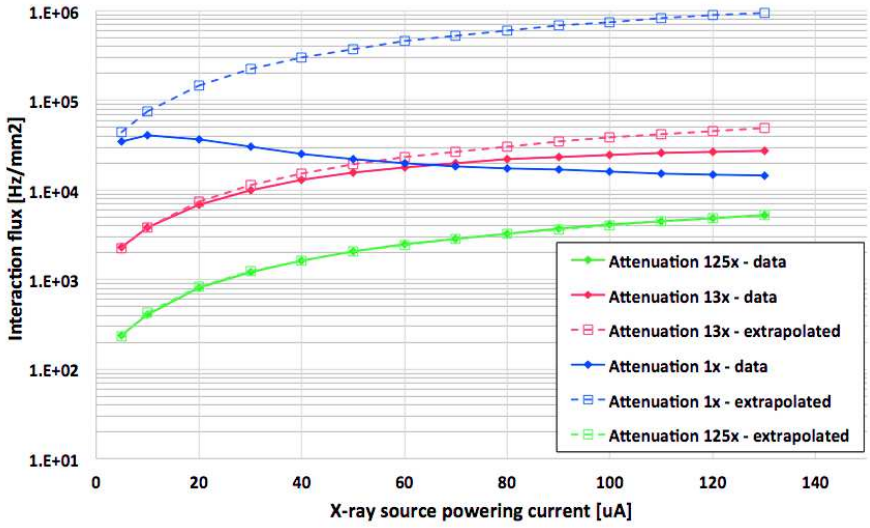

FIGURE 6.11: Interaction rate as a function of the X-ray source supply current. While the measured data show the pile-up effect from 30 kHz, the extrapolated rate, based on the highest attenuation configuration, gives the real interaction rate in the detector.

The rate capability with X-ray photons was measured with the double-mask and single-mask detectors in Ar/CO_2 $(70:30)$ with an initial gain of 2.2×10^4. The data points, normalized with the initial gain, are presented in Fig. 6.12.

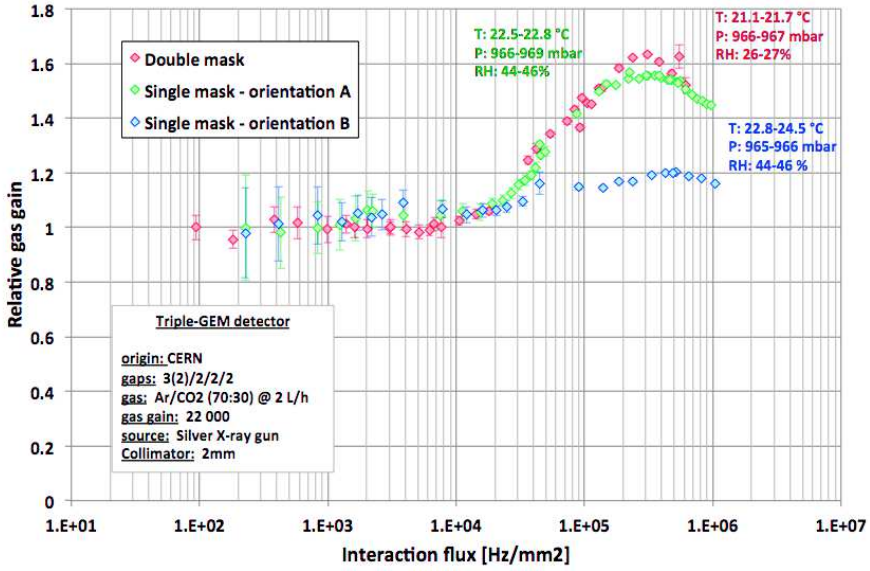

FIGURE 6.12: Rate capability of a triple-GEM detector in the double-mask and the two single-mask configurations. For each point, the gain is normalized with the absolute value 2.2×10^4.

The results indicate that even with larger entrance holes, the rise of the gain in the orientation A is identical to the double-mask configuration. This means that the increase of the collection efficiency caused by the ion space-charge is negligible and the rising of the gain is dominated by the increase of the extraction efficiency. It is confirmed in the orientation B, where the extraction efficiency is already closer to the maximum value because of larger exit holes. The increase of the effective gain due to the space-charge is thus reduced compared to the other configurations. Then, the drop of the effective gain, which mostly relates on the amplification field and the electron-ion recombination, occurs at fluxes around $3 - 5 \times 10^5$ Hz/mm^2 for the three configurations.

This last comparison test highlighted the role of the extraction efficiency for the rate capability. It confirmed once again the similitude between the single-mask orientation A and the double-mask configuration and the different characteristics of the single-mask orientation B.

However, the maximum flux expected in the CMS end-caps will not exceed 10 kHz/cm^2, far below the region where the effective gain starts rising. Therefore, the effective gain is expected to be constant and the differences between the two single-mask and the double-mask configurations should not be relevant. In order to confirm this statement, the rate capability was measured with a full-size GE1/1 detector in the CMS GEM configuration (given in Tab. 5.2) with the GEM foils in the orientation B. The test was

restricted to the low fluxes region in order to match the real CMS conditions. Fig. 6.13 shows that the effective gain remains stable up to 500 kHz/cm^2. Since the space-charge effect also depends on the primary charge, a dashed line is added to indicate the photon flux equivalent to the MIP flux of 10 kHz/cm^2 expected in CMS after the LS3 upgrade.

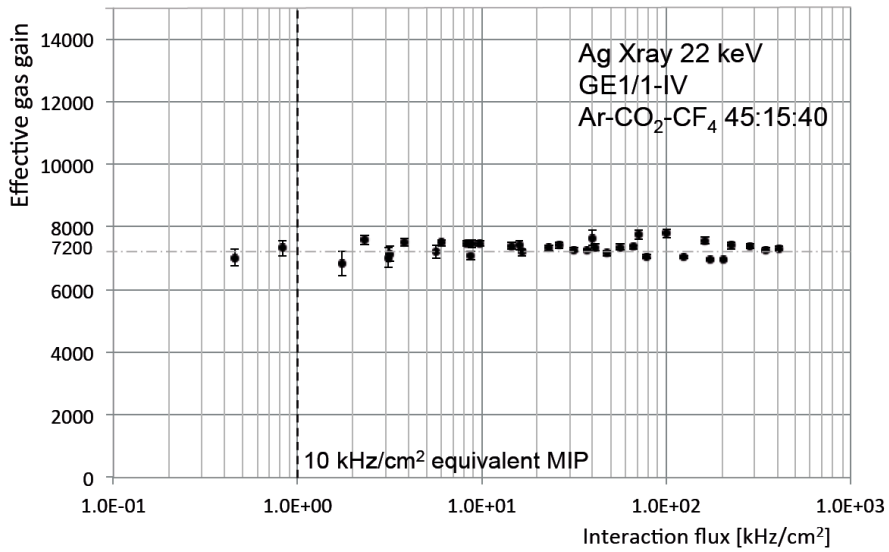

FIGURE 6.13: Rate capability of a GE1/1 detector in $Ar/CO_2/CF_4$ (45 : 15 : 40) irradiated with 23 keV photons. The dashed line indicates the MIP equivalent flux expected in the CMS end-caps during phase 2.

6.2.5 Conclusions

The geometrical differences induced by the single-mask production technique affect the operation of the triple-GEM detector. However, in the orientation A, the increase of the collection efficiency seems to have a negligible impact on the characteristics of the detectors, either because it is already close to the maximum with the standard hole diameter, or because the differences are compensated by other effects like the reduction of the amplification in the holes. On the contrary, in the orientation B, the increase of the extraction efficiency clearly improves the operation of the chamber. Generally speaking, for the same operating conditions, the orientation B has a higher effective gain that is more stable in time and less affected by high fluxes of particles.

Several hypothesis were formulated to explain the results of this study but the full understanding of the situation would require additional measurements supported by the simulation. One interesting option would consist of measuring the characteristics of the two single-mask orientations while changing the various transfer and amplification fields independently and measuring simultaneously the charge collected on all the electrodes of the detectors. In this way it would be possible to better define the transparency of the foils and how it is affected by the variations of the electric fields.

Nevertheless, this study demonstrated the capability of the single-mask triple-GEM detectors to operate in the CMS environment. It also demonstrated that the orientation B offers a higher gain, a better stability and is therefore the most appropriate configuration for the GE1/1 application.

6.3 Evaluation of the discharge probability at high flux

As for all the MPGD technologies, the triple-GEM detectors have to operate at a sufficiently high gain to ensure the maximum detection efficiency and, for the CMS application, good time performance. However, in the case of very intense particle fluxes or heavily ionizing trails, operating at high gain increases the probability of producing discharges that can seriously damage the detectors. Discharges initiate when the amplification factor exceed the Raether limit (Sec. 4.3.1). The resulting local perturbation of the electric field can transform the avalanche into a streamer (Sec. 4.17) that can propagate in both directions toward the GEM electrodes and provokes the electrical breakdown of the gas.

Triple-GEM detectors have two main benefits compared to other MPGDs. First, the discharge probability is significantly reduced because of the sharing the gain on several amplification layers. The overall gain can reach values up to 10^5 while each single layer is kept far from the electrical breakdown. Secondly, since the various amplification structures are independent from the readout plane, it is possible to stop the propagation of a streamer before further amplification and before it reaches the readout electronics. Therefore, a discharge may induce a large signal on the readout board but it won't damage the detector.

The CMS GEM detectors follow the recommendations given from the past studies [69] to prevent the production of discharges and their propagation. The three amplification layers are set to a different gain by offsetting the voltage across the GEM foils. Therefore, the voltage across GEM 1 is 3 % higher than on GEM 2, itself 5 % higher than GEM 3. This configuration ensures the lowest discharge probability even for a total gain of several 10^5. Moreover, the GEM electrodes facing the drift plane are divided in several sectors, each sector being restricted to 100 cm^2 in order to limit the available electrostatic charge and thus the maximum energy of the discharges. The sectors are connected to the HV divider via 10 MΩ protection resistances. In the case of a discharge, the current flowing through the resistance will induce a voltage drop on the top electrode and prevent the propagation of the discharge.

6.3.1 Description of the setup

In order to validate CMS GEM configuration, the discharge probability was tested with a small triple-GEM detector in the CMS operating conditions. The gap configuration and the corresponding electric fields at the nominal voltage 4250 V are described in Tab. 5.2. Since the discharge probability of a triple-GEM detector is very low at the normal CMS operation ($< 10^{-10}$), the gain was set to the extreme values $3 - 6 \times 10^5$ and the detector was irradiated by heavily ionizing α-particles. These extreme operating conditions are not realistic but help to measure the discharge probability in a reasonable time. Then, the real probability in normal conditions is extrapolated by following its exponential behavior with the effective gain. The detector under test, shown on Fig. 6.14, has a special 3.14 mm^2 opening in the Kapton window and the drift plane to make sure the 5.6 MeV α from an ^{241}Am source can penetrate the drift volume. The gas volume is closed thanks to a 2 μm-thick Mylar window.

The signals induced by discharges were identified through three different readout systems: over-current from the HV power supply; fast fluctuations of the anode current; large signals induced on the last GEM foil. However, the integration time of the I/V monitoring unit and the pico-ammeter did not allow identifying some of the fast and low-energetic discharges. The most reliable method consisted of counting the number of events inducing pulses simultaneously on the bottom of the last GEM and on the readout. Normal events induce pulses with opposite polarities while discharge pulses temporarily affect the stability of the electrodes and induce large signals with the same polarity.

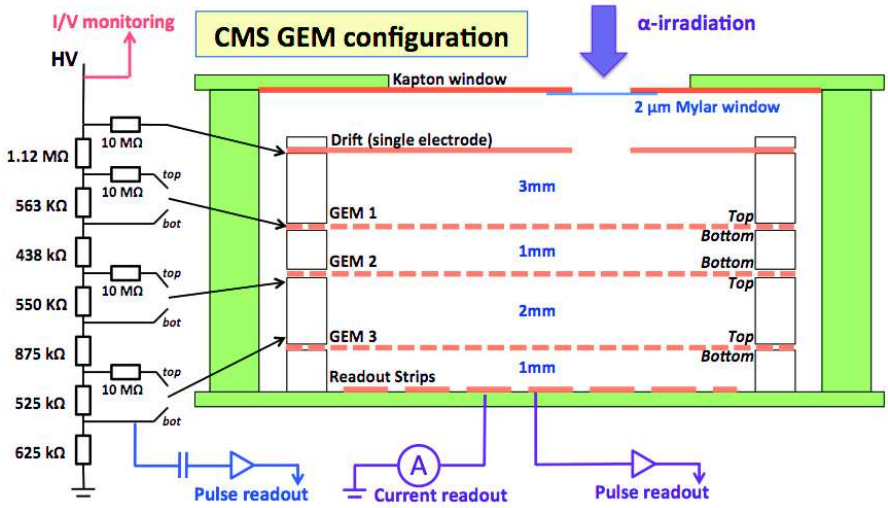

FIGURE 6.14: Schematic view of the triple-GEM prototype for the discharge probability test. The gap configuration and the electric fields are set to the CMS configuration. The 3.14 mm^2 opening in the drift board and the Kapton window allows the α-particles to penetrate the drift volume with a direction perpendicular to the GEM foils.

6.3.2 Results and conclusions

The results of the discharge probability test in Ar/CO_2 (70 : 30) are shown on Fig. 6.15 for different values of effective gain. The exponential fit is extended to the lower gain values to estimate the probability in realistic conditions. At a gas gain of 4×10^5, one discharge occurs every 10^5 heavily ionizing events. The probability increases exponentially to 10^{-3} at a gain of 6×10^5. By extrapolating this trend to an effective gain of $1-2\times10^4$, the discharge probability is estimated to 10^{-10}. However, one should consider that with 5.6 MeV alphas arriving perpendicular to the detector, a very large primary charge is deposited in the chamber and drift toward few holes. In the case of a MIP, since the primary charge is almost two orders of magnitude lower than for an α-particle, the probability of triggering a streamer is expected to be lower than 10^{-12}.

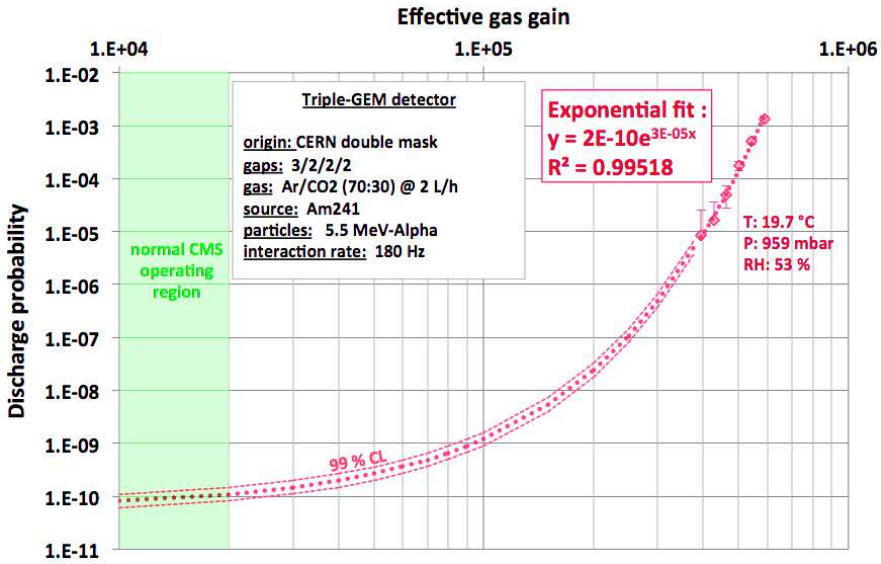

FIGURE 6.15: Discharge probability of a triple-GEM detector in the CMS configuration. The realistic operating conditions for the CMS application are indicated by the green region.

Despite of the very low discharge probability, the detector accumulated a total of 450 discharges over 1 cm^2 during the entire study. Gain calibrations were performed before and after the test in order to identify a possible degradation of the GEM foils in the irradiated areas. As seen in Fig. 6.16, the effective gain was not affected by the discharges, nor the energy response of the detector. Nevertheless, the detector was opened so that the GEM foils could be observed with a microscope (Fig. 6.17). In the region irradiated by the α-particle, the bottom electrode of each GEM is covered with a thin layer of copper oxide, except near the edge of the holes where we see shiny copper rims. The effect seems to be due to superficial copper etching in the region where the streamers are terminated and where most of the charges are collected. Similar effects were observed with the large GE1/1 chamber that experienced accidental discharges after an aging test

(see Sec. 7.3.3.2). However, in both cases the experiment shows that this phenomenon doesn't affect the general operation and the performance of the triple-GEM detectors.

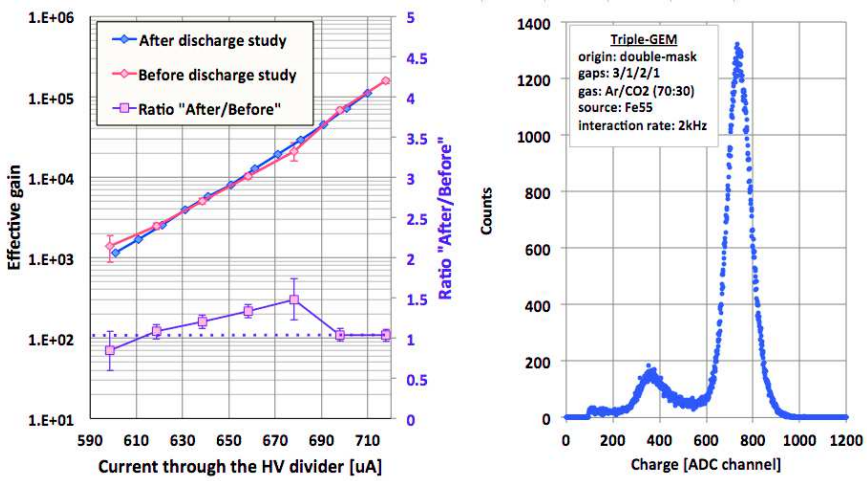

FIGURE 6.16: Comparison of the effective gain before and after the discharge probability study, in the position where the GEMs were irradiated by the ^{241}Am source (left) and the typical ^{55}Fe energy spectrum collected after the 450 discharges at a gas gain of 10^4.

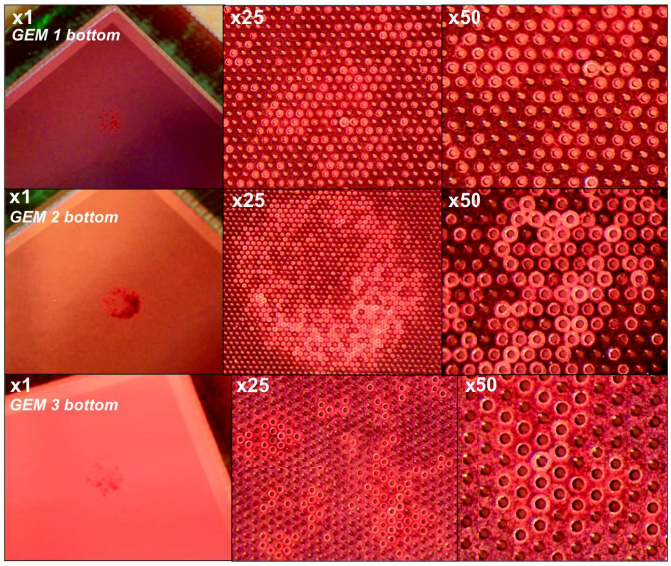

FIGURE 6.17: Microscopic views of the bottom layers of the three GEM foils after a total of 450 discharges accumulated.

At CMS, the GE1/1 detectors will be operating during 10 years with a maximum particle flux of the order of 1 kHz/cm^2, which means a total rate of 4.1×10^6 Hz over the entire surface of the detectors. Considering that the LHC will operate continuously during 6×10^7 s (10 years), the total number of particles seen by one detector during its entire lifetime will approach 2.5×10^{14}. Therefore, the total number of discharges expected after 10 years of operation is expected to be of the order of 250 over the entire surface of the detector. As discussed in this section, the discharges will not damage the detector

but simply induce a dead time of several milliseconds before the detector resumes the normal operation.

6.4 Detection performance of the GE1/1 detectors

The second phase of the CMS GEM *R&D* program consists of measuring the typical response of the GE1/1 chambers with MIPs in different configurations of gas mixture, power supply and with different electronics systems. The measurements were conducted during several irradiation campaigns at CERN or at Fermilab, often called "test beam". The goal was to demonstrate that the GE1/1 detectors fulfill the CMS requirements, especially in term of efficiency, spatial and time resolutions. It was also the opportunity to test the first prototypes of the final readout electronics foreseen for CMS.

Six generations of GE1/1 prototypes were produced, calibrated in laboratory and tested in test beam. After the generation II, the modifications between the generations didn't aim to improve the performance of the detector but to optimize the scheme of the readout board, the stretching technique and more generally to adapt the GE1/1 structure to the CMS environment. Therefore, the irradiation campaigns were also necessary to confirm that the modifications between the generations didn't affect the detection performance.

The study of the GE1/1 operation in magnetic fields was conducted during the early stages of the project. The experimental setup and the results were published in [79] and discussed in details in [75].

6.4.1 Gain calibration with different gas mixtures

The first step consists of calibrating the effective gain of the detectors before any irradiation test with the two CMS gas mixtures Ar/CO_2 (70 : 30) and $Ar/CO_2/CF_4$ (45 : 15 : 40). Because of the possible non-uniformity of the gain, all the sectors that are going to be tested are calibrated. This operation is crucial to understand the general behavior of the chambers and to determine the appropriate operating points for the test beam period. The testing procedure is identical to the gain measurement discussed in Sec. 6.2.2. Since the GE1/1 detectors are closed with a thick layer of PCB, the low energy photons cannot penetrate the gas volume so the ^{55}Fe source was replaced by an X-ray tube with a silver target emitting 23 keV photons. Most of these photons converts in the drift electrode, which de-excites by fluorescence, emitting the characteristic 8.9 keV copper X-rays. Then the photons fully convert in the gas volume via photoelectric effect. Additional background is also observed, decreasing from lowest energies to the

energy corresponding to the voltage applied on the X-ray tube, as shown on Fig. 6.18 . This effect is mainly due the Bremsstrahlung of electrons penetrating the silver target, resulting in the emission of radiations with a large energy distribution.

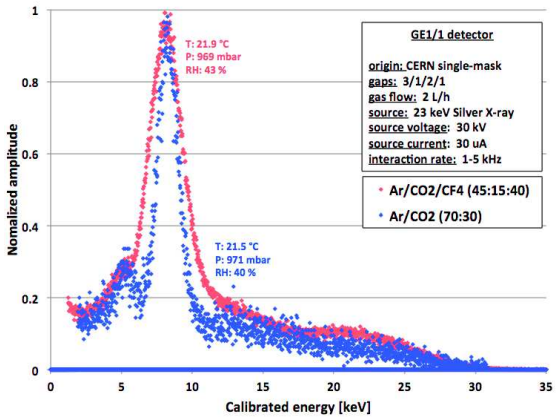

FIGURE 6.18: Typical energy distribution of the silver X-ray source in Ar/CO_2 (70 : 30) (blue) and $Ar/CO_2/CF_4$ (45 : 15 : 40) (red).

Fig. 6.19 shows the gain curves of all the GE1/1 generations for both CMS gas mixtures. The HV configuration, given in Tab. 5.2, was implemented after the second generation in order to optimize the electric fields distribution and to ensure the best time resolution. As a result, the gain of the two first generations differs from the other chambers. The effective gains of the generations III, V and VI are identical while the gain of the generation IV, represented by the blue curves, is lower by a factor $3-4$. Because of technical constraints, the GEM foils in the generation IV are inverted. Since the foils are produced by single-mask technique, the gain difference can therefore be explained by the geometrical asymmetry of the GEM holes. Using the definition discussed in Sec. 6.2.2, the detectors of the generation "IV" are in the single-mask configuration A while the other generations are in the configuration B.

6.4.2 Description of the irradiation campaigns

After being calibrated in laboratory, all the generations were tested in beam facilities such as the $H2$, $H8$ and $H4$ lines at the CERN SPS North Area and at the Fermilab Test Beam Facility (FTBF) in USA. At CERN, the beam is initially extracted from the SPS accelerator and can be converted to a muon, electron or mixed hadron beam after the secondary target, with momenta up to 400 GeV/c.

The test setups were similar for all the test beam periods. The beam particles were selected by means of three scintillators placed in coincidence. The beam trajectories were reconstructed thanks to a tracking telescope made of three small triple-GEM detectors with a two-directions strips readout plane. An aluminum structure holding one or several

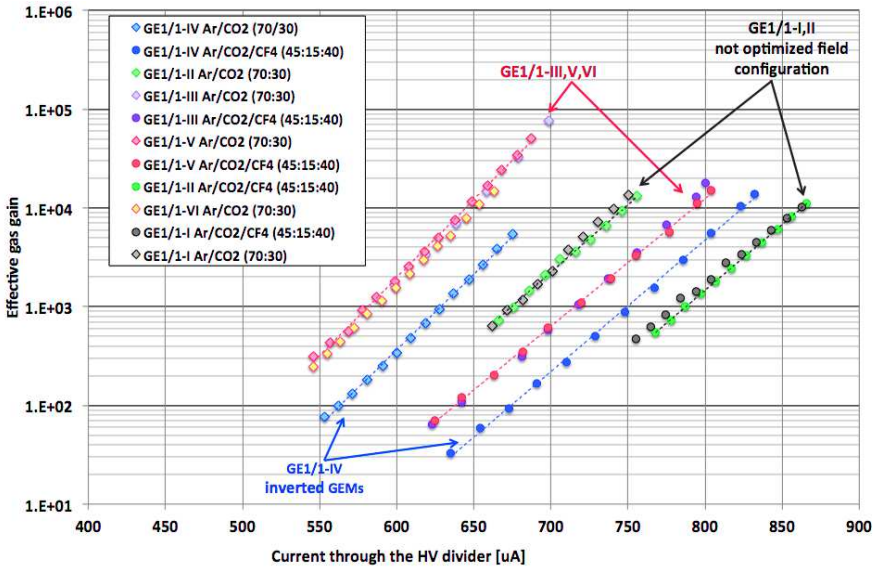

FIGURE 6.19: Gain curves of GE1/1 detectors in Ar/CO_2 (70 : 30) (diamonds) and $Ar/CO_2/CF_4$ (45 : 15 : 40) (circles) as functions of the current flowing through the HV divider.

GE1/1 chambers was placed in front the tracking telescope. The whole structure was mounted on a movable platform enabling the translations in ϕ and η directions in order to align the beam with different GE1/1 readout sector. Fig. 6.20 shows the typical setup used in the various beam test campaigns in 2010 [80], 2011 [79], 2012 [81], 2014 and 2015. In 2013, the first GE1/1chamber assembled outside CERN, at the FIT institute, was tested at Fermilab with a 32 GeV mixed hadron beam, using a similar setup [82].

The analog pulses from the three plastic organic scintillators, named $S1$, $S2$ and $S3$, are converted into digital gates after discriminator units and put in coincidence before being sent to the other DAQ systems (Fig. 6.21). The delays between the signals are adjusted to ensure that the time resolution of the trigger system is below 400 ps. At the CERN irradiation facility, the tracking telescope, initially designed by the RD51 collaboration, was equipped with the digital chips VFAT2 [83] [84], which provides a binary output with a variable latency for the position information and a fixed latency output, called $SBIT$, for the timing information. The GE1/1 chambers were mainly readout with the same system, however, the first and second versions of the CMS GEM electronics, described in Sec. 5.3.4, were also used to readout the detectors during the 2014 and 2015 irradiation campaigns. At Fermilab, the detectors were instrumented with analog APV chips and the RD51 Scalable Readout System (SRS) [85] [86]. With the APV+SRS system, the analog shape of the particle signals are sampled at a frequency of 40 MHz over a time period of $200-400$ ns after the reception of the external trigger. A threshold was applied to the analog pulses to emulate the VFAT response (OFF-line) so that the results of this particular test can be compared to the other test beam periods.

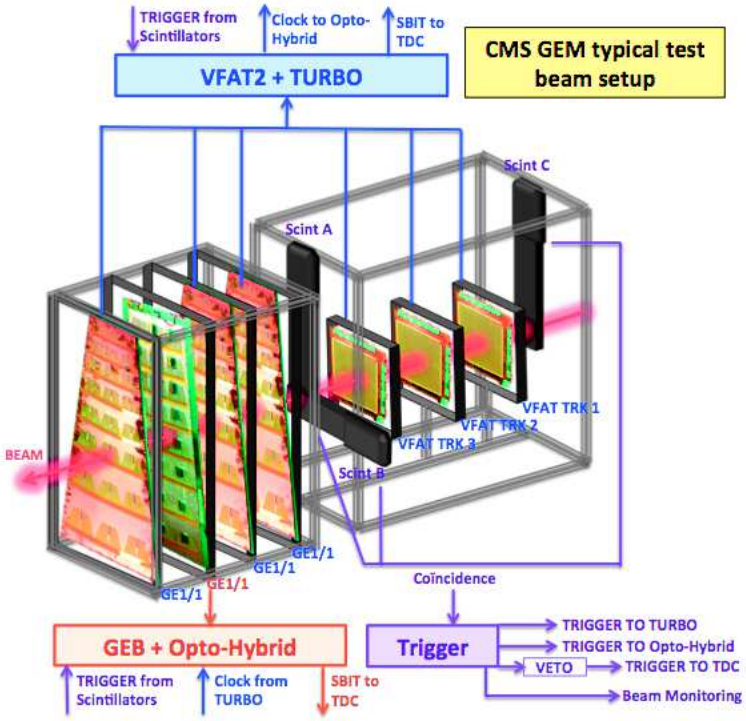

FIGURE 6.20: Perspective view of the typical experimental setup for performance measurement in test beam. The tracking telescope is made of three triple-GEM detectors with two orthogonal directions readout. The trigger system is ensured thanks to three scintillators connected in coincidence. The GE1/1 detectors under test are mounted onto a movable support to align various readout sectors with the beam line.

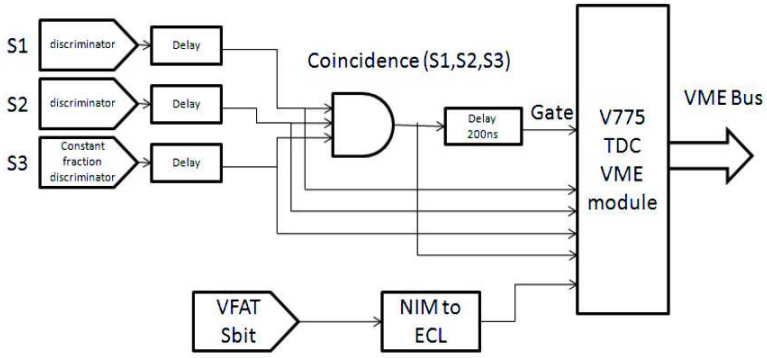

FIGURE 6.21: Schematic view of the trigger generation and timing DAQ systems.

6.4.3 Detection efficiency

The detection efficiency ε represents the probability to record an electrical signal when a particle is crossing the detector. It is evaluated by comparing the number of triggers N generated by the coincidence of the three scintillators and the number of hits $N1$ recorded in the region under test. The number of hits of the neighboring regions $N2$ is removed from the total number of triggers to compensate the scattering of particles and a possible misalignment of the region under test with the scintillator planes:

$$\varepsilon = \frac{N1}{N - N2} \tag{6.3}$$

Another method, more accurate, consists of comparing the number of reconstructed tracks with the number of hits measured in the detector in the close neighborhood of the expected hit position.

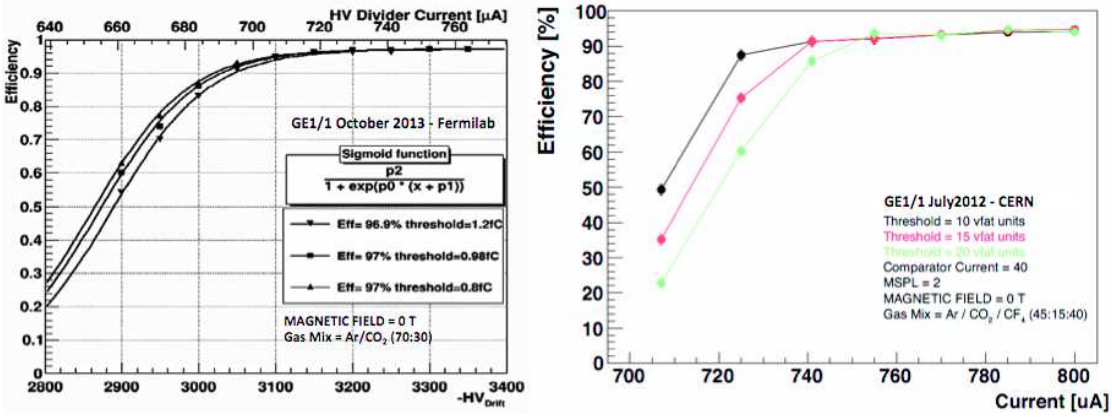

FIGURE 6.22: Left: detection efficiency of a GE1/1 detector in Ar/CO_2 (70 : 30) measured at Fermilab with the analog SRS APV readout system. The VFAT-like binary hit data are obtained by applying thresholds of 0.8 fC, 0.98 fC and 1.2 fC equivalent to 10, 12 and 15 VFAT units. Right: detection efficiency in $Ar/CO_2/CF_4$ (45 : 15 : 40) measured at CERN with the binary TURBO VFAT readout system.

As shown on Fig. 6.22, the efficiency of the GE1/1 detectors was measured for the two CMS gas mixtures Ar/CO_2 (70 : 30) and $Ar/CO_2/CF_4$ (45 : 15 : 40) at different operating points. A large plateau is reached at effective gains of $6 - 7 \times 10^3$ with an average efficiency over 97 %. During the CERN campaign in 2012 (right plot), the measurements did not include the neighbor regions. Therefore, the maximum efficiency was slightly underestimated (> 95 %). Finally, by using a simple combination method, we can expect the detection efficiency of a super-chamber to be 99.9 % (i.e. one detection layer records the hit out of the two layers).

6.4.4 Spatial and angular resolutions

The space resolution relates to the accuracy in measuring the position of the particle hits on the readout board. It is therefore a crucial property that refer to the muon track reconstruction in the CMS muon system. The space resolution is measured by evaluating the difference between the expected hit positions (i.e. where the tracks impact the detector) and the measured positions, called residuals.

The first step is the software alignment of the detectors, done by translating and rotating all the detection layers with respect to a reference chamber until the offset between

the mean of the hit distribution and the origin is minimized. The tracks are then reconstructed using the tracking telescope only (exclusive) or the tracking telescope and the detector under test (inclusive). In the exclusive method, the tracks are extrapolated to the detector region to give the expected position and therefore the residuals. However with this method, the resolution of the measurement is degraded because of the convolution between the intrinsic resolution of the detector and the uncertainty in the tracks extrapolation. With the inclusive method, this uncertainty is removed but the intrinsic resolution is underestimated since the hits in the detector under test also affect the track reconstruction. A good approximation of the intrinsic resolution can be obtained by taking the geometrical mean of both exclusive and inclusive solutions [87],[88]:

$$\sigma_{resolution} = \sqrt{\sigma_{inclusive} \times \sigma_{exclusive}} \tag{6.4}$$

The exclusive residual distribution measured in the central sector of GE1/1 detectors operating in $Ar/CO_2/CF_4$ (45 : 15 : 40) is shown on Fig. 6.23 (top). The width of this distribution in Cartesian coordinates is $\sigma = 268.8 \pm 2$ μm in the azimuthal $\hat{\phi}$ direction. In the polar coordinate system, more appropriate for trapezoidal chambers, the residuals deviation becomes $\sigma = 137 \pm 1$ μrad. This value was measured with a strip pitch of 455 μrad (0.88 mm in the $\hat{\phi}$ direction) and is very close to the expected resolution:

$$\sigma_{resolution} = \frac{strip\ pitch}{\sqrt{12}} = \frac{455}{\sqrt{12}} = 131\ \mu rad \tag{6.5}$$

At Fermilab, both exclusive and inclusive residuals were measured with a GE1/1 detector operating in Ar/CO_2 (70 : 30) (Fig. 6.23 - bottom). The angular resolution, calculated from Equ. (6.4) was estimated to 132 μrad and is fully compatible with the previous measurements at CERN and well below the minimal precision of 300 μrad required to significantly improve the angular muon position measurement in CMS.

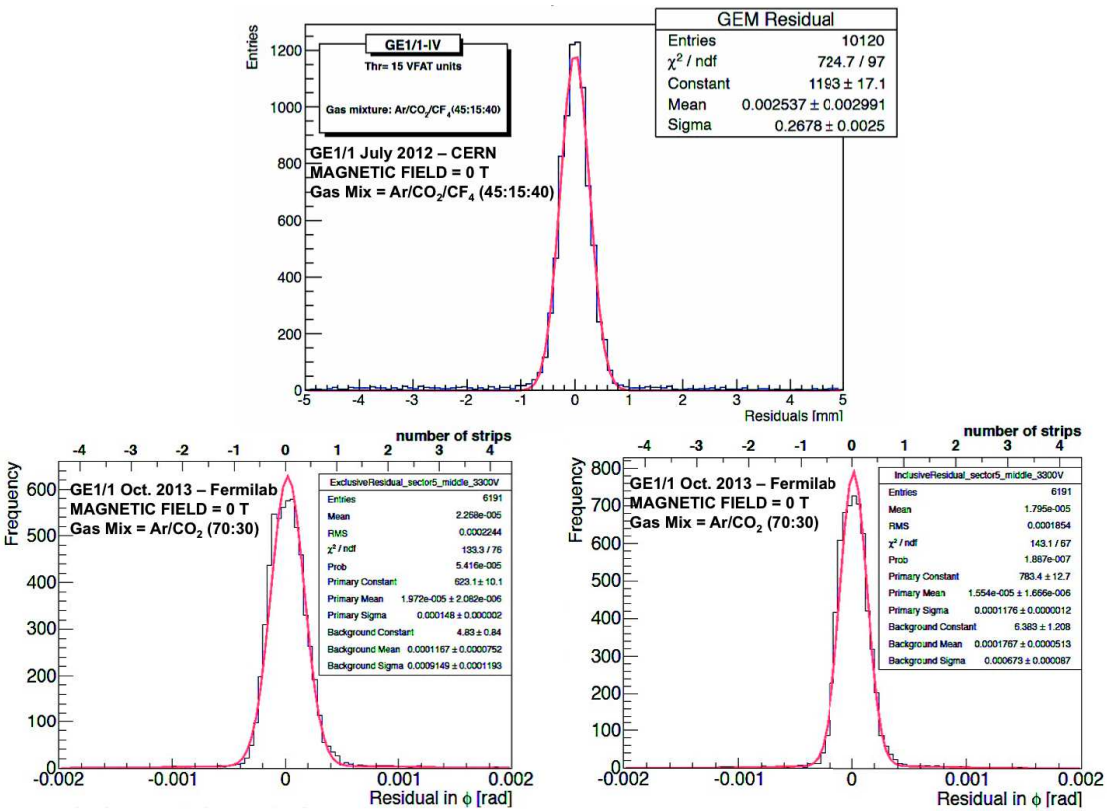

FIGURE 6.23: Top: exclusive residuals distribution in Cartesian coordinates (x, y) for a central sector of a GE1/1 detector operating with $Ar/CO_2/CF_4$ $(45 : 15 : 40)$. Bottom : exclusive (left) and inclusive (right) residuals distribution in polar coordinates (r, ϕ) for a GE1/1 detector operating in Ar/CO_2 $(70 : 30)$.

6.4.5 Time resolution

The good time resolution of the GE1/1 detectors is essential to ensure a fast triggering system in CMS with the correct bunch crossing (BX) identification. It is defined as the standard deviation of the time distribution of the recorded events, the time reference being the moment when the particles cross the drift volume. The time period between the reference time and the detection of the amplified signal, defined as the arrival time, can fluctuate mostly because the distance between the last primary cluster (i.e. the rising edge of the signal) and the first GEM varies from one event to another. The charges then follow the same path after crossing the first GEM. However, the diffusion of the signals between the amplification layers can also induce time variations and participate to the degradation of the time resolution. Therefore, the addition of a fast gas molecule with a low diffusion coefficient and high number of primary clusters per unit length, such as CF_4, can significantly reduce the time fluctuations and thus improve the time resolution (see Tab. 4.1).

The time resolution was initially estimated by measuring the time distance between the trigger signals and the detection of the hits in the chambers. Do to so, the coincidence of the three scintillators is sent to the common stop input of a CAEN V775 Time to Digital Converter unit (TDC). The fixed latency output of each detector under test, also called the *SBIT* signal, is sent to one of the inputs of the same TDC module (see Fig. 6.21). For each event, the time distance between these two digital signals is determined by the TDC and collected via optical fiber. The time resolution of the detector corresponds to the width of the resulting time distribution. However, since the DAQ electronics only reacts on the leading edge of a 40 MHz common clock, the random position of the trigger with respect to the clock also induces time fluctuations that sum up with the fluctuations due to the detector. Fig. 6.24 shows a schematic view of the DAQ system for timing measurements and the different contributions to the time distribution.

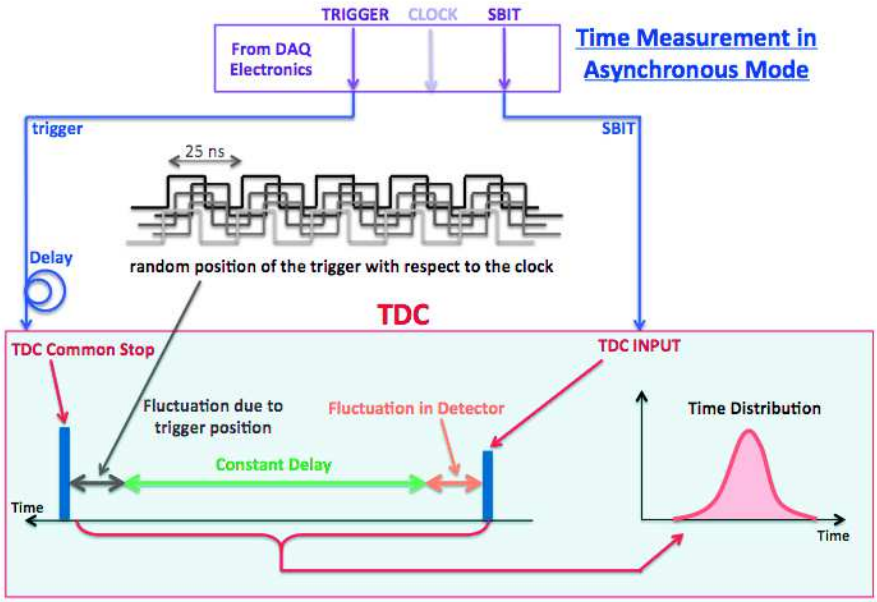

FIGURE 6.24: Schematic representation of the timing DAQ showing the different contributions to the delay between the trigger signal and the *SBIT* from the GE1/1 chamber.

The fluctuations induced by the clock are equivalent to the convolution of the intrinsic time distribution with a 25 ns square function. The effects of this convolution is represented on Fig. 6.25 (simulation). Several Gaussians were generated with initial RMS from 2 to 20 ns and convoluted with a 25 ns gate. After adding random noise fluctuations, the resulting distribution was deconvoluted. The RMS of both convoluted and deconvoluted signals were compared to the initial RMS. This quantitative study clearly demonstrates that the clock effects significantly affect the time resolution measurements. In particular, for intrinsic resolutions between 4 and 5 ns (i.e. the expected values for GE1/1 detectors), the measured RMS is almost two times bigger than the real expected

value. Therefore, it is necessary to perform the deconvolution of the measured time distribution in order to obtain a good approximation of the intrinsic time resolution.

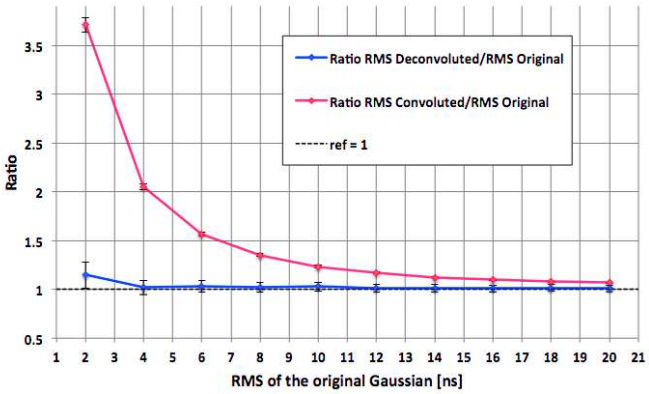

FIGURE 6.25: Comparison of the RMS of a Gaussian convoluted with a 25 ns square function and the RMS of the corresponding deconvoluted signal after the addition of random noise. The RMS are normalized with the original RMS.

Fig. 6.26 shows the deconvoluted time resolution as a function of the drift electric field for a triple-GEM detector in the GE1/1 configuration. The chamber was irradiated by 150 GeV muons at the CERN irradiation facility. The $Ar/CO_2/CF_4$ (45 : 15 : 40) mixture gives a resolution as good as 4 ns [75].

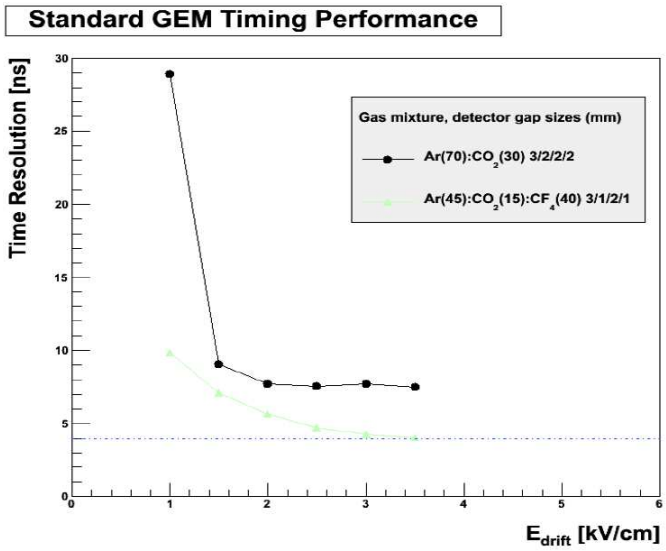

FIGURE 6.26: Time resolution of GE1/1 detectors operating in Ar/CO_2 (70 : 30) and $Ar/CO_2/CF_4$ (45 : 15 : 40) as a function of the electric field in the drift region.

Since the bunch crossings in the LHC are synchronized with a 40 MHz clock common to all the DAQ electronics devices, the time fluctuations induced by the DAQ clock during the irradiation campaigns are not foreseen in CMS. Therefore the time resolution measurements discussed previously are not fully representative of the real operation and the deconvolution step is necessary to remove the additional fluctuations. A different approach was proposed in order to directly measure the efficiency of assigning the correct

BX to the recorded events, without suffering from the effects induced by the clock. The method, called synchronous mode, consists of selecting only the triggers occurring in very thin window (typically $3-4$ ns) synchronized with the clock of the electronics. In this way, the clock effects are reduced to a convolution with a $3-4$ ns square function, which has a negligible impact on Gaussians with initial RMS bigger than 4 ns. Moreover, this configuration is very close to the real operation in CMS since the trigger selecting window represents the distribution of the proton collisions at the LHC, for a given BX. Fig. 6.27 shows the schematic principle of the synchronous mode.

The synchronization of the trigger with the clock gives a discrete time distribution in which each bin corresponds to the leading edge of a particular clock cycle and contains the number of events detected in the previous 25 ns time period. With an intrinsic time resolution of ~ 4 ns, the events recorded in a GE1/1 chamber are usually shared between three clock cycles.

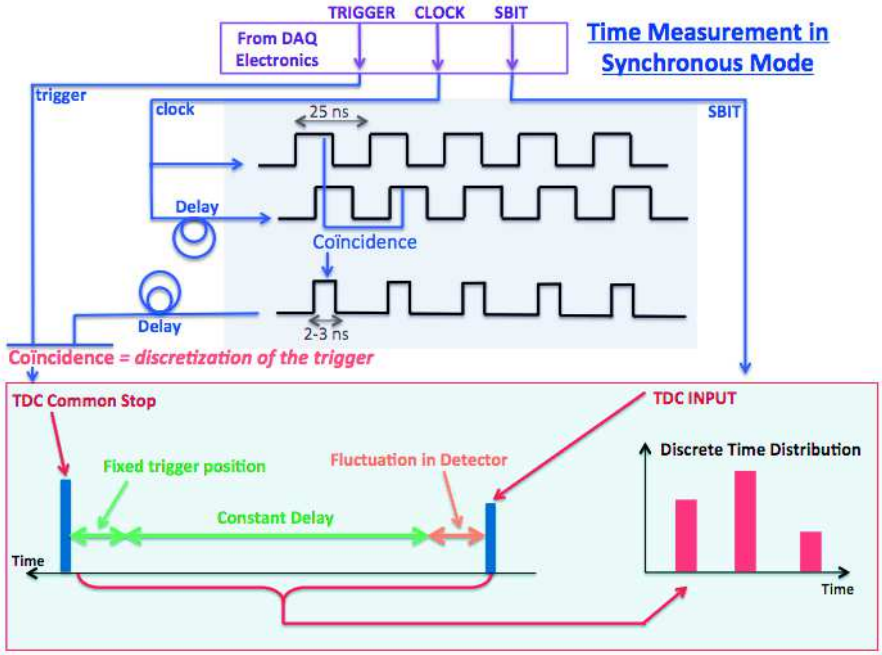

FIGURE 6.27: Schematic representation of the synchronous mode for the time resolution measurements. The clock of the electronics is used to generate a trigger window that represents the BX at the LHC.

In the synchronous mode, the time position of the clock edges is fixed with respect to the edge immediately following the trigger window, called the reference edge. As shown in Fig. 6.28, it is possible to "move" the intrinsic time distribution over the three clock cycles by adjusting the delay between the trigger window and the reference edge. The optimum delay is found when the majority of the events are detected in the central clock cycle, called the main clock. Fig. 6.29 shows the fraction of events in the main clock cycle as a function of the delay applied on the trigger window.

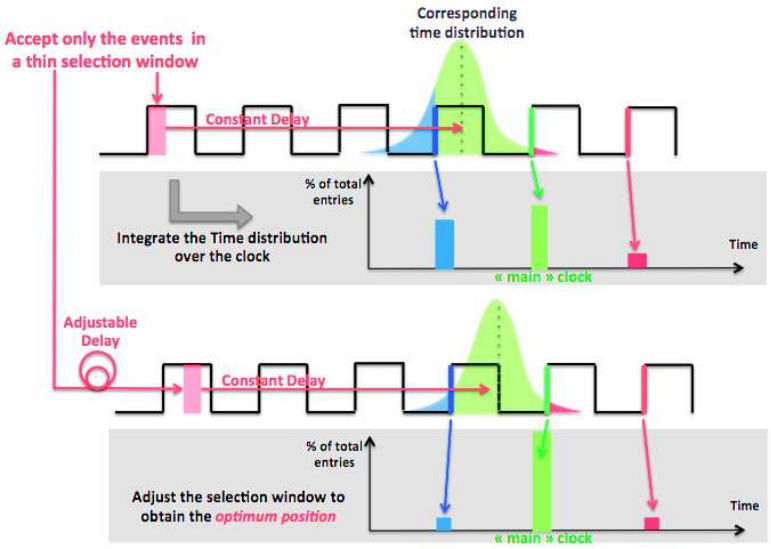

FIGURE 6.28: Schematic view of the position of intrinsic time distribution with respect to the clock of the electronics. The optimum delay on the trigger window gives the maximum number of events in the main clock cycle.

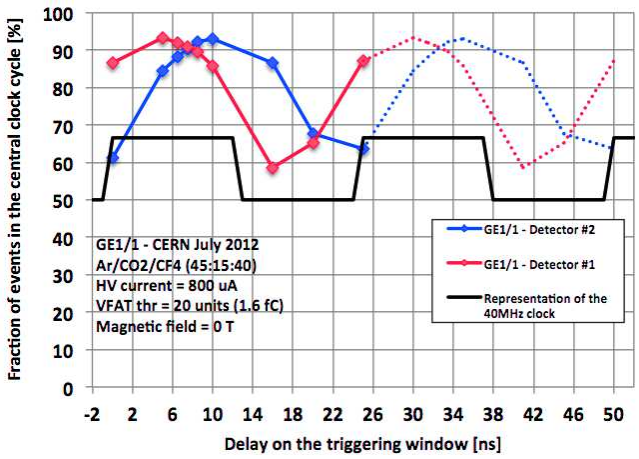

FIGURE 6.29: Results of the delay scan during for the synchronous measurements.

Therefore, by comparing the number of hits in the main clock to the total number of entries, we can determine the time efficiency in a 25 ns time window, which represents the BX identification efficiency. An example of the synchronous time resolution measurements is shown on Fig. 6.30 for a GE1/1 detector operating in $Ar/CO_2/CF_4$ $(45:15:40)$ at a gain of 2×10^4. The resulting BX identification efficiency is greater than 97 %.

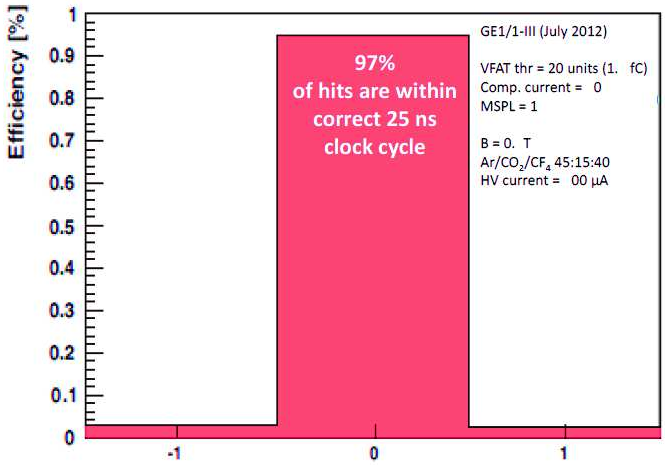

FIGURE 6.30: BX identification efficiency of a GE1/1 detector operating in $Ar/CO_2/CF_4$ $(45:15:40)$ at a gas gain of 2×10^4.

6.5 Conclusions

The results obtained during the extensive *R&D* phases confirmed the fundamental characteristics of the latter-day GEM technology and helped to define a set of working configurations that suit the CMS requirements.

The triple-GEM detectors for the CMS application are designed to operate with two possible gas mixtures : Ar/CO_2 $(70:30\ \%)$ and $Ar/CO_2/CF_4$ $(45:15:40\ \%)$. In both cases, the chambers can reach gas gains up to 10^5 in safe conditions. At the CMS operation gain (i.e $1-2\times10^4$), the detection efficiency with charged particles is greater than 97% for a single chamber. In the same conditions, the angular resolution has been measured at 132 μrad for an angular strip pitch of 455 μrad, well below the 300 μrad required by CMS. In addition, it has been shown that 97 % of the hits measured in a single detector are assigned to the correct 25 ns clock cycle, allowing the proper bunch crossing identification. Thanks to the sharing of the total gas gain on several amplification layers and among several holes, the triple-GEM technology can detect charged particles at fluxes up to 100 MHz/cm^2 without suffering of gain and efficiency losses. For the same reasons, the discharge probability doesn't exceed $10^{-12}-10^{-11}$ in normal conditions of operation. A summary of the GE1/1 characteristics and the comparison with the CMS requirements is shown in Tab. 6.1.

Properties	**CMS requirements**	**GE1/1 performance**
Rate capability	> 10 KHz/cm^2	100 MHz/cm^2
Single chamber efficiency (MIP)	> 97 %	$97 - 98$ %
Angular resolution	< 300 μrad	~ 135 μrad
Single chamber time resolution	< 10 ns	$4 - 5$ ns with $Ar/CO_2/CF_4$ $(45 : 15 : 40)$ $7 - 8$ ns with Ar/CO_2 $(70 : 30)$
Gain uniformity	< 15 %	< 15 % with the last GE1/1 generation (see Sec. 8.5.5.3)

TABLE 6.1: Comparison of the CMS minimum requirements and the GE1/1 performance.

The good performance at reasonable gas gains, the very high rate capability and the low discharge probability make the GE1/1 technology the most suitable choice for the CMS end-cap muon system.

Chapter 7

Long-term operation study

7.1 Introduction

7.1.1 General description of the aging

The previous study, showing the characteristics of the triple-GEM technology, helped to define the best configurations to ensure the good performance and a safe operation in the CMS high rate environment. The next step consists of measuring the long-term stability to make sure that the good performance will be stable during the entire life of the detectors.

Several mechanisms can affect the long-term operation of particle detectors and lead to a gradual and permanent degradation of the detection performance. The mechanical deformations of the structure of the detector can induce gain fluctuations of the order of several per cents over the surface of the detector, resulting in drastic non-uniformity of the performance. Moreover, the physical and electrical properties of some materials may change after several years causing bad electrical contacts, gas leaks, oxidation ... These effects are multiple and can be avoided most of the time with an appropriate choice of materials, operating conditions and the validation of the detectors with a strict quality control.

However, the main contribution of the aging of gaseous detectors is due to chemical processes occurring during the amplification of the electrons. This phenomenon, called "classical aging", lead to the formation of polymer layers inside of the detectors, causing gain loss, degradation of energy, space and time resolutions but also dark current, self-sustained discharges and irreversible damages of the amplification structure. The goals of the long-term study is to evaluate the effects of the classical aging on GE1/1 detectors

after 10 years of sustained operation and establish a set of recommendations in order to maximize the useful lifetime of the chambers in the CMS configuration.

7.1.2 Evaluation of the accumulated charge

For the GE1/1 project, the triple-GEM chambers will operate continuously during 10 years with a background rate of MIPs of the order of 1 kHz/cm^2 in the hottest regions at the HL-LHC instantaneous luminosity $\mathcal{L} = 5 \times 10^{34}$ cm^{-2}s^{-1}(see Sec. 3.2 and [10]). The total accumulated dose after 10 years is estimated to 500 Gy (50 krad). However, in the case of gaseous detectors, one prefers another expression, the total accumulated charge Q_{tot}, which includes the maximum interaction rate R_{max}, the primary charge induced by particles n_{tot}^{pairs}, the gain of the detector G and the exposure time at the LHC t_{LHC}:

$$Q_{tot} = R_{max} \times n_{pairs}^{tot} \times q_e \times G \times t_{LHC} \tag{7.1}$$

Since the particles crossing the detector arrive with a maximum angle of 23° (at $\eta = 1.5$), the maximum path length in the drift gap is 3.3 mm. Using the numbers of primary electron-ion pairs given in Tab. 7.1, the maximum number of primary charges deposited by MIPs in Ar/CO_2 (70 : 30) and $Ar/CO_2/CF_4$ (45 : 15 : 40) are respectively 31 and 32 pairs.

Gas	n_{pairs} $[pair/cm]$	n_{pairs}^{tot} $[pair/3.3mm]$
Ar	94	31
CO_2	91	30
CF_4	100	33

TABLE 7.1: Electric field configuration of the CMS GEM detector in the 3/1/2/1 gap configuration at the nominal voltage 4250 V.

Based on the previous operation of the LHC, the effective exposure time after 10 years is estimated to 6×10^7 s/y. Therefore, at a nominal gain of 2×10^4, the total accumulated charges after 10 years in Ar/CO_2 (70 : 30) and $Ar/CO_2/CF_4$ (45 : 15 : 40) are respectively 5.89 and 6.08 mC/cm^2. The goal of the long-term study is to reproduce this lifetime with a safety factor 10 by accumulating a charge of $\sim$ 60 mC/cm^2 in laboratory before the final installation.

7.2 Aging of gaseous detectors

7.2.1 Aging: a historical matter

The aging of gaseous detectors was initially identified with Geiger counters in the 1940's [89] [90] with a reduction of the operation plateau after a sustained irradiation (Fig. 7.1). Because most of the early detectors were sealed, it was often impossible to determine if the aging was due to a modification of the amplification structure (deterioration of the electrodes, deposits, cracks ...) or a change in the gas composition (molecular dissociation, pollutants ...).

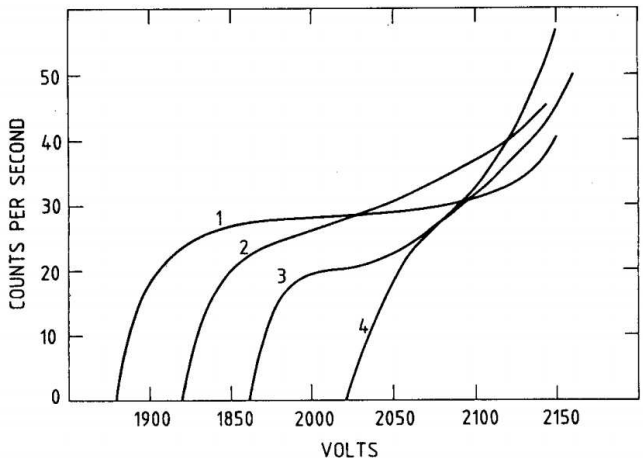

FIGURE 7.1: Count rate plateau of a Geiger tube filled with methane [14]. The curves were taken at different ages (curve 1 after 10^7 counts, curve 4 after 10^8 counts).

Later, aging effects were observed in wire proportional chambers in the form of a gradual and permanent gain loss, energy degradation and self-sustained discharges [91]. The aging issue received a more serious attention when particle detectors, such as MWPCs, started to become widely used in HEP experiments [92] [93]. After many years of trial-and-error approach with the idea of extending the lifetime of detectors, a chemical explanation of the aging mechanism was proposed, describing its main causes and the origin of the deposits previously observed in aged chambers ([92], [94]). The analogy between the detector's operation and the plasma chemistry didn't lead to the full understanding of the phenomenon but helped to define clean gas mixtures and the most appropriate operating conditions to prevent aging effects ([94], [62]). This work was crucial for the development of MPGD technologies foreseen for very high-rate applications [15] and, more recently, for the upgrade of the LHC experiments.

Since the first observation of the aging phenomenon, the systematic study on the long-term operation of gaseous detectors helped to better understand the aging processes and

to define a set of "rules" and recommendations on the assembly and the operation of detectors in order to minimize the aging consequences ([95],[96]).

7.2.2 Classical aging of gaseous detectors

The classical aging of gaseous detectors relates to the chemical reactions that take place in the avalanche plasma surrounding the amplification region. Because the dissociation energy of a gas molecule is $2-5$ times lower than its minimum ionization energy, the electron avalanche is accompanied with the production of a large variety and a high concentration of free radicals. The majority of these radicals is chemically very active (i.e. with unsatisfied covalent bonds) and can therefore recombine to form the original molecule or react with other active species to form monomers. The monomers released in the gas, or attached to the surfaces of the detector, associate in chain reaction and continue growing up until the bonds of the chain radicals are satisfied by a complementary fragment [92]. The large molecules thus created, called polymers, can migrate through the detector and condense on electrodes and walls, changing the geometry of the amplification structure and its electrical properties. Fig. 7.2 shows an example of a clean gold plated tungsten wire (A) and microscopic pictures of aged wires (B, C, D) used in proportional counters and affected by different type of polymer deposits.

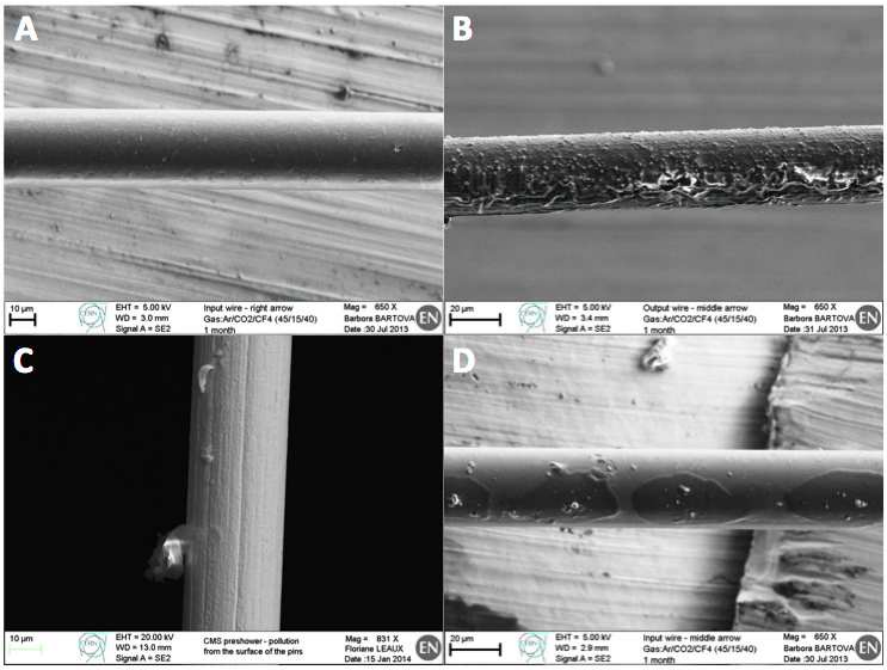

FIGURE 7.2: Microscopic pictures of a clean gold plated tungsten wire (A) and aged wires (B,C,D) extracted after 15 days of operation in a proportional counter in contaminated gas mixtures.

The effects of the polymer deposition are various and strongly depend on the physical and the electrical properties of the polymer and on the shape, the thickness and the location of the deposits:

- The deposition of insulating or conductive layers on the anode may disturb the electric field by changing the geometry of the amplification structure. As a result, the amplification process is modified, provoking in most of the cases a permanent gain loss, the decrease of the energy resolution and more generally the degradation of the performance of the detectors (see Fig. 7.3).

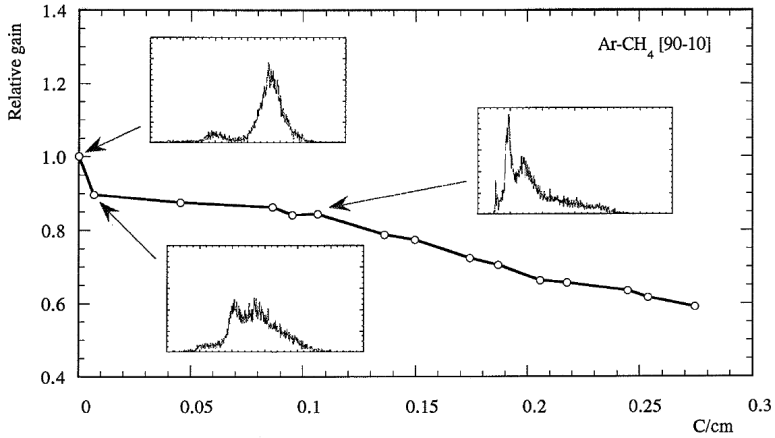

FIGURE 7.3: Aging of a wire chamber operating in Ar/CH_4 (90 : 10) at a gain of 2×10^4 [15]. The curve represents the evolution of the gas gain normalized with the initial value as a function of the accumulated dose, expressed as the total charge accumulated per centimeter of wire. The energy response to an X-ray source was also measured at different times to illustrate the degradation of the energy resolution.

- The deposition of polymers on the cathode can have even more dramatic effects on the detector. In normal conditions, the ions produced during the amplification drift toward the cathode before being evacuated through the metal layers. However, in case of insulating polymer deposits, the ions are trapped in the polymer and start accumulating, creating a large electric dipole. Because the polymer films are usually very thin, an electric field can develop between the positive-charged layer and the charge induced on the cathode, exceeding the threshold for field emission ($\sim 10^7$ V/cm). Electrons are therefore extracted from cathode and some of them will penetrate the gas volume and trigger further avalanche processes, creating more ions that can be attached to the polymer layer (see Fig. 7.4). This phenomenon, known as the Malter effect, is responsible for an increase of the dark current in the detector, self-sustained discharges and the electrical breakdown of the gas [97].

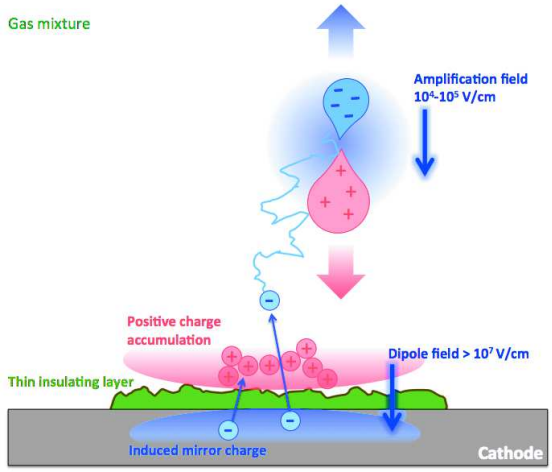

FIGURE 7.4: Schematic representation of the Malter effect. The accumulation of positive charges on a film insulating layer creates a local electric field strong enough to "pull" electrons from the cathode. Some of the electrons can reach the amplification volume, trigger avalanches and produce dark current and self-sustained discharges.

- Another aging effect is the production and the release of electronegative species in the gas that can absorb the electrons induced by a particle and lower the effective gain of the chambers [92].

Past studies show that the gas mixtures containing hydrocarbon quenchers (e.g. CH_4, $C_2H_2F_4$ ...) will mostly produce hydrogen-deficient radicals that can easily make bonds with other fragments and form large polymers ([92], [98], [99]). Even if the aging rate of hydrocarbon mixtures can be reduced by adding a small concentration of oxygen-based molecules ([100],[101],[102]), such mixtures are usually excluded for the long-term operation in high-rate experiments and replaced by hydrogen-free mixtures like Ar/CO_2. In this case, the resulting oxygen-based radicals, which are relatively inactive, can block the polymerization process and absorb other radicals to form volatile products that can be evacuated from the gas volume. Such mixtures, considered as clean from aging point of view, were adopted in most of the HEP experiments, and also for the GE1/1 project in CMS.

However, even if gas mixtures like Ar/CO_2 does not lead to the production of polymers in a clean environment, the presence of pollution in the gas can bring additional molecules and very active radicals that can trigger the polymerization process. In practical cases, a small concentration of unknown molecules is always present in large gas systems. The pollution has various origins: residuals in the gas cylinders, contamination of the tubing, gas leaks or most probably from the spontaneous release of molecules trapped in the materials forming the detectors, also called outgassing. Extensive studies were performed in the last decades to understand the effects of material outgassing and to identify the sources of pollution ([15] [103]). A list of banned materials was then

established to ensure the cleanliness of gas systems for the future experiments. In particular, the components containing silicon-based molecules can easily be consumed in avalanche plasma and produce very active radicals that can propagate in the detector ([91],[92]). Silicon is present in many materials: glues, adhesives and greases but more problematic, it is usually found as a residual of a production process that is rarely mentioned by the manufacturers. Similarly, electronegative compounds such as halogens must be banned from the gas volume. Because of their low dissociation energy, such materials will produce large quantities of free radicals in the avalanche plasma and feed the polymerization. Traces of halogens can be introduced into the detectors after certain cleaning procedures or by the outgassing of rubber and some plastic materials.

Therefore, the identification and the elimination of polluting materials is a crucial step of any long-term study and must be seriously studied alongside the classical aging tests.

7.2.3 Etching issues

In addition to the standard mixture Ar/CO_2 (70 : 30) adopted for the GE1/1 project, another candidate mixture containing CF_4 molecules was proposed in order to achieve a time resolution below 5 ns. As described in Sec. 4.3.3 , CF_4 is very interesting for fast timing applications due to its low electron diffusion, high drift velocity and primary ionization. Moreover, since CF_4 is an excellent etching gas for most of the Si-based compounds, it can be used to clean the detectors contaminated with Si and to prevent further polymerization ([104],[105]-CMS CSC).

However, the use of CF_4 can also lead to irreversible damages of the detectors because of its etching power. The dissociation of the CF_4 molecules in the avalanche plasma gives birth to fluorine radicals that can react with metal layers, inducing metal fluorides and etching [106]. Moreover, the presence of water in the gas volume, in association with fragment of CF_4 can lead to the production of HF acid which can strongly etch the materials in contact with the gas volume [107]. In the particular case of triple-GEM detectors, it has been shown that the use of CF_4-based mixture can seriously damage the GEM holes and provoke the fast aging of the detectors, as seen on Fig. 7.5 [16]. The solution to this problem consists of increasing the gas flow rate in order to remove from the gas volume the fluorine radicals and the HF molecules before it damages the foils.

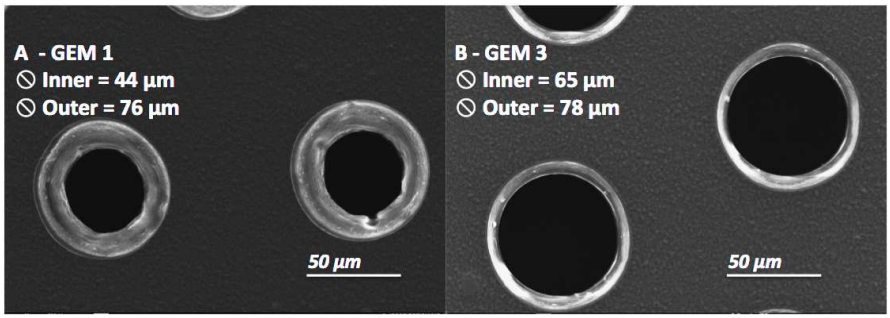

FIGURE 7.5: Microscopic view of GEM holes of a triple-GEM detector showing the etching induced by HF acid [16].

7.2.4 Aging of GEM-based detectors

7.2.4.1 The GEM structure from the aging point of view

The GEM technology can be particularly resistant to classical aging, mainly because of two geometrical particularities:

- The first advantage is the clear separation between the amplification stages and the readout plane. The absence of a strong amplification field near the readout board significantly reduces the possibility of direct polymer deposition on the strips. Thus, the collection of the charge is not affected by the long-term operation, even if the polymerization occurs in the GEM foils. In the same way, the possibility of deposits on the cathode drift plane is eliminated, as well as the possible Malter effect.
- The second benefit is the sharing of the gain over three foils and, for each foils, over several holes, resulting in multiple amplification channels for a single event. Therefore, each channel gives birth to smaller avalanches with a lower energy available for the dissociation of the gas. At the end, there are less radicals and monomers available for the polymerization compared to a single stage detector.

However, despite of a very low polymerization rate, the GEMs are not completely protected from classical aging. Indeed, most of the electric field lines going through the GEM holes terminate on the hole rims. Even at a very low polymerization rate, the accumulation of polymers in this critical and tiny region could lead to the formation of large structures that could disturb the amplification. Additionally, insulating deposits on the top rims could capture some of the ions from the avalanches and provokes Malter discharges.

7.2.4.2 Past experience on the aging of GEMs

In spite of the choice of non polymerizing gas mixtures and the geometrical benefits of the triple-GEM technology, the presence of a small concentration of pollutants in the detection volume can lead to the formation of polymer structures in the critical regions of the GEM holes, which can disturb the amplification fields and the evacuation of the positive charges after a long exposure. Therefore, it is essential to confirm the longevity of the detectors before the installation in the experiments and to validate the use of non-outgassing materials. The aging of GEM-based detectors was extensively studied in the last decade with different sizes and configurations related to the various GEM applications:

- The double-GEM technology was tested in 2000 with Ar/CO_2 (70 : 30) at a gas gain of 2.2×10^3 ($\Delta V_{gem} = 410$ V). The chamber was exposed to a X-ray source during 900 hours with an average rate of 4.75 MHz/cm^2. No significant aging or performance loss was observed after an accumulated charge of 1.2 C/cm^2 [108].

- An aging study was performed in 2001 with a triple-GEM structure operating in Ar/CO_2 (70 : 30) at a gain of 8.5×10^3 ($\Delta V_{g1} = 425$ V,$\Delta V_{g2} = 380$ V,$\Delta V_{g3} = 340$ V) and a gap configuration 3/2/2/2 mm, corresponding to the COMPASS configuration. After 240 hours of X-ray irradiation at 630 kHz/cm^2 and 240 hours at 2.5 MHz/cm^2, the chamber accumulated a total charge of 700 mC/cm^2 without showing any signs of aging or resolution loss [109]. A similar test was performed with the triple-GEM detector in Ar/CO_2 (70 : 30) at a gain of 6×10^3 ($\Delta V_{g1} = 400$ V,$\Delta V_{g2} = 390$ V,$\Delta V_{g3} = 380$ V) and a gap configuration 5.5/1.5/3/3.5 mm. The chamber was exposed during 750 hours to an X-ray source at a rate of 6 MHz/cm^2, accumulating a total charge of 2.7 C/cm^2. Neither aging effects nor polymer deposition were observed in this configuration, confirming the previous studies [110].

- Another set of aging tests for the LHCb application started in 2004 with triple-GEM detectors operating in $Ar/CO_2/CF_4$ (45 : 15 : 40) at a gas gain of 6×10^3 and a gap configuration 3/1/2/1 mm, identical to the GE1/1 configuration. Several chambers were exposed to a 1.25 MeV gamma source at $1 - 20$ MHz/cm^2 and to an X-ray source at 50 MHz/cm^2. In this case, a strong and gradual gain loss (up to 80 % loss at 2 C/cm^2) was observed immediately after the beginning of the test. After chemical analysis of the GEM foils, this aging effect was attributed to the etching of the holes by HF-acid produced in the avalanche plasma after the fragmentation of CF_4 molecules. This observation was confirmed in laboratory

and solved by increasing the gas flow rate to remove the F-based radicals before they react with the foils ([16],[111]).

- Additional aging test of triple-GEM+CsI chambers in pure CF_4 was proposed in 2004 for the PHENIX experiment. The gas gain was set to 10^4 ($\Delta V_{gem} = 510$ V) with a gap configuration 1.5/1.5/1.5/2 mm. The chamber was exposed to UV photons at rates up to 1 GHz/cm^2. After a total accumulated charge of 10 mC/cm^2, no degradation of performance or etching of the holes were observed [112].

These aging studies all confirmed the insensitivity of GEM detectors to classical aging. However, most of the tests were done on small prototypes ($< 30 \times 30\ cm^2$) with various electric fields and gap configurations. Moreover, the aging tests were mainly performed on small areas with interaction rates of the order of MHz/cm^2. Such testing conditions and detectors configurations are very different from the GE1/1 application and may lead to a different aging behavior.

7.2.4.3 Motivations for additional aging studies

The classical aging of gaseous detectors is a complex phenomenon, depending on multiple parameters related to the detector physics and chemistry. The analogy with the plasma and polymer chemistry provides a good basis knowledge ans explains some of the aging processes, but it doesn't describe quantitatively the full mechanism that occurs during an avalanche. Therefore, the causes of classical aging as well as the chemical reactions involved during the polymerization are not completely understood, and some experiments that were performed in similar conditions even produced contradictory results (e.g. the effect of the CF_4 molecule on the longevity of wire chambers). The detection technology, the dimensions of the chamber and the electric field configuration obviously play a major role in the aging process. Similarly, the properties of the gas, such as the composition, the flow rate, the temperature and the pressure are fundamental parameters of the amplification and thus the polymerization processes. Moreover, the quantity and the nature of the pollutants present in the gas mixture, usually unknown during the operation, can trigger the polymerization and significantly increase the deposition rate. Finally, the characteristics of the avalanche plasma also define the polymerization rate. One of the most important parameter is the temperature of the plasma, which includes the power density, the electron energy and density and the average path between collisions. The temperature of the plasma is particularly important for aging studies: as explain in the literature ([113],[114]), the rate of formation of certain polymers, and thus the aging rate, is significantly reduced when the temperature of the plasma increases.

In other terms, the operating conditions and the irradiation environment during aging tests must be as close as possible from the conditions expected in the real application, under the penalty of biasing the polymerization conditions and therefore the aging rate.

The GE1/1 chambers proposed for the CMS application are based on the new single-mask technique not yet tested from the aging point of view. Moreover, the mechanical structure used to stretch the GEM foils involves new materials and components that were not validated in aging tests. In a more general way, the composition and the operating conditions of the GE1/1 detectors are different from the configurations used in other experiments. Therefore, the results obtained in the previous aging studies are not sufficient to predict the longevity of the GE1/1 chambers.

7.3 Classical aging of the GE1/1 detectors

Since the aging depends on a large number of input parameters and relies on several possible chemical mechanisms, it is not possible to build reliable models or simulation tools that can predict the long-term behavior of gaseous detectors. Therefore, the only reliable way to predict the longevity of a detector consists of accelerating the aging in controlled conditions while monitoring its characteristics and performance. In order to reproduce 10 years of real operation in a reasonable time, the GE1/1 detectors were irradiated by a very intense source of photons at the Gamma Irradiation Facilities (GIF and GIF++) at CERN. The acceleration factor, which depends on the interaction flux, the primary charge and the gas gain, was kept below 30 in order to ensure realistic aging conditions and to avoid biasing the polymerization process (see Sec. 7.2.4.3). The gas gain and the energy resolution of the detectors were continuously monitored during the tests, as well as the environmental parameters.

Three sets of aging tests were performed in the framework of the GE1/1 project. During the initial test, the GE1/1 concept was irradiated for the first time by an intense and wide gamma beam. This first step was crucial to validate the design of the aging test setup and to define the operating conditions (gain, interaction flux and gas flow rate) corresponding to realistic acceleration factors. The first analysis tools were also created based on the data collected during the initial test. Then, a first classical aging test was performed during 12 months at GIF with the latest prototype of GE1/1 chambers operating in $Ar/CO_2/CF_4$ (45 : 15 : 40). A second aging test setup was then built at GIF++ in order to test the long-term operation in Ar/CO_2 (70 : 30). The charges accumulated during the two aging tests were equivalent to almost 10 years of real operation in CMS with a safety factor 10.

7.3.1 Description of the aging experiments

7.3.1.1 The GE1/1 detectors under test

Two different types of GE1/1 detectors were used for the aging studies:

- The initial test was performed with a full-size GE1/1 detector of the 3^{rd} generation (also named "GE1/1-III"), including the final geometry but not the final set of materials. In particular, it contains a significant amount of epoxy glue Araldite 2011 (AW 106/HV 935U) that was used to fix the external frame to the drift PCB (see Fig. 7.6). The presence of the glue in contact with the gas volume increases the risk of contamination [15]. However this chamber was not used to demonstrate the longevity of the GE1/1 technology but to validate the aging setup and define the operating conditions and the acceleration of the aging.

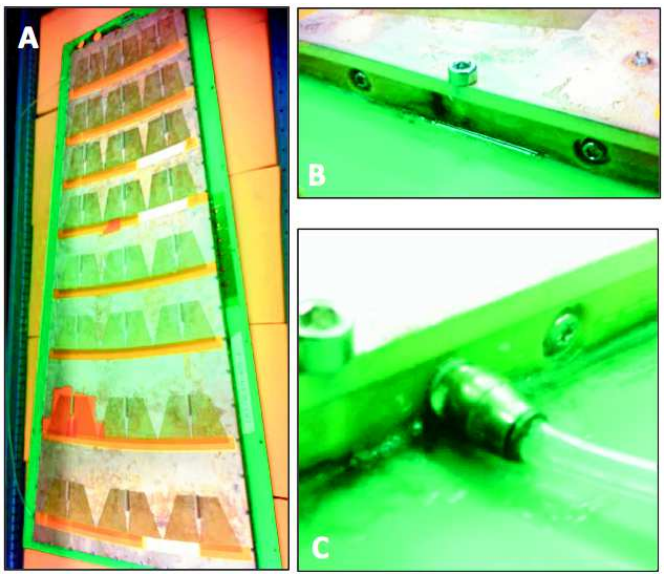

FIGURE 7.6: A: overview of a 3^{rd} generation prototype. B: close lateral view of the external frame showing the epoxy glue used to fix the frame and the drift PCB. C: close view of the gas input.

- For the classical aging tests in $Ar/CO_2/CF_4$ $(45:15:40)$ and Ar/CO_2 $(70:30)$, two full-size GE1/1 prototypes of the 4^{th} generation ("GE1/1-IV") with the final geometry and materials were irradiated for several months at GIF and GIF++. For this generation, the glue was abandoned and the external frames were fixed to the drift board thanks to metallic screws, as seen in Fig. 7.7. Two rubber O-rings embedded in the lateral frame ensure the gas tightness. These prototypes are representative of the detectors that will be installed in the CMS end-caps.

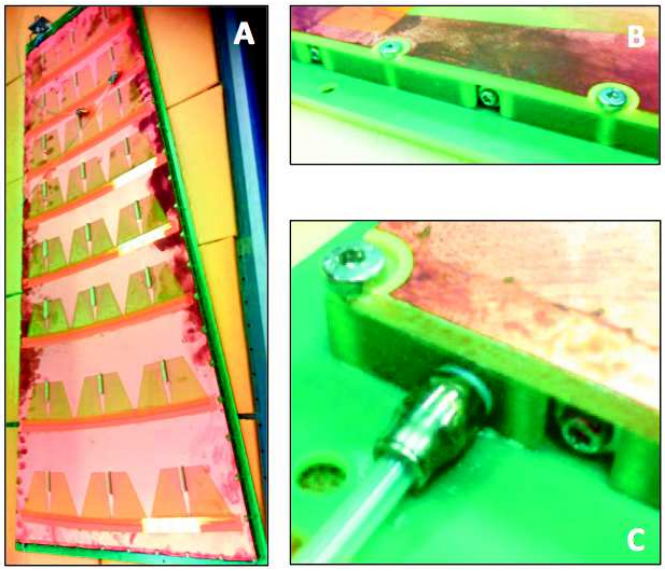

FIGURE 7.7: A: overview of a 4^{th} generation prototype. B: close lateral view of the external frame. The frame is fixed to the PCB with vertical screws. C: close view of the gas input.

The three detectors were powered through an HV divider corresponding to the CMS configuration described in Tab. 5.2. The gas gain was kept constant during the entire test at an effective value of 2×10^4 for both gas mixtures.

7.3.1.2 The monitoring wire chambers

Additionally, several Single Wire Proportional Counters (SWPC) were connected to the GE1/1 gas circuit in order to monitor the purity of the gas mixture before the tests and to identify possible contamination during the tests. Later, the same chambers will be used to study the outgassing of the GE1/1 materials.

The use of wire chambers to detect the pollution in the the gas mixture could be justified by three points:

- The amplification field and the readout of the signals are done by a unique and central microscopic wire. Therefore, even a small deposition of polymer will significantly affect the amplification and the collection of the signals induced by particles.
- The SWPC helps to detect not only the presence of pollution in the gas, but also the reaction of the pollutants with the gas molecules and the possibility to form polymers in the avalanche plasma.
- The SWPC is a simple object that can easily be dismounted and cleaned after a possible contamination.

The SWPCs available for this aging study were initially designed for aging tests within the RD10 collaboration. They consist of a stainless steel cathode box containing a gold-plated tungsten wire with a diameter of 30 μm. The cathode box is opened on one side and covered with a thin metallic window that allows the low energy X-rays penetrating the gas volume. The SWPCs operate at a gas gain of 10^4 and are irradiated by ^{55}Fe or ^{109}Cd sources, emitting X-rays of 5.9 and 23 keV respectively. The full energy is converted into primary charges via photoelectric effect. The readout signals are picked up from the wire after a decoupling capacitance.

7.3.1.3 The GIF installation

The GIF installation is an irradiation bunker located at CERN and containing a ^{137}Cs source of 566 GBq. The source beams 662 keV photons through two windows with a large opening angle as shown in Fig. 7.8. Both the initial test and the first classical aging test in $Ar/CO_2/CF_4$ (45 : 15 : 40) took place at GIF.

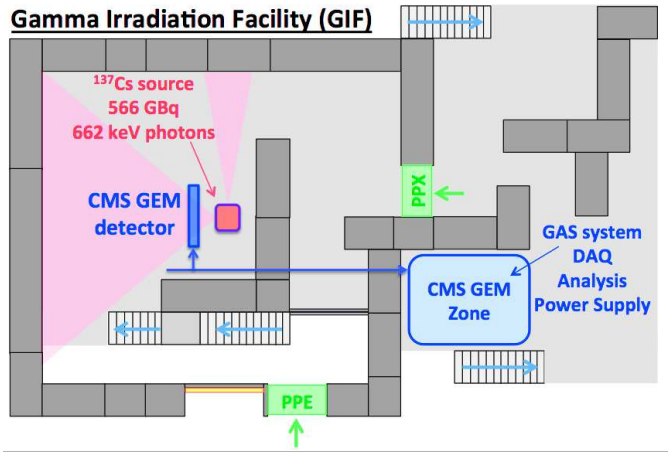

FIGURE 7.8: Schematic view of the GIF bunker showing the irradiator, the position of the GE1/1 detector and the DAQ area.

The GE1/1 chamber under test was placed at 30 cm from the main irradiator and received a particle flux of the order of 10^7 Hz/cm^2. Half of the chamber was protected with a 5 cm thick lead shielding in order to attenuate the source and measure the aging at different dose rates.

The probability of direct interaction of the 662 keV gammas in the 3 mm drift gap of the detector is of the order of 10^{-5} (derived from the mass attenuation coefficient). Nevertheless, the probability of Compton interaction with the 35 μm thick copper layer that forms the drift electrode is of the order of 10^{-3}. Most of the Compton electrons will be emitted in the forward direction in the drift gap with a peak energy between $400 - 500$ keV, i.e. close the minimum ionization energy (see Fig. 7.9).

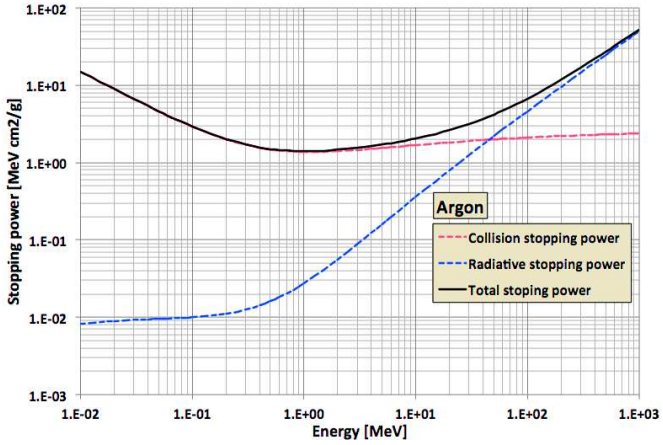

FIGURE 7.9: Stopping power of electrons in pure argon.

Therefore, the 662 keV photons crossing the chambers at a flux of 10^7 Hz/cm^2 are seen as MIPs at an interaction flux of the order of 10^4 Hz/cm^2. Considering that the maximum flux in CMS will be 1 kHz/cm^2, the resulting aging acceleration factor is about 10.

Since the purity of the gas mixture plays a major role in the aging processes, the design and the quality of the gas system must be carefully studied. Two different setups were installed at GIF for the initial test and the classical aging test:

- The initial test setup, shown in Fig. 7.10, was designed so that all the relevant parameters of the gas were continuously monitored during the experiment. The gas flow rate and its composition were ensured by a set of Mass Flow Controllers (MFC) and a mixing unit. Then the gas was sent to the GE1/1 chamber through copper tubing. In addition to the Meteo-station that monitored the environment of the detector, several temperature and pressure sensors were connected directly to the gas line. Finally, two SWPCs were placed at the input and the output of the GE1/1 chamber in complement to a gas chromatography unit in order to identify possible outgassing and contamination of the mixture. This system operated successfully during six months. However, a significant amount of pollution was identified with the SWPCs after the installation of the GE1/1 detector (see Sec. 7.3.3.1). The origin of the contaminants being unknown, the gas system was reviewed and modified for the classical aging test in order to minimize the amount of external devices connected to the gas line.

- The gas system for the classical aging test, presented in Fig. 7.11, was essentially made of stainless steel tubing. All the parts, glass tube flow-meters and connectors were previously cleaned with alkaline soap, DI water and BlueGold agent [115]. The MFCs and the mixer unit were replaced by a simple pre-mixed cylinder connected to a high-purity pressure regulator. The initial test revealed that the

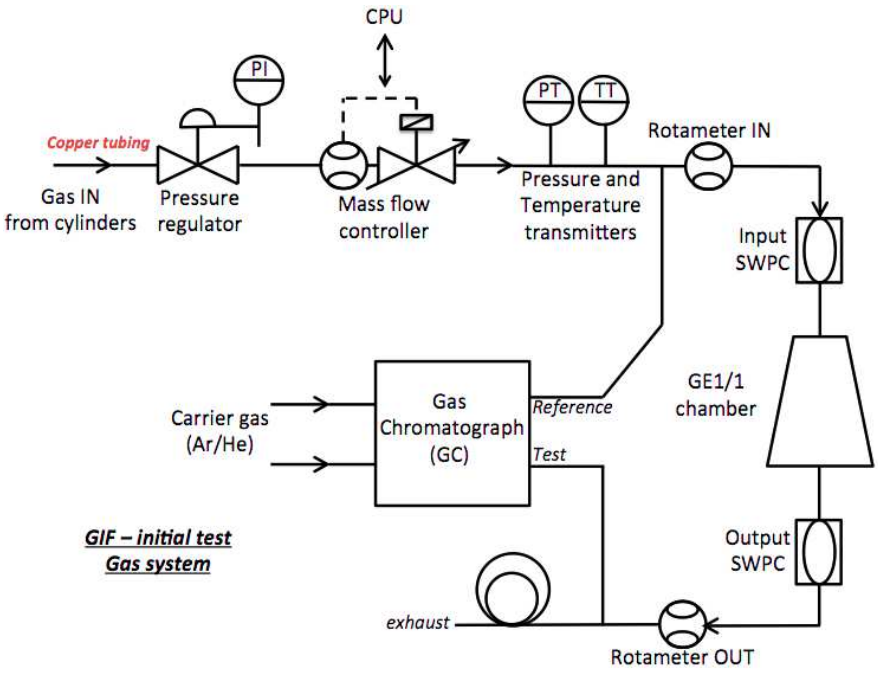

FIGURE 7.10: Overview of the gas system for the initial test at GIF.

temperature and the pressure in the gas line were identical to the external environment, even during the sustained operation. The sensors were therefore removed from the gas line. Finally, the use of SWPCs during the initial test helped to identify the contamination but not its origins. The wire chamber were then removed from the classical aging setup and were installed into an independent setup dedicated to the outgassing study of the GE1/1 materials (see Sec. 7.4). Nevertheless, the purity of the gas circuit is still verified with a SWPC before the installation of the GE1/1 chamber.

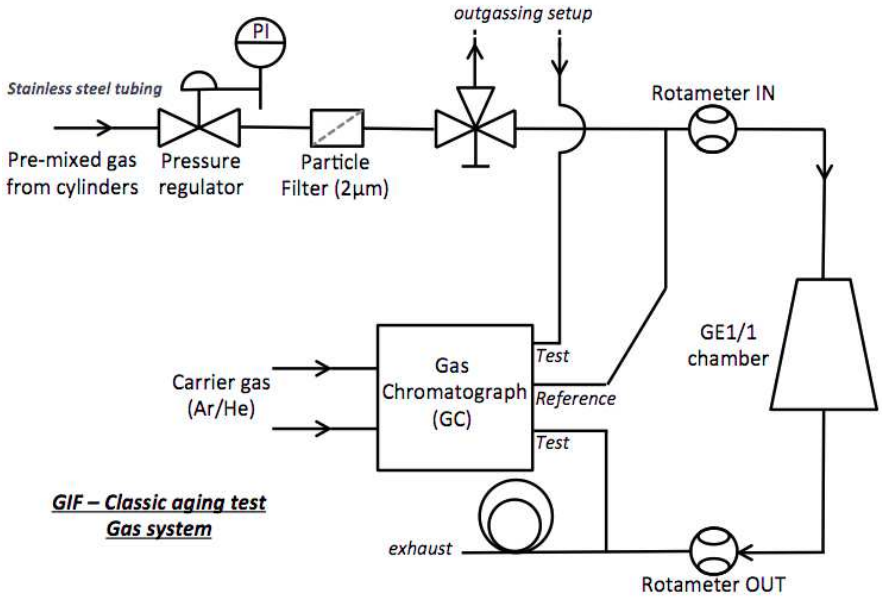

FIGURE 7.11: Overview of the gas system for the classical aging test at GIF. The new design was proposed based on the experience from the initial test.

Finally, the Data Acquisition systems (DAQ) and the control area were set outside the GIF bunker. It included the gas supply, the HV modules as well as the DAQ stations. The picture of the initial test and the DAQ area can be seen on Fig. 7.12 and Fig. 7.13.

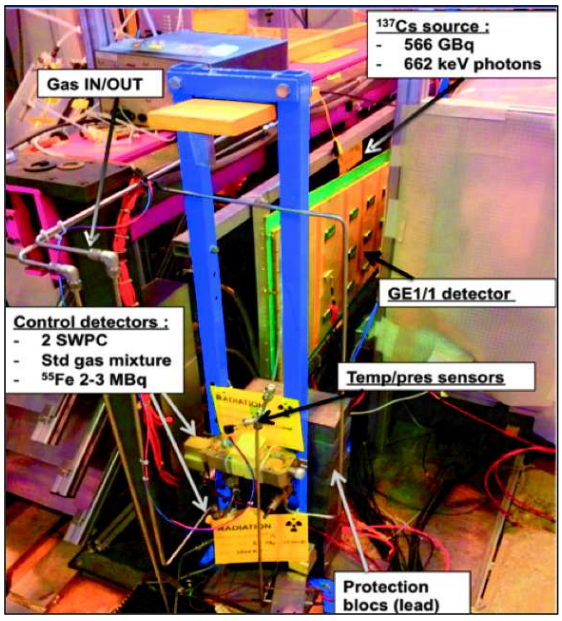

FIGURE 7.12: Picture of the initial test setup showing the GE1/1 chamber in front of the GIF irradiator. The SWPCs are protected from the ^{137}Cs source by a lead shielding, and irradiated by ^{55}Fe sources.

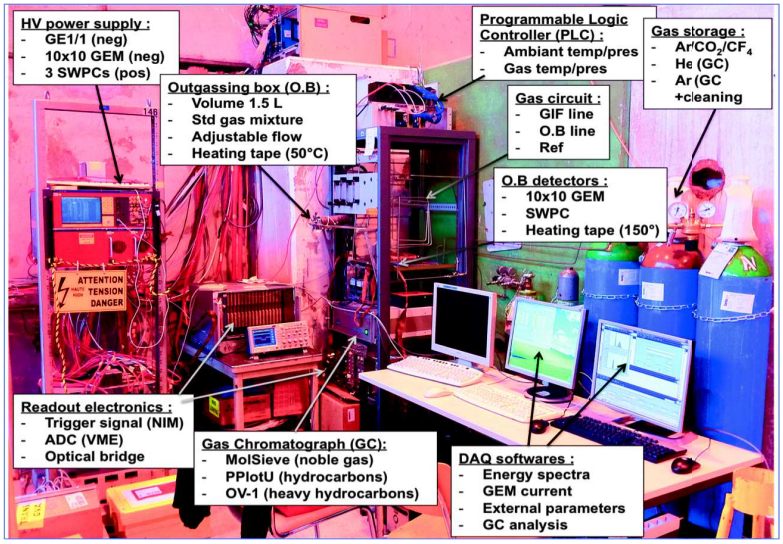

FIGURE 7.13: Picture of the DAQ area outside the GIF bunker showing the gas supply, the HV power system, the DAQ stations and the outgassing stand.

7.3.1.4 The GIF++ installation

After the closing and the dismantling of the GIF facility in September 2014, a new irradiation bunker, called GIF++, was built at CERN and started the continuous operation in April 2015. The GIF++ design, shown on Fig. 7.14, is very similar to the previous facility. It contains a ^{137}Cs source of 14 TBq embedded into an irradiator structure with two wide openings. The second classical aging test in Ar/CO_2 (70 : 30) is taking place at GIF++.

The GE1/1 detector under test is placed at 50 cm from the source point. Half of the chamber is directly in front of the irradiator and is operating under a particle flux just below 10^8 Hz/cm^2 while the other half, protected by the shielding of the irradiator, receive a fluxes lower by four orders of magnitude. The energy distribution of the photon background and the GE1/1 sensitivity to the source are similar to the GIF experiment. With the interaction flux in the detector of the order of 3×10^4 Hz/cm^2, the resulting aging acceleration factor is estimated at 30 at the CMS gas gain equal to 2×10^4.

The gas system for the GIF++ installation is substantially identical to the classical aging setup at GIF (see Fig. 7.15). However, the outgassing setup is not connected anymore to the GE1/1 gas system. The GC, which is not essential for the classical aging test, was removed from the gas line. A second gas line was added to the system to possibly supply a second chamber with a different gas mixture. Once again, the purity of the entire tubing was validated with a wire chamber before the installation of the GE1/1 detector.

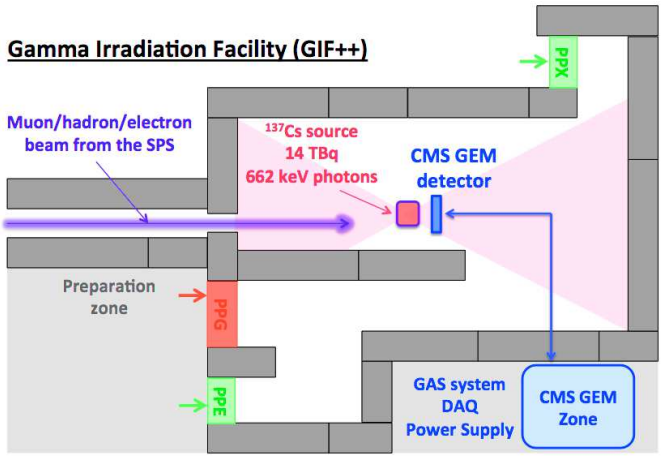

FIGURE 7.14: Schematic view of the GIF++ irradiation facility. The GE1/1 chamber is placed in front of the source, in the downstream area.

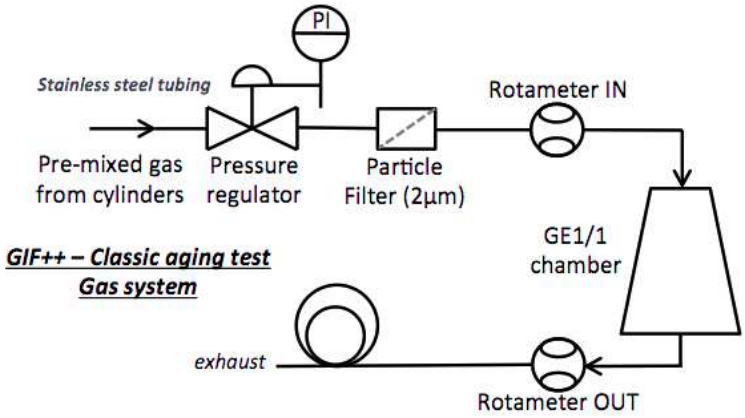

FIGURE 7.15: Overview of the gas system for the classical aging test at GIF++.

The operating point and the parameters of the DAQ electronics are remotely controlled from outside of the GIF++ bunker via optical fibers and serial cables. Therefore, the control of the full experiment and the collection of the data can be done from the CERN network, minimizing the need of stopping the irradiation to access the detector. The picture of test setup at GIF++ can be seen on Fig. 7.16.

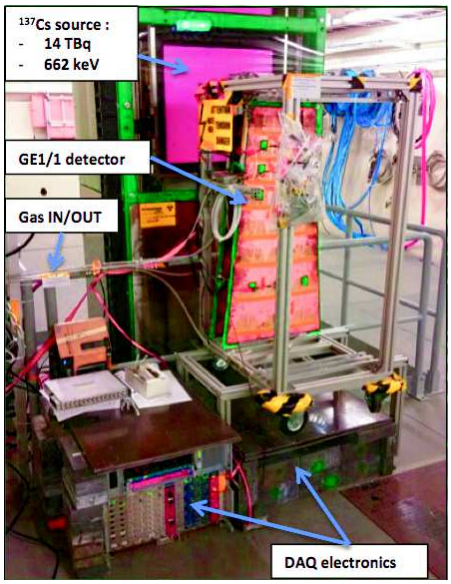

FIGURE 7.16: Picture of the classical aging test at GIF++. The GE1/1 chamber is placed directly in front of the ^{137}Cs source. The DAQ electronics is placed below the detector structure and is protected by several centimeters of Pb shielding. The entire system is connected to the DAQ station via optical and USB links.

7.3.1.5 The readout system

The readout system for the classical aging at GIF, GIF++ and the initial test consists of three main readout channels, summarized on Fig. 7.17:

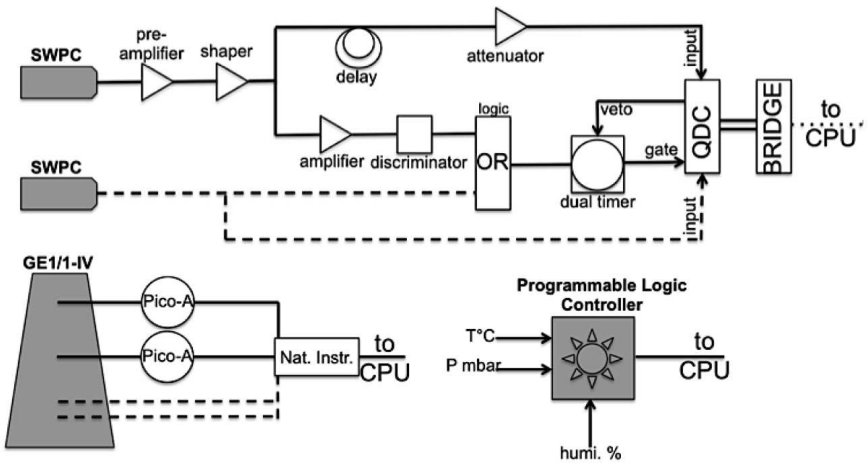

FIGURE 7.17: Schematic view of the DAQ system at GIF and GIF++. The pico-ammeters and the NIM electronics are responsible for the gain variations measurement while the Meteo-station records the fluctuations of the ambient temperature, pressure and humidity.

- The gain fluctuations of the wire chambers are measured thanks to a NIM electronics chain. After the pre-amplification and the shaping stages, the signal is split

into two lines. The first is converted into a digital gate by a discriminator unit and sent as a trigger signal to the Charge to Digital Converter (QDC). The second signal, representative of the gain of the chamber, is directly sent to the QDC input. The data is then transferred to an optical bridge via VME communication before being sent to the DAQ station through an optical link. After 10 minutes of continuous acquisition, the resulting charge spectrum is saved and reset before a new measurement.

- In order to measure the gain variations in the GE1/1 detectors, four KEITHLEY 6487 pico-ammeters are connected to several sectors of the readout board, two in the irradiated area and two in the protected part. The devices are connected in series with a GPIB protocol and controlled with a LabView interface. The anode current is recorded every 5 minutes for each sector. At GIF++, the GE1/1 chamber was also connected to a QDC in order to measure the energy resolution at different values of the accumulated charge.

- The environmental fluctuations, responsible for the temperature and pressure variations of the gas mixture, are measured every minutes by thermo-couples and an absolute pressure sensor connected to a SIEMENS S7 Programmable Logic Controller (PLC). The relative humidity in the vicinity of the detector is also recorded.

All the data files are then transferred to several computer stations outside the GIF facilities for backup saves and analysis.

7.3.2 The analysis procedure

The purpose of the analysis step is to extract from the data the gain variations as a function of the accumulated charge or as a function of time. However, for long-duration tests, the response of the detectors can fluctuate not because of aging effects but because of variations of the density of the gas, themselves induced by variations of the ambient temperature and pressure. Additionally, the temperature variations can slightly affect the operation of the readout electronics and induce baseline fluctuations to the data. It is thus essential to remove the environmental effects to isolate the possible aging effects.

The overview of analysis procedure is shown on Fig. 7.18. It consists of five main steps: the conversion of the raw files; the synchronization of the data; the zero-suppression; the correlation with the environment; the correction and the normalization of the gain.

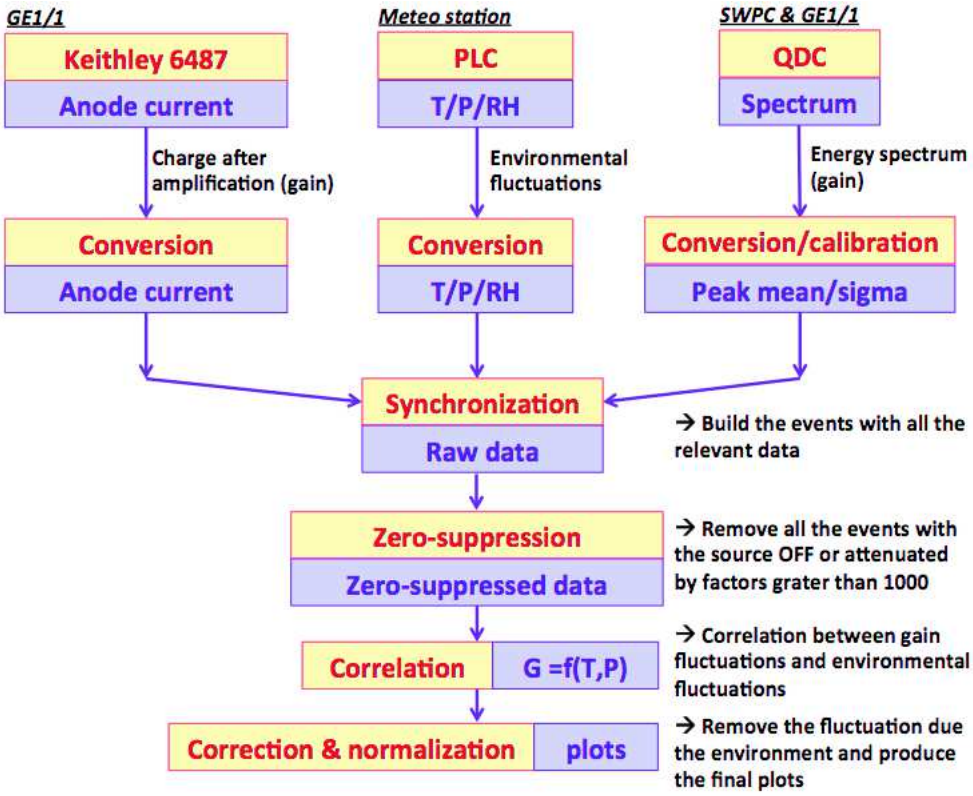

FIGURE 7.18: Schematic representation of the analysis steps. After all the data are converted into the same format, the events are built and selected depending on the status of the source. After defining the parameters of the correlation between the gain of the detector and the ambient conditions, the fluctuations related to the environment are removed.

7.3.2.1 Data conversion and zero-suppression

As a first step, the data files from the various DAQ systems are converted into the same format, including the relative time of each measurement, the average value of the anode current and the environmental parameters. The charge spectra from the QDC are processed with a separate fitting algorithm in order to keep only the useful information: the ADC mean and the width of the noise peak and the ^{55}Fe peak (for the SWPC data) or the most probable value of the ^{137}Cs landau distribution (for the GE1/1 data). Fig. 7.19 shows the typical ADC spectra for both SWPC and GE1/1.

Then, the relative time of each data point is compared to a reference time common to all the DAQ systems in order to do the synchronization of the data and to assign the correct environmental parameters to each gain measurement. After the synchronization, all the relevant information is stored into events, including the gain indicator (i.e. the anode current or the peak position), the environmental parameters and the absolute time. Finally, all the events corresponding to the source OFF or the detectors not powered are removed from the data set.

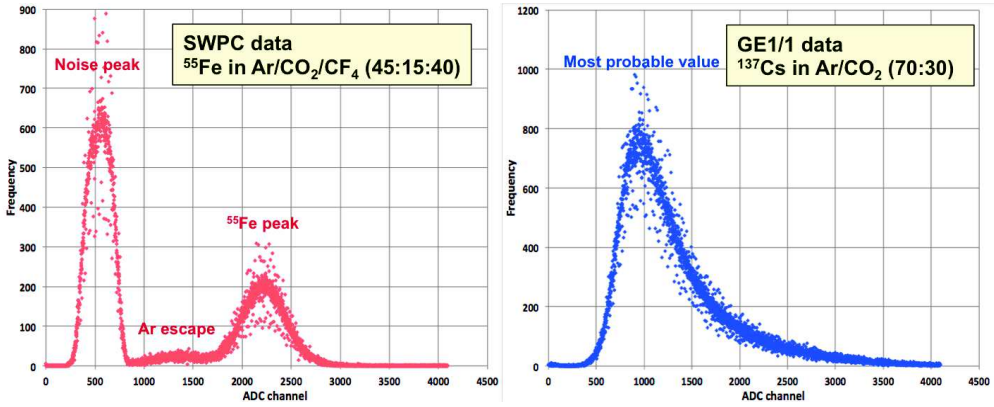

FIGURE 7.19: Left: typical ADC spectrum of ^{55}Fe in $Ar/CO_2/CF_4$ $(45:15:40)$ collected by the wire chambers. Right: typical ADC spectrum of the GIF++ of ^{137}Cs in Ar/CO_2 $(70:30)$ collected by the GE1/1 detector.

7.3.2.2 Correlation with the environmental parameters and normalization

The purpose of the correlation step is to parameterize the influence of the environmental variations on the response of the detector. As mentioned earlier, this influence may induce large fluctuations on the gas gain that can hide the possible aging effects. Fig. 7.20 shows a sample of data collected at GIF with a GE1/1 detector during two weeks of operation. The gain fluctuations, of the order of 30 %, clearly follow the ratio temperature over pressure (T/P).

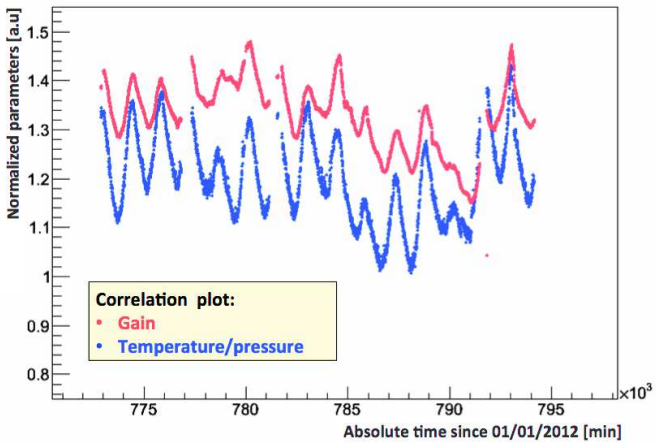

FIGURE 7.20: Typical data points taken at GIF showing the normalized anode current and the ratio temperature over pressure of the gas. The large fluctuations of the anode current are essentially correlated to the variations of the environmental conditions. The ratio "T/P" is used to better visualize the phenomenon but the environmental fluctuations must be treated separately.

A theoretical approach indicates that the amplification factor is an exponential function of the first Townsend coefficient (see Sec. 4.3.1), itself inversely proportional to the density of the gas. Therefore, the amplification can be expressed as an exponential

function of the ratio T/P. The relation between the measured gain $G_{meas.}$ and the real gain $G_{real.}$ is given by :

$$G_{meas.} = \frac{G_{real.}}{A \cdot exp(B \cdot T/P)} \tag{7.2}$$

where A and B are experimental constants depending on the gas and on the temperature range. They are determined by fitting the exponential functions of T and P plotted on Fig. 7.21.

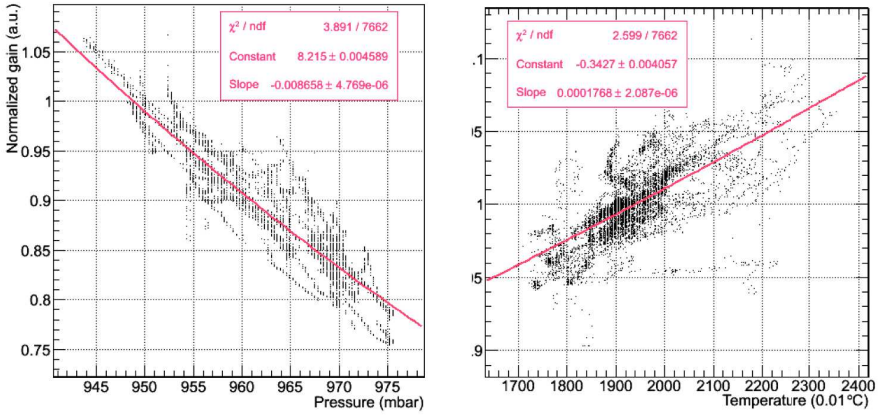

FIGURE 7.21: Correlation plots showing the dependency of the detector's gain with the atmospheric pressure (left) and the ambient temperature (right).

Past experiences [15] show that in some cases the correlation with the environment is better described by power functions of T and P. The relation (7.2) becomes :

$$G_{meas.} = G_{real.} \cdot exp(A \cdot ln(T) + B \cdot ln(1/P)) = G_{real.} \cdot (A \cdot T)^a \times (B/P)^b \tag{7.3}$$

with A, B and C constants and a and b correlation factors defined by the experiment. These factors represent the strength of the gain dependency with T and P, including not only the gas density effects but also other effects such as the influence of the environment on the DAQ electronics.

Fig. 7.22 represents the typical distributions of the measured gain (red) and the gains corrected with the exponential (blue) and the power (purple) functions. All the data points were normalized with the initial value of the gain. The width of the corrected distributions show the quality of the correlation and the effect on the raw data. Considering the small ranges of temperature and pressure covered during the aging tests, the difference between the exponential and the power methods is smaller than 1 %.

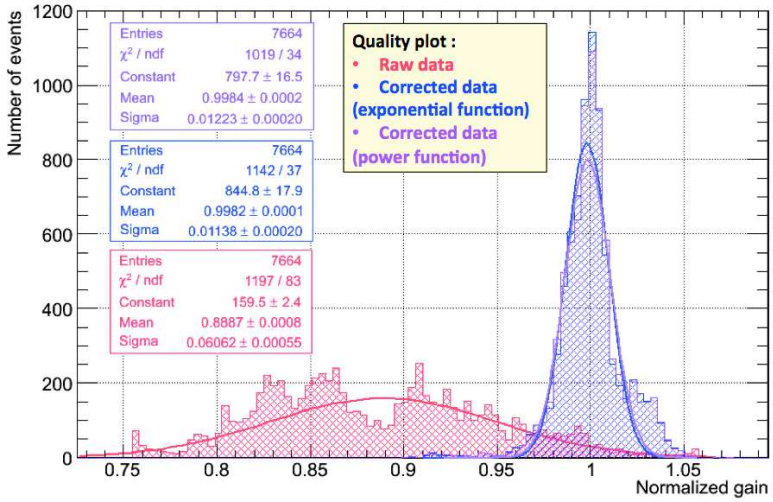

FIGURE 7.22: Correlation quality plot showing the effect of the exponential and the power corrections compared to the raw data.

After the corrections based on T and P, the resulting normalized gain is totally independent from the external perturbations and represents the intrinsic behavior of the chamber when operating under sustained radiations.

7.3.3 Classical aging test results

7.3.3.1 Initial aging test

After 7 months of continuous operation in $Ar/CO_2/CF_4$ (45 : 15 : 40) at the GIF facility, the GE1/1-III detector accumulated a total charge of 12 mC/cm^2, corresponding to 10 years of real operation in CMS at HL-LHC with a safety factor 2. The results of the aging test are shown in Fig. 7.23. The normalized gain is stable over the entire test, with small fluctuations within 3 % of its initial value. Fig. 7.24 shows the the amplitude of the gain fluctuations and the effect of the environmental correction on the raw data. The initial test demonstrated the successful long-term operation of the classical aging setup and the absence of chemical processes that could affect the amplification of the detector.

However, after the installation of the GE1/1 chamber and the T/P sensors in the gas line, a fast and permanent gain drop was observed in the wire chamber placed downstream the detector. Similarly, the gain of the upstream SWPC became unstable, with fluctuations greater than 10 %. Fig. 7.25 shows the gain variations of both input and output SWPCs in comparison to the measurement performed before the installation of the GE1/1 detector and the sensors. The monitoring SWPCs were dismounted and the

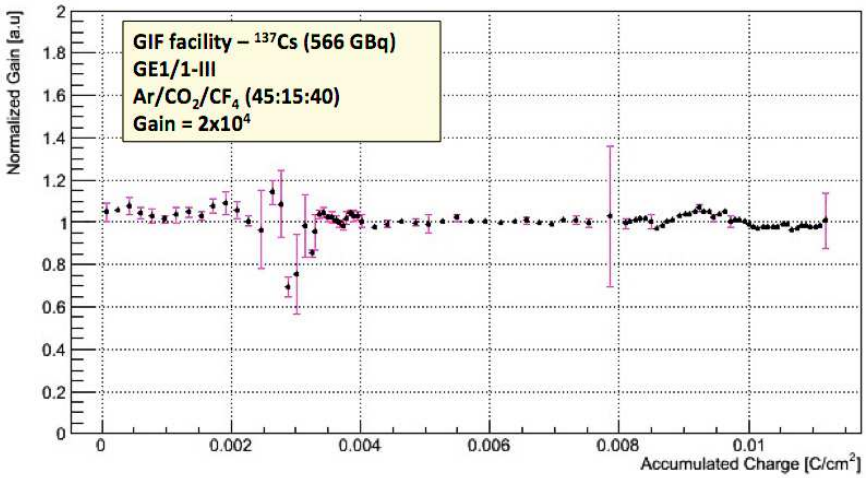

FIGURE 7.23: Normalized corrected gain of the GE1/1 detector as a function of the accumulated charge. The entire test represent 10 years of real operation in CMS with a safety factor 2.

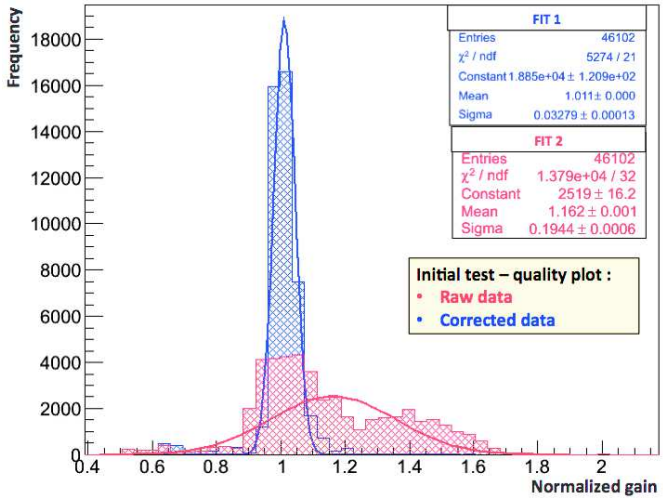

FIGURE 7.24: Quality plot of the initial aging test comparing the raw data and the normalized and corrected gain.

wires sent to a chemistry laboratory to be analyzed with a Scanning Electron Microscope (SEM). The SEM observations, presented in Fig. 7.26, confirmed the presence of polymer deposits on the wires. The deposits mostly contain carbon and oxygen-based structures, in particular in the irradiated region. The polymers seem to grow up around smaller white deposits containing traces of sulfide and silicon. This effect, more pronounced on the downstream wire, is the typical expression of the classical aging induced by the presence of pollutants in the gas mixture. Since the initial test did not allow to determine if the pollution came from the GE1/1 chamber, from the sensors or other elements in contact with the gas, a new system was designed for the classical aging tests and all the unnecessary materials were removed from the gas volume.

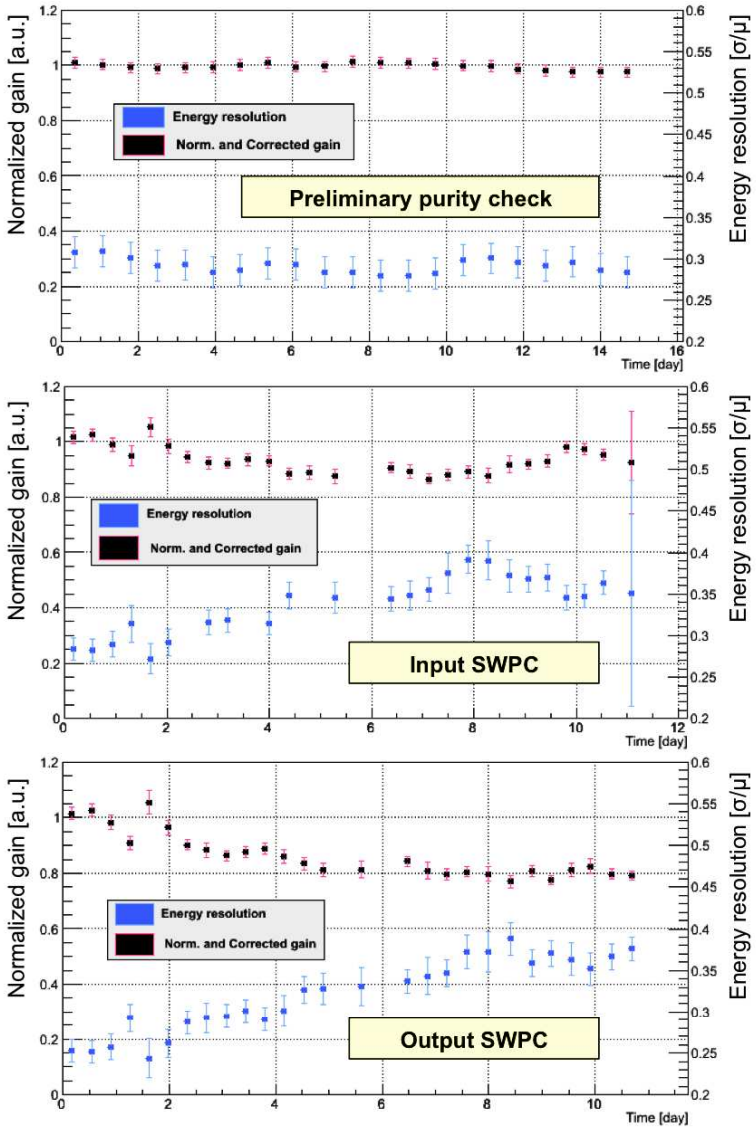

FIGURE 7.25: Gain fluctuations of the SWPCs operating in the initial aging setup. The first chamber (top) was used to validate the purity of the gas system before the installation of the GE1/1 chamber and several temperature and pressure sensors. After the insertion of the GEM detector, the operation SWPCs placed upstream (middle) and downstream (bottom) was degraded by the polymerization induced by the presence of pollutants in the gas mixture.

As a preliminary conclusion, the initial aging test was essential to optimize the gas system and prepare the setup for the classical aging test with the next generation of detectors. It demonstrated that even in the presence of pollution, the triple-GEM technology is resistant to classical aging and could survive several years in CMS without the degradation of its performance. This experience also highlighted the necessity of

studying independently the outgassing properties of the materials present in the GE1/1 detectors to prevent the release of contaminants in the gas mixture. The details of the outgassing study will be presented in Sec. 7.4.

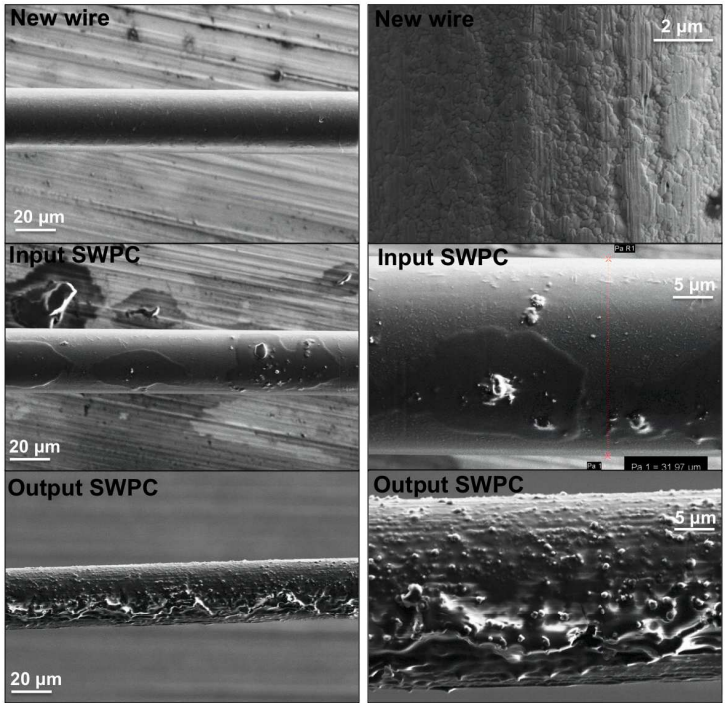

FIGURE 7.26: SEM pictures of the 30 μm gold-plated tungsten wires used in the upstream (middle) and the downstream (bottom) SWPCs in comparison to a new wire (top).

7.3.3.2 Aging in $Ar/CO_2/CF_4$ (45 : 15 : 40)

The first classical aging test was performed with a GE1/1 detector of the 4^{th} generation operating in $Ar/CO_2/CF_4$ (45 : 15 : 40) at the GIF facility. After 12 month of sustained operation in front of the ^{137}Cs source, the detector accumulated a total charge of 53 mC/cm^2, corresponding to 10 years of real operation in CMS with a safety factor 8.8. The results, shown on Fig. 7.27 indicate that the operation of the detector is not affected by any classical aging process nor etching of the GEM holes. The gas gain is stable during the entire test and only fluctuates within $2-3$ % of its initial value. The distribution of the raw data and the corrected gain are presented in Fig. 7.28. The test ended few days before the GIF facility was closed and the chamber was prepared to continue the irradiation at the new GIF++ facility.

Unfortunately, the chamber was filled by mistake with the wrong gas mixture during the installation at GIF++. Because the mixture contained 93 % of argon instead of 70 %, several destructive discharges occurred immediately after the ^{137}Cs source was turned ON, resulting in the permanent degradation of the performance of the detector. Even if

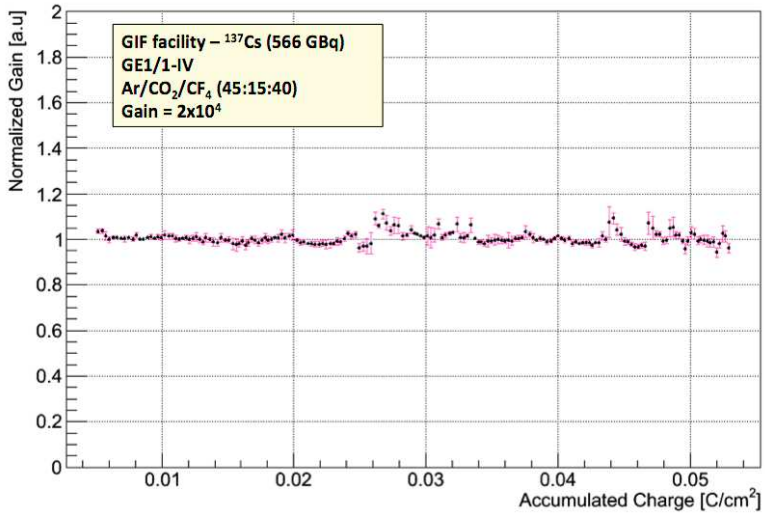

FIGURE 7.27: Normalized corrected gain of the GE1/1 detector operating in $Ar/CO_2/CF_4$ (45 : 15 : 40) as a function of the accumulated charge. The entire test represent 10 years of real operation in CMS with a safety factor 8.8.

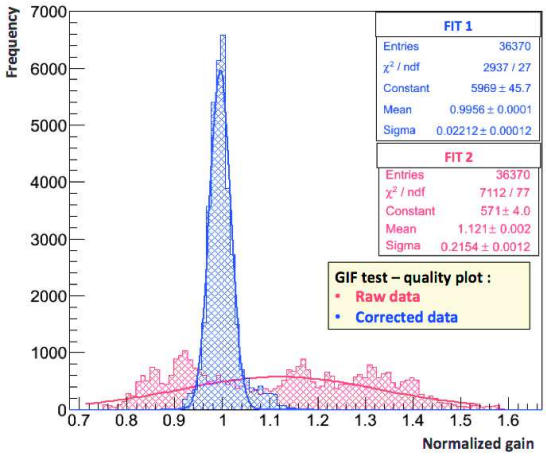

FIGURE 7.28: Quality plot of the classical aging test in $Ar/CO_2/CF_4$ (45 : 15 : 40) comparing the raw data and the normalized and corrected gain.

the GEM foils could have been cleaned in solvent baths with a great chance to recover the initial performance, the CMS GEM Collaboration decided to open the chamber and perform SEM analysis to understand the effects of the long-term operation at GIF and the consequences of the accidental discharges.

Three effects were observed:

- The first observation, shown on Fig. 7.29, is the coloration of the copper layers subject to radiations for a long period. This phenomenon was already observed in other detectors containing copper electrodes but it is still not fully understood. One possible hypothesis involves the electrochemical corrosion of the copper, triggered by the current collected by the GEM electrodes and the presence of oxygen-based

radicals produced in avalanche plasma. The corrosion can lead to the formation of a very thin layer of oxide on the electrodes [116], in particular in the regions subject to heavy radiations, i.e. where the current collected on the electrodes is the highest. However, the oxide layer is invisible to the SEM, which indicates that the layer is as conductive as pure copper. It does not affect the surface structure of the electrodes and thus the operation of the detector. This is confirmed by the fact that no change in the detector's behavior was observed during the test. The energy resolution and the general performance of the chamber were also measured in laboratory after the aging test, showing no particular degradation.

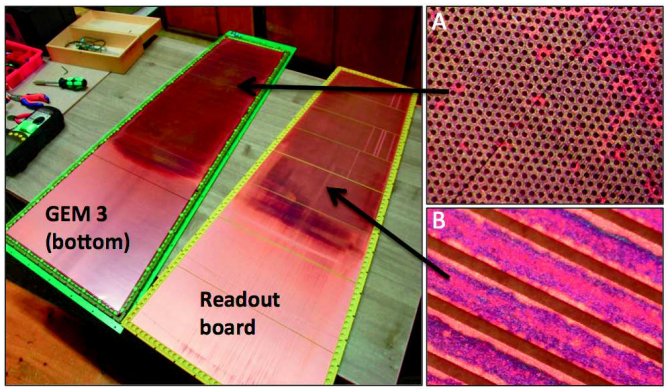

FIGURE 7.29: Left: overview of the inside of the GE1/1 detector used for the classical aging test at GIF. Magnifying view (50×) of the bottom of the last GEM and the readout strips are shown in A and B.

- The second effect that can be seen only with the SEM is the local deposition of polymers near the GEM hole rims. These deposits are very rare and concentrated near groups of few holes ($5-10$ per 100 cm^2 of GEM foil), which indicates that they are not caused by a global aging effect but by a local phenomenon, probably non-destructive discharges. Fig. 7.30 shows examples of discharge deposits observed on the bottom of the third GEM foil. In CMS, the detectors will accumulated about 250 discharges after 10 years of operation, as indicated in Sec. 6.3. Regarding the SEM observations, each discharge involves a group of $2-3$ holes. Therefore, the possible discharge-induced polymerization would affect a total of ~ 750 holes after 10 years of operation, a negligible fraction of the total number of holes estimated at 6×10^7 for the three GEM foils. Moreover, the deposits contains traces of silicon and sulfide as it was observed in the SWPCs during the initial again test (Sec. 7.3.3.1). This observation indicates that the polymerization is triggered by the presence of pollutants in the gas mixture, certainly released by outgassing materials in the GE1/1 detectors. The outgassing study, detailed in the next sections, will help to identify the source of contamination and minimize the discharge-induced polymerization during the operation in CMS.

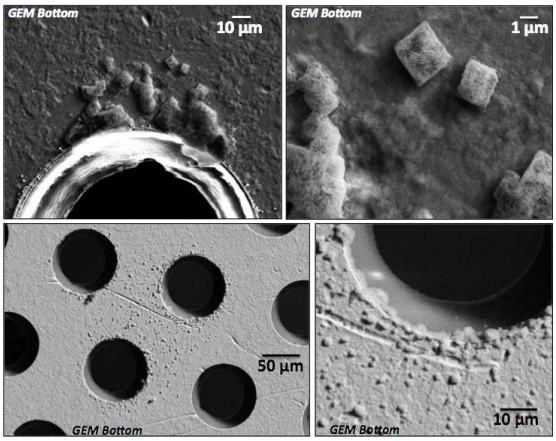

FIGURE 7.30: SEM view of holes affected by polymerization provoked by non-destructive discharges. The polymers contain traces of sulfide and silicon, already identified by wire chambers and caused by the outgassing of some GE1/1 materials.

- Finally, the third effect identified with the SEM is the deterioration of several tens of holes, mainly on the bottom side of the GEM foils (Fig. 7.31). Large carbon-based deposits, cracks of the polyimide and signs of burns are most probably related to the accidental discharges provoked by the GIF source when the detector was operating with the wrong gas mixture. This phenomenon is not associated to the normal long-term operation but results from the unusual operation well beyond the limits of the triple-GEM technology.

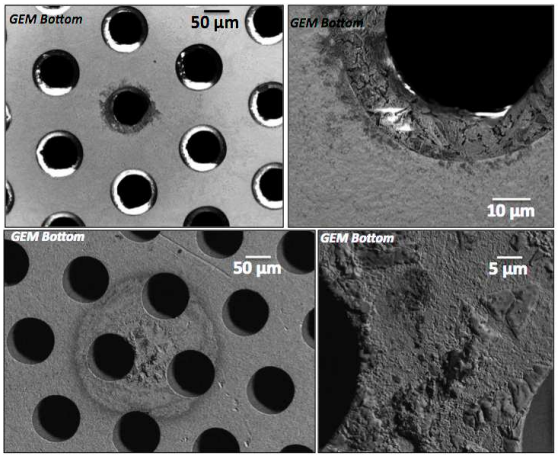

FIGURE 7.31: SEM picture of holes damaged by the accidental destructive discharges when the detector was operating with 93 % of argon instead of 70 %. The deposits near the holes moslty contain carbon-based molecules.

In spite of the several tens of holes affected by non-destructive or accidental discharges, the rest of the detector is perfectly clean both from electrical and geometrical points of view, as seen in Fig. 7.32. In particular, the diameters of the GEM holes in the irradiated regions are identical to the ones in the protected region of the first GEM foil, proving that the use of CF_4 in the gas mixture did not provoke the etching of

the holes. Moreover, optical inspections indicate the the stretching of the foils is still optimum even after 12 months of operation in an environment with large temperature fluctuations. The HV contact pins between the drift PCB and the GEM foils are also in perfect state, as well as the VITON O-rings and the protection resistances (Fig. 7.33.). Once again, all these observations are confirmed by the good operation of the detector before, during and after the aging test.

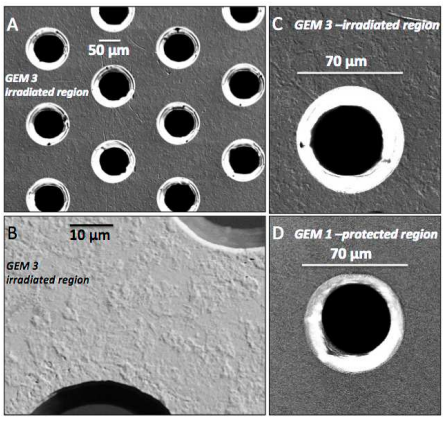

FIGURE 7.32: SEM view the 3^{rd} GEM foil in the region facing the gamma source (A and B) showing the normal geometry and the cleanliness of the GEM. Picture *C* and *D* show respectively a typical GEM hole of the 3^{rd} GEM facing the source and a hole of the first GEM in the protected area (considered as the reference). The comparison of the diameters and the shape of the holes indicate that the foils is not affected by HF etching.

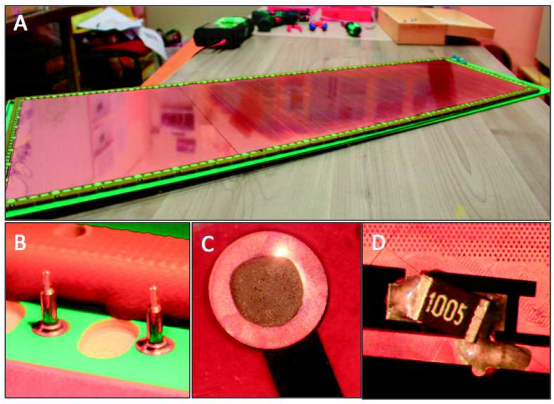

FIGURE 7.33: A: side view of the GE1/1 detector showing the stretching of the foils, which act as perfect mirrors. B and C: HV pins and HV contact point on the GEM foils. D: protection resistance placed on the top electrode of the GEM foils

As a conclusion, despite of the unusual polymer deposits that were triggered by the non-destructive discharges and the burns provoked by accidental discharges, no widespread classical aging was observed in the GE1/1 chamber after the long exposure to gamma rays. The chamber behaves normally, with detection performance identical to the initial ones. Similarly, the gain measurements and the SEM analysis show that the GEM holes are not etched by F-based compounds. Therefore, it is confirmed that the GE1/1

detectors can continuously operate in safe and stable conditions during 10 years with a safety factor 8.8 with the gas mixture $Ar/CO_2/CF_4$ (45 : 15 : 40) in the CMS end-cap muon system.

7.3.3.3 Aging in Ar/CO_2 (70 : 30)

Another aging study was performed at GIF++ with a GE1/1 detector of the 4^{th} generation operating in Ar/CO_2 (70 : 30). The chamber accumulated a total charge of 55 mC/cm^2 after 6 months of continuous irradiation, i.e. 10 years of real operation with a safety factor 9.1. The normalized and corrected gain as a function of the accumulated charge is shown on Fig. 7.34. The energy spectrum of the ^{137}Cs source was measured every two weeks and the corresponding energy resolution stays stable during the entire test.

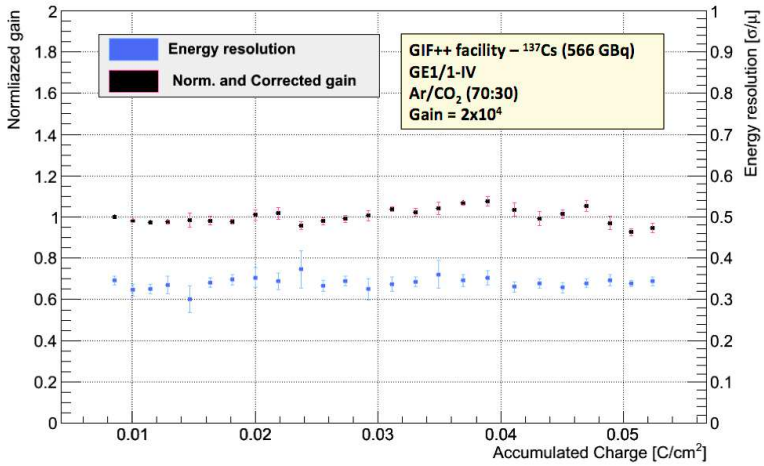

FIGURE 7.34: Normalized corrected gain and energy resolution of the GE1/1 detector operating in Ar/CO_2 (70 : 30) as a function of the accumulated charge. The entire test represents 10 years of real operation in CMS with a safety factor 9.1.

Once again, the aging study demonstrated that the operation of the GE1/1 the triple-GEM detectors in the CMS configuration is not affected by the classical aging. The GE1/1 chambers are then expected to survive a minimum of 10 years of real operation (safety factor 9.1) with Ar/CO_2 (70 : 30) in the CMS end-cap environment at HL-LHC. The GE1/1 chamber will continue the accelerated operation until it reaches a safety factor 10 compared to the real operation.

7.4 Outgassing study of the GE1/1 materials

7.4.1 Introduction

7.4.1.1 Effects on gaseous detectors

Past studies, discussed in the introduction of this chapter, revealed that a small concentration of contaminants could trigger and enhance the classical aging, even in gas mixtures that were initially validated in aging tests (e.g. Ar/CO_2 (70 : 30) and $Ar/CO_2/CF_4$ (45 : 15 : 40)). Extensive investigations helped to define sets of recommendations in order to ensure ultra-clean gas systems with, among others, the use of stainless steel tubing, the pre-cleaning and the de-greasing of the gas parts, valves and flow-meters, and the prohibition of polluting elements such as oil bubbler and greased O-rings ([117], [118]). However, the polluting species can come directly from the outgassing of the materials present in the detectors. The outgassing is defined as the spontaneous release of gas molecules initially trapped or absorbed in materials, mostly hydrocarbons, silicon-based molecules and halogen compounds. Then, these molecules can dissociate in the avalanche plasma and react to form polymers. The origin and the type of pollution is usually unknown. It strongly depends on the composition of the materials, the type of lubricants, oils and solvents possibly used during the fabrication process and also the conditions of transport and storage of the materials.

In addition to the studies performed by material scientists in order to measure the outgassing properties of materials [119], the detector physicists investigated the compatibility of some materials frequently used in detectors with various gas mixtures and detection technologies ([92], [15]).

7.4.1.2 Motivations for additional studies

The first indications of outgassing from the GE1/1 detectors were observed during the initial test at GIF with the presence of polymer deposits on the wires of the SWPCs. This observation triggered the need of performing independent outgassing tests with all the materials present in the GE1/1 chambers.

Even if the GE1/1 materials are chosen following the recommendations discussed earlier, a set of new critical materials were introduced in the gas volume of the detectors:

- The internal surface of the frames and the PCBs are covered with Polyurethane (PU) CellPack URETHAN Art. n°124017 in order to prevent the production of

dust by friction with the metallic screws. It also helps to impede the possible leakage current flowing between the GEMs through the surface of the internal frames.

- The coverlay film Krempel KDF 0/25/25 HT was also introduced with the 5^{th} generation of detectors to close the vias connecting the readout strips to the external readout connectors.
- Another critical material present in the GE1/1 detectors is the soldering mask Elpemer 2467 that covers part of the readout and drift PCBs.

In addition to the new materials, the composition and the production techniques of the known materials could have been modified without the explicit notification from the manufacturers. Because such unfortunate surprises were experienced by several experiments in the past, the CMS GEM Collaboration also proposed to cross-check the outgassing properties of: the VITON O-rings; the silver glue MSDS-Polytec-EC that make the contact between the HV circuit and the GEM foils; the polyamide washers used to seal the gas volume near the closing screws.

Fig. 7.35 show the various elements and the corresponding materials present in the last generation of GE1/1 prototypes.

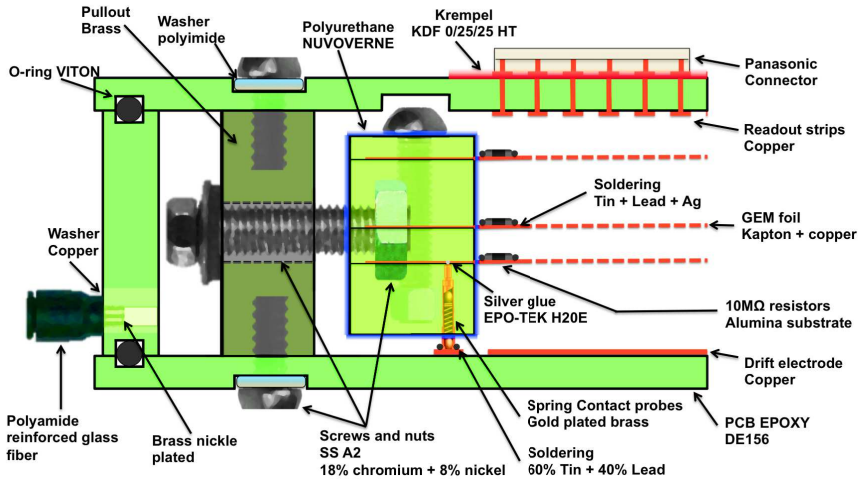

FIGURE 7.35: Schematic cross-section of the 5^{th} generation of GE1/1 prototype showing the different elements composing the detector and the corresponding materials.

The outgassing study aims to understand the compatibility of these materials with the GEM technology operating with CMS gas mixtures and reject the materials that could contaminate the detectors. Moreover, it will help to validate the preparation and the cleaning procedures of each material.

7.4.2 Description of the outgassing experiments

7.4.2.1 Overview of the setup

The GE1/1 materials are tested separately in the CMS gas mixture $Ar/CO_2/CF_4$ (45 : 15 : 40). The first outgassing setup was assembled at GIF, as a preliminary study in addition to the classical aging test. After several successful tests, a second setup was build at the CMS GEM R&D laboratory with four parallel and independent testing channels. Each channel consists of a stainless steel cylinder, called Outgassing Box (OB), containing the material under test. The OB is wrapped with resistive tape that can reach temperatures up to 150 °C, both for heating the sample and for the cleaning the OB after a possible contamination. The clean gas mixture from a pre-mixed cylinder flows through the OB at 2 L/h. Then, the gas with the possible pollutants from the material is sent to a SWPC that can measure the effects of the polymerization. Fig. 7.36 shows an overview of the gas system.

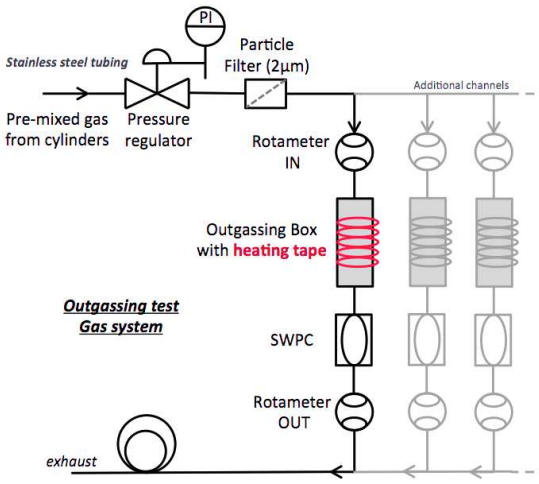

FIGURE 7.36: Overview of the gas system for the outgassing study. Additional testing channels were added after the successful preliminary tests.

The DAQ system is similar to the one used during the classical aging tests (presented in Sec. 7.3.1.5). The signals collected on the microscopic wire are sent to NIM logic modules to generate the trigger signals. The triggers are sent to a VME-controlled QDC in order to record the charge induced by the X-ray source. A SIEMENS S7 PLC connected to temperature and pressure sensors takes care of the monitoring of the environmental fluctuations. Pictures of the preliminary outgassing setup and the complete setup at the CMS GEM R&D laboratory are shown on Fig. 7.37.

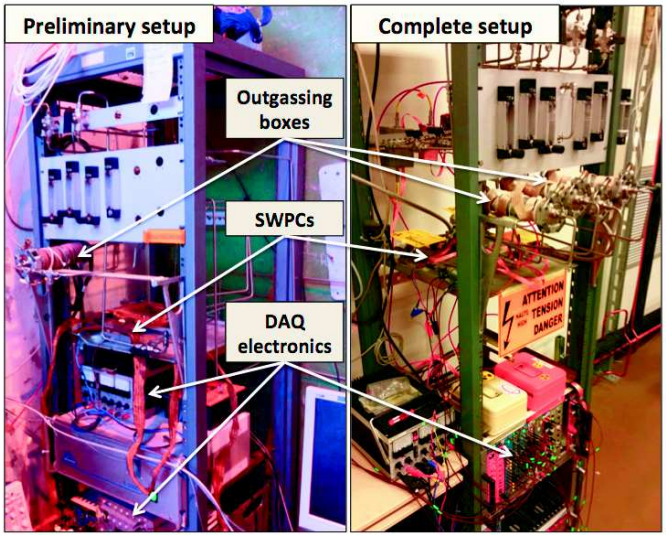

FIGURE 7.37: Left: preliminary outgassing setup at the GIF facility. Right: complete setup with the four parallel outgassing boxes and SWPCs.

7.4.2.2 Testing procedure

The outgassing test procedure and the operating conditions were chosen to be identical to the initial aging test at GIF, for which the monitoring SWPCs revealed the contamination.

The cleanliness of the gas system is systematically checked before inserting a new set of materials thanks to a wire chamber operating during one month under sustained X-ray radiations. After the samples are placed in the outgassing boxes, the SWPCs operate continuously during two weeks at room temperature. Then, the samples are heated to 50 °C during two more weeks in order to enhance the possible outgassing. During the entire test, the charge spectra induced by the radioactive sources in the wire chambers are recorded every 10 minutes.

The complete test, including the purity check, lasts two months for each set of materials. In case classical aging is observed in the wire chambers, the gas tubing is cleaned during several days by being heated up to 150 °C and flushed with high flow of pure argon (typically 50 L/h). The contaminated chambers and the outgassing boxes are removed from the setup and sent to a specialized laboratory for a surface treatment and advanced cleaning procedures. The aged wires are sent to a chemistry laboratory for further SEM analysis.

7.4.2.3 Data analysis

The data analysis is similar to the one described in Sec. 7.3.2.1. It consists of following the evolution of the photo-peaks of the energy distributions collected by the SWPC. Fig. 7.38 shows the typical energy spectra of ^{55}Fe and ^{109}Cd in $Ar/CO_2/CF_4$ (45 : 15 : 40) obtained during the outgassing tests.

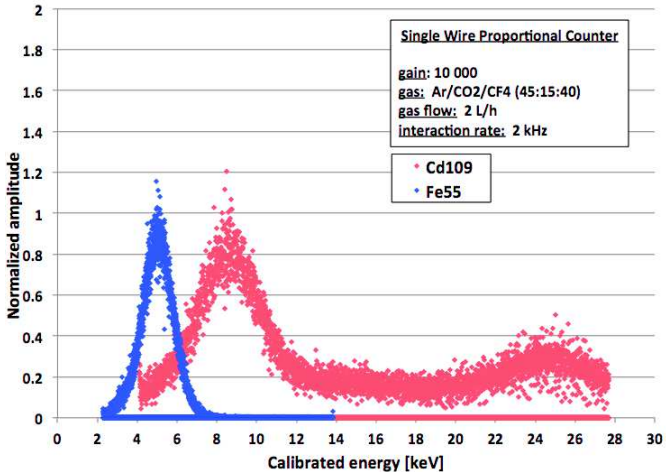

FIGURE 7.38: Typical energy spectra of ^{55}Fe and ^{109}Cd collected in $Ar/CO_2/CF_4$ (45 : 15 : 40) with by a SWPC.

Each spectrum is processed by a fitting algorithm to determine the mean and the width of the photo-peaks that represent to the gain and the energy resolution of the chambers. Finally, the data are correlated with the environment to remove the fluctuations due to the temperature and the pressure variations.

In case of material outgassing, the presence of pollution in the gas mixture will trigger polymerization on the wires that will degrade the energy resolution and/or provoke gain losses.

7.4.3 Tests and results

Seven GE1/1 materials were prepared and tested in the outgassing setup: VITON O-rings; Polyamide washers; PU CellPack URETHAN Art. n°124017; PU NUVOVERN LW; film Krempel KDF 0/25/25 HT; soldering mask Elpemer 2467; silver glue MSDS-Polytec-EC. Additionally, Kapton and Teflon tapes, often used in R&D prototypes, were tested in identical conditions.

The surface of the samples in contact with the gas is approximately 10 times bigger than the real surface in the GE1/1 chambers. All the materials are cleaned beforehand in ultrasonic baths with DI water, following the procedure foreseen for the final detectors. A

particular attention is given to the VITON O-rings that can easily absorb contaminants during the fabrication process and release it later in the detectors. The VITON materials are baked during two hours at 200 °C in vacuum (10^{-2} mbar) before being used in the GE1/1 detectors.

The polyurethane (PU) CellPack Art. n°124017 was the only material that induced a gain drop of 20 % in the wire chamber when heated to 50 °C. This effect was accompanied with a clear degradation of the energy resolution from 18 % to 24 % (Fig. 7.39 - middle). These results were compared to the purity check performed with the same wire chamber before the insertion of the PU (Fig. 7.39 - top).

The SEM analysis of the aged wire revealed the presence of large polymer structures along the portion of wire irradiated by the source. The deposits mainly consists of carbon, oxygen and silicon. SEM pictures of the aged wire can be seen in Fig. 7.40. Similar deposits were observed in the GE1/1 detectors used for the classical aging test in $Ar/CO_2/CF_4$ (45 : 15 : 40) at GIF (Sec. 7.3.3.2). Therefore the PU CellPack, widely present in this particular detector, could have released pollution in the mixture that triggered polymerization during non-destructive discharges.

As a conclusion, the PU CellPack was considered as polluting material and was therefore excluded from the final GE1/1 detectors.

The PU NUVOVERN LW, already used in other applications, was proposed to replace the PU CellPack. The corresponding outgassing test, done in identical conditions, did not indicate any aging effects or degradation of the SWPC performance, even at 50 °C. The gain evolution and the energy resolution of both polyurethanes are shown in Fig. 7.39-bottom.

Except for the PU CellPack, the other materials did not affect the operation of the wire chambers. They were therefore validated for the GE1/1 production. The evolution of the normalized gain and the energy resolution of all the tested materials can be seen in Appendix A. The final results of the outgassing test campaign are summarized in Tab. 7.2.

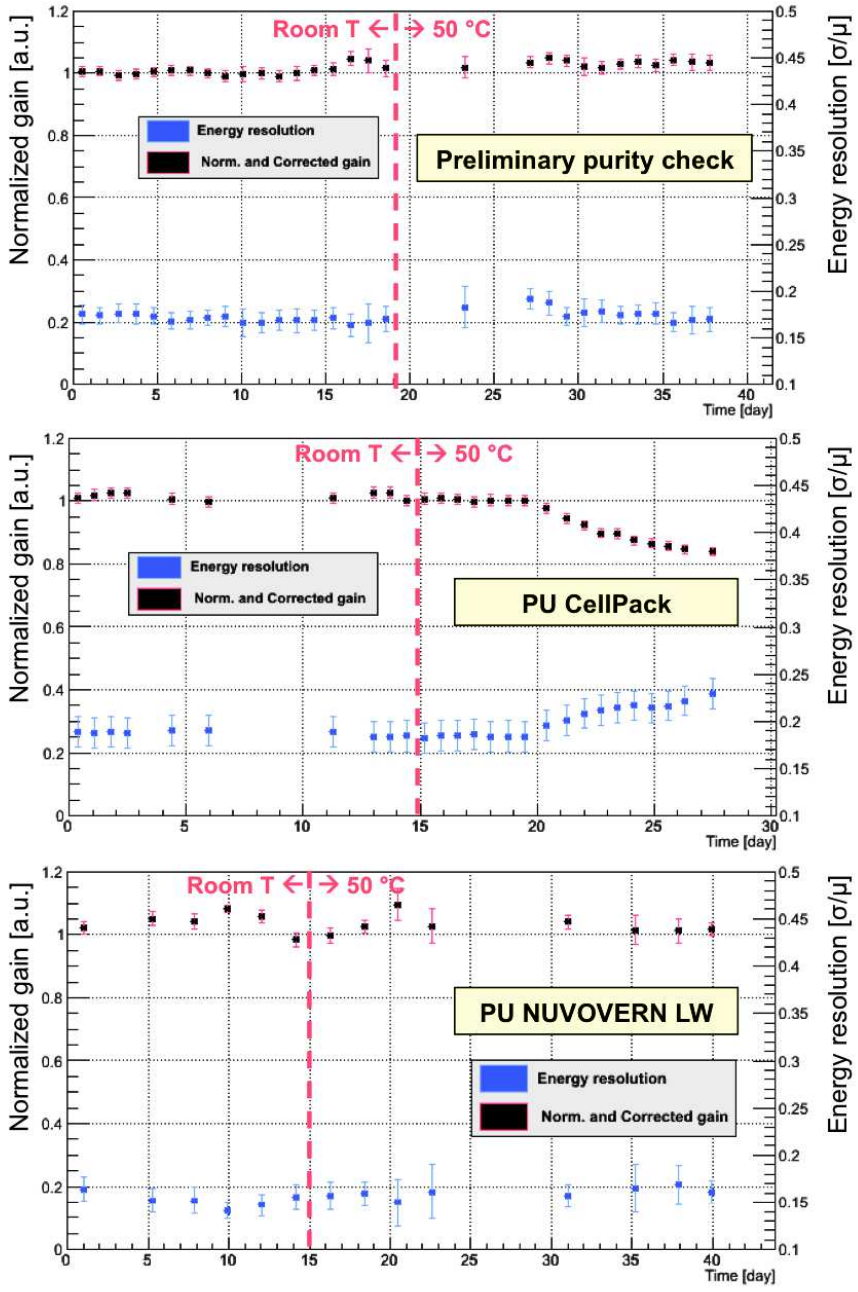

FIGURE 7.39: Gain stability of the wire chambers operating in $Ar/CO_2/CF_4$ (45 : 15 : 40) at 2 L/h. The gas mixture was in contact with the PU CellPack Art. n°124017 (middle) and the PU NUVOVERN LW (bottom). The outgassing results are compared to the preliminary purity check performed before the materials were inserted in the outgassing boxes (top).

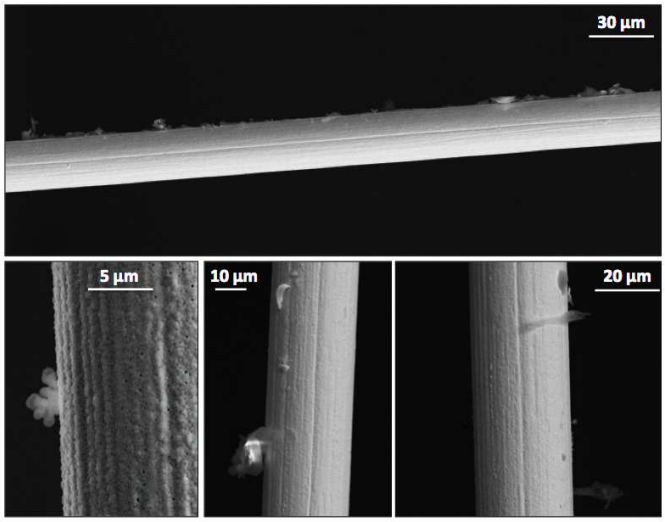

FIGURE 7.40: SEM pictures of the aged wire from the SWPC operating with PU CellPack. The polymer deposits mainly contain atoms of carbon, oxygen and silicon.

GE1/1 element	Material	Aging	Comments
O-rings	VITON	No	Baked 2 hours in vacuum
PU layer	CellPack n°124017	Yes	20 % gain drop - silicon deposits
PU layer	NUVOVERN LW	No	-
Soldering mask	Elpemer 2467	No	-
Sealing film	Krempel KDF HT	No	-
Silver glue	MSDS-Polytec-EC	No	-
Washer	Polyamide	No	-
Tape	Kapton	No	Energy resolution increased by 4 %
Gas tape	Teflon	No	-

TABLE 7.2: Summary of the outgassing test results.

7.4.4 A new design of SWPC

7.4.4.1 Motivations

After the first identification of the contamination in the GIF gas system and the successful outgassing campaign with GE1/1 materials, it was clear that SWPCs are very convenient and suitable tools for gas purity measurements, identification of pollution or monitoring of the gas composition. The RD10 prototypes demonstrated their a great flexibility in term of operating conditions and easy maintenance. Nevertheless, the duplication of such chambers is a source of concerns for several reasons:

- The price of a new chamber is estimated to 2000 EUR, mostly because of the use of elements like the glass holding support of the wire and the special pins

to maintain the wire tension. Moreover, the machining of the stainless steel box requires a specific equipment and expertise.

- The fragility of the thin stainless steel window and the glass support make the handling of the detector very challenging. It is all the more problematic since the replacement of the wire requires the dismounting of the entire structure.
- These prototypes contain suspicious materials like the epoxy glue that fixes the stainless steel window to the box and also used on the wire pin to ensure the gas tightness. Moreover, the wire needs to be soldered to the pins with no possibilities of cleaning afterwards.

For these reasons, the CMS GEM collaboration proposed a new design of a clean wire chamber that can be produced at low price in order to equip many gas systems in the production laboratories, in CMS, and also for additional outgassing test stands.

7.4.4.2 Description of the detector

The wire chamber design is based on a simple cylindrical structure made of stainless steel. Most of the parts come from gas systems and vacuum applications, which are easily procurable at CERN and relatively cheap. The total price for one chamber does not exceed 250 EUR. The novel concept is the wire holding structure that can be easily extracted from the cylinder for maintenance and cleaning: the input cap of the cylinder, including the HV connector and the gas inlet, is attached to an L-shape stainless steel bar on which the wire is fixed; the first wire holding piece, made of brass, is welded to the HV input, while the second element is inserted in the opposite side of the L-shape bar and insulated from the ground thanks to a ceramic cylinder (see Fig. 7.41); the wire is then embedded between the brass elements and a small plate of pure copper maintained with metallic screws.

After the wire is in place with the appropriate tension, the entire structure is inserted into the stainless steel cylinder and sealed with a metallic O-ring, as shown in Fig. 7.42. To make sure the low energy X-rays can penetrate the gas volume, a narrow rectangular slit was drilled in the cylinder. The radioactive source can be moved along the slit to scan the wire and identify possible local depositions. The gas tightness is ensured by a 50 μm thick copper-beryllium window sandwiched between two stainless steel plate, one being welded to the cylinder.

All the elements present in the chamber are fully metallic and arranged thanks to mechanical fixation or welding. The wire chamber is therefore free of any kind of polluting

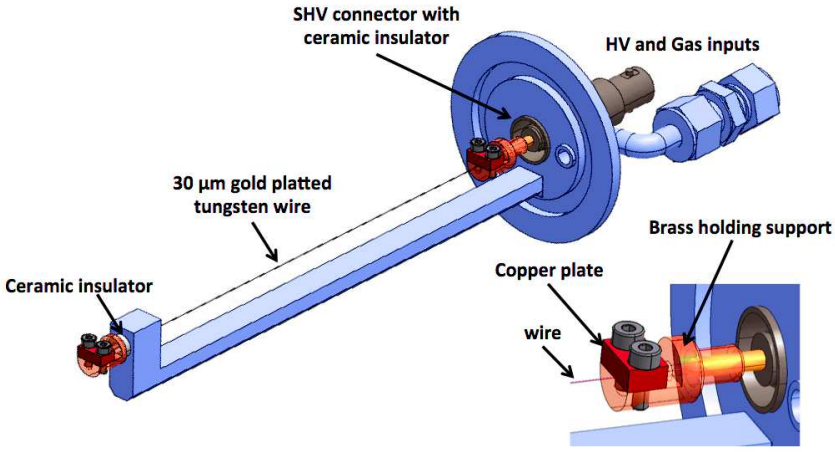

FIGURE 7.41: Technical design of the wire holding structure. The wire is mechanically fixed between brass pieces and copper plates. The two brass elements are insulated from the stainless steel structure thanks to ceramic cylinders.

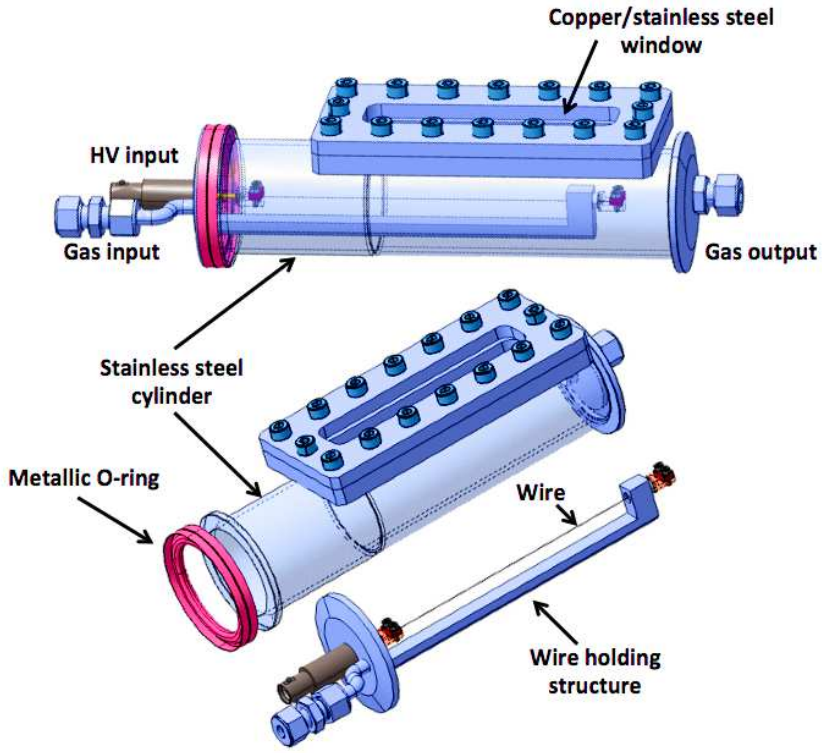

FIGURE 7.42: Technical design of the CMS GEM wire chamber showing the outer cylinder and the independent wire holding structure.

material such as glue, soldering material, rubber or polyamide O-rings. The detectors are easily cleaned with ethanol in ultra-sonic bath and can be heated to high temperatures in vacuum to remove all possible contaminants. After the wire holding structure is moved outside the cylinder, the replacement of the wire takes not more than 1 minute.

7.4.4.3 Calibration tests and further developments

The first prototype of wire chamber was assembled at CERN with the help of technicians from the Italian National Institute for Nuclear Physics (INFN). The very first calibration test consists of measuring the effective gain as a function of supply voltage. As for the GEM detectors, the gain is calculated from the interaction rate and the current induced by the particles and amplified. However, since the wire is set to high voltage, the reading of the current requires a specific floating pico-ammeter inserted in the HV line. The interaction rate is measured by counting the number of pulses induced on the wire and sent to a pre-amplifier and shaper unit through a de-coupling capacitance. The readout schemes and a picture of the experimental setup are shown in Fig. 7.43 and Fig. 7.44.

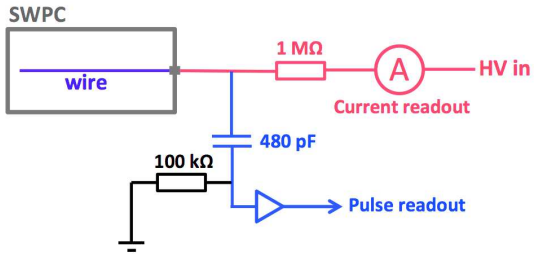

FIGURE 7.43: Readout scheme of the gain calibration of the CMS GEM wire chamber.

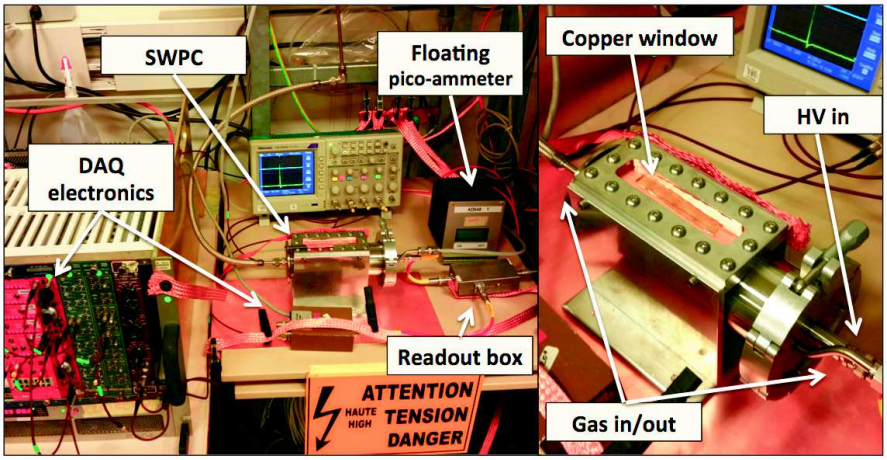

FIGURE 7.44: Typical setup for the gain calibration of the CMS GEM wire chamber.

The detector was flushed with a mixture of Ar/CO_2 (70 : 30) and irradiated with a ^{55}Fe source of 30 MBq. As shown on Fig. 7.45, the chamber reached a maximum gain of 4×10^4 at 2200 V before the apparition of a leakage current between the wire holding structure and the outer cylinder.

After a successful first operation, the chamber will be calibrated with $Ar/CO_2/CF_4$ (45 : 15 : 40) and different radioactive sources. The irradiation window will be also replaced

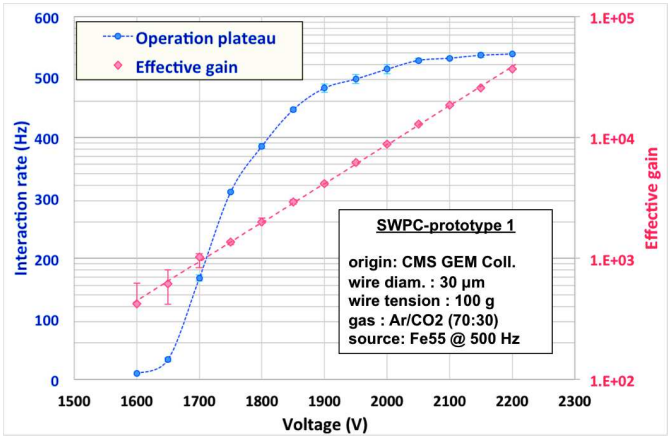

FIGURE 7.45: Operation plateau (blue) and gain curve (red) of the first prototype of CMS GEM wire chamber irradiated with ^{55}Fe in Ar/CO_2 (70 : 30).

by a 20 μm thick stainless steel window in order to minimize the photon attenuation. Finally, the detector will be placed in the outgassing stand to operate continuously during several months. After the final validation, several detectors will be assembled and installed in the gas systems of the production sites to monitor the purity and the composition of the gas mixtures.

7.5 Conclusions

The aging studies conducted at GIF and GIF++ revealed that the GE1/1 detectors can operate at least 10 years in CMS, with a safety factor 8.8 in $Ar/CO_2/CF_4$ (45 : 15 : 40) and 9.1 in Ar/CO_2 (70 : 30). The performance of the detectors under test did not change during the entire test period.

Nevertheless, polymerization effects were observed in the detector after 12 months of continuous operation in an intense gamma flux. The polymers only affected few holes over the entire chamber, most probably due to non-destructive discharges and triggered by the presence of pollution in the gas mixture.

The extensive outgassing study indicated that the PU CellPack URETHAN Art. n°124017 present in this generation of GE1/1 detectors could be responsible for this pollution. It was finally replaced by the PU NUVOVERN, validated during the outgassing test campaign.

Tab. 6.1 gives a summary of the long-term requirements of CMS and the performance of the GE1/1 detectors.

At the end of the long-term study, a specific design of single wire proportional chambers was proposed by the CMS GEM collaboration in order to monitor continuously the

Property	**CMS requirements**	**GE1/1 performance**
Longevity	60 mC/cm^2	53 mC/cm^2 in $Ar/CO_2/CF_4$ (45 : 15 : 40) 55 mC/cm^2 in Ar/CO_2 (70 : 30) (ongoing)

TABLE 7.3: Comparison of the CMS minimum requirements and the GE1/1 long-term performance.

purity and the composition of the gas mixtures at the GE1/1 production sites and possibly for the CMS gas system. The first prototype was assembled and calibrated at the end of 2015.

Chapter 8

Assembly, Quality Control and Commissioning of the GE1/1 detectors

8.1 Introduction

Regarding the excellent performance and the longevity of the triple-GEM technology, the GE1/1 project was approved in 2015 for the CMS muon upgrade during the Long Shutdown 2 (LS2) in 2018. The CMS collaboration approved at the same time the preliminary installation of eight GE1/1 detectors in the YE1/1 region of the negative end-cap, called "slice test", in order to demonstrate the integration of the GE1/1 technology into the current muon system. For the GE1/1 project, 144 single chambers will be assembled and tested at several production sites before being shipped to CERN for a last verification. To ensure the best quality and the good performance of each detector, a precise Quality Control (QC) was established for the production sites and the CMS GEM facility at CERN.

In this chapter we will describe the main production and QC steps: the qualification of the GEM foils; the assembly of the large detectors; the gas leak test. Then we will focus on the gain uniformity test that was developed especially for the GE1/1 application.

8.1.1 Schedule

As shown in Tab. 8.1, the production of the 144 chambers will start in May 2016 at the production sites. The installation is planned to be ready in March 2018 after all the

super-chambers are validated at CERN.

Production step	Date
Technical Design Report	01/2015
Components reception at production sites	06/2016
DAQ production complete	12/2016
Chamber reception at CERN	05/2017
Electronics complete	12/2017
One end-cap complete	01/2018
Second end-cap complete	03/2018
One end-cap installation	04/2018
Second end-cap installation	05/2018

TABLE 8.1: Milestones of the GE1/1 production and schedule.

Therefore, all the large detectors must be produced and tested within two years. The production plan should be designed in such a way that the production, the assembly and the QC can be conducted in parallel in the various production sites. Moreover, the QC tests must be optimized to ensure the fast and the efficient characterization of the chambers.

8.1.2 Overview of the quality control

Fig. 8.1 shows the details of the QC procedure for the GE1/1 project. All the components are first prepared for the assembly of the single detectors. Then, after the validation of the detection characteristics, two single chambers are assembled together to form a super chamber. The super-chambers are finally equipped with the final electronics and tested with MIPs before being stored and installed in CMS.

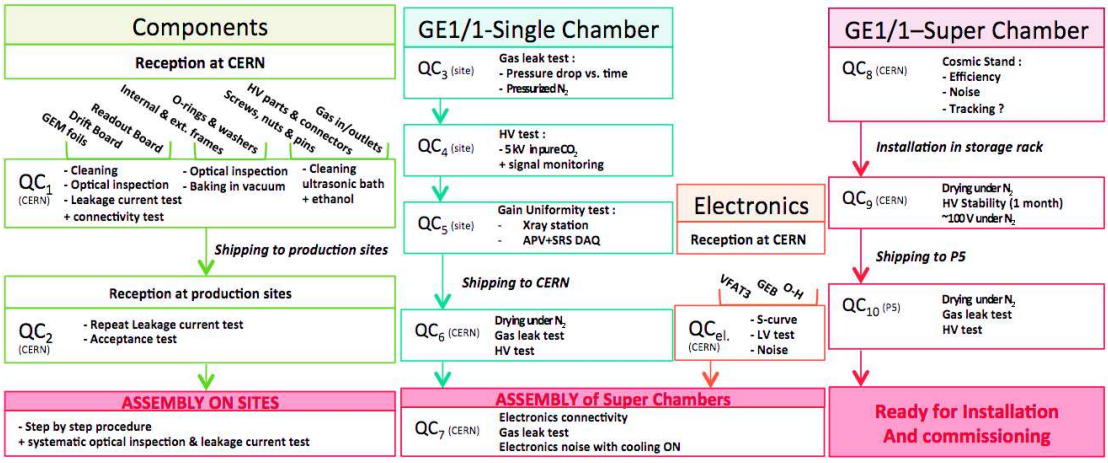

FIGURE 8.1: Process of Quality Control of GE1/1 chamber and super modules.

All the operations and the manipulations of the detectors are done in a well defined environment, following precise procedures to prevent any type of contamination and

mismeasurements of the detector's performance. In other words, the assembly room, the gas system layout and the equipment of all the production sites must be identical. The QC procedures, initially established at CERN during the *R&D* phase, was shared with all the production sites in order to make sure that the QC results are obtained in the same conditions, regardless the origin of the chambers.

8.2 Leakage current test

All the elements forming the GE1/1 chambers are immediately verified after the reception at the production sites. An optical inspection is first performed to ensure the integrity and the quality of the frames, O-rings, connectors and the flatness of the drift and readout PCBs. All the parts are then cleaned with DI water in ultrasonic baths. Specific cleaning procedures, like the baking of the VITON O-rings in vacuum are based on the recommendations from the outgassing study.

However, it is not possible to verify the quality of the GEM foils with a simple optical inspection because of the microscopic scale of the GEM structure and the large dimensions of the foils. A specific electrical test was designed for this purpose.

8.2.1 Principle

When applying a voltage across the GEM electrodes, we can observe a leakage current that is mostly driven by the surface conductivity of the polyimide. This conductivity strongly depends on the quality of the foil but also on its cleanliness. The presence of dust, contamination or defects will act as an electrical bridge between the electrodes and provoke an increase the current flowing through the foil (see Fig. 8.2). By measuring this current we can therefore determine the quality of the GEMs.

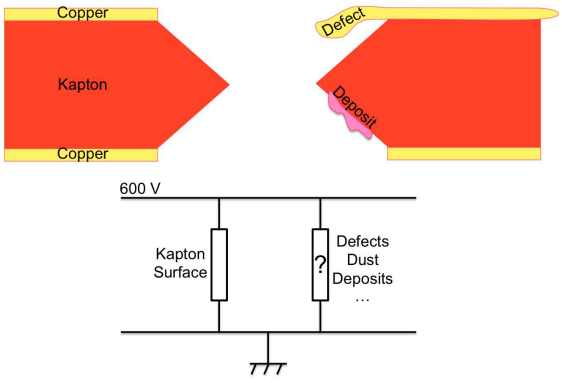

FIGURE 8.2: Schematic cross section of a GEM foil and its equivalent resistive circuit.

The value of the voltage applied on the GEM should be higher than the real operation voltage with a large safety factor. However, it should not exceed the breakdown voltage V_b of the medium under the penalty of triggering strong discharges in the gas. The breakdown voltage is the empirical value necessary to start a discharge in a gas between two electrodes. It depends on the gas composition, the gas pressure and the distance between the electrodes. It is given by Paschen's law:

$$V_b = \frac{B.pd}{C + ln(pd)} \quad , \quad C = ln\left(\frac{A}{1 + 1/\gamma}\right) \tag{8.1}$$

where A and B are experimental constants related to the gas, γ the second Townsend coefficient, "p" the gas pressure and "d" the distance between the electrodes. Then, we can calculate the product "pd" corresponding to the GEM setup:

$$7,5.10^2(1\ atmosphere\ [Torr]) \times 5.10^{-3}(Polyimide\ thickness\ [cm]) = 3,8\ [pd] \tag{8.2}$$

Finally we can obtain the breakdown voltage in Nitrogen given by Paschen's curves (Fig. 8.3 [120]). The acceptable limit for the leakage current, determined by the experiment, corresponds to 1 nA per 100 cm^2 of GEM foil when applying 600 V in pure nitrogen.

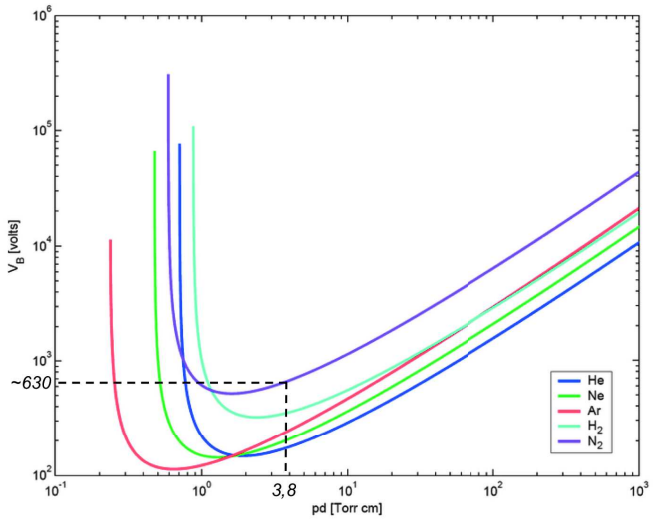

FIGURE 8.3: The Paschen's curves for different media.

In order to control the environment (i.e. the polyimide surface conductivity and the breakdown voltage), the GEM foils are placed in a sealed box filled with pure nitrogen. Additionally, a Meteo-station is placed near the foils to monitor the temperature and the relative humidity of the medium. This information is crucial to properly understand the

leakage current fluctuations and compare the results from GEM foils tested at different periods and different locations. A specific epoxy support is necessary to prevent the GEM electrodes from touching the box and to ensure a safe handling. The GEMs are then connected to the power supply, remotely controlled by a LabView interface. A schematic view of the typical leakage current test setup is shown on Fig. 8.4. At this point it is also possible to measure the capacitance of the foils to check the connectivity. Moreover, the capacitance is a good indicator of the quality of GEM and should be close to 5.6 nF for a good 100 cm^2 GEM foil.

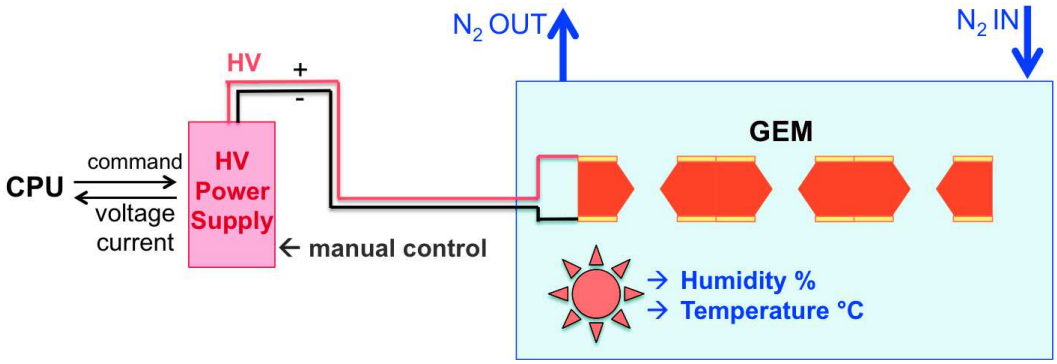

FIGURE 8.4: Typical test setup for the leakage current measurement.

8.2.2 Tests and results

The leakage current test consists of two main steps, the fast test and stability test:

- The fast test consists of directly applying 600 V to the foils with a total ramping time of couple of seconds. Doing so, the possible dust trapped in the holes is burnt and blown away by non-destructive discharges. On the contrary, applying the same voltage with a long ramping time or applying a lower voltage could fix the particles of dust to the holes and lead to a permanent contamination. This technique is also performed during the assembly of the GE1/1 detector in order to quickly eliminate the dust resulting from the manipulation of the GEMs.

- After the fast test comes the stability test: the voltage across the foils is slowly set to 600 V, by steps of 100 V. After a long stabilization time at the maximum voltage (typically $1-2$ hours), the voltage is set to 100 V for several minutes, then back to 600 V and so on. The difference of current delivered by the power supply between these voltage cycles corresponds to the real leakage current of the foil.

Fig. 8.5 shows the typical leakage current test results of an accepted and a rejected GEM foil. In addition to the discharges observed with the rejected foil, the leakage current after stabilization is higher than 5 nA, $far above the acceptable limit of 1 nA$.

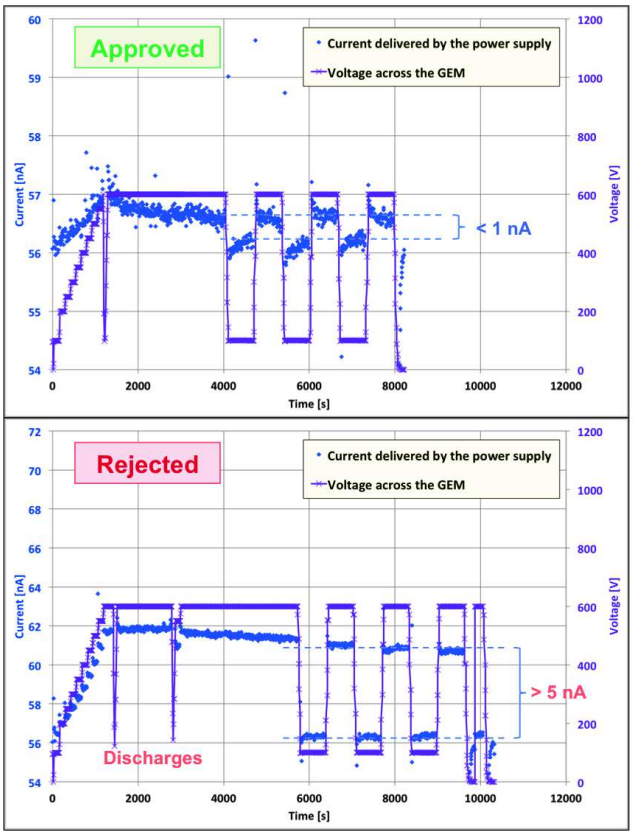

FIGURE 8.5: Typical leakage current of a approved (top) and rejected (bottom) GEM foil.

8.3 Assembly of the GE1/1 detectors

After all the components are accepted and cleaned, the chambers can be assembled in a clean room. Thanks to the new mechanical stretching developed for the CMS GEM application (see Sec. 5.3.3), the assembly of a GE1/1 chamber requires not more than $2-3$ hours of work by two trained operators. The major steps of the assembly of a GE1/1 detector of the last generation (i.e. the final design for CMS) are shown in Appendix B. The details of each step are mentioned in the caption of the pictures Fig. B.1 to Fig. B.17. Additional details and technical aspects on the production of the GE1/1 detectors can be found at [10].

8.4 Gas leak test

The first quality control after the closure of the detector consists of verifying the gas tightness. The drift and readout PCBs are closed with several hundred of screws, which can be possible openings to the external environment. Gas leaks are not only a waste of gas but also a source of pollution, bringing water and unknown species from the environment that can strongly affect the properties of the gas mixture and react in the avalanche plasma. Several techniques for measuring the gas leaks were investigated for the GE1/1 project:

- The first solution consists of comparing the input and output gas flow rates. It can be measured with mechanical devices such as glass tube flow-meters, or with digital flow meters and mass flow controllers, which have a better resolution and automatic backup (see Fig. 8.6). Any gas mixture can be used for this test as long as it is clean and compatible with the measurement devices. The time of flushing depends on the input flow rate and should correspond to at least 10 volume exchanges in the detector. A calibration line excluding the detector is essential to identify leaks in the gas system.

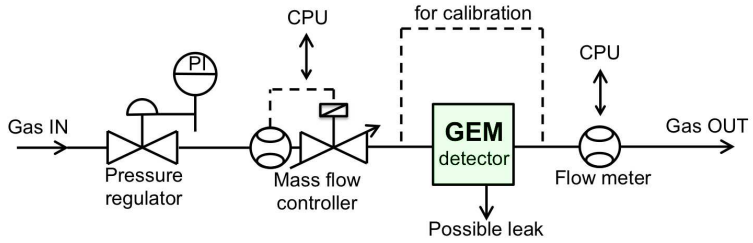

FIGURE 8.6: Schematic view of the gas circuit for the gas flow rate measurement.

- A more accurate technique consists of monitoring the pressure drop in the chamber as a function of the time (Fig. 8.7). The idea is to first pressurize the detector under the safe limit of 50 mbar and then close the gas volume with input and output valves. In case of gas leaks, the overpressure in this volume drops down to zero with a time scale that depends on the leak rate and on the initial overpressure. Knowing the initial pressure P_0, the initial volume V_0 and the pressure drop $\Delta P(t)$, we can calculate the gas leak rate $\Delta V(t)$ with the Boyle-Mariotte law:

$$\frac{\Delta P(t)}{P_0} = \frac{\Delta V(t)}{V_0} \tag{8.3}$$

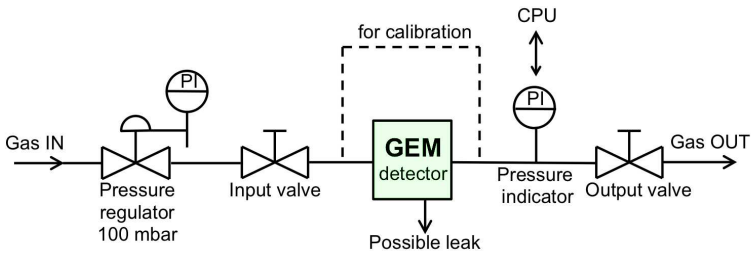

FIGURE 8.7: Typical setup for the pressure drop measurement with pressure indicator.

- A "low cost" version of the pressure drop setup involves a simple U-shape tube. As shown in Fig. 8.8, the U-tube is filled with water and connected to the detector through a safety container to prevent water overflow. When the output valve is open, both water levels are equal to h_0. When the valve is closed, raising the left tip of the U-tube creates a difference of water levels that corresponds to an overpressure in the detector. In case of a gas leak, the water levels will go back to the equilibrium level h_0. The linear dependency between the difference of levels Δh and the overpressure P is given by:

$$\Delta h = 10\ m \iff P = 1\ bar \tag{8.4}$$

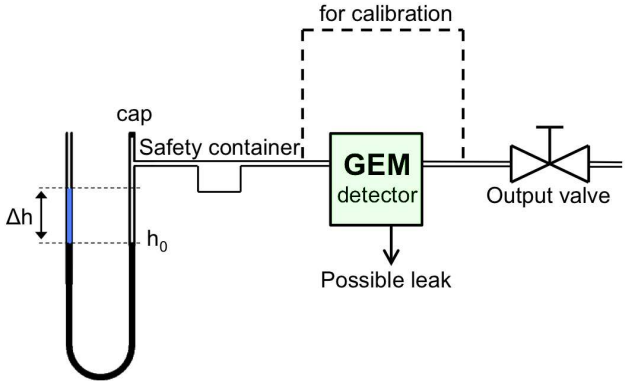

FIGURE 8.8: Typical setup for the pressure drop measurement using the U-tube.

Finally, the option chosen for the GE1/1 production is a combination of the two first techniques. The internal overpressure, the atmospheric pressure and the temperature are measured thanks to a set of sensors controlled by an ARDUINO board. Additional flow meters are used to quickly identify large leaks.

After the chambers are validated, the HV components that form the HV divider and the filters are mounted on the drift PCB and tested. At this point the chambers are ready to start their first operation.

8.5 Gain uniformity test

The gas gain is the central parameter of a triple-GEM detector, referring to the gas composition, the hole geometry, the electric fields inside and between the amplification layers and the quality of the readout board. The uniformity of the gain can be affected by various elements: non-uniformity of the GEM geometry, local contamination, poor stretching or defects on the readout plane. All the characteristics (e.g. discharge probability, charging up) and the detection performance (e.g. efficiency, time and spatial resolutions) are functions of the gain. Therefore, gain variations over the surface of a large chamber is a serious concern and the measurement of the gain uniformity of every GE1/1 detectors is a crucial step of the QC.

However, it is important to mention that the goal of this QC step is not to identify the causes of the gain variations, but only to provide sufficient information to accept or reject the chambers before the next QC step. The full understanding of possible gain variations is only possible with more specific tests (e.g. precise measurement of the detector parallelism, uniformity of the GEM holes, leakage current between the GEMs etc...).

8.5.1 Motivations and principle

8.5.1.1 The sector-by-sector technique and its limitations

Initially, the gain was measured sector-by-sector, one after the other, while the X-ray source was moved along the chamber. For each sector, all the 128 readout strips were connected together to a single output and to the readout chain. As described in Sec. 6.2.2, the measurement consists of comparing the input particle rate to the output amplified current. However, three main limitations were then identified with this method:

- The measurement requires several hours for one readout sector and up to several days to scan the 24 sectors of a full chamber. In ideal conditions, only $4-5$ detectors can be tested per month, which is not compatible with the production schedule.
- Because of the long duration of each test, the environmental temperature and pressure can fluctuate and induce gain variations between the readout sectors. Moreover, the readout chain and the grounding must be moved manually between the sectors, resulting in possible changes of the experimental conditions during the test. At the end, the sector-by-sector technique can induce additional non-uniformity that is not representative of the quality of the detectors.

- Since all the 128 strips of each sectors are connected together, there are only 24 measurement points for a full chamber, while the total number of strips in the detector is equal to 3072. This drastic loss of granularity could be improved by reading out smaller groups of strips but it would increase significantly the duration of the test.

Fig. 8.9 shows typical results obtained with the sector-by-sector method for the two first prototypes of the 4^{th} generation. The effective gain of the second detector (bottom) increases gradually toward the lowest η-sectors (i.e. the largest base of the trapezoid) with maximum values up to 25 % higher than the average gain. This phenomenon was easily explained by geometrical deformation of the drift and the readout planes caused by the over stretching of the foils. On the other hand, the first prototype (top) shows random-like variations that can't be explicitly referred to a geometrical effect or to fluctuations of the experimental conditions.

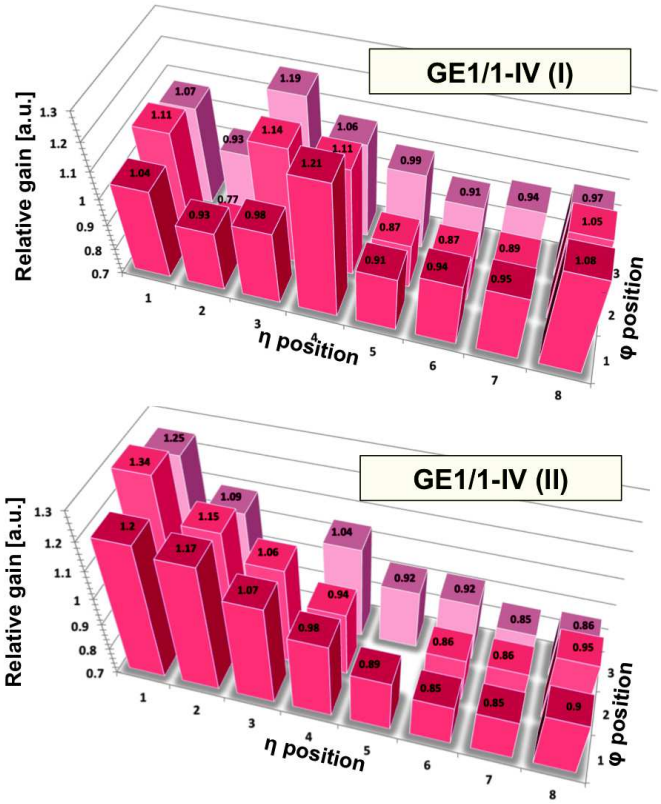

FIGURE 8.9: Typical results of the gain uniformity test with the first (top) and the second (bottom) prototypes of the 4^{th} generation of GE1/1 chambers.

8.5.1.2 A new technique for the gain uniformity test

A new solution was developed to overcome the limitations of the sector-by-sector technique. The method consists of measuring simultaneously the 3072 readout strips of a detector fully irradiated by a large X-ray beam. Therefore, all the readout channels are affected in the same way by the environmental fluctuations without disturbing the measurement of the gain uniformity. Moreover, there is no need to manipulate the setup during the test since all the connections are prepared before the data acquisition. Finally, measuring the gain with the full granularity allows selecting interesting regions of the detector and adjust the fineness of the analysis.

The first attempt was successfully conducted in 2012 with a GE1/1 detector of the 3^{rd} generation. After the optimization of the procedure and the installation of a new X-ray station dedicated to this QC step, several detectors of the $4th$ and the 6^{th} generations were tested. The next sections will describe the final setup, the analysis procedure and the results.

8.5.2 Description of the experiment

The detector under test is placed in front of a AMPTEK miniX X-ray source with a silver target emitting 23 keV photons. Since the aperture of the X-ray gun is of the order of 120°, the detector is fully irradiated at a distance of 1.2 m from the source. The structure is fixed inside of a large copper box that acts as a radiations shielding and a Faraday cage. The chamber is flushed with the CMS gas mixtures $Ar/CO_2/CF_4$ (45 : 15 : 40) or Ar/CO_2 (70 : 30).

The readout electronics is based on the Scalable Readout System (SRS) designed by the RD51 collaboration. It consists of APV25 Front-End ASICs with 128 readout channels connected to the readout board of the detector. Each channel contains a pre-amplifier and a shaper working at a frequency of 40 MHz. The analog information of the pulses is sent to an ADC card via HDMI cables, itself connected to the Front End Card (FEC) responsible for the communication with the external devices and the control of the chips. Then, a Scalable Readout Unit (SRU) acts as a common readout concentrator to ensure the DTC link (Data, Trigger and Control) between all the FECs and the DAQ station. It also performs the synchronization of the clocks of all the electronics cards and chips.

The SRS system requires an external trigger to send out the data packets. The detector being irradiated by X-rays, it is not possible to generate trigger signals with a scintillator. However, the signal amplified in the triple-GEM structure and moving between the last GEM foil and the readout plane also induces a pulse on the bottom electrode of the

last GEM, almost identical to the one induced on the readout strips. This signal can be collected directly on the HV divider through a de-coupling capacitance before being sent to a pre-amplifier, a shaper and a discriminator unit to generate a digital gate. The trigger signal is then sent to the SRU to start the acquisition. When the SRU receives a trigger, all the APV25 chips open an acquisition window of 375 ns during which the signals on all the channels are sampled every 25 ns.

Fig. 8.10 shows the typical raw data from an APV25 (left), containing the ADC charge of all the channels inside of the acquisition window (top right) and the typical cluster size at a gain of 1×10^3 with X-rays (bottom right).

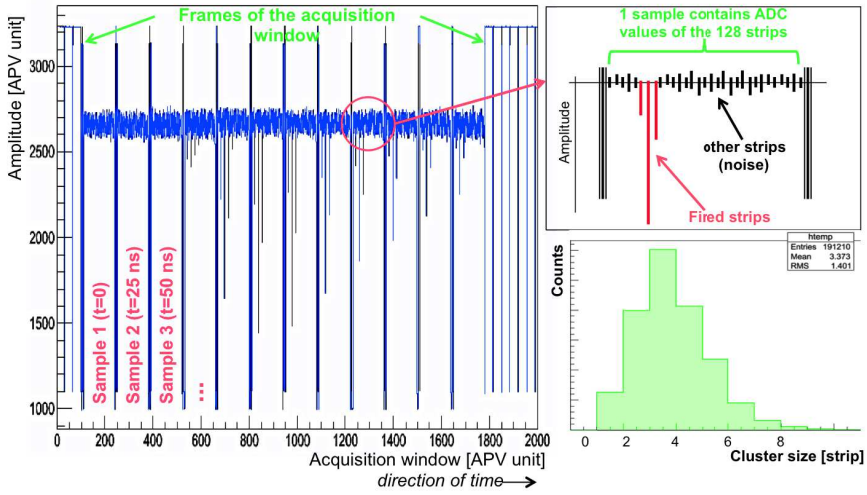

FIGURE 8.10: Raw data of an APV25 triggered by an X-ray photon. The acquisition window contains 12 samples delayed by 25 ns. Each sample includes the ADC values of all the 128 strips, fired or not by the particle. The average number of strips fired by a 8 keV X-ray is 3.3 at a gas gain of 1×10^3.

Finally, the data collected inside of the APV25 acquisition windows are recorded with the DATE software (Data Acquisition and Test Environment) designed by the ALICE community and fully compatible with the SRU+SRS+APV25 system. Fig. 8.11 gives an overview of the test setup (left) and the layout of the DAQ elements (right). Fig. 8.12 shows the complete setup with a GE1/1 prototype in place and ready for the data acquisition.

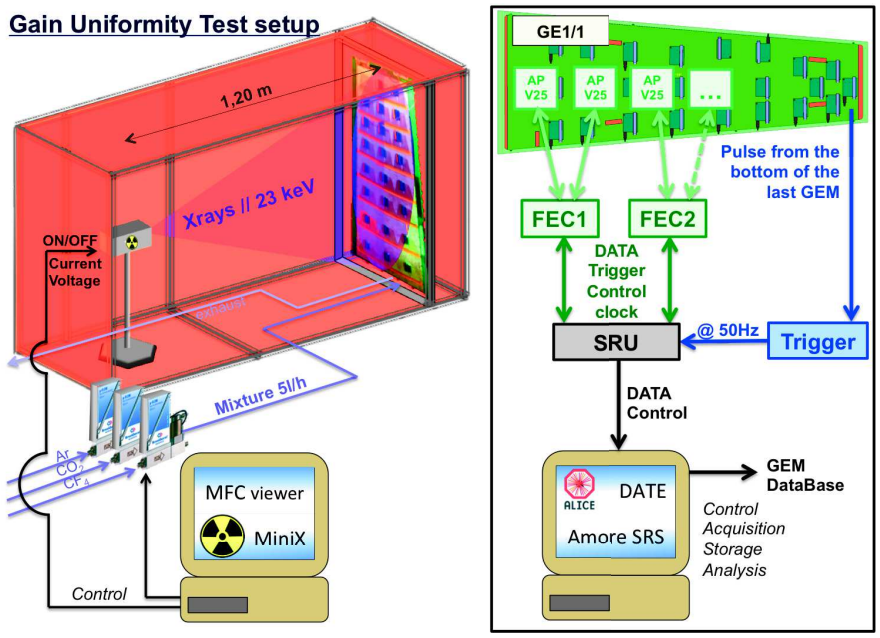

FIGURE 8.11: Schematic view of the gain uniformity test setup showing the detector under test irradiated by the silver X-ray source, the DAQ electronics and the trigger line .

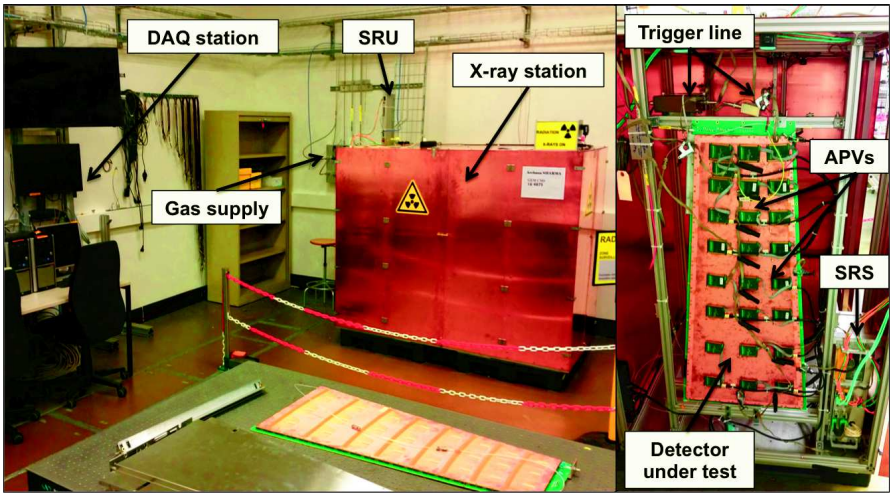

FIGURE 8.12: Picture of the gain uniformity stand showing the X-ray source, the DAQ stations ((left)) and the inside of the copper box (right) with the electronics in place on the detector.

8.5.3 The DAQ procedure

The GE1/1 detector under test is operating at an effective gain of 1×10^3, which ensures that the maximum amplitude of the readout signals is just below the saturation level of the APV25.

The first step consists of measuring the average noise and the offset of every readout channels. To do so, the X-ray source is kept OFF and the acquisition is performed with

a random trigger signal. The so-called "pedestal run" takes no more than few minutes for one chamber.

Then the X-ray source is powered ON to perform the "physics run". The recording of the data only starts 30 minutes after the ray source was turned ON to avoid the short-term variations of the gain induced by the charging up of the GEM foils. The duration of the run depends on the number of events that has to be collected. Since the SRS system is working with a common trigger, only the few channels fired by the particle signals records interesting information, while all the other channels record zeros (the typical cluster size is equal to 3 strips). Therefore, to acquire a sufficient number of good events per measurement point, the total number of events that must be collected by the entire system should be multiplied by the total number of points. For example, in order to acquire 10 000 good events for every single strips, the total number of events collected by the system is 3072 times bigger, so about 30 millions. In practice, it is sufficient to collect 10 000 events per cluster size (i.e. 3 strips) to build a representative charge spectrum. In this case, called the 1-cluster granularity, a total of 10 millions of events is required to allow the proper gain characterization over 1000 points on the detector.

8.5.4 The analysis procedure

The first phase of the analysis is based on the AMORE framework designed by the ALICE community and adapted to the SRS+APV25 system [121]. It consists of three main steps:

- The first step consists of defining the appropriate threshold to perform the zero-suppression on all the recorded events. Using the data collected during the pedestal run, AMORE builds the noise distribution and extract the corresponding RMS for all the channels. Then, a cut is applied on all the data with the source ON, typically at 5 σ of the average noise level. For each event, all the channels with a charge below the threshold are suppressed.

- The next step is the clusterization: for a same event, the hits in neighbor strips are organized in a single object, a cluster, which contains the total charge induced by the particle. Additional cuts are possible at this level, such as the maximum and the minimum cluster sizes and the cluster multiplicity that are useful to reject possible noise, cross-talk or fake events.

- Finally, the results are stored in a ROOT tree. For every event the tree contains the number of clusters, the total charge, the size, the position and the timing information of the clusters.

Then, the second phase of the analysis is the extraction of the gain uniformity from the ROOT file thanks to a dedicated algorithm. It is organized in three main steps:

- First, the geometry of the detector is built in the software, including the position of all the strips in the ϕ and the η directions. The readout plane is divided in several regions of interest defined by the user. With the example of the 1-cluster granularity, each η-partition is divided into 128 slices, each slice corresponding to 1 cluster size (3 strips).

- Then, in a given slice, the maximum cluster charge for all the events occurring in this slice is added to a charge histogram. A second selection is performed at this stage to clean the data set: the events with a very low energy and a cluster size lower than 2 strips are considered as noise and thus they are simply rejected. Additionally, the events with the maximum charge in the first or the last sample of the acquisition window are also removed since the useful part of the signal could be outside of the DAQ window.

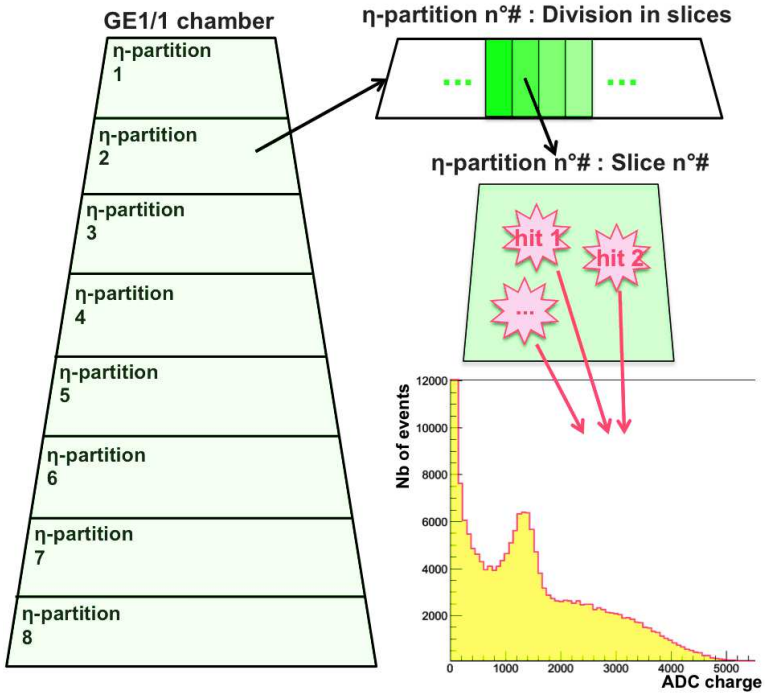

FIGURE 8.13: Schematic view of the detector built in the analysis code. The η-partitions are divided in several slices defined by the user. For each slice, the accumulation of the maximum charge of all the clusters gives a distribution related to the energy deposited by the particles and the effective gain.

Fig. 8.13 shows a schematic representation of the second analysis phase. The resulting charge distribution, shown in Fig. 8.14, is similar to the one described in Sec. 6.4.1. The fluorescence of the drift electrode induces the typical copper

photo-peak around 8 keV in addition to the X-ray background mostly due to the Bremsstrahlung of electrons in the silver target.

- A Gaussian fit is then applied to charge histograms of all the slices to determine the ADC mean of the photo-peaks and the corresponding energy resolution. The charge collected on the readout plane being proportional to the effective gas gain, variations of the ADC position of the photo-peak indicates the variations of the effective gain, possibly induced by geometrical non-uniformity or defects on the readout board. Finally the mean and the RMS of all the slices are plotted as a function of the slice position in order to provide a $3D$ map of the effective gain of the GE1/1 chamber.

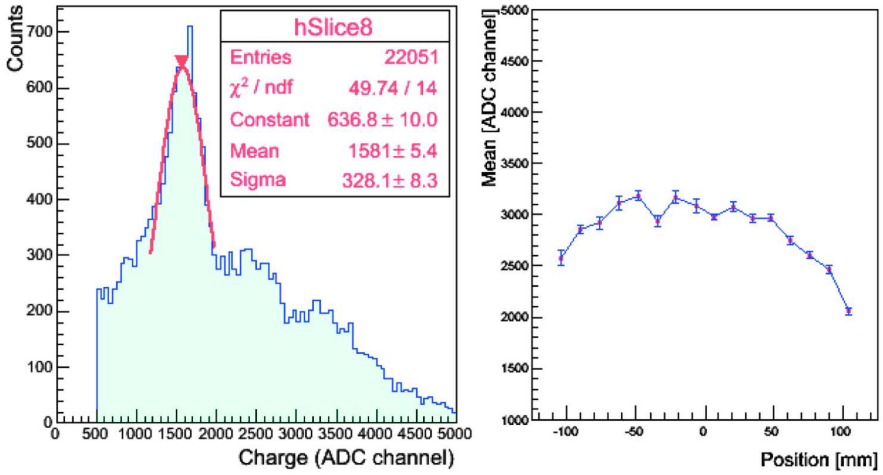

FIGURE 8.14: Typical charge spectrum induced by the silver X-ray source in the GE1/1 detectors filled with Ar/CO_2 (70 : 30) (left) and stability of the mean ADC as a function of the position of the slice in the corresponding η-partition (right).

8.5.5 Tests and results

Five large detectors were tested in the same conditions with the gain uniformity test setup. The detectors were operating in Ar/CO_2 (70 : 30) at an effective gain of 1×10^3. After five hours of continuous irradiation, each chamber accumulated about 7×10^5 events. For convenience reasons, the results discussed in this section are presented with the 8-cluster granularity i.e. each of the 128 measurement points is $2-3$ cm wide in the ϕ direction and corresponds to about 0.8 % of the total area.

8.5.5.1 GE1/1-III

The first detector tested with the SRS+APV25 system was a GE1/1 prototype of the 3^{rd} generation. Fig. 8.15 shows the $2D$ map of the effective gain normalized with the

average value (left) and the map of the energy resolution over the entire surface (right).

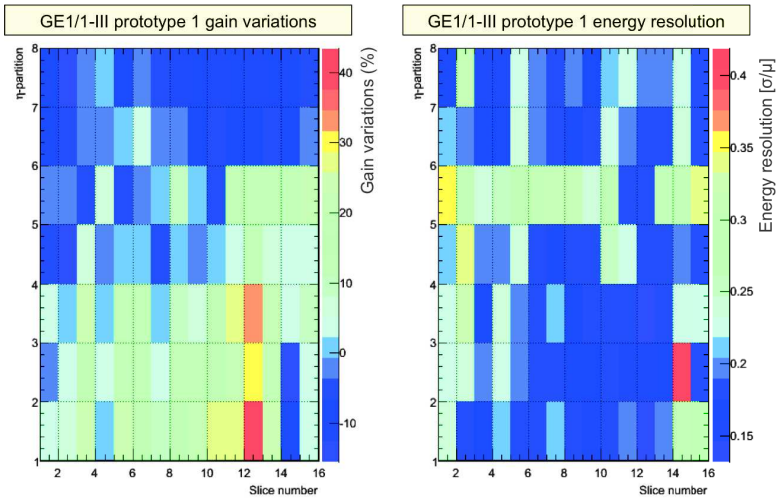

FIGURE 8.15: Effective gain (left) and energy resolution (right) of a 3^{rd} generation GE1/1 prototype as a function of the η-partition and the analysis slice.

The gain is mostly contained within 20 % of the average value, except near the slice number 12 of the first η-partition where it is higher by 40 %. The map shows that the gain decreases gradually from the narrow side of the trapezoid (η-partition 8) to the largest side (η-partition 1) with lower values close the lateral sides. This effect can be explained by the slight bending of the drift and the readout PCBs causing variations of electric fields between the various elements of detectors. As a result, the transparency of the GEM foils is not uniform, as well as the effective gain. The energy resolution is uniform over the chamber, with an average value just below 20 %. However, larger resolutions are measured in the η-partition 5, probably resulting from the low quality of one or several HV sectors on the GEM foils (which are parallel to the η-partitions). Finally, a $3D$ view of the gain map is shown on Fig. 8.16. The coordinates of each measurement point are expressed in millimeters, the origin being the center of the narrow side of the trapezoid.

This particular test helped to identify for the first time the bending issue with large chambers. The bending, already present when the boards are delivered, can get worse because of the over stretching of the GEM stack.

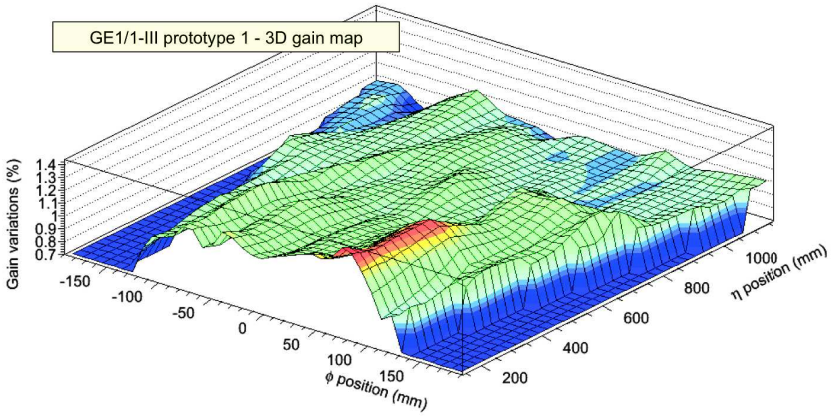

FIGURE 8.16: $3D$ map of the effective gain of the 3^{rd} generation GE1/1 prototype, normalized with the average value. The origin of the axis is the central point of the narrow side of the chamber.

8.5.5.2 GE1/1-IV

The bending effect was confirmed with two chambers of the next generation of GE1/1, as seen in Fig. 8.17 and Fig. 8.18.

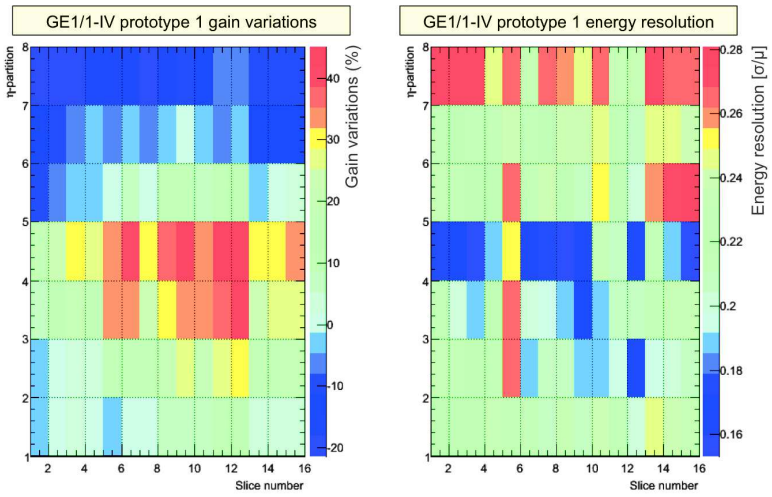

FIGURE 8.17: Effective gain (left) and energy resolution (right) of the first GE1/1 prototype of the 4^{th} generation as a function of the η-partition and the analysis slice.

The corresponding $3D$ gain maps, on Fig. 8.19, show that the variations over the surface of the GE1/1-IV detectors are similar to the ones observed with the 3^{rd} generation. In this case, the effect is even more pronounced with variations above 40 % of the average gain. It is also interesting to notice that these two detectors were also tested with the sector-by-sector technique discussed in Sec. 8.5.1. The results, previously shown Fig. 8.9, are compatible with the ones obtained with the SRS system.

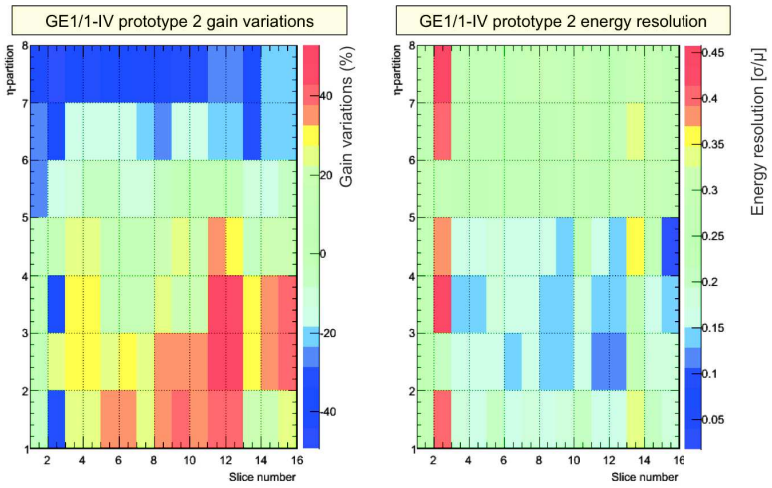

FIGURE 8.18: Effective gain (left) and energy resolution (right) of the second GE1/1 prototype of the 4^{th} generation as a function of the η-partition and the analysis slice.

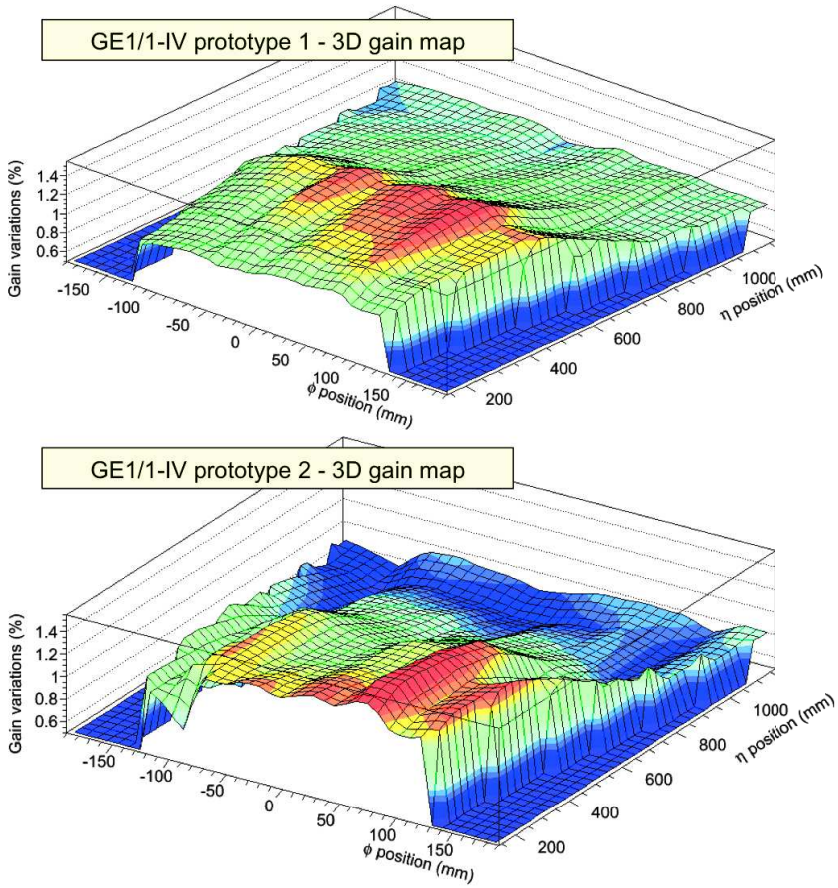

FIGURE 8.19: Comparison of the $3D$ maps of the effective gain of the first and second GE1/1 prototypes of the 4^{th} generation, normalized with the average value.

8.5.5.3 GE1/1-VI

The bending issue was then solved by pre-bending the boards in the opposite direction of the initial bending and by releasing the tension on the foils. After several trials, two GE1/1 chambers of the 6^{th} generation were tested. The effective gain and the energy resolution maps are presented in Fig. 8.20 and Fig. 8.21. The gain variations are below 15 %, with few points just above 20 % for the first prototype.

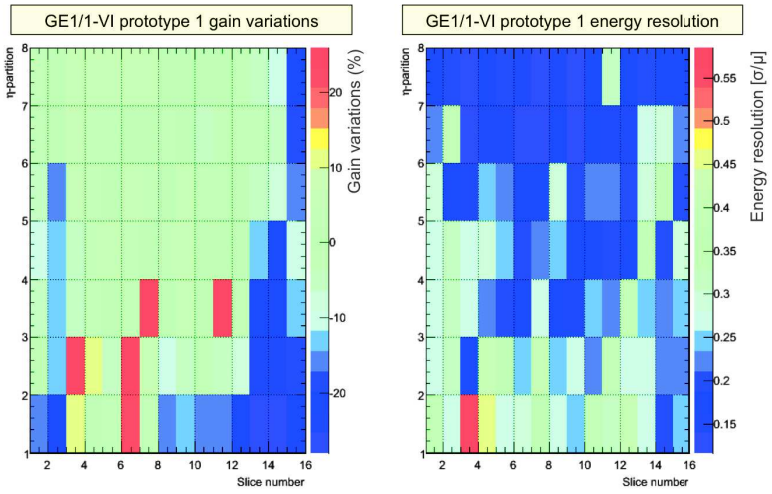

FIGURE 8.20: Effective gain (left) and energy resolution (right) of the first GE1/1 prototype of the 6^{th} generation as a function of the η-partition and the analysis slice.

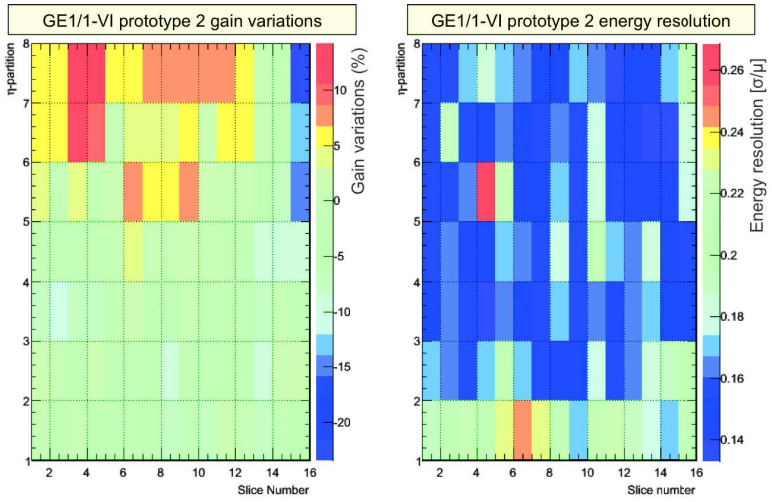

FIGURE 8.21: Effective gain (left) and energy resolution (right) of the second GE1/1 prototype of the 6^{th} generation as a function of the η-partition and the analysis slice.

The corresponding $3D$ gain maps on Fig. 8.22 are plotted with the same scale than for the other generations. These results therefore confirm the significant improvement of the planarity of the chambers and the uniformity of the gain.

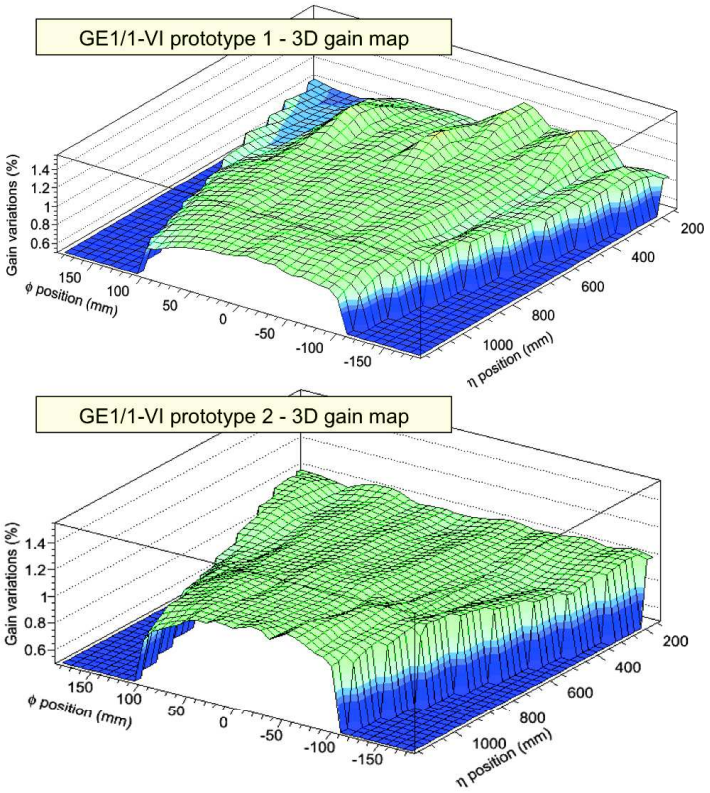

FIGURE 8.22: Comparison of the $3D$ maps of the effective gain of the first and second prototypes of 6^{th} generation GE1/1, normalized with the average value.

8.5.6 Limitations and plans

The gain uniformity test is a major step of the QC of the GE1/1 detectors and a great tool to accept or reject faulty chambers at the early stage of the production. The use of the SRS+APV25 system substantially improved the gain uniformity measurement: the duration of the entire test was reduced from one week to two days per detector and the charge can be collected on every single strip to keep the best granularity and thus more information for in-depth investigations. However, we can identify two limitations with this system:

- First, the trigger is not generated by scintillators but extracted from the bottom of the last GEM. This electrode, covering the entire surface of the detector, is very large and induces a lot of noise in the trigger readout channel. The high frequency noise can be easily removed with an appropriate filter but there are also contributions at frequencies close the typical signal frequencies and slower baseline fluctuations that cannot be filtered. Therefore, the poor quality of the trigger signal induces time jittering on the digital gate sent to the SRU, and then time fluctuation of the acquisition window with respect to the readout signals. In addition, since the

detectors have to operate at a low gain in order to not saturate the APVs (typically 1×10^3) , the time resolution is not optimum and also participates to the jittering of the trigger signal. A solution consists of increasing the size of acquisition window to make sure that all the readout pulses are correctly sampled, but doing so, the amount of data transferred to the DAQ also increases and limits the maximum acquisition rate. In the current configuration, the acquisition window consists of 15 time bin (i.e. 375 ns) for an acquisition rate limited to 50 Hz, very low regarding the particle rate provided by the X-ray source (100 kHz).

- The second limitation is the absence of Zero Suppression (ZS) at the level the electronics. For each trigger received by the SRU, all the APVs have to transfer the full content of the acquisition window for all the 128 readout channels. Consequently, 3072 channels are recorded while, in reality, only 3 strips (one cluster) are fired by a particle and contain useful information. The absence of ZS is responsible for very large data files, about 100 Gb per million of events. The handling of the data is therefore problematic and the analysis step in charge of the ZS takes more than 12 hours for a single chamber.

A major upgrade of the SRS system is being investigating by the RD51 research group at CERN and the Florida Institute of Technology (CMS GEM Collaboration) in order to implement the ZS in the firmware of the acquisition boards and propagate the modifications to the DAQ and the analysis softwares. With this new configuration, only the few readout channels fired by the particle would transfer the data to the DAQ station. Therefore, the acquisition rate would increase by almost a factor 1000 and reach several tens of kHz. The size of the data files would be significantly reduced, as well as the time required to analyze all the events. With the upgraded system, it is expected to perform the entire gain uniformity test in few hours, for a total number of events more than one order of magnitude larger than with the current system.

After successful preliminary tests with small prototypes, the new configuration is being tested on large GE1/1 detectors with the entire set of APV25s.

8.6 Conclusions

The production, the assembly and the testing of the 144 large detectors for the GE1/1 station will be shared between several production sites over the world. The entire process will start in 2016 and must be completed in 2018 before LS2. The CMS GEM Collaboration aims to provide the detailed testing procedure to make sure that all the chambers will have the best performance in CMS.

The experience gained during the *R&D* phase helped to identify the critical characteristics of the large detectors and to precisely define the structure of the quality control. Several major QC steps were established at CERN during the Ph.D thesis.

The characterization of a large GEM foil is a challenge because of its microscopic structure. Nevertheless, the measurement of the leakage current between the GEM electrodes helps to identify the presence of defects or contamination. The testing configuration and the procedure were optimized after a set of trials with several GEMs of various quality. A new large setup is being designed to allow the characterization of several full-size GEM foils and therefore minimize the duration of the test.

After the assembly of the single detectors, a gas leak test is necessary to ensure that no pollution or air molecules can penetrate the amplification region, degrade the performance of the detector and trigger premature aging. Several options were considered and the final test will include the measurement of the gas flow rate and the pressure drop inside of the chambers. A dedicated test stand, recently designed, includes several high purity pressure and temperature sensors that are automated thanks to micro-controllers.

One of the most important step is the gain uniformity test, which is necessary to ensure that the detection performance will be uniform along the detectors. A new technique was developed in order to measure simultaneously the effective gain at every readout strips. A new procedure helped to reduce the duration of the test to 2 days with the maximum granularity. After several successful tests with several generations of detectors, the setup and the procedure will be duplicated in the all production sites.

The next major step of the quality control is the performance test of all the detectors with cosmic rays. The dedicated cosmic stand that will contain up to 30 detectors will operate with the final CMS electronics and DAQ system, which will be available during 2016.

Chapter 9

General conclusions

When I first joined the CMS GEM Collaboration, the GE1/1 project was still only an *R&D* interest of CMS. The first prototype of the second generation had just been assembled and prepared for its very first operation. The project was still mainly conducted within the RD51 laboratory, where it was initially born.

Most of the major aspects of the project were not yet established and it was essential to demonstrate that the GE1/1 technology was the most suitable choice for the upgrade of the CMS end-caps. In particular, it was necessary to measure the fundamental characteristics of the world largest triple-GEM detectors and show that they were perfectly adapted to the CMS forward environment. The CMS GEM Collaboration also had to demonstrate that the detection performances of the GE1/1 prototypes were good enough to fulfil the requirements of CMS, both for the L1 trigger system and the OFF-line reconstruction. Finally, it was crucial to study the long-term operation of the GE1/1s and make sure that the detectors can survive for several decades in a harsh environment. Apart from the detector's aspects, it was also necessary to show that the CMS GEM Collaboration had the resources, the experience and the manpower to support such a big project. Numerous tools and techniques had to be developed by the collaboration to facilitate the integration of the GE1/1 project to the CMS system. Moreover, the production plan and the quality control of the chambers had to be established and validated.

My PhD subject was proposed in this context. It can be divided into three main projects.

The first one was the study of the operating characteristics of the modern triple-GEM detectors. The recent development of the single-mask production technique gives the possibility of producing large GEM foils with a very good uniformity. However, it also induces non-negligible differences in the geometry of the GEM holes that could affect the

general performances of the technology. A series of test setups and procedures were then designed in order to understand the variations between the single-mask and the standard double-mask foils. Therefore, the effective gas gain, the short-term stability, the rate capability and the discharge probability were precisely measured in controlled environments with small prototypes especially designed for this purpose. The unexpected differences of operation between the two orientations of the single-mask foils were highlighted by this study and helped to define the best configuration for the large GE1/1 chambers. Additionally, a lot of effort was dedicated to the test of the full-size prototypes in test beam facilities in order to determine the detection efficiency, the spatial and the time resolutions. Besides that, a new technique was established to measure the bunch crossing identification efficiency by synchronizing the beam trigger with the clock of the readout electronics. All the tests were performed at different operating points and for different gas mixtures, with the idea of proposing several working configurations for the CMS application. The excellent performances of the GE1/1 detectors were presented at international conferences and published in several scientific journals (full list available at [122]).

The second project was the extensive study of the long-term operation of the GE1/1 chambers. When operating in high-rate environments, gaseous detectors can be subject to "classical aging", i.e. the degradation of their performances induced by polymerization processes in the avalanche plasma. Three accelerated aging tests were conducted in the Gamma Irradiation Facility at CERN. In order to maintain the realistic operating conditions, the acceleration factors were set to low values (< 30). After several months of sustained irradiation, the detectors accumulated a total charge higher than 50 mC/cm^2 that corresponds to 10 years of real operation at HL-LHC with a safety factor ~ 9. Since no aging effects were observed during this period, the detectors are expected to survive in CMS with the two possible gas mixtures Ar/CO_2 (70 : 30) and $Ar/CO_2/CF_4$ (45 : 15 : 40). The tests will continue until the chambers accumulate a safety factor 10. It was also demonstrated that the presence of pollutants in the gas mixture could trigger and enhance the classical aging. Therefore, in addition to the classical aging tests, a set of outgassing tests was performed with the materials composing the GE1/1 detectors. About two years of consecutive measurements helped to identify a polluting material, the CellPack URETHAN, and confirm that the other components will not affect the operation of the detectors. Finally, based on the experience from the long-term study, I proposed a new design of ultra-clean single wire chamber in order to monitor the purity and the composition of the gas mixtures. Such devices could be implemented in the gas systems at the GE1/1 production sites and at CMS to prevent the possible contamination of the GE1/1 detectors. A first prototype was build and successfully tested at CERN.

The last subproject was the assembly and the quality control of the triple-GEM detectors. In order to ensure the proper operation of all the GE1/1 chambers, a set of control tests was established before, during and after the assembly. One of the major QC step is the characterization of the GEM foils, done by measuring the leakage current between the two copper electrodes. The presence of defects or contamination would induce an over current. This step is also very important during the assembly process to identify and eliminate possible dust particles on the foils. Another crucial step of the QC is the effective gain calibration and the measurement of its uniformity across the chambers. Since the effective gain impacts all the detection performances, large variations over the detector's surface would degrade the operation in CMS. A specific test station was design in order to measure simultaneously the effective gain and the energy resolution at every readout channel. The DAQ system is based on the SRS+APV25 electronics, initially developed for the CMS tracker. The entire test takes no more than two days for a single detector and allows extracting the gain information with the full granularity. The technical specifications, the procedure and the analysis tools were shared with all the production sites, which are going to duplicate the system.

My PhD work contributed to the success of the *R&D* phase and lead to the approval of the GE1/1 project by the CMS collaboration. The results I obtained and the corresponding conclusions helped to design the most suitable detectors for the upgrade of the CMS end-caps and also to better understand the modern triple-GEM technology. In particular, the realistic aging study I performed could be useful for other high-rate applications involving GEMs, for the upgrade of the current HEP experiments and for the future colliders.

As a personal conclusion, I must say that I consider myself as very lucky. Firstly because I had the opportunity to work at CERN, one of the most incredible scientific complex in the world. I have seen and used many types of detection technologies, research tools and other extraordinary objects like a 3 T superconducting magnet, large irradiation bunkers and the first MWPC ever built. I also had the chance to work with a great team, within the CMS GEM Collaboration and the RD51 research group. I could see how the mutual assistance and the close collaboration helped resolving any kind of scientific issues. Finally, I was involved in an extraordinary project: the installation of a new detection technology in CMS. I participated in many activities including fundamental research, analysis, hardware and software developments, both in particle physics and general engineering. After three years of intense work, I feel myself more confident and more than ever ready to continue my career in scientific research.

Chapter 10

Conclusion générale

Quand j'ai rejoint pour la première fois la collaboration CMS GEM, le projet GE1/1 n'était alors qu'un simple programme de *R&D* CMS parmi d'autres. A ce moment là, le premier prototype de la seconde génération venait d'être assemblé et préparé en vue de sa première mise en fonctionnement. L'essentiel des travaux de recherches était encore mené dans les laboratoires du groupe de recherche RD51, où le projet était né quelques mois plus tôt.

La plupart des aspects les plus importants du projet GE1/1 n'étaient pas encore établis et il fallait démontrer que la technologie des GEM était la plus adaptée pour le projet de consolidation du détecteur à muons de CMS. En particulier, il était nécessaire de mesurer les propriétés fondamentales de fonctionnement des premiers grands détecteurs triple-GEM produits par la technologie simple-maque, et de s'assurer qu'ils pourraient fonctionner en toute sécurité dans l'environnement des bouchons de CMS. La collaboration CMS GEM devait aussi démontrer que les performances de détection seront suffisamment bonnes pour améliorer à la fois le système de déclenchement sur les muons et la reconstruction "OFF-line" nécessaire pour l'observation d'une nouvelle physique après la montée en puissance du LHC. Enfin, il était crucial d'étudier le fonctionnement à long terme des chambres GE1/1 et de s'assurer qu'elles pourront fonctionner pendant des décennies dans les bouchons de CMS haute luminosité.

Au delà de l'aspect détecteur, il était également important de montrer que la collaboration CMS GEM avait les ressources, l'expérience et la main d'oeuvre nécessaire pour mener à bien ce projet ambitieux. Plusieurs outils et techniques ont été développés par la collaboration pour faciliter l'intégration de ces nouveaux détecteurs dans l'expérience CMS. De plus, la production et le contrôle qualité des chambres devaient être définis et validés avant d'être partagés avec les différents sites de production à travers le monde.

Dans ce contexte, mon projet de thèse s'est organisé en trois parties.

La première partie consistait à étudier les caractéristiques de fonctionnement des détecteurs triple-GEM. La technique de fabrication simple-masque, récemment développée au CERN, permet de produire les feuilles de GEM de grande dimension nécessaires aux détecteurs GE1/1. Cependant la géométrie des trous ainsi obtenue diffère de la technique usuelle double-maque déjà utilisée dans d'autres expériences de physique à hautes énergies, ce qui pourrait affecter le comportement des détecteurs. Plusieurs études ont donc été menées affin de comprendre ces différences. Ainsi, le gain effectif, la stabilité à court terme, le taux maximum de détection et la probabilité de décharge ont été mesurés avec précision dans un environnement contrôlé à l'aide de détecteurs spécifiques représentatif des chambres GE1/1. Des différences de fonctionnement entre les deux orientations possibles de la technologie simple-masque et la technologie double-masque ont été mises en évidences et ont permis de définir la configuration la plus adaptée à l'application CMS. Par ailleurs, ces résultats pourront aussi profiter à d'autres groupes de recherche souhaitant inclure la technologie GEM dans leurs détecteurs, soit pour un programme d'amélioration au LHC, soit pour équiper certains des futurs accélérateurs. Dans un second temps, un effort significatif a été dédié au test des grands détecteurs GE1/1 lors de campagnes d'irradiations sur faisceau. Ces tests ont permis de mesurer les performances fondamentales des détecteurs comme l'efficacité de détection, la résolution spatiale, qui définit la précision avec laquelle les muons seront localisés dans CMS, et la résolution temporelle qui décrit la qualité des signaux de déclenchement générés par les chambres GE1/1. De nouvelles techniques ont également été proposées, notamment pour reproduire la collision des paquets de protons au LHC et ainsi mesurer directement l'efficacité d'identification de ces paquets. Tout les tests ont été effectués à différents points de fonctionnement et pour différentes configurations d'alimentation et de mixture de gaz. Les excellentes performances des chambres GE1/1 ont ensuite été présentées lors de conférences internationales et publiées dans plusieurs revues spécialisées (la liste complète est disponible à [122]). Le tableau 10.1 résume cette première partie de la thèse en présentant les propriétés les plus importantes des détecteurs, en comparaison aux valeurs minimales imposées par CMS.

Le second projet a été l'étude du fonctionnement à long terme des chambres GE1/1. Lors du fonctionnement continu dans un environnement à fort taux de particules, les détecteurs gazeux peuvent être sujets au vieillissement classique, c'est à dire la dégradation de leurs performances induite par la production de polymères dans les avalanches électroniques lors de l'amplification des signaux. Trois tests de vieillissement accélérés ont donc été effectués au "Gamma Irradiation Facility" au CERN, avec des facteurs d'accélérations réalistes maintenus en dessous de 30 fois l'environnement de CMS haute luminosité. Après plusieurs mois de fonctionnement sous constante irradiation, les détecteurs ont

Properties	**CMS requirements**	**GE1/1 performance**
Rate capability	> 10 KHz/cm^2	100 MHz/cm^2
Single chamber efficiency (MIP)	> 97 %	$97 - 98$ %
Angular resolution	< 300 μrad	~ 135 μrad
Single chamber time resolution	< 10 ns	$4 - 5$ ns with $Ar/CO_2/CF_4$ (45 : 15 : 40) $7 - 8$ ns with Ar/CO_2 (70 : 30)
Gain uniformity	< 15 %	< 15 % with the last GE1/1 generation

TABLE 10.1: Comparison of the CMS minimum requirements and the GE1/1 performance.

accumulés une charge totale supérieure à 50 mC/cm^2, ce qui représente 10 ans de fonctionnement réel au HL-LHC avec un facteur de sécurité ~ 9. L'absence de signes de vieillissement a ainsi permis de prouver que les détecteurs GE1/1 pourront survivre pendant plusieurs décennies avec les mixtures de gaz Ar/CO_2 (70 : 30) et $Ar/CO_2/CF_4$ (45 : 15 : 40) proposées pour CMS. Les tests vont se poursuivre jusqu'à ce que la charge totale accumulée représente un facteur de sécurité de 10. Le tableau 10.2 présente un résumé des tests de vieillissement comparé au cahier des charges de CMS.

Property	**CMS requirements**	**GE1/1 performance**
Longevity	60 mC/cm^2	53 mC/cm^2 in $Ar/CO_2/CF_4$ (45 : 15 : 40) 55 mC/cm^2 in Ar/CO_2 (70 : 30) (ongoing)

TABLE 10.2: Comparison of the CMS minimum requirements and the GE1/1 long-term performance.

Cette étude a également démontré que la présence de polluants dans la mixture de gaz pouvait déclencher un vieillissement prématuré des chambres. En plus des tests de vieillissement classique, une étude de dégazage a été mené sur tout les matériaux qui composent les détecteurs GE1/1. Près de deux ans de tests consécutifs ont permis d'identifier un élément polluant, le CellPack URETHAN, et de confirmer que les autres composants n'affecteront pas le fonctionnement des chambres. Enfin, sur la base de ces expériences, j'ai proposé un nouveau concept de chambre à fil qui permettra de contrôler de manière très précise la pureté et la composition des mixtures de gaz. Ces détecteurs pourront être produits en grande quantité pour équiper tout les sites de production des chambres GE1/1 et le système de gaz de CMS. Un premier prototype a été assemblé et testé au CERN.

Le troisième et dernier projet concerne la production des 144 grands détecteurs qui seront installés à CMS pendant l'arrêt technique LS2 en 2019. La production étant partagée entre plusieurs sites de production à travers le monde, il a fallut établir une liste de tests de contrôle qualité pour assurer des performances uniformes pour tout les

détecteurs. Le contrôle qualité s'effectue dès la réception des composants et se prolonge jusqu'à l'installation des super-modules dans les bouchons de CMS, en passant par l'assemblage et la caractérisation des chambres triple-GEM. L'une des étapes les plus importantes est la caractérisation électrique des feuilles de GEM, qui consiste à mesurer le courant de fuite entre les deux électrode de la GEM lorsqu'elle est mise sous tension. La présence de contamination ou de défauts de fabrication provoquerait un excès de courant facilement identifiable avant l'assemblage des détecteurs. Cette étape permet également d'identifier et d'éliminer les particules de poussière qui pourraient s'être fixées dans les trous microscopiques des GEM. Une autre étape essentielles au bon fonctionnement des chambres est le test d'uniformité du gain effectif. Le gain, qui représente les propriétés géométriques et électriques des détecteurs, décrit également les performances de détection. Ainsi, de grandes variations de gain entraîneraient des variations de performances qui ne sont pas acceptables pour CMS. Une station de test particulière a été conçue pour mesurer de manière simultanée le gain effectif pour tout les canaux de lectures d'une chambre. Le système d'acquisition fonctionne à partir des cartes électroniques SRS+APV25, développées initialement pour le trajectographe de CMS. Après seulement quelques heures de test il est possible de mesurer avec précision le gain et la résolution en énergie sur toute la surface du détecteur. Les détails techniques de l'installation, les méthodes de mesure et d'analyse ont ensuite été partagés avec les sites de production qui vont dupliquer le système et intégrer cet étape à leur contrôle qualité.

Mon travail de thèse a participé au succès de la phase *R&D* et la plupart de mes travaux ont permis de faire approuver le projet GE1/1 par la collaboration CMS et le comité du LHC. Les résultats que j'ai obtenus ainsi que mes conclusions ont aidé à concevoir les détecteurs les plus adaptés à l'amélioration du détecteur a muons de CMS. Ils seront également utiles à tous les projets basés sur la technologie GEM. L'étude des caractéristiques de fonctionnement et les études de vieillissement notamment pourront servir de point de départ pour un projet de détecteurs gazeux devant fonctionner dans un environnement à fort taux de particules.

D'un point de vue plus personnel, je me considère comme très chanceux. D'abord parce que j'ai eu l'opportunité de travailler au CERN, l'un des complexes scientifiques les plus incroyables et certainement le plus impressionnant. J'ai eu l'occasion de voir ou d'utiliser une grande variété de technologies de détection, des outils de recherche les plus avancés et d'autres objets extraordinaires comme une aimant supra-conducteur de 3 T, des bunkers d'irradiations et même l'une des toutes premières chambres à fils de Georges Charpak. J'ai également eu la chance de travailler avec une équipe fantastique, au sein de la collaboration CMS GEM et du groupe de recherche RD51. J'ai pu me rendre compte comment le travail d'équipe et l'entraide permanent permet de résoudre

la plupart des problèmes scientifiques. Enfin, j'ai eu l'occasion de participer à un projet ambitieux : l'installation d'une nouvelle technologie de détection dans une expérience aussi célèbre que CMS. J'ai pu participer à beaucoup d'activités scientifiques incluant la recherche fondamentale, l'analyse de données et le développement matériel et logiciel (physique des particule mais également ingénierie). Après trois années de travail intense, j'ai pris confiance en moi et je me sens plus que jamais prêt à continuer ma carrière dans la recherche scientifique.

Appendix A

Results of the outgassing test campaign

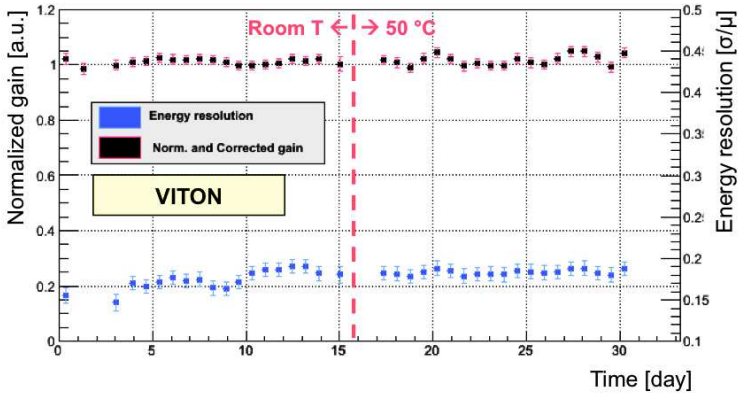

FIGURE A.1: Outgassing test result for the VITON O-rings in $Ar/CO_2/CF_4$ (45 : 15 : 40) at 2 L/h.

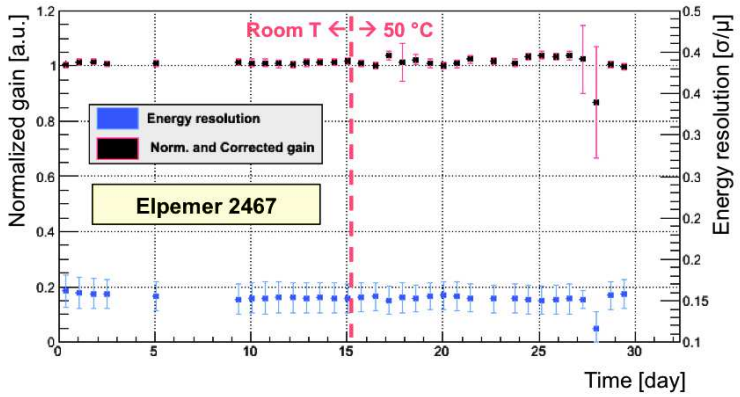

FIGURE A.2: Outgassing test result for the soldering mask Elpemer 2467 in $Ar/CO_2/CF_4$ (45 : 15 : 40) at 2 L/h.

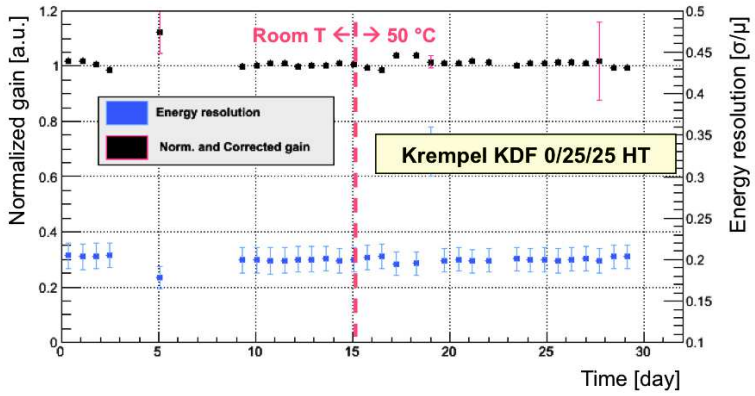

FIGURE A.3: Outgassing test result for the sealing film Krempel KDF 0/25/25 HT in $Ar/CO_2/CF_4$ (45 : 15 : 40) at 2 L/h.

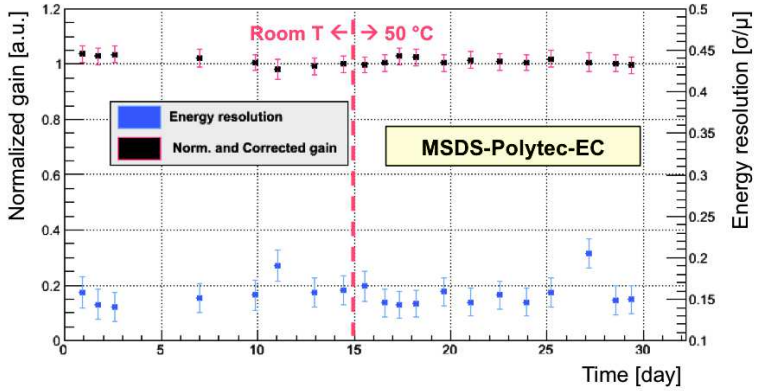

FIGURE A.4: Outgassing test result for the silver glue MSDS-Polytec-EC in $Ar/CO_2/CF_4$ (45 : 15 : 40) at 2 L/h.

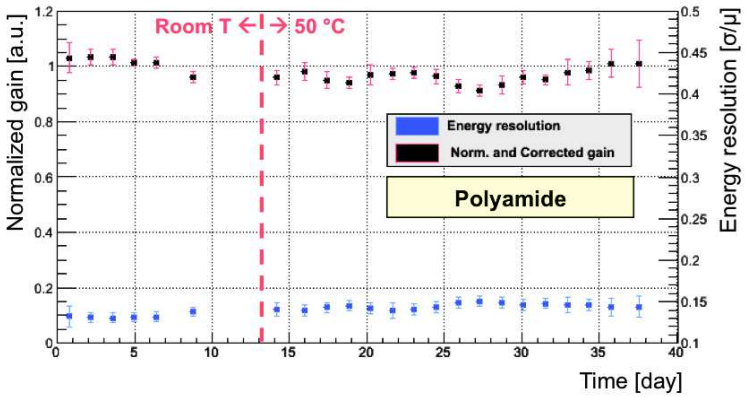

FIGURE A.5: Outgassing test result for the polyamide washers in $Ar/CO_2/CF_4$ (45 : 15 : 40) at 2 L/h.

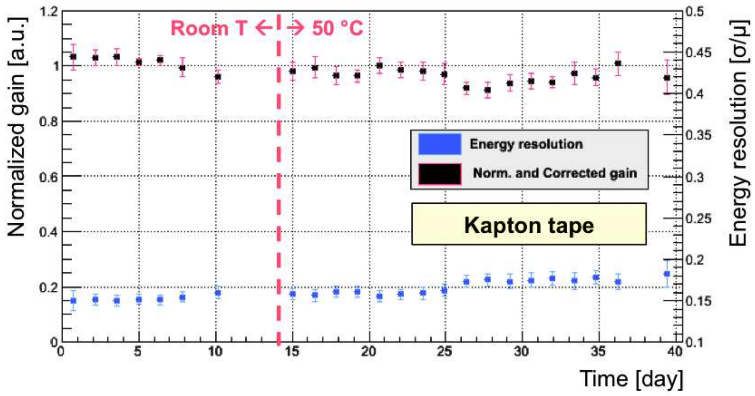

FIGURE A.6: Outgassing test result for the Kapton tape in $Ar/CO_2/CF_4$ (45 : 15 : 40) at 2 L/h.

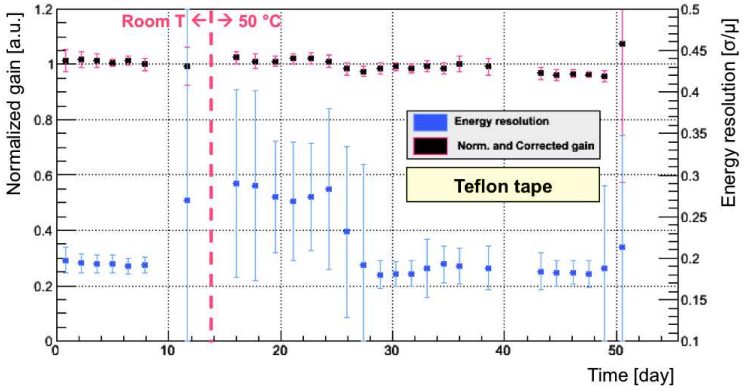

FIGURE A.7: Outgassing test result for the Teflon tape in $Ar/CO_2/CF_4$ (45 : 15 : 40) at 2 L/h.

Appendix B

Assembly of the GE1/1 detectors

FIGURE B.1: Step 1: all the tools and components are prepared and carefully organized for the assembly (left). The working table, made of PolyMethyl MethAcrylate (PMMA), is cleaned with an adhesive roll (right).

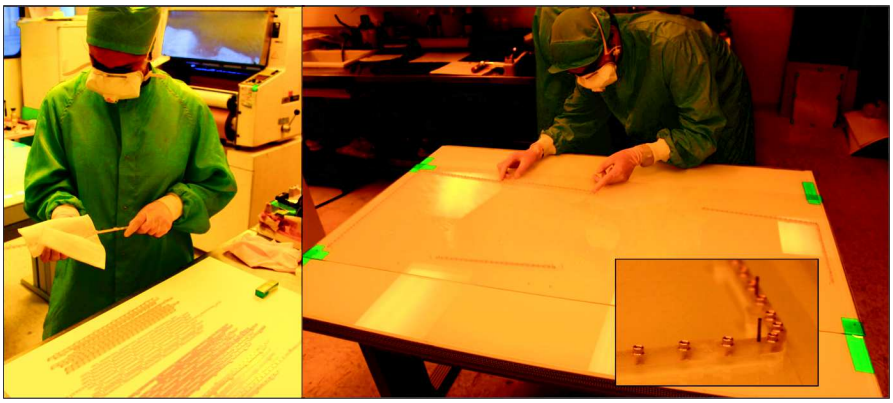

FIGURE B.2: Step 2: the internal frames, responsible of holding the GEM stack, are cleaned with an adhesive paper (left) and placed on working table thanks to guiding pins (right).

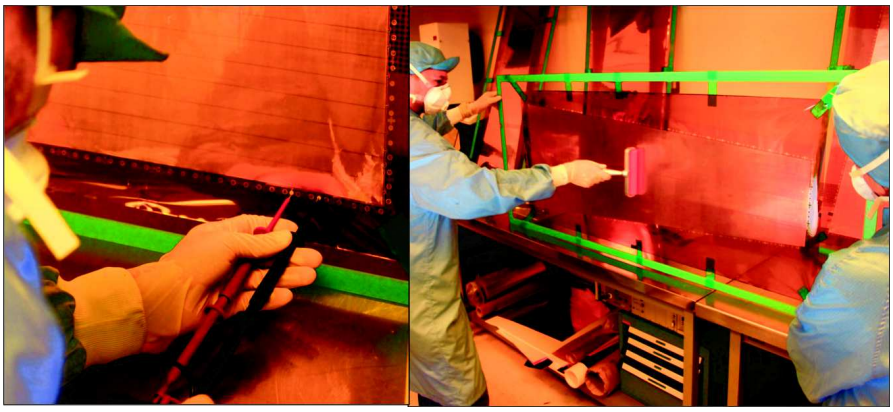

FIGURE B.3: Step 3: the first GEM foil is tested at 600 V and cleaned again with the adhesive roll.

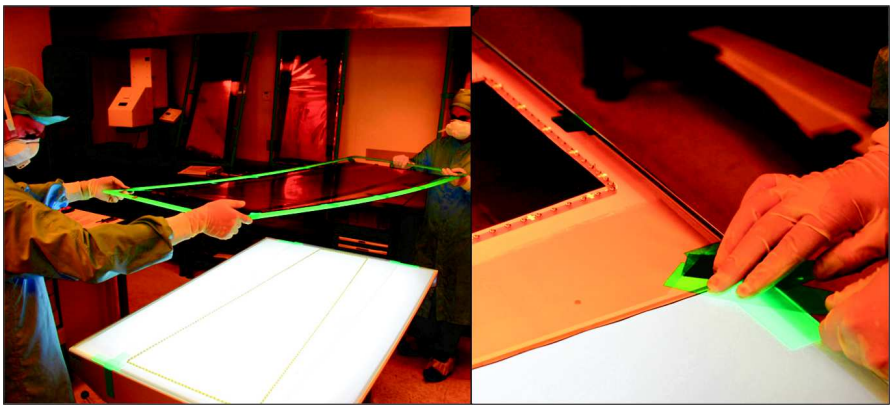

FIGURE B.4: Step 4: the first GEM is placed on the first layer of internal frames (left). The foils is stretched by hand and attached to the working table to ensure the flatness and stability of the structure (right).

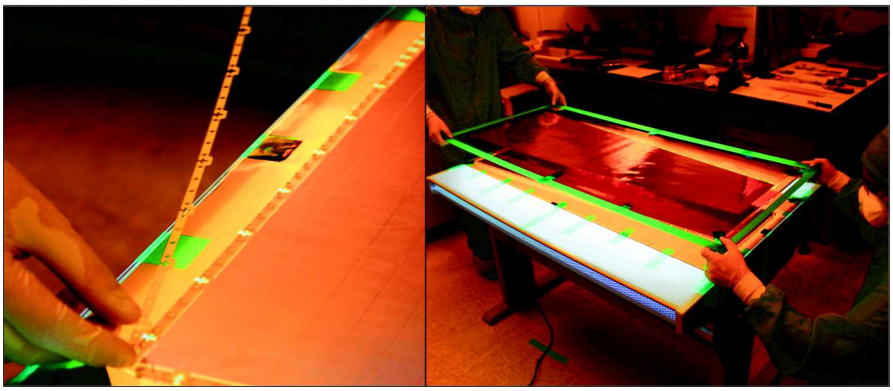

FIGURE B.5: Step 5: the second layer of internal frames is placed on top of the first GEM (left). After testing and cleaning, the second GEM is added to the stack (right).

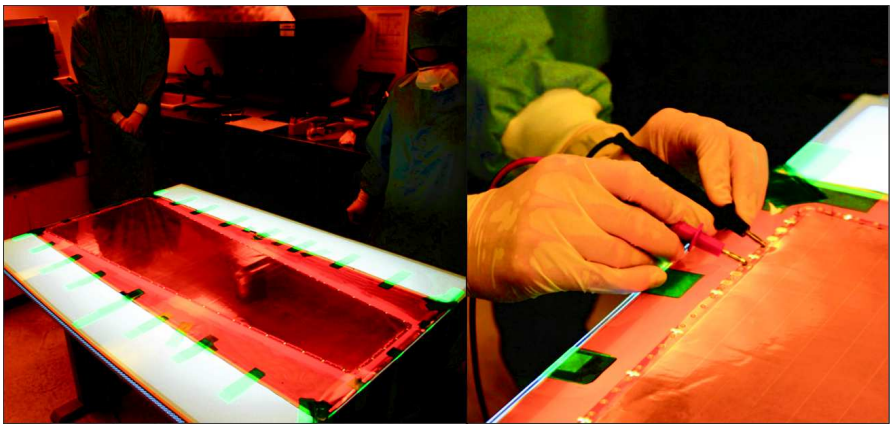

FIGURE B.6: Step 6: same operation as before, the second GEM is stretched manually (left) and tested at 600 V (right).

FIGURE B.7: Step 7: after the third layer of internal frames is in position, metallic nuts are inserted in the dedicated housing of the frames. Then, the last GEM foils is added to the structure as well as the last layer of internal frames to close the stack.

FIGURE B.8: Step 8: after another cleaning step (left), the GEM stack is protected by a PMMA cover placed fixed to the top of the internal frames.

FIGURE B.9: Step 9: vertical screws are inserted into the frames in order to attach all the frame layers and GEM together.

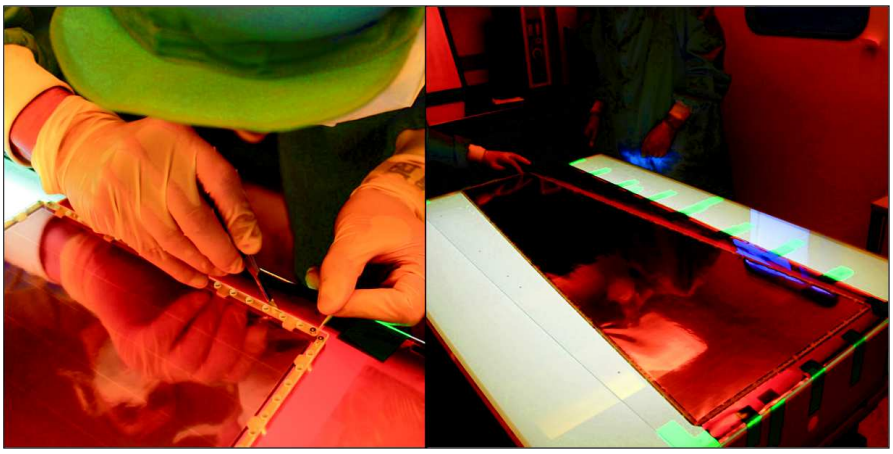

FIGURE B.10: Step 10: the excess of polyimide foil is cut and detached from the GEM stack.

FIGURE B.11: Step 11: after being cleaned with the adhesive roll (left), the drift plane is positioned below the GEM stack (right).

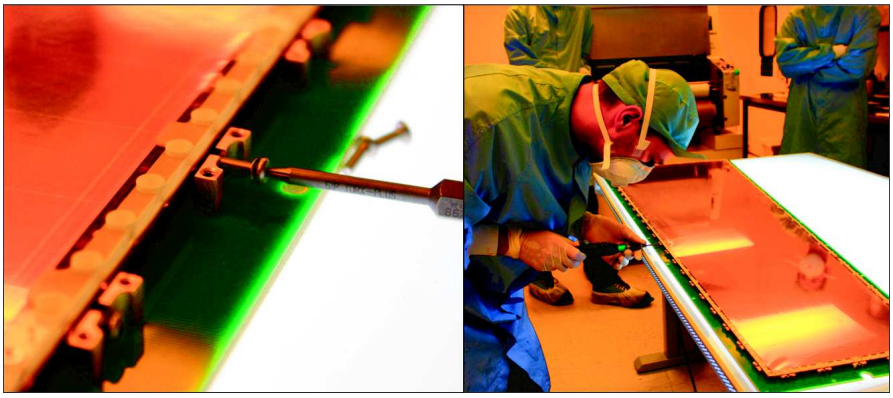

FIGURE B.12: Step 12: lateral screws are inserted in the brass pull-outs attached to the drift board until it reaches the embedded nuts (left). Then, torque control tools are used to stretch the foils, for a tension about 5 N/cm.

FIGURE B.13: Step 13: the possible dust produced during the stretching step is removed with an adhesive paper (left) and the three GEM foils are tested once again at 600 V.

FIGURE B.14: Step 14: the PMMA protection cover is removed from the stack (left). Then, external frames equipped with the O-rings is placed around the GEM stack (right).

FIGURE B.15: Step 15: after being cleaned (left), the readout board is placed on top of the external frame to close the chamber.

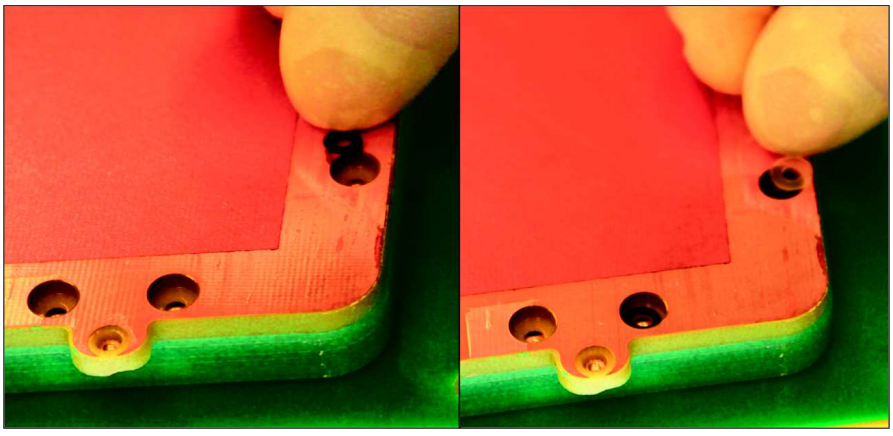

FIGURE B.16: Step 16: finally, O-rings and washers are inserted in the dedicated housings of the readout board before the last screws are used to attach all the elements together and close the gas volume.

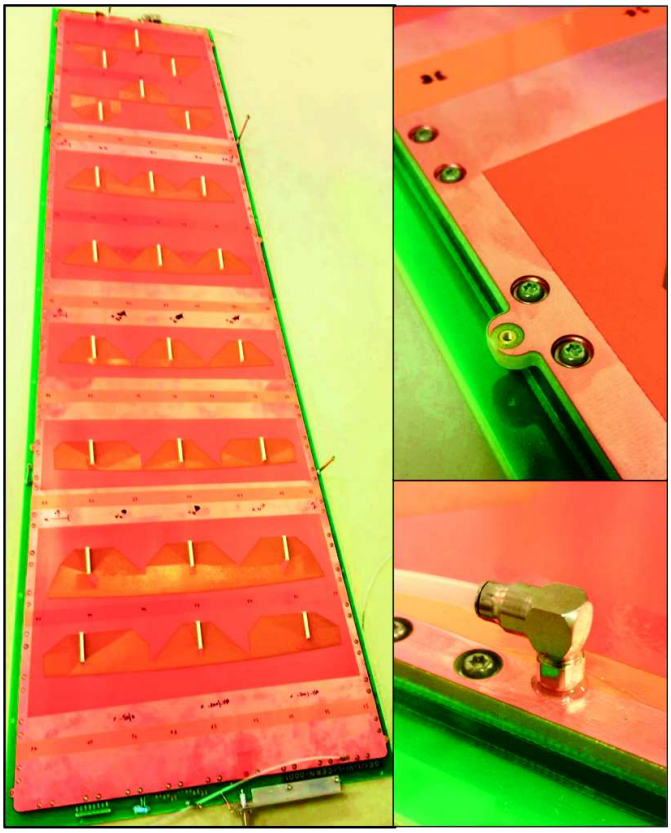

FIGURE B.17: Picture of a last generation GE1/1 detector just after the assembly (left). When the chamber is closed, the gas input and output are fixed to the readout PCB (right).

Bibliography

[1] LHC/LC Study Group Collaboration. Physics Interplay of the LHC and the ILC. *Phys. Rep.*, 426(hep-ph/0410364. ANL-HEP-PR-2004-108. CERN-PH-TH-2004-214. DCPT-2004-134. DESY-04-206. DESY-2004-206. IFIC-2004-59. IISc-CHEP-2004-13. IPPP-2004-67. SLAC-PUB-10764. UB-ECM-PF-2004-31. UCD-2004-28. UCI-TR-2004-37. 2-6):47–358. 472 p, Oct 2004. URL https://cds.cern.ch/record/800650.

[2] S. Dittmaier et al. *Handbook of LHC Higgs Cross Sections: 1. Inclusive Observables*. CERN, Geneva, 2011. URL https://cds.cern.ch/record/1318996. Comments: 153 pages, 43 figures, to be submitted to CERN Report. Working Group web page: https://twiki.cern.ch/twiki/bin/view/LHCPhysics/CrossSections.

[3] Abdelhak Djouadi. Higgs Physics: Theory. Technical Report arXiv:1203.4199. LPT-ORSAY 12-29, Mar 2012. URL https://cds.cern.ch/record/1433331. Comments: 21 pages, 15 figures. Talk given at the XXV International Symposium on Lepton Photon Interactions at High Energies (Lepton Photon 11), 22-27 August 2011, Mumbai, India.

[4] CMS Collaboration. Precise determination of the mass of the Higgs boson and tests of compatibility of its couplings with the standard model predictions using proton collisions at 7 and 8 TeV. *Eur. Phys. J. C*, 75(arXiv:1412.8662. CERN-PH-EP-2014-288. CMS-HIG-14-009):212. 75 p, Dec 2014. URL https://cds.cern.ch/record/1979247. Comments: Submitted to Eur. Phys. J. C.

[5] CMS Collaboration. Study of the Mass and Spin-Parity of the Higgs Boson Candidate via Its Decays to Z Boson Pairs. On the mass and spin-parity of the Higgs boson candidate via its decays to Z boson pairs. *Phys. Rev. Lett.*, 110 (arXiv:1212.6639. CMS-HIG-12-041. CERN-PH-EP-2012-372):081803. 25 p, Dec 2012. URL https://cds.cern.ch/record/1502670. Comments: Submitted to Phys. Rev. Lett. Final version.

[6] A Djouadi and R M Godbole. Ewsb at LHC. Technical Report arXiv:0901.2030, Jan 2009. URL https://cds.cern.ch/record/1155823. Comments: 27 pages,

45 figures, uses LaTeX (insa.sty). Invited review for volume on LHC physics to celebrate the Platinum Jubilee of the Indian National Science Academy, edited by Amitava Datta, Biswarup Mukhopadhyaya and Amitava Raychaudhuri.

[7] Projected Performance of an Upgraded CMS Detector at the LHC and HL-LHC: Contribution to the Snowmass Process. Technical Report CMS-NOTE-2013-002. CERN-CMS-NOTE-2013-002, CERN, Geneva, Jun 2013. URL https://cds.cern.ch/record/1565454. Comments: to be included in the Snowmass 2013 report.

[8] CMS Collaboration. Search for top-squark pair production in the single-lepton final state in pp collisions at $\sqrt{s} = 8$ TeV. *Eur. Phys. J. C*, 73(arXiv:1308.1586. CMS-SUS-13-011. CERN-PH-EP-2013-148):2677. 61 p, Aug 2013. URL https://cds.cern.ch/record/1567175. Comments: Replaced with published version. Added journal reference and DOI.

[9] Exclusion limits on gluino and top-squark pair production in natural SUSY scenarios with inclusive razor and exclusive single-lepton searches at 8 TeV. Technical Report CMS-PAS-SUS-14-011, CERN, Geneva, 2014. URL https://cds.cern.ch/record/1745586.

[10] A Colaleo, A Safonov, A Sharma, and M Tytgat. CMS TECHNICAL DESIGN REPORT FOR THE MUON ENDCAP GEM UPGRADE. Technical Report CERN-LHCC-2015-012. CMS-TDR-013, CERN, Geneva, Jun 2015. URL https://cds.cern.ch/record/2021453.

[11] . URL http://pdg.lbl.gov.

[12] M J Berger et al. Photon cross sections database.

[13] Fabio Sauli. Principles of operation of multiwire proportional and drift chambers. page 92 p, Geneva, 1977. CERN, CERN. URL https://cds.cern.ch/record/117989. CERN, Geneva, 1975 - 1976.

[14] E C Farmer and S C Brown. *Physics Review*, 74:902, 1948.

[15] Mar Capeáns and Jose M Garabatos Cuadrado. *Study of Ageing of Gaseous Detectors and Solutions for the Use of MSGCs in High Rate Experiments*. PhD thesis, Santiago de Compostela U., Santiago de Compostela, 1995. URL https://cds.cern.ch/record/1331835. Presented 13 Oct 1995.

[16] M Alfonsi, G Bencivenni, P De Simone, F Murtas, M P Poli Lener, W Bonivento, A Cardini, D Raspino, B Saitta, D Pinci, and S Baccaro. Aging measurements

on triple-GEM detectors operated with CF_4-based gas mixtures. *Nucl. Phys. B, Proc. Suppl.*, 150:159–163, 2006. URL https://cds.cern.ch/record/1025773.

[17] F Halzen and A D Martin. *Quarks and Leptons*. John WILEY and SONS, 1985.

[18] K A Olive. *(PDG) Chin. Phys.*, C(38), 2014.

[19] F Gianotti. Collider physics: LHC. (CERN-OPEN-2000-293), 2000. URL https://cds.cern.ch/record/458489.

[20] André Rougé. *Introduction à la physique subatomique*. Ecole Polytechnique, 2005.

[21] CMS Collaboration. Cms supersymmetry physics results, .

[22] Combination of standard model Higgs boson searches and measurements of the properties of the new boson with a mass near 125 GeV. Technical Report CMS-PAS-HIG-13-005, CERN, Geneva, 2013. URL https://cds.cern.ch/record/1542387.

[23] ATLAS Collaboration. Observation of a new particle in the search for the Standard Model Higgs boson with the ATLAS detector at the LHC. *Phys. Lett. B*, 716 (arXiv:1207.7214. CERN-PH-EP-2012-218):1–29. 39 p, Aug 2012. URL https://cds.cern.ch/record/1471031. Comments: 24 pages plus author list (38 pages total), 12 figures, 7 tables, revised author list.

[24] CMS Collaboration. Observation of a new boson at a mass of 125 GeV with the CMS experiment at the LHC. *Phys. Lett. B*, 716(arXiv:1207.7235. CMS-HIG-12-028. CERN-PH-EP-2012-220):30–61. 59 p, Jul 2012. URL https://cds.cern.ch/record/1471016.

[25] CMS Collaboration. Observation of the diphoton decay of the Higgs boson and measurement of its properties. *Eur. Phys. J. C*, 74(arXiv:1407.0558. CMS-HIG-13-001. CERN-PH-EP-2014-117):3076. 79 p, Jul 2014. URL https://cds.cern.ch/record/1728107. Comments: Replaced with published version. Added journal reference and DOI.

[26] CMS Collaboration. Measurement of the properties of a Higgs boson in the four-lepton final state. *Phys. Rev. D*, 89(arXiv:1312.5353. CMS-HIG-13-002. CERN-PH-EP-2013-220):092007. 73 p, Dec 2013. URL https://cds.cern.ch/record/1637951. Comments: Published in Phys. Rev. D.

[27] CMS Collaboration. Measurement of Higgs boson production and properties in the WW decay channel with leptonic final states. *J. High Energy Phys.*, 01(arXiv:1312.1129. CMS-HIG-13-023. CERN-PH-EP-2013-221):096. 83 p, Dec

2013. URL https://cds.cern.ch/record/1633401. Replaced with published version. Added journal reference and DOI.

[28] Georges Aad et al. Combined Measurement of the Higgs Boson Mass in pp Collisions at $\sqrt{s} = 7$ and 8 TeV with the ATLAS and CMS Experiments. *Phys. Rev. Lett.*, 114(arXiv:1503.07589. ATLAS-HIGG-2014-14. CMS-HIG-14-042. CERN-PH-EP-2015-075):191803. 45 p, Mar 2015. URL https://cds.cern.ch/record/2004386. Comments: Submitted to Physical Review Letters. Figures and auxiliary material are available at https://atlas.web.cern.ch/Atlas/GROUPS/PHYSICS/PAPERS/HIGG-2014-14 and https://twiki.cern.ch/twiki/bin/view/CMSPublic/Hig14042PaperTwiki.

[29] Search for additional neutral Higgs bosons decaying to a pair of tau leptons in pp collisions at $\sqrt{s} = 7$ and 8 TeV. Technical Report CMS-PAS-HIG-14-029, CERN, Geneva, 2015. URL https://cds.cern.ch/record/2041463.

[30] CMS Collaboration. Search for the standard model Higgs boson produced in association with a W or a Z boson and decaying to bottom quarks. *Phys. Rev. D*, 89(arXiv:1310.3687. CMS-HIG-13-012. CERN-PH-EP-2013-188):012003. 49 p, Oct 2013. URL https://cds.cern.ch/record/1610290. Comments: Replaced with published version. Added journal reference and DOI.

[31] CMS Collaboration. Search for a standard model-like Higgs boson in the $\mu^+\mu^-$ and e^+e^- decay channels at the LHC. *Phys. Lett. B*, 744(arXiv:1410.6679. CMS-HIG-13-007. CERN-PH-EP-2014-243):184. 35 p, Oct 2014. URL https://cds.cern.ch/record/1957177. Comments: Submitted to Phys. Lett. B.

[32] S Heinemeyer, Wolfgang F L Hollik, and Georg Weiglein. Constraints on tan β in the MSSM from the Upper Bound on the Mass of the Lightest Higgs boson. *J. High Energy Phys.*, 06(hep-ph/9909540. DESY-99-120. KA-TP-99-12):009. 11 p, Sep 1999. URL https://cds.cern.ch/record/401773.

[33] CMS Collaboration. Search for neutral MSSM Higgs bosons decaying into a pair of bottom quarks. Technical Report arXiv:1506.08329. CMS-HIG-14-017. CERN-PH-EP-2015-133, CERN, Geneva, Jun 2015. URL https://cds.cern.ch/record/2029348. Comments: Submitted to J. High Energy Phys.

[34] Higgs to tau tau (MSSM). Technical Report CMS-PAS-HIG-13-021, CERN, Geneva, 2013. URL https://cds.cern.ch/record/1623367.

[35] W Beenakker, R Höpker, Michael Spira, and Peter M Zerwas. Squark and Gluino Production at Hadron Colliders. *Nucl. Phys. B*, 492(hep-ph/9610490. DESY-96-150. CERN-TH-96-215):51–103. 60 p, Oct 1996. URL https://cds.cern.ch/record/313638.

[36] Vladlen Timciuc. Search for High-Mass Resonances in the Dilepton Final State with the CMS Detector. Technical Report CMS-CR-2011-273, CERN, Geneva, Oct 2011. URL https://cds.cern.ch/record/1406803.

[37] D L Evans. Search for di-lepton resonances and Wprimes with CMS. Technical Report CMS-CR-2009-006, CERN, Geneva, Dec 2008. URL https://cds.cern.ch/record/1167921.

[38] Vardan Khachatryan et al. CMS Tracking Performance Results from Early LHC Operation. *Eur. Phys. J. C*, 70(arXiv:1007.1988. CERN-PH-EP-2010-019. CMS-TRK-10-001):1165. 29 p, Jul 2010. URL https://cds.cern.ch/record/1277738.

[39] Serguei Chatrchyan et al. Energy calibration and resolution of the CMS electromagnetic calorimeter in pp collisions at $\sqrt{s} = 7$ TeV. *J. Instrum.*, 8 (arXiv:1306.2016. CMS-EGM-11-001. CERN-PH-EP-2013-097):P09009. 51 p, Jun 2013. URL https://cds.cern.ch/record/1554142. Comments: Submitted to JINST.

[40] *The CMS muon project: Technical Design Report*. Technical Design Report CMS. CERN, Geneva, 1997. URL https://cds.cern.ch/record/343814.

[41] G L Bayatian et al. *CMS Physics: Technical Design Report Volume 1: Detector Performance and Software*. Technical Design Report CMS. CERN, Geneva, 2006. URL https://cds.cern.ch/record/922757. There is an error on cover due to a technical problem for some items.

[42] CMS Collaboration. Performance of CMS muon reconstruction in pp collision events at $\sqrt{s} = 7$ TeV. *J. Instrum.*, 7(arXiv:1206.4071. CMS-MUO-10-004. CERN-PH-EP-2012-173):P10002. 81 p, Jun 2012. URL https://cds.cern.ch/record/1456510. Comments: Submitted to the Journal of Instrumentation.

[43] CMS Collaboration. Cms muon analysis, . URL https://twiki.cern.ch/twiki/bin/view/CMSPublic/WorkBookMuonAnalysis#Calorimeter_based_muons.

[44] CMS Collaboration. Technical proposal for the upgrade of the CMS detector through 2020. Technical Report CERN-LHCC-2011-006. LHCC-P-004, CERN, Geneva, Jun 2011. URL https://cds.cern.ch/record/1355706.

[45] J Butler, D Contardo, M Klute, J Mans, and L Silvestris. Technical Proposal for the Phase-II Upgrade of the CMS Detector. Technical Report CERN-LHCC-2015-010. LHCC-P-008, CERN, Geneva. Geneva, Jun 2015. URL https://cds.cern.ch/record/2020886. Upgrade Project Leader Deputies: Lucia Silvestris (INFN-Bari), Jeremy Mans (University of Minnesota) Additional contacts: Lucia.Silvestris@cern.ch, Jeremy.Mans@cern.ch.

[46] A Djouadi, U Ellwanger, and A M Teixeira. Phenomenology of the constrained NMSSM. *J. High Energy Phys.*, 04(arXiv:0811.2699. LPT ORSAY 08-82):031, Nov 2008. URL https://cds.cern.ch/record/1140392. Comments: 29 pages, 14 figures.

[47] Tao Han, Zongguo Si, Kathryn M Zurek, and Matthew J Strassler. Phenomenology of Hidden Valleys at Hadron Colliders. *J. High Energy Phys.*, 07(arXiv:0712.2041): 008. 21 p, Dec 2007. URL https://cds.cern.ch/record/1075508. Comments: 21 pages, 12 figures.

[48] L Basso, A Belyaev, S Moretti, G M Pruna, and C H Shepherd-Themistocleous. Phenomenology of the minimal B-L extension of the Standard Model. Technical Report arXiv:0909.3113. SHEP-09-18. DFTT 56-2009, Sep 2009. URL https://cds.cern.ch/record/1207403. Comments: 4 pages, no figures. LaTeX. Talk given at The 2009 Europhysics Conference on High Energy Physics, Krakow, Poland, July 16-22, 2009.

[49] J Butler, D Contardo, M Klute, J Mans, L Silvestris, and Collaboration on behalf of the CMS. CMS Phase II Upgrade Scope Document. Technical Report CERN-LHCC-2015-019. LHCC-G-165, CERN, Geneva, Sep 2015. URL https://cds.cern.ch/record/2055167.

[50] J. Collot. Interaction of particles with matter (lecture i and ii). European School of Instrumentation in Particle and Astroparticle Physics (ESIPAP), http://lpsc.in2p3.fr/collot .

[51] H A Bethe. World Scientific vol. 18, 1996.

[52] Emilio Segrè. *Nuclei and particles: an introduction to nuclear and subnuclear physics; 1st ed.* Benjamin, New York, NY, 1964. URL https://cds.cern.ch/record/100961.

[53] Luc Valentin. *Physique subatomique: noyaux et particules; 1e éd.* Enseignement des sciences. Hermann, Paris, 1975. URL https://cds.cern.ch/record/110459.

[54] H. L. Bradt and B Peters. *Physics Review*, 75, 1948.

[55] Tom Francke and Vladimir Peskov. *Innovative applications and developments of micro-pattern gaseous detectors*. Advances in chemical and materials engineering (ACME) book series. Engineering Science Reference, Hershey, PA, 2014. URL https://cds.cern.ch/record/1703935.

[56] Eugenio Nappi and Vladimir Peskov. *Imaging gaseous detectors and their applications*. Wiley-VCH, Weinheim, 2013. URL https://cds.cern.ch/record/1418128.

[57] Georges Charpak, Roger Bouclier, Tullio Bressani, Jean Favier, and Crtomir Zupancic. The use of multiwire proportional counters to select and localize charged particles. *Nucl. Instrum. Methods*, 62:262–268, 1968. URL https://cds.cern.ch/record/347202.

[58] Fabio Sauli and A Sharma. Micro-pattern gaseous detectors. *Nucl. Instrum. Methods Phys. Res., A*, 477(CERN-EP-99-069. 1-3):1–7. 45 p, May 1999. URL https://cds.cern.ch/record/431069.

[59] T Beckers, Roger Bouclier, C Garabatos, Gilbert Million, Fabio Sauli, and L I Shekhtman. Optimization of microstrip gas chamber design and operating conditions. *Nucl. Instrum. Methods Phys. Res., A*, 346(CERN-PPE-94-27):95–101. 15 p, Feb 1994. URL https://cds.cern.ch/record/259630.

[60] F Angelini, R Bellazzini, L Bosisio, M M Massai, G Spandre, and M R Torquati. A microstrip gas chamber on a silicon substrate. Technical Report INFN-PI-AE-91-10, Pisa Univ. INFN, Pisa, Oct 1991. URL https://cds.cern.ch/record/226207.

[61] Roger Bouclier, Gilbert Million, Leszek Ropelewski, Fabio Sauli, Yu N Pestov, and L I Shekhtman. Performance of gas microstrip chambers on glass substrates with electronic conductivity. *Nucl. Instrum. Methods Phys. Res., A*, 332(CERN-PPE-93-04):100–106. 12 p, Jan 1993. URL https://cds.cern.ch/record/245234.

[62] Fabio Sauli. Development of high rate MSGCS: overview of results from RD28. *Nucl. Phys. B, Proc. Suppl.*, 61B(CERN-PPE-97-019):236–243. 9 p, Jan 1997. URL https://cds.cern.ch/record/321533.

[63] *Internal Workshop on Micro-Strip Gas Chambers*, Lyon-1996.

[64] B Boimska, Roger Bouclier, M Capéans-Garrido, S Claes, Wojciech Dominik, M Hoch, Gilbert Million, Leszek Ropelewski, Fabio Sauli, A Sharma, L I Shekhtman, W K Van Doninck, and L Van Lancker. Study of ageing and gain limits of microstrip gas chambers at high rates. (CERN-PPE-96-201):7 p, Nov 1996. URL https://cds.cern.ch/record/321532.

[65] B Boimska, Roger Bouclier, M Capéans-Garrido, Wojciech Dominik, Michael Hoch, Gilbert Million, Leszek Ropelewski, Fabio Sauli, and Abhishek Sharma. Investigation of discharge limits in diamond coated microstrip gas chambers. Technical Report CMS-NOTE-1996-016, CERN, Geneva, Dec 1996. URL https://cds.cern.ch/record/687363.

[66] Dirk Macke. *Micro strip gas chambers with gas electron multipliers and their application in the CMS experiment*. PhD thesis, Aachen U., Aachen, 2000. URL https://cds.cern.ch/record/1287874. Presented on 16 Oct 2000.

[67] C Krauss. Charged particle tracking with the HERA-B detector. 2002. URL https://cds.cern.ch/record/643265.

[68] M L Titov. Mpgd concepts for physics projects at energy / intensity / cosmic frontiers. In *MPGD2015 Trieste*, 2015.

[69] S Bachmann, A Bressan, M Capéans-Garrido, M Deutel, S Kappler, B Ketzer, A Polouektov, Leszek Ropelewski, Fabio Sauli, E C Schulte, L I Shekhtman, and A Sokolov. Discharge studies and prevention in the gas electron multiplier (GEM). *Nucl. Instrum. Methods Phys. Res., A*, 479(CERN-EP-2000-151. 2-3):294–308. 25 p, Dec 2000. URL https://cds.cern.ch/record/483487.

[70] P Abbon et al. The COMPASS Experiment at CERN. *Nucl. Instrum. Methods Phys. Res., A*, 577(arXiv:hep-ex/0703049. CERN-PH-EP-2007-001. 3):455–518. 84 p, Jan 2007. URL https://cds.cern.ch/record/1028264.

[71] Eraldo Oliveri, Stefano Lami, and Nicola Turini. *The forward inelastic telescope T2 for the TOTEM experiment at the LHC*. PhD thesis, Siena U., Siena, 2010. URL https://cds.cern.ch/record/1319607. Presented on 2010.

[72] Alessandro Cardini, Giovanni Bencivenni, and Patrizia De Simone. The Operational Experience of the Triple-GEM Detectors of the LHCb Muon System: Summary of 2 Years of Data Taking. Technical Report LHCb-PROC-2012-060. CERN-LHCb-PROC-2012-060, CERN, Geneva, Nov 2012. URL https://cds.cern.ch/record/1495070.

[73] W Anderson et al. Design, Construction, Operation and Performance of a Hadron Blind Detector for the PHENIX Experiment. Technical Report arXiv:1103.4277, Mar 2011. URL https://cds.cern.ch/record/1337923.

[74] S. Duarte Pinto and R. De Oliveira. A method of manufacturing a gas electron multiplier. Patent Wipo WO/2009127220.

[75] A Marinov. *Feasibility of a GEM-based muon system for the CMS detector at the LHC*. PhD thesis, UNIVERSITEIT GENT, 2013.

[76] S Bachmann, A Bressan, Leszek Ropelewski, Fabio Sauli, A Sharma, and D Mörmann. Charge amplification and transfer processes in the gas electron multiplier. *Nucl. Instrum. Methods Phys. Res., A*, 438(CERN-EP-99-048):376–408. 45 p, Apr 1999. URL https://cds.cern.ch/record/385380.

[77] Gabriele Croci, Leszek Ropelewski, Fabio Sauli, and S Ragazzi. *Study of relevant parameters of GEM-based detectors*. PhD thesis, Milan U., Milano, 2007. URL https://cds.cern.ch/record/1084208. Presented on 24 Sep 2007.

[78] S. Franchino et al. Effects of High Charge Densities in Multi-GEM Detectors. IEEE NSS proceedings arXiv:1512.04968, 2015.

[79] D Abbaneo et al. Test beam results of the GE1/1 prototype for a future upgrade of the CMS high-η muon system. Technical Report arXiv:1111.4883. RDSI-Note-2011-013, Nov 2011. URL https://cds.cern.ch/record/1401079.

[80] D Abbaneo et al. Characterization of GEM Detectors for Application in the CMS Muon Detection System. Technical Report arXiv:1012.3675. RD51-NOTE-2010-005, Dec 2010. URL https://cds.cern.ch/record/1316084. Comments: 7 pages, 19 figures, submitted for publication in conference record of the 2010 IEEE Nuclear Science Symposium, Knoxville, TN.

[81] D Abbaneo et al. Beam Test Results for New Full-scale GEM Prototypes for a Future Upgrade of the CMS High-eta Muon System. Technical Report arXiv:1211.3939, Nov 2012. URL https://cds.cern.ch/record/1494965. Comments: 5 pages, 9 figures, submitted to Proc. 2012 IEEE Nucl. Sci. Symposium, Anaheim, CA.

[82] D Abbaneo et al. Performance of a Large-Area GEM Detector Prototype for the Upgrade of the CMS Muon Endcap System. *PoS*, EPS-HEP2013 (arXiv:1412.0228):123. 8 p, Nov 2014. URL https://cds.cern.ch/record/1973272. Comments: 8 pages, 32 figures, submitted to Proc. 2014 IEEE Nucl. Sci. Symposium, Seattle, WA.

[83] P Aspell, G Anelli, P Chalmet, J Kaplon, K Kloukinas, H Mugnier, and W Snoeys. VFAT2: A front-end system on chip providing fast trigger information, digitized data storage and formatting for the charge sensitive readout of multi-channel silicon and gas particle detectors. page 5 p, 2007. URL https://cds.cern.ch/record/1069906.

[84] D Abbaneo et al. The status of the GEM project for CMS high-η muon system. *Nucl. Instrum. Methods Phys. Res., A*, 732:203–207. 5 p, 2013. URL https://cds.cern.ch/record/1709932.

[85] K Gnanvo, B Benson, W Bittner, F Costa, L Grasso, M Hohlmann, J B Locke, S Martoiu, H Muller, M Staib, A Tarazona, and J Toledo. Detection and Imaging of High-Z Materials with a Muon Tomography Station Using GEM Detectors. Technical Report arXiv:1011.3231. RD51-NOTE-2010-004, Nov 2010. URL https://cds.cern.ch/record/1307282. Comments: 8 pages, 17 figures, subm. for publication in conference record of 2010 IEEE Nucl. Sci. Symp., Knoxville, TN.

[86] *ALICE DAQ and ECS Manual ALICE-INT-2010-001*. ALICE, 2010.

[87] R K Carnegie, M S Dixit, J Dubeau, Dean A Karlen, J P Martin, H Mes, and K Sachs. Resolution studies of cosmic-ray tracks in a TPC with GEM readout. Technical Report physics/0402054, Feb 2004. URL https://cds.cern.ch/record/711592.

[88] D C Arogancia. Study in a beam test of the resolution of a Micromegas TPC with standard readout pads. Technical Report arXiv:0705.2210, May 2007. URL https://cds.cern.ch/record/1036731. Comments: To be submitted to NIM A, 25 pages.

[89] S Korff and R Present. *Physics Review*, 65:274, 1944.

[90] S Friedland. *Physics Review*, 74:898, 1948.

[91] J Vavra. Review of wire chamber aging. Technical Report SLAC-PUB-3882, SLAC, Stanford, CA, Feb 1986. URL https://cds.cern.ch/record/167139.

[92] J A Kadyk. Wire chamber aging. *Nucl. Instrum. Methods Phys. Res., A*, 300(LBL-29852):436–479. 78 p, Mar 1990. URL https://cds.cern.ch/record/221648.

[93] Georges Charpak, H G Fischer, Charles R Gruhn, Adolf G Minten, Fabio Sauli, G Plch, and G Flügge. Time degeneracy of multiwire proportional chambers. *Nucl. Instrum. Methods*, 99:279–284, 1972. URL https://cds.cern.ch/record/252187.

[94] J Wise. *Chemistry of radiation damage to wire chambers*. PhD thesis, Calif. Univ. Berkeley, Berkeley, CA, 1992. URL https://cds.cern.ch/record/243580. Presented on Aug 1992.

[95] M L Titov, M Hohlmann, C Padilla, and N Tesch. Summary and Outlook of the International Workshop on Aging Phenomena in Gaseous Detectors (DESY, Hamburg, October, 2001). *ICFA Instrum. Bull.*, 24(hep-ex/0204005. 4):22–53. 14 p, Apr 2002. URL https://cds.cern.ch/record/546220.

[96] M Hohlmann, C Padilla, N Tesch, and M Titov. Aging phenomena in gaseous detectors - perspectives from the 2001 workshop. *Nucl. Instrum. Methods Phys. Res., A*, 494(1-3):179–193, 2002. URL https://cds.cern.ch/record/773220.

[97] L Malter. Thin film field emission. *Physics Review*, (50):48, 1936.

[98] Proceedings of the international workshop on aging phenomena in gaseous detectors. *Nuclear Instruments and Methods in Physics Research*, A(515), 2003.

[99] M Capéans-Garrido. Aging and materials: Lessons for detectors and gas systems. *Nucl. Instrum. Methods Phys. Res., A*, 515:73–88, 2003. URL https://cds.cern.ch/record/808011.

[100] D Bailey and R Hall-Wilton. Proceedings of the International Workshop on Aging Phenomena in Gaseous Detectors. *Nucl. Instrum. Methods Phys. Res., A*, 515:37, 2003.

[101] C Niebuhr. Proceedings of the International Workshop on Aging Phenomena in Gaseous Detectors. *Nucl. Instrum. Methods Phys. Res., A*, 515:43, 2003.

[102] M Binkley. Proceedings of the International Workshop on Aging Phenomena in Gaseous Detectors. *Nucl. Instrum. Methods Phys. Res., A*, 515:53, 2003.

[103] Maxim Titov. Radiation Damage and Long-Term Aging in Gas Detectors. *ICFA Instrum. Bull.*, 26(physics/0403055):002. 19 p, 2004. URL https://cds.cern.ch/record/722642. Comments: 19 pages, 6 figures. Presented at the 42nd workshop of the INFN ELOISATRON Project 'Innovative Detector for Supercolliders', September 28 - October 4 (2003), Erice, Italy.

[104] M J Kushner. *J. Appl. Phys.*, 53(4):2923, 1982.

[105] S Chatrchyan et al. The CMS experiment at the CERN LHC. The Compact Muon Solenoid experiment. *J. Instrum.*, 3:S08004. 361 p, 2008. URL https://cds.cern.ch/record/1129810. Also published by CERN Geneva in 2010.

[106] J Wise, J A Kadyk, D W Hess, and M C S Williams. Effects of freons on wire chamber aging. Technical Report LBL-29252, Lawrence Berkeley Nat. Lab., Berkeley, CA, Jun 1990. URL https://cds.cern.ch/record/212608.

[107] T Åkesson et al. Aging studies for the ATLAS Transition Radiation Tracker (TRT). *Nucl. Instrum. Methods Phys. Res., A*, 515:166–179, 2003. URL https://cds.cern.ch/record/808009.

[108] S Bachmann, A Bressan, Alfredo Placci, Leszek Ropelewski, and Fabio Sauli. Development and test of large size GEM detectors. *IEEE Trans. Nucl. Sci.*, 47(4, pt.1):1412–15, 2000. URL https://cds.cern.ch/record/500795.

[109] M C Altunbas, K Dehmelt, S Kappler, B Ketzer, Leszek Ropelewski, Fabio Sauli, and F Simon. Aging measurements with the gas electron multiplier (GEM). *Nucl. Instrum. Methods Phys. Res., A*, 515(CERN-EP-2001-091. 1-2):249–254. 6 p, Dec 2001. URL https://cds.cern.ch/record/530679.

[110] L Guirl, S Kane, J May, J Miyamoto, and I Shipsey. An aging study of triple GEMs in Ar-CO sub 2. *Nucl. Instrum. Methods Phys. Res., A*, 478(1-2):263–266, 2002. URL https://cds.cern.ch/record/771995.

[111] M Alfonsi, G Bencivenni, P De Simone, F Murtas, M Poli-Lener, W Bonivento, A Cardini, C Deplano, D Raspino, and D Pinci. High-rate particle triggering with triple-GEM detector. *Nucl. Instrum. Methods Phys. Res., A*, 518:106–112, 2004. URL https://cds.cern.ch/record/802361.

[112] A Kozlov, I Ravinovich, L I Shekhtman, Zeev Fraenkel, M Inuzuka, and Itzhak Tserruya. Development of a triple GEM UV-photon detector operated in pure CF4 for the PHENIX experiment. *Nucl. Instrum. Methods Phys. Res., A*, 523 (physics/0309013. 3):345–354. 14 p, Aug 2003. URL https://cds.cern.ch/record/640470.

[113] A T Mitchel, S Bell. *Plasma Polymerization*, volume 108 of *ACS Symposium*. American Chemical Society, 1979.

[114] H Yasuda. *Plasma Polymerization*. Academic Press, 1985.

[115] . URL http://www.bluegoldcleaner.com/default.aspx.

[116] *Fundamentals of Electrochemical Corrosion*. ASM International, 2000.

[117] R Bouclier et al. Study of materials outgassing and their effect on gaseous detector lifetime. *CMS TN/96-038*, 1996.

[118] M Capéans-Garrido. Aging and materials: Lessons for detectors and gas systems. *Nucl. Instrum. Methods Phys. Res., A*, 515:73–88, 2003. URL https://cds.cern.ch/record/808011.

[119] . URL https://outgassing.nasa.gov/.

[120] F Paschen. *Wied. Ann.*, 37:69, 1889.

[121] K Gnanvo. Monitoring apv25-srs with amore. In *RD51 Electronics School*, 2014.

[122] CMS GEM Collaboration, . URL https://twiki.cern.ch/twiki/bin/view/MPGD/CmsGEMConferences.

Jérémie MERLIN

Etude du fonctionnement à long terme de détecteur gazeux l'environnement à haut flux de CMS

Résumé

Le spectromètre à muons de CMS doit permettre l'identification rapide et efficace des muons produits lors des collisions proton-proton au LHC. Cependant, à cause d'un environnement de détection extrême, seules les chambres à pistes cathodiques équipent actuellement les bouchons de CMS. Cette faiblesse dans le système de détection pourrait devenir problématique après l'amélioration du LHC. L'augmentation du taux de particules dans les bouchons va dégrader les performances du système de déclenchement L1 ainsi que l'efficacité de sélection des phénomènes physiques intéressants. Le but du programme d'amélioration de CMS est de maintenir le taux de déclenchement L1 tout en gardant une efficacité de sélection maximale. La collaboration CMS GEM propose d'équiper les régions vacantes des bouchons avec des détecteurs basés sur la technologie d'amplification des électrons dans un gaz (GEM), appelés GE1/1.

Le sujet de thèse proposé par la collaboration CMS GEM a pour but de justifier le choix de la technologie GEM pour l'amélioration de CMS. Trois projets ont été suivis pendant la thèse.

La première partie du projet de thèse consistait à mesurer précisément les caractéristiques fondamentales et les performances de détection des détecteurs triple-GEM produit par la technique simple-masque. Ces éléments sont essentiels pour s'assurer que les détecteurs GE1/1 pourront fonctionner en toute sécurité dans l'environnement des bouchons de CMS.

Le deuxième projet consistait à prouver que les excellentes performances des détecteurs GE1/1 ne vont pas se dégrader pendant leur utilisation dans CMS. Cette étape comprend l'étude du fonctionnement à long terme des détecteurs GE1/1, en particulier le phénomène de vieillissement, qui inclue tous les processus physiques et chimiques qui provoquent la dégradation graduelle et permanente des performances de détection. Plusieurs tests de vieillissement ont été menés dans des zones d'irradiations spécifiques au CERN pour reproduire un minimum de 10 ans de fonctionnement réel dans l'environnement de CMS après la montée en puissance du LHC.

Enfin, les excellentes propriétés mesurées lors de la phase de R&D ont permis de valider la technologie triple-GEM, qui fut ensuite approuvée par la collaboration CMS et le comité du LHC. La production de 144 grands détecteurs GE1/1 sera partagée entre différents sites de production à

travers le monde. Le troisième projet de thèse fut donc le développement des principales étapes du contrôle qualité nécessaire pour assurer une production uniforme et une même qualité pour tous les détecteurs GE1/1.

Mots clés : CMS, amélioration, détecteurs gazeux, GEM, caractérisation, performances, vieillissement, gain effectif.

Résumé en anglais

The muon system of CMS aims to provide an efficient and fast identification of the muons produced in the proton-proton collisions. However, the forward region of the end-caps is only instrumented with Cathode Strip Chambers. This lack of redundancy will be problematic after the high-luminosity upgrade of the LHC (HL-LHC), for which the increase of the background rate would degrade the Level-1 trigger performance and thus the selection of interesting physics channels. The goal of the CMS muon upgrade is to maintain the L1 trigger rate with maximum selection efficiency in order to fully exploit the HL-LHC. The CMS GEM Collaboration has proposed to instrument the vacant high-eta region of the muon end-caps with Gas Electron Multiplier (GEM) detectors, called GE1/1 chambers.

The Ph.D. subject proposed by the CMS GEM Collaboration aims to demonstrate that the GE1/1 technology is the most suitable choice for the upgrade of the muon end-caps. Three main research projects were conducted in this context.

The first project included the precise measurement of the fundamental characteristics and the detection performance of the triple-GEM detectors produced with the single-mask technique. Those characteristics are essential to ensure that the detectors can operate in the forward region of CMS.

The second project was focused on the long-term operation of GE1/1 detectors, in particular the study of the aging phenomenon, which includes all the processes that lead to a significant and permanent degradation of the performance of the detectors. Several aging tests were performed at the CERN irradiation facilities to prove that the GE1/1 chambers can operate during at least 10 years at HL-LHC without suffering from performance losses.

The excellent properties measured during the R&D phase led to the approval of the GE1/1 project by the CMS Collaboration. The third project, conducted in the framework of the mass production, consisted of developing of the main steps of the Quality Control of the GE1/1 chambers.

Key words: CMS, upgrade, gaseous detectors, GEM, characterization, performance, aging, effective gain